HAL
open science

Détection de l'endommagement dans un composite tissé PA66,6/Fibres de verre à l'aide de techniques ultrasonores en vue d'une prédiction de la durabilité de pièces automobiles

Pascal Pomarede

To cite this version:

Pascal Pomarede. Détection de l'endommagement dans un composite tissé PA66,6/Fibres de verre à l'aide de techniques ultrasonores en vue d'une prédiction de la durabilité de pièces automobiles. Mécanique des matériaux [physics.class-ph]. Ecole nationale supérieure d'arts et métiers - ENSAM, 2018. Français. NNT : 2018ENAM0024 . tel-01932575

HAL Id: tel-01932575

https://pastel.hal.science/tel-01932575

Submitted on 23 Nov 2018

HAL is a multi-disciplinary open access archive for the deposit and dissemination of scientific research documents, whether they are published or not. The documents may come from teaching and research institutions in France or abroad, or from public or private research centers.

L'archive ouverte pluridisciplinaire **HAL**, est destinée au dépôt et à la diffusion de documents scientifiques de niveau recherche, publiés ou non, émanant des établissements d'enseignement et de recherche français ou étrangers, des laboratoires publics ou privés.

2018-ENAM-0024

École doctorale n° 432 : Sciences des Métiers de l'ingénieur

Doctorat ParisTech

T H È S E

pour obtenir le grade de docteur délivré par

l'École Nationale Supérieure d'Arts et Métiers

Spécialité " Mécanique et Matériaux "

présentée et soutenue publiquement par

Pascal POMAREDE

le 18 Mai 2018

Damage detection in PA 66/6|Glass woven fabric composite material using ultrasonic techniques towards durability prediction of automotive parts

Directeur de thèse : **Fodil MERAGHNI**
Co-encadrement de la thèse : **Nico F. DECLERCQ**

Jury

M. Christ GLORIEUX, Professeur, Department of Physics and Astronomy, KU Leuven	Président - Rapporteur
M. Ahmad OSMAN, Professeur, Fraunhofer IZFP, HTW des Saarlandes	Rapporteur
Mme Nathalie GODIN, Maitre de conférences, Mateis, INSA Lyon	Examinateur
Mme Lynda CHEHAMI, Maitre de conférences, UVHC, Université de Valenciennes	Examinateur
M. Fodil MERAGHNI, Professeur, LEM3, Arts et Métiers ParisTech - Metz	Examinateur
M. Nico F. DECLERCQ, Professeur, LUNE, Georgia Tech Lorraine	Examinateur
M. Stéphane DELALANDE, Docteur, PSA Group– Centre Technique Vélizy	Examinateur

T H È S E

Arts et Métiers ParisTech - Campus de Metz
Laboratoire d'Etude des Microstructures et Mécanique des Matériaux (LEM3)

Remerciements

Ce sujet s'est déroulé dans le cadre de l'Open Lab Materials & Processes mené par le Groupe PSA que je tiens à remercier pour avoir proposé ce sujet de thèse et pour son financement. Un grand merci à Mr Stéphane Delalande, mon contact privilégié avec le groupe PSA, qui a toujours montré un grand intérêt pour ce projet. Ses retours et discussion ont toujours été d'une grande aide.

Mes remerciements vont à présent à mes deux encadrants de thèse, MM Fodil Meraghni et Nico F. Declercq. Merci à eux pour leur disponibilité et leur soutien durant ces trois (et un peu plus) années même durant les moments de doute. Je tiens à les remercier pour leur écoute et leur investissement sur ce projet qui a permis l'étude de nombreuses méthodes (notamment de Contrôle Non Destructif); ce qui a participé grandement à l'enrichissement de ce sujet de thèse auquel je tiens énergiquement à les associer. Je vous remercie finalement pour les nombreux échanges, scientifique ou non, que nous avons eu durant ces années.

Je souhaite remercier les membres de mon jury de thèse, tout d'abord Mr Christ Glorieux, qui a accepté de présider ce jury, ainsi que Mmes Lynda Chehami et Nathalie Godin et Mr Ahmad Osman pour les discussions enrichissantes durant la soutenance de thèse.

Ces travaux ont été réalisé conjointement au laboratoire LEM3 du campus Arts et Metiers ParisTech de Metz et au laboratoire LUNE (Laboratory for Ultrasonic Nondestructive Evaluation), UMI 2958, de Georgia Tech Lorraine. Je tiens donc à remercier leurs équipes respectives pour leur accueil durant ce projet.

Tout d'abord merci, merci à l'équipe de Georgia Tech Lorraine que j'ai eu la chance de côtoyer. Patrick Guillaume., Olivier Konne. pour leur support technique à Georgia Tech Lorraine. Je remercie toute l'équipe TeraHertz (Junliang Dong (DR.!), Alexandre Locquet, David S. Citrin) avec laquelle une forte collaboration a été possible. Merci à Lynda et Esam qui ont été d'un grand soutien (moral et scientifique) durant leurs post-docs au labo LUNE.

Je remercie également toute l'équipe du LEM3. Laurent (continue d'écouter et de propager du bon son !!) et Patrick pour leur GRANDE aide durant les essais et leur bonne humeur communicative.

Merci à tous les doctorants (maintenant docteurs) de l'équipe au LEM3 pour tous les bons moments passés ensemble, au labo mais aussi à la ville: Francis A., Dimitris C., Marie, Nicolas. Merci aussi à Sebastian, Akbar, Boris, Georgina, Aziz « T'a pas encore fini? », Pierre, Gael, Sylvain, Dominique. Merci aux petits (?) derniers El Hadi, Paul(s) D. et L. (Nord et Sud).

Merci à Nada et Soraya pour leur soutien jusque durant la dernière ligne droite et grâce à qui un « certain bureau » a continué à être « régulièrement transformé en salle de pause ».

Je n'oublie pas Clément « CND » et Francis P. qui ont formé avec moi la team des « trois mousquetaires » qui a commencé leurs thèses en même temps. J'ai pu affronter grâce à eux ces trois années avec succès et je rejoins enfin avec eux le cercle des docteurs. Je me permets d'ajouter Kevin (d'Artagnan ?) à cette team, lui qui nous a supporté aussi longtemps que nos encadrants. Merci pour tes conseils et ton enthousiasme.

Je remercie aussi tous mes amis, Bob leur sera éternellement reconnaissant ;-)

Merci enfin à ma famille pour leur soutien sans faille sans lequel je ne serais pas là où je suis aujourd'hui.

Contents

Contents i

List of figures vi

List of tables xxv

Part I : Résumé étendu en Français 1

1) Introduction générale 3

2) Présentation du composite tissé de l'étude : Un polyamide 66/6 renforcé par des fibres de verre tissées 5

a) La matrice polyamide 66/6 6

b) Le renfort en fibres de verres tissées 7

3) Caractérisation du comportement mécanique du composite étudié lors de sollicitations monotone et cyclique en traction 8

4) Etude des mécanismes d'endommagement : analyses quantitatives et qualitatives 14

5) Méthodes ultrasonores de Contrôle Non Destructif (CND) 18

a) Détermination du tenseur de rigidité par mesure des vitesses de propagation ultrasonore 19

b) Mesures par ondes de Lamb guidées 24

6) Validation sur échantillon impacté par poids tombant 31

7) Conclusion générale et perspectives 41

Part II: Damage detection in PA 66/6|Glass woven fabric composite material using ultrasonic techniques towards durability prediction of automotive parts 45

I) Introduction 46

1) Context 46

2) Objectives and research orientations 50

II) Description of the studied composite material: Woven glass reinforced polyamide 66/6 53

1) Overview of composite material 55

a) Matrix Parts 55

b) Reinforcements 56

2) Components of the studied composite material 57

a) Glass fibers 58

b) Polyamide 66/6 matrix 64

c) Properties of the composite material 70

3) Conclusion 73

III) Characterization of the mechanical behavior of the studied composite material under monotonic and cyclic loading 75

1) Description of the experimental procedure 76

2) Monotonic tensile test for the 0° configuration 79

3) Monotonic tensile test for the 45° configuration 82

4) Incremental cyclic tensile test 88

5) Conclusion 92

IV) Damage mechanisms investigation: quantitative and qualitative analysis 95

1) Optical microscopy analysis of undamaged composite 97

2) Damage initiation 99

3) Fractography analysis 102

4) X-ray tomography analysis 104

a) 0° oriented - Undamaged sample 108

b) 0° oriented - Damaged sample 111

c) 45° oriented – Damaged sample 113

d) Void volume fraction evolution 116

5) Conclusion 117

V) Non Destructive Evaluation (NDE) methods based on ultrasound 119

1) Review of ultrasonic method of Non Destructive Evaluation (NDE) of damage 122

a) Ultrasonic imaging techniques: transmission and reflection 122

b) Multi angle ultrasonic investigation of material 125

c) Guided waves based testing methods 139

d) Nonlinear acoustic method 146

e) Coda waves in Non-Destructive Testing 154

f) Synthesis of the Non Destructive Evaluation method review 159

2) Ultrasonic C-scan in transmission 160

3) Stiffness tensor components determination 161

a) Description of the experimental procedure and first analysis 162

b) Experimental results: 0° configuration after tensile test..... 180

c) Experimental results: 45° configuration after tensile test..... 184

d) Proposed damage indicators 190

4) Guided Lamb waves 195

a) Preliminary investigation on an aluminum plate 196

b) Investigations of the woven glass fiber reinforced polyamide 66/6 samples damaged by tension 199

5) Conclusion 215

VI) Validation on samples impacted by drop weight 219

1) Drop weight impact tests 221

2) X-Ray tomography investigations of the impacted plates 225

3) Ultrasonic C-scan results 226

4) Validation of the ultrasonic based damage indicators 232

a) Ultrasonic measurement of stiffness components on the impacted plates ... 232

b) Guided waves based approach..... 235

5) Conclusion 239

VII) Concluding remarks and further works 243

1) Concluding remarks 243

2) Further works 246

VIII) References 247

IX) Appendix 257

1) Appendix 1: Damage investigation using nonlinear acoustic methods on different woven fiber reinforced composite materials 257

a) Nonlinear Wave Modulation Spectroscopy (NWMS) method 259

b) Resonance frequency shift study 265

c) Nonlinear Resonant Ultrasound Spectroscopy (NRUS) 267

d) Conclusion 269

2) Appendix 2: Damage investigation using Coda Waves Interferometry (CWI) technique on a woven carbon fibers reinforced composite material 270

a) Presentation of the investigated composite material 270

b) Experimental set-up 271

c) Conclusion 280

List of figures

Figure 1 : Procédé de moulage par thermo-compression pour la fabrication des composites de série Vizilon (Source: DuPont) 5

Figure 2 : Courbe contrainte/déformation, en traction à 23°C, pour un Polyamide 66/6 (Ultramid® C3U de BASF) sec (vert) et après conditionnement 50% HR (rouge) [http://iwww.plasticsportal.com/] 7

Figure 3 : Position des éprouvettes orientées à 0° et 45° par rapport au sens chaine (direction du sens de l'écoulement) pour la plaque en composite. 9

Figure 4 : Réponses contrainte/déformation obtenues par corrélation d'image (Gauche) et extensomètre (Droite) sur trois échantillons dans la configuration 0°. 10

Figure 5 : Réponses contrainte/déformation obtenues par corrélation d'image (Gauche) et extensomètre (Droite) sur trois échantillons dans la configuration 45°. 10

Figure 6 : (a) Champs de déformation ε_{11} pour un échantillon dans la configuration 0°. (b) Champs de déformation ε_{22} pour un échantillon dans la configuration 45°. Les deux champs sont calculés peu avant la ruine. 12

Figure 7 : Mesure des modules E_0 et E_n sur une courbe charge/décharge 13

Figure 8 : Comparaison de l'évolution de la réduction du module d'Young lors d'essais cycliques incrémentaux en traction pour des échantillons dans la configuration 0° et 45°. 13

Figure 9: Images MEB lors d'essais de traction in-situ pour différents niveaux de changements appliqués suivant l'axe des fibres 15

Figure 10 : Courbes contrainte/déformation typiques du polyamide 66/6 renforcé de fibres de verre tissées dans la configuration 0° et 45°. Les cercles rouges indiquent le niveau de

contrainte et de déformation pour lesquels les essais de traction (réalisés sur différents échantillons) ont été interompus comme resumé dans le Tableau 3. 15

Figure 11 : Récapitulatif des mécanismes d'endommagement et leurs tailles caractéristiques associées pour les échantillons dans la configuration 0° and 45° 17

Figure 12 : Evolution de la fraction volumique de vides obtenue par tomographie aux rayons X pour des échantillons précédemment endommagées suivant les valeurs de chargement en traction..... 18

Figure 13 : Essai C-scans préliminaires sur le composite polyamide 66/6 renforcé avec des fibres de verre tissée chargé en traction à différents niveaux. (a): Echantillons en configuration 0°; (b): Echantillons en configuration 45°. Pour ces derniers,de large zones d'endommagement sont clairement visible. 19

Figure 14 : Schéma représentatif des différents plans de propagation des ondes de volume (a) Plans de propagation pour la configuration 0° (b) Plans de propagation pour la configuration 45° 20

Figure 15 : Evolution de sept des constantes de rigidité en fonction du chargement, pour différents échantillons orientés à 0°. 22

Figure 16 : Evolution de onze des constantes de rigidité en fonction du chargement pour différents échantillons orientés à 45°. 23

Figure 17 : Evolution des différents indicateurs d'endommagement utilisés jusqu'ici. a) Fractions volumiques de vides obtenues par tomographie à rayons X. b) Réduction du module élastique. c) Norme de Frobenius du tenseur de rigidité obtenue par mesure ultrasonore. d) Déphasage des signaux ultrasonores utilisé pour le calcul du tenseur de rigidité..... 24

Figure 18 : Montage expérimental pour la mesure des modes d'ondes guidées 25

Figure 19 : Spectrogramme d'un signal transmis dans un échantillon dans (a) la configuration 0° et (b) la configuration 45 ° avec le signal temporel correspondant..... 26

Figure 20 : Transformée de Fourier 2D pour un échantillon intact dans la configuration 0° avec les modes S_0, A_0, S_1 et A_1. Le tenseur de rigidité obtenu par homogénéisation périodique a été utilisé pour les modes en lignes continues. Le tenseur obtenu par mesures ultrasonores, a lui été utilisé pour celles en lignes discontinues. 26

Figure 21 : Transformée de Fourier 2D pour un échantillon intact dans la configuration 45° avec les modes S_0, A_0, S_1 and A_1. Le tenseur de rigidité obtenu par homogénéisation périodique a été utilisé pour les modes en lignes continues. Le tenseur obtenu par mesures ultrasonores, a lui été utilisé pour celles en lignes discontinues. 27

Figure 22 : Deux signaux transmis avec un exemple de mesure des vitesses de (a) groupe et de (b) phase..... 28

Figure 23 : Courbes de dispersion des vitesses de phase en fonction de la fréquence pour des échantillons dans (a) la configuration 0° et (b) la configuration 45°. La matrice de rigidité, obtenue par homogénéisation périodique, a été utilisée pour les modes représentés par la moyenne des lignes continues. Alors que la matrice de rigidité obtenue par acquisitions ultrasonores a été utilisée pour les lignes discontinues. 29

Figure 24 : Comparaison entre les évolutions des deux indicateurs d'endommagement considérés (a) DI_3 et (b) DI_4 pour les deux orientations d'échantillon considérées. 31

Figure 25 : (a) Coubes force/temps, (b) courbes déplacement/temps et (c) courbes énergie/temps pour les quatre énergies de poids tombant considérées. Le capteur de déplacement sature pour une hauteur de chute de 2.00 M..... 33

Figure 26 : Faces non-impactée des plaques pour des énergies d'impact de (a) 10 J, (b) 15 J, (c) 17.5 J, et (d) 20 J. 34

Figure 27 : C-scans ultrasonore en transmission obtenue avec un transducteur de 10 MHz pour les plaques impactée à des niveaux d'énergies de (a) 10, (b) 15, (c) 17.5 et (d) 20 J. 35

Figure 28 : (a) Carte des temps d'arrivés du premier pic positif de la plaque impactée à 20 J. L'indentation permanente est colorée en rouge (b) Zoom sur un des B-scans de la plaque impactée à 20 J. 35

Figure 29 : Evolution des neuf composantes du tenseur de rigidité du matériau composite testé en fonction de l'énergie d'impact..... 38

Figure 30 : (a) Evolution de la norme de Frobenius du tenseur de rigidité obtenu par mesures ultrasonores et (b) evolution du déphasage avec l'énergie d'impact 39

Figure 31 : Résultat de la corrélation croisé effectué sur les quatre plaques impactées..... 40

Figure 32 : (a) Evolution du maximum de coefficient de corrélation avec la position des transducteurs. (b) Evolution du décalage temporelle avec la position des transducteurs. Les mesures sont faites sur la plaque impactée à 20 J..... 41

Figure 33 : Required reduction of $C0_2$ emission for large scale produced cars in different countries over years [Groupe PSA] 47

Figure 34 : Forecast volumes of advanced composites components in the automotive industry [Composites, Forecasts and Consulting] 48

Figure 35 : Representation of the different textile fabrics used in the composite industry [114] 60

Figure 36 : Meshing of a 2/2 twill weave fabric [115] (Courtesy of Francis Praud) 61

Figure 37 : Schematic representation of the differents woven armor classicaly used in composites material [15] 62

Figure 38 : Damage mechanisms in a woven composite loaded in tension along the fibers axis [18] 63

Figure 39 : Fibers rotations during tensile tests on samples oriented at 45° from the warp direction [116] 64

Figure 40 : Post failure damage mechanisms after tensile tests on samples oriented at 45° from the warp direction [116]..... 64

Figure 41 : Stress/strain curve, in tension at 23°C, for a Polyamide 66/6 (Ultramid® C3U from BASF) dry (Green) and after conditionning 50% RH (Red) [http://iwww.plasticsportal.com/]..... 66

Figure 42 : Moisture absorption function of time for different polyamide and different thickness when conditioning in “atmosphere 23” conditions. The moisture equilibrium for a polyamide 66 (*Ultramid* A) by *BASF* is reached around 2.5% [22]..... 67

Figure 43 : Young’s modulus of classical polymers as function of their temperature and crystallinity [117] 69

Figure 44 : Evolution of the vitreous transition temperature T_g with the relative humidity (Courtesy of Solvay)..... 69

Figure 45 : Compression molding process for a composite of the Vizilon series (Source: DuPont)..... 70

Figure 46 : (a) RVE of the material and (b) 3D representation of the 2/2 twill weave fabric of the Vizilon$_{TM}$ SB63G1-T1.5-S3 obtained by X-ray tomography 71

Figure 47: Comparison of the ratio rigidity/formability (Left) and weighted strength/ weighted modulus (right) of the studied composite material with others classically used material: (Source: *DuPont*)..... 72

Figure 48 : Position of the samples oriented at 0° and 45° from warp direction (mold flow direction) on the composite plate. The direction “1” is the loading direction in tension. 77

Figure 49 : Experimental set-up of the tensile test with all the displacement measurement sensors 78

Figure 50 : Stress/Strain curves for one of the samples with fibers oriented at 0° with the four displacement sensors considered 79

Figure 51 : 0° oriented samples after tensile test until failure 80

Figure 52 : Stress/Strain curve obtained with DIC (Left) and Extensometer (Right) for the three tested samples oriented at 0° from fiber's axis 80

Figure 53 : Nonlinearity point on the stress-strain curve from DIC acquisitions 81

Figure 54 : a): $\boldsymbol{\varepsilon_{11}}$ strain field during tensile tests right before failure. b) : sample right after failure 82

Figure 55 : 45° oriented sample after tensile test until failure 83

Figure 56 : Stress/Strain curves for the 45° orientation for the entire displacement sensor considered (Here the sample was not solicited until breakage) 83

Figure 57 : Stress/Strain curve obtained with DIC (a) and Extensometer (b) for the three tested samples oriented at 45° from fiber's axis 84

Figure 58 : $\boldsymbol{\varepsilon_{22}}$ strain field at the (a) beginning (b) middle (c) end of the test for a sample in the 45° configuration during a tensile test 85

Figure 59 : Tested sample in the 45° configuration just before failure (Left) and after failure (Right) from a tensile test 86

Figure 60 : $\boldsymbol{\varepsilon_{11}}$ (Left) and $\boldsymbol{\varepsilon_{12}}$ (Right) strain field for the 45° configuration during a tensile test 87

Figure 61 : Comparison between the behavior in the 0° configuration and the 45° configuration. Displacement measured with Digital Image Correlation 87

Figure 62 : Monotonic tensile test and incremental (20 MPa) cyclic test for the 0° configuration 88

Figure 63: Monotonic tensile test and incremental (20 MPa) cyclic test for the 45° configuration 89

Figure 64 : Measurement of the E_0 and E_n moduli on a loading unloading curve 90

Figure 65 : Evolution of damage function of the maximal stress of the cycle for a 0° (Left) and 45° (Right) oriented sample 91

Figure 66 : Comparison of the Young modulus reduction during incremental cyclic test for 0° and 45° oriented samples 92

Figure 67: Microstructure observation via optical microscope of the polyamide 66/6 reinforced with woven glass fibers. (a) and (b) depict respectively 0° and 45° configurations. (c) is a magnification on a sample in the 0° configuration 98

Figure 68 : a) Crack visible in transversal yarns, b) Micro porosities in the 45° configurations c) Micro porosities in the 0° configurations. 99

Figure 69 : Transversal yarns during SEM in-situ tensile test for different applied force . 101

Figure 70 : Fiber/matrix deboning obtained with SEM 101

Figure 71 : Rupture mechanisms observed for samples oriented along the fiber axis 103

Figure 72 : Rupture mechanisms observed for samples oriented at 45° from fiber axis.... 103

Figure 73 : Principle of the X-Ray tomography techniques [http://www.techmaxasia.com] 105

Figure 74 : Slices of an undamaged sample; Top: Raw image, Middle: After a Median filter, Bottom: After a Median filter + a Despeckle filter 106

Figure 75 : Schematic representation of the observed area on a polyamide 6,6 /Woven glass fiber samples and the associated 3D reconstruction 107

Figure 76 : Typical stress/strain curve of the PA66/6 reinforced with woven glass fiber in the 0° and 45° configurations. The red circles show schematicaly the strain and stress levels where the different tensile tests (performed on several specimens) have been interrupted as summarized in Table 12. Ultrasonic measurements and X-ray tomography investigations are then performed on those specimens 107

Figure 77 : Transversal (Weft) yarns measurement on a slice of an undamaged sample obtained via X-Ray tomography 109

Figure 78 : Slices of the undamaged sample oriented along the fiber axis in different directions before 3D reconstruction 109

Figure 79 : Three dimensional reconstruction of undamaged samples, in the 0° and 45° configuration, with initial porosity (Yellow) 110

Figure 80 : mCT-3D reconstructions of composite samples in the 0° configuration respectively (a) before and (b) after tensile loading at a stress level of 92.6 %σUTS0°. ... 112

Figure 81 : Slices of the sample loaded at 300 MPa in tension along the warp axis before 3D reconstruction 112

Figure 82 : Damage mechanisms observed in woven composite sample loaded in tension at 45° from the warps axis. 114

Figure 83 : Pseudo-delamination in a woven composite sample loaded in tension at 45° from the warps axis at a stress level of 120MPa. 114

Figure 84 : mCT-3D reconstructions of composite samples in the 45° configuration respectively (a) before and (b) after tensil loading at a stress level of 91.6 %σUTS0°..... 115

Figure 85 : Summary of the damage mechanisms and their associated typical scale for both 0° and 45° oriented samples. 116

Figure 86 : Void volume fraction evolution obtained with X-ray tomography on previously damaged samples with respect to the tensile loading values. 117

Figure 87 : Left: Ultrasonic Pulse Echo (UPE); Right: Ultrasonic in transmission (UPV) [Krautkramer NDT Ultrasonic Systems] 123

Figure 88 : Examples of C-scan with 12 slices cut on top of each other of a fiber reinforced composites materials damaged by impact [49] 124

Figure 89 : Slowness curve of the different waves mode that propagate inside a carbon-epoxide composite sample immersed in water [118] 128

Figure 90 : Schematic representation of the wave mode conversion principle propagating in a plane of symmetry [www.olympus-ims.com] 129

Figure 91 : Schematic representation of the principle of time of flight measurement of the stiffness components measurement in immersion 130

Figure 92 : Schematic representation of the wave velocity measurement method in immersion [Inspired from perso.univ-lemans.fr] 132

Figure 93 : Figure of the three planes used to compute the nine rigidity constants of an orthotropic material [51] 133

Figure 94 : Left: Polar scan with two transducers in transmission mode [62]; Right: Polar scan with an acoustic mirror [39] 136

Figure 95 : Left: Pulsed polar scan on a satin weave carbon fabric/PPS laminate [67]; Right: Pole figure for an aluminum sample [119] 137

Figure 96 : Carbon/Epoxy [$0°_2$,$90°_2$] sample; a) : microscope observation of the surface of the sample; b) Double transmitted signal; c) Backscattered signal [67] 138

Figure 97 : Carbon/Epoxy UD sample; a) : microscope observation of the surface of the sample; b) Double transmitted signal; c) Backscattered signal [67] 138

Figure 98 : Backscattered signal on Glass/Epoxy $[-45°,+45°]_s$; a) :Undamaged; b) Loaded in shear stress at 42.5 MPa [60]..... 139

Figure 99 : Left :Signal of Lamb waves from numerical results with a S0 and A0 mode visible [120]..... 140

Figure 100 : Typical phase velocity dispersion curves for aluminum..... 141

Figure 101 : Decomposition of a Lamb waves signal in A0 and S0 modes [121]..... 144

Figure 102 : Results of a 2D-FFT in the wavenumber-frequency domain [72]..... 144

Figure 103 : Schematic representation of the considered aluminum sample with a notch type defect. a) Top observation, b) Side observation, c) Side observation + ultrasonic wave's propagation through the sample (Based on [77])..... 145

Figure 104 : Side observation of the sample + ultrasonic wave's propagation through the sample. 2D Fourier transform results for the incident, reflected and transmitted wave with the theoretical dispersion curves. (Based on [77]) 145

Figure 105 : Schematic representation of the different Nonlinear Elastic Waves Spectroscopy (NEWS) with references for each of them..... 148

Figure 106 : Schematic spectrum that can be obtain with the NRUS method for an undamaged (left) and damaged (right) sample [83] 149

Figure 107 : Schematic representation of the principle of the NWMS technique: spectral analysis of the nonlinear acoustic response of a damaged sample caused by apparition of harmonics and sidebands (Based on [108])..... 151

Figure 108 : Numerical results obtained after identification of the attenuation model parameters for concrete 154

Figure 109 : Schematic representation of the different wave propagation regime [122] ... 155

Figure 110 : Signal waveforms collected on a CRFP composite before (h0) and after (h1) an increase of temperature [96] ... 156

Figure 111 : Preliminary C-scan results on 2/2 twill weave fabric reinforced polyamide composite previously loaded in tension with different amplitude. (a): Samples in 0° configuration ; (b): Samples in 45° configuration. For the latter, besides the large damage zones, one can easily distinguish the 45° orientation of the yarns. ... 161

Figure 112 : Schematic representation of the different propagation planes of ultrasonic waves. (a) Propagation planes in the 0° configuration, (b) Propagation planes in the 45° configuration. ... 162

Figure 113 : LUNE lab's 5 axis ultrasonic robot from Inspection Technology ... 163

Figure 114 : Emitted pulse shape (Left) and spectrum (Right) for a 2.25MHz centered frequency transducer; The experimentally mesured central frequency is about 2.1 MHz . 163

Figure 115 : Response signal of a wave traveling in water (without the sample) ... 164

Figure 116 : Schematic representation of the two planes of interest. The plane 1-3 on the left and 2-3 on the right ... 164

Figure 117 : Transmitted signal (left) and associated spectral response (Right) propagated in an undamaged sample for incidence angle of 0° and 13°. Information for a signal propagated only in water was added for comparison purpose ... 166

Figure 118 : Experimental set-up for measurement in the plane 1-2 ... 167

Figure 119 : Relative difference between the velocities values obtains with two considered calculation method ... 170

Figure 120 : Comparison of numerically and experimentally determined propagation wave velocities in the plane (1-3). The experimental values are represented by points whereas numerical values are represented in continuous line. 171

Figure 121 : Comparison of numerically and experimentally determined propagation wave velocities in the plane (2-3). The experimental values are represented by points whereas numerical values are represented in continuous line. 171

Figure 122 : Dispersion curves computed with the *Disperse software* for guided wave propagation in a 1.53mm thick studied composite along the fibers direction. (a) Phase Velocities, (b): Group Velocities. 172

Figure 123 : Comparison between experimental and numerical phase velocities for different propagation direction in the 1-2 plane. 173

Figure 124 : Time of flight of longitudinal wave (Left) and transversal wave (Right) for all the chosen incidence angles 179

Figure 125 : Stress/strain curve for a tensile test on a 0° oriented sample. The red circles indicate the chosen loading for the five tested samples 181

Figure 126 : Evolution of seven of the stiffness components with the increase of the loading for different 0° oriented sample 182

Figure 127 : Stiffness curves for two samples oriented at 0° from the fiber's axis. An undamaged sample and a sample loaded in tension at 300 MPa 183

Figure 128 : Schematic representation of the different propagation planes of ultrasonic waves. For samples in the 0° configurations, the planes 1-3 and 1-2 were used. For the samples in the 45° configuration, the plane X_1-3 and 1-2 were used. 185

Figure 129 : Stress/strain curve for a tensile test on a 45° oriented sample. The red circles indicate the chosen loading for the three tested 185

Figure 130 : Evolution of eleven of the rigidity constants with the increase of the loading for different 45° oriented sample with a third order interpolation 186

Figure 131 : Stiffness curves for two samples oriented at 45° from the fiber's axis. An undamaged sample and a sample loaded in tension at 120MPa 188

Figure 132 : Damage evolution with stress level of samples oriented at 0° and 45° obtained via ultrasonic measurements 190

Figure 133 : Evolution of the maximal amplitude for sample in the (a) 0° configuration and (b) 45° configuration. Evolution of the frequency shift for sample in the (c) 0° configuration and (d) 45° configuration. 191

Figure 134 : Evolution of the Frobenius norm of the stiffness matrix for the two configurations of samples (a): 0° and (b) 45° configuration. In (c) both configurations are plotted for comparison purpose. 193

Figure 135 : Phase shift indicators evolution with increasing tensile stress for samples oriented at 0° and 45° (Resp; Left and Right) and for the two tested principal plane 1-2, 1-3 and the average on the two plane (Resp: a, b and c) 194

Figure 136 : Evolution of the void volume fraction evolution measured with X-ray tomography; Signal phase shase shift measured with an ultrasonic method and the elastic modulus loss measured during incremental cycling tensile tests 195

Figure 137 : Investigated aluminum plate. Several defects are appearing in the plate, mostly holes of different diameter. A large notch is also visible 197

Figure 138 : Transmitted signal for different defects and a reference case when a burst of a) 500KHz and b) 1MHz is emitted 198

Figure 139 : Experimental set-up of the guided waves experiment 200

Figure 140 : 2D Fast Fourier Transform for the undamaged specimen in the 0° configuration for mode S_0, A_0, S_1 and A_1. The stiffness matrix obtained by periodic homogenization was used for the modes represented by mean of continuous lines. Whereas the matrix obtained by ultrasonic acquisitions was used for the ones plotted in dashed lines. 201

Figure 141 : Two transmitted signals with an example of (a) group and (b) phase velocity measurement 202

Figure 142 : Distance/time evolution obtained for the undamaged samples oriented at 0° used in order to calculate the phase velocity 203

Figure 143 : Phase velocity/Frequency dispersion curves for sample in the 0° configuration. The stiffness matrix obtained by periodic homogenization was used for the modes represented by mean of continuous lines. Whereas the matrix obtained by ultrasonic acquisitions was used for the ones plotted in dashed lines. 204

Figure 144 : 2D Fast Fourier Transform for the undamaged specimen in the 45° configuration for mode S_0, A_0, S_1 and A_1. The stiffness matrix obtained by periodic homogenization was used for the modes represented by mean of continuous lines. Whereas the matrix obtained by ultrasonic acquisitions was used for the ones plotted in dashed lines. 205

Figure 145 : Phase velocity/Frequency dispersion curves for sample in the 45° configuration. The stiffness matrix obtained by periodic homogenization was used for the modes represented by mean of continuous lines. Whereas the matrix obtained by ultrasonic acquisitions was used for the ones plotted in dashed lines. 205

Figure 146 : a) Complete experimental set-up used to measure the top and bottom signals from a transmitted Lamb waves. b) Zoom in on the transducers holder system 206

Figure 147 : 2D Fast Fourier Transform for (a) the signal recorded on the top surface in the 0° configuration and (b) the signal recorded on the bottom surface in the 0° configuration.

2D Fourier transform for (c) the signal recorded on the top surface in the 45° configuration and (d) the signal recorded on the bottom surface in the 45° configuration. 207

Figure 148 : Typical signals measured on top and bottom surface of sample in the (a) 0° configuration and (b) 45° configuration 208

Figure 149 : Spectrogramme d'un signal transmis dans un échantillon dans (a) la configuration 0° et (b) la configuration 45 ° avec le signal temporel correspondant..... 209

Figure 150 : 2D Fast Fourier Transform for the samples, in the 0° configuration, loaded in tension at a) 150, b) 200, c) 250 and d) 300MPa..... 210

Figure 151 : 2D Fast Fourier Transform for the samples, in the 45° configuration, a) undamaged and loaded in tension at b) 40, c) 80 and d) 120MPa..... 211

Figure 152 : Time signal of guided waves propagation inside an undamaged and a highly damage sample for a): Sample oriented at 0° from the yarns direction; b): Sample oriented at 45° from the yarns direction 212

Figure 153 : Evolution the damage indicators DI_3 for the samples oriented at 0° and 45° in respectively a) and b)..... 214

Figure 154 : Comparison of the evolution of the two considered damage indicator, DI_3 in (a) and DI_4 in (b), for the two considered samples' orientation..... 215

Figure 155 : Drop weigh test machine installation of LAMPA at ENSAM Angers campus 222

Figure 156 : (a) Force time curves, (b) displacement time curves and (c) Energy time curves for the four considered drop weight energies. The displacement sensor saturates during the 20 J impact test. 223

Figure 157 : Visual observation of the plates on the impacted side for an impact energy of (a) 10, (b) 15, (c) 17.5 and (d) 20 J..... 224

Figure 158 : Visual observation of the damage in the plates on the opposite of the impacted side for an impact of (a) 10, (b) 15, (c) 17.5 and (d) 20 J 224

Figure 159 : X-ray tomography observations performed on the impacted at an energy level of 17.5 J 225

Figure 160 : X-ray tomography observations performed on the sample impacted at an energy level of 20 J 226

Figure 161 : Ultrasonic C-scan in transmission on specimens prior impact tests with some visible defects 227

Figure 162 : Ultrasonic C-scan imaging in transmission with 10 MHz transducers for the plates impacted at an energy level of (a) 10, (b) 15, (c) 17.5 and (d) 20 J 228

Figure 163 : Ultrasonic C-scan imaging in transmission with 5 MHz transducers for the plates impacted for an impact of (a) 10, (b) 15, (c) 17.5 and (d) 20 J 228

Figure 164 : Ultrasonic imaging in reflection of the plate impacted at 20 J. Impacted side (Left) and the opposite one (Right). B-scan in the X and Y directions for both side..... 229

Figure 165 : Impact damage tolerance and permanent indentation concept [123]..... 230

Figure 166 : (a) Times of arrival map for the first peak in the plate impacted at 20 J. The permanent indentation is highlighted in red (b) Zoom in on one of the b-scan from Figure 164. 231

Figure 167 : Evolution of the nine stiffness components of the tested composite material when increasing drop weight energy 233

Figure 168 : (a) Evolution of the Frobenius norm of the stiffness tensor obtained by ultrasound method and (b) evolution of the phase shift indicator with the impact energy 234

Figure 169 : (a) Transmitted guided wave signals measured on the plates impacted at different energy levels. (b) Cross-correlation results obtained on the plates impacted at different energy levels with considering the plate impacted at 10 J as a reference 236

Figure 170 : Schematic representation of the experimental set-up for the guided waves investigations of the plate 237

Figure 171 : (a) Evolution of the maximum correlation coefficient with the transducers position. (b) Evolution of the time lag with the transducers position 238

Figure 172 : Example of three typical L-scans obtained from the plate impacted at 20 J . 239

Figure 173 : Photo of the sample of each selected woven composite materials. 258

Figure 174 : Experimental set-up. The differents components are labeled and the path's signal is shown by yellow arrows 260

Figure 175 : Spectrum response of an undamaged woven glass fiber reinforced vinylester composite sample excited by 10 kHz and 13 kHz. Markers use to define the “background function” are plotted in green 261

Figure 176 : Spectrum response of an undamaged woven glass fiber reinforced vinylester composite sample excited by 10 kHz and 13 kHz. The background function has been subtract and the identified peak are marked in red 262

Figure 177 : Frequency response of the vinylester/glass composite submitted to different loading value. The input frequencies are indicate by the green arrow 263

Figure 178 : Frequency response of the epoxy matrix sample submitted to a tensile loading value of 250 MPa 263

Figure 179 : Standard measure of the nonlinear transmission behavior of the epoxy matrix samples under excitation of 11 kHz and 14 kHz including the plot of a cubic regression. 264

Figure 180 : TDFD parameter function of the loading value for a) Vinylester, b) epoxy and c) polyamide 6.6/6 matrix based woven glass fiber reinforced composites 265

Figure 181 : Frequency response of the undamaged vinylester matrix based sample (In blue) and the 400MPa previously loaded in tension vinylester matrix based sample (in green) for a white noise as input signal 266

Figure 182 : Normalized frequency shift evolution function of the tensile loading level for the woven glass fiber reinforced and a) Vinylester based samples, b) Epoxy based samples, c) Polyamide 6.6/6 based samples 267

Figure 183 : Spectrum of the epoxy matrix sample damaged by a tensile stress of 400 MPa and excited by white noise under a stepwise increase of the excitation's power for the a) Vinylester samples, b) Epoxy samples, c) Polyamide 66 samples 268

Figure 184 : a) Schematic representation and b) photography of the four points bending setup 272

Figure 185 : Force displacement curve for the 12mm and 9mm four points bending tests 272

Figure 186 : Evolution of damage, calculated as the reduction of the bending modulus, with increasing the magnitude of the 4 points bending applied displacement 273

Figure 187 : a) Complete experimental set-up for the ultrasonic signal recording. b) Zoom in on one of the tested sample with indication of transducers position. 274

Figure 188 : Signal waveform recorded (in red continuous line) before any loading and (in dashed black line) after 3mm of four points bending applied. 275

Figure 189 : a) Normalized cross-correlation coefficient between the sample loaded (200-1200N) and the sample before loading. b) Normalized cross-correlation coefficient for the reference sample between different moment and the first signal record for this sample. c) Time shift between the sample loaded (200-1200N) and the sample before loading. d) Time

shift coefficient for the reference sample between different moment and the first signal record for this sample 277

Figure 190 : Variation of δV/V over the whole recorded signals for the sample 1 (in dashed red line) and the sample 2 (in continuous black line)..... 279

Figure 191 : Relative velocity changes (dashed line) and the normalized bending modulus evolution (continuous line) obtained for different loading values 280

List of tables

Table 1 : Mechanical properties of the most used fibers in composite materials [15]. E_L, E_T: Respectively longitudinal and transverse Young modulus; $\boldsymbol{\sigma_{rL}}$, $\boldsymbol{\varepsilon_{rL}}$: Respectively stress and strain to failure. 57

Table 2 : Comparison of various types of glass fiber by mass ratio of the different components 59

Table 3 : Mechanical properties of various types of glass fibers 59

Table 4 : Typical properties of polyamide 66/6. The values with a ”*” correspond to a conditioned PA66/6 (Source: www.matweb.com) 65

Table 5 : Properties of the Vizilon SN63G1-T1.5-S3 (Source: DuPont) 72

Table 6 : Summary of the results for tensile tests on samples oriented along the fiber’s axis 82

Table 7 : Summary of the results for tensile test on samples oriented at 45° from fiber’s axis 84

Table 8 : Elastic modulus and associated damage for each cycle for the sample oriented at 45° from fiber’s axis 90

Table 9 : Elastic modulus and associated damage for each cycle for samples oriented at along the fiber’s axis 91

Table 10 : Polishing procedure 97

Table 11: X-ray tomography acquisition parameters 106

Table 12 : Samples and their defined tensile loading for 0° and 45° oriented samples 108

Table 13 : Volume fraction of the matrix and fiber on the undamaged sample the 0° configuration 110

Table 14 : Volume fraction of the matrix, fiber and void on the undamaged samples in the 0° configuration 111

Table 15 : Relation the nonlinear parameter with the sidebands amplitude and relation of the sidebands frequencies with the input frequencies 151

Table 16 : Numerical stiffness components for the 0° and 45° configurations obtained by periodic homogenization courtesy of Francis Praud 168

Table 17: Average relative difference between the two computational methods of the wave mode velocities 169

Table 18 : Identified stiffness components for different orthotropic stiffness tensor as initial guess of the solution. 239 velocity values are used as an input 175

Table 19 : Identified stiffness components for different isotropic stiffness tensor as initial guess of the solution. 239 velocity values are used as an input 176

Table 20 : Identified stiffness components for different orthotropic stiffness tensor as initial guess of the solution. 77 velocity values are used as an input 177

Table 21 : Identified stiffness components for different isotropic stiffness tensor as initial guess of the solution. 77 velocity values are used as an input 177

Table 22 : Identified stiffness components with different level of perturbation on the simulated input velocity values 179

Table 23 : Stiffness constants of the studied composite material obtained with numerical periodic homogenization method and obtained with the experimental ultrasonic method for 0° and 45° fibers orientation. The confidence interval of each identified stiffness constants is indicated under parenthesis 180

Table 24 : Stiffness components of the studied composite material with an ultrasonic method for various values of loading in tension for samples in the 0° configuration..... 182

Table 25 : Rigidity constants of the studied composite material with an ultrasonic method for various values of loading in tension for a 45° fiber orientation..... 187

Table 26 : Maximum amplitude for two fixed angles for all the loading value used..... 192

Table 27 : List of defects on the investigated plate and their respective dimensions the reference signal energy measured using a 500 KHz signal and a 1MHz signal is respectively of 0.006 $V^2.s^{-1}$ and 0.104 $V^2.s^{-1}$. 199

Table 28 : Values of the two proposed damage indicators for the two considered sample' orientations 213

Table 29 : Stress level of each sample considered for the experimental set-up using guided waves 214

Table 30 : Drop height and impact energies of the four impacted composite plates. The displacement sensor saturates during the test. The values with (*) must be considered with caution because of the displacement sensor saturation noticed during some impact tests. 222

Table 31 : Permanent indentation size measured using ultrasonic C-scan method in reflection..... 231

Table 32: Time lag obtained with cross correlation with the 10 J impacted plate considered as a reference 236

Table 33 : Materials tested and loading value used on the different sample..... 258

Table 34 : Displacement and loading values for monotonic four points bending loading. 271

Part I : Résumé étendu en Français

Sommaire

1) Introduction générale 3

2) Présentation du composite tissé de l'étude : Un polyamide 66/6 renforcé par des fibres de verre tissées 5

a) La matrice polyamide 66/6 6

b) Le renfort en fibres de verres tissées 7

3) Caractérisation du comportement mécanique du composite étudié lors de sollicitations monotone et cyclique en traction..... 8

4) Etude des mécanismes d'endommagement : analyses quantitatives et qualitatives..... 14

5) Méthodes ultrasonores de Contrôle Non Destructif (CND) 18

a) Détermination du tenseur de rigidité par mesure des vitesses de propagation ultrasonore 19

b) Mesures par ondes de Lamb guidées 24

6) Validation sur échantillon impacté par poids tombant 31

7) Conclusion générale et perspectives 41

1) Introduction générale

Durant ces dernières années, un effort de plus en plus important a été effectué par les constructeurs automobiles afin de réduire le poids total de leurs véhicules de série. Ceci s'explique par le durcissement de plus en plus important, notamment en Europe, des normes sur les émissions de CO_2. Différentes solutions sont envisagées par les constructeurs automobiles afin d'atteindre ces seuils. Sachant que d'après des données des fabricants d'équipements d'origine, plus d'1/3 de la consommation de carburant d'un véhicule peut être imputé à sa masse, la réduction de cette dernière est une priorité de nombreux constructeurs automobiles. Les matériaux composites ont rapidement été considérés comme étant une solution adaptée au vu de leur ratio densité/rigidité très intéressant.

Les parties principales du véhicule visant à être remplacées par des matériaux composites peuvent être séparées en deux. Premièrement, celles près du moteur qui vont devoir résister à de hautes températures ; ensuite, celles qui servent à renforcer les performances structurelles du véhicule. Pour ce deuxième cas, on peut noter une étude réalisée par DuPont de Nemours et le groupe PSA visant à remplacer des poutres de protection antichoc métalliques par un équivalent en polyamide 66/6 renforcé de fibres de verre tissées (série Vizilon$_{TM}$). Ils ont montrés que leur solution permettait une réduction de 40% de la masse par rapport au matériau métallique. De plus, le composite peut également absorber plus d'énergie lors d'impacts.

Cependant, l'utilisation de ces matériaux pour la conception de véhicules de grande série peut entrainer l'apparition d'endommagement durant le procédé de fabrication. Conséquemment, une solution de contrôle non destructif (CND) est nécessaire afin de contrôler la qualité des pièces après production. Cette méthode devrait également permettre un contrôle local du véhicule lors d'évènements inattendus tel qu'un choc à faible vitesse. Les méthodes basées sur les ultrasons ont pour avantages de pouvoir être implantées à un cout relativement peu élevé par rapport à d'autres techniques de CND. De plus, elles peuvent être utilisées sans risque pour la santé de la personne en charge du contrôle, par

rapport notamment aux rayons X. Enfin, étant présent dans l'industrie depuis longtemps, les méthodes basées sur les ultrasons sont nombreuses et assez bien documentées. En conséquence, ce sont ces méthodes qui ont été choisies pour étudier l'endommagement des pièces automobiles en matériaux composite.

Cependant, avant d'étudier différentes méthodes de CND, le comportement mécanique et l'endommagement induit doivent être caractérisés. Pour cela, différents types de sollicitations mécaniques doivent être considérés. Des cas de chargement en traction et d'impacts à basse vitesse seront donc discutés.

Le matériau au centre de l'étude est le polyamide 66/6 renforcé par trois plis de fibres de verre tissées. Ce composite est développé par DuPont de Nemours et sa conception a été optimisée en partenariat avec le groupe PSA. Plus généralement, ce sujet s'inscrit dans le cadre de l'Open Lab PSA « Materials and Processes » financé par le groupe PSA. Celui-ci implique également trois partenaires académiques : les Arts et Métiers ParisTech, l'UMI Georgia Tech-CNRS (UMI 2958) tous deux basés à Metz et le Luxembourg Institute of Science and Technology (LIST). Le présent sujet a été réalisé principalement au sein des laboratoires LEM3-UMR CNRS 7239 et LUNE (Laboratory for Ultrasonic Nondestructive Evaluation), respectivement basés sur le campus ENSAM-Arts et Métiers le campus de Georgia Tech Lorraine, tous deux à Metz. La proximité de ces deux laboratoires a permis une interaction forte avec ces deux établissements.

Ce rapport est organisé ainsi :

- La présentation du matériau composite et des composants dont il est constitué
- La caractérisation de la réponse macroscopique du composite lors de chargements en traction suivant l'axe des fibres et hors axes (45°) des fibres
- L'étude à l'échelle microscopique des mécanismes d'endommagement induits par ces chargements en traction

- L'utilisation de deux méthodes ultrasonores d'évaluation de l'endommagement : la détermination du tenseur de rigidité par mesure de vitesses de phase; et l'analyse des ondes guidées transmises dans le matériau endommagé.
- Validation des méthodes de Contrôle Non Destructif (CND) sur des échantillons impactés par poids tombant

2) Présentation du composite tissé de l'étude : Un polyamide 66/6 renforcé par des fibres de verre tissées

Le composite sélectionné pour cette étude est un polyamide 66/6 renforcé par trois plis de fibres tissées suivant un motif sergé 2,2. Ce matériau est produit par DuPont de Nemours par thermo-compression pour l'industrie automobile. Le procédé de fabrication est résumé sur la Figure 1. Des informations additionnelles sur le composite sont indiquées dans le Tableau 1. Comme mentionné précédemment, ce composite a été sélectionné pour remplacer des matériaux métalliques servant de pièces structurelles sur les voitures de grande série. Les propriétés visées sont essentiellement une bonne résistance à des sollicitations en fatigue ainsi que lors d'impact. La matrice et le type de renforts ont été sélectionnés afin de satisfaire ces exigences.

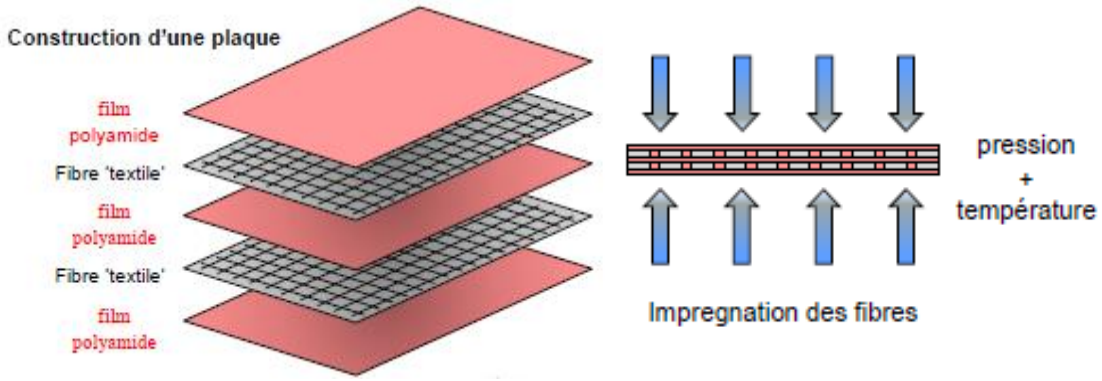

Figure 1 : Procédé de moulage par thermo-compression pour la fabrication des composites de série Vizilon (Source: DuPont)

Epaisseur (mm)	≈ 1,53
Taux de vide (%)	< 2
Densité des fibres (kg/m^3)	1300
Densité de la matrice (kg/m^3)	2500
Densité du composite (kg/m^3)	1780
Fraction massique de fibres (%)	63
Fraction volumique de fibres (%)	43

Tableau 1 : Propriétés du Vizilon SN63G1-T1.5-S3 (Source: DuPont)

a) La matrice polyamide 66/6

Les polyamides font partie de la famille des polymères thermoplastiques. Ces derniers permettent à la fois une production plus rapide et à plus grande échelle ainsi qu'un recyclage plus efficace. Ces trois points sont critiques dans l'industrie automobile, qui doit assurer une production de véhicules suffisante par heures tout en satisfaisant les normes européennes. Ces dernières fixent le taux de réutilisation et de valorisation de 95% du poids total du véhicule depuis 2015.

D'un point de vue mécanique, les polyamides sont connus pour leur haute charge à rupture, leur résistance aux chocs et à l'abrasion. Plus spécifiquement, le polyamide 66/6 est un copolymère de polyamide 6 et polyamide 66. Il a été développé afin d'avoir un compromis entre ces deux types de composites. En effet, le polyamide 6, présente une haute résistance à l'impact et une haute dureté alors que le polyamide 66, a une meilleure rigidité. Ainsi, le polyamide 66/6 permet d'avoir la bonne résistance à l'impact du polyamide 6, indispensable pour les applications automobiles, sans sacrifier les propriétés mécaniques. Cependant, les polyamides sont également très sensibles à l'humidité relative.

En effet, la réaction des liaisons hydrogènes avec l'eau va entrainer leur affaiblissement ce qui a un impact direct sur les propriétés mécaniques du polyamide. Plus précisément, lorsque le taux d'humidité relative augmente, leur module élastique a tendance à diminuer et leur ductilité à augmenter. L'influence de l'humidité relative sur le comportement est sur la Figure 2.

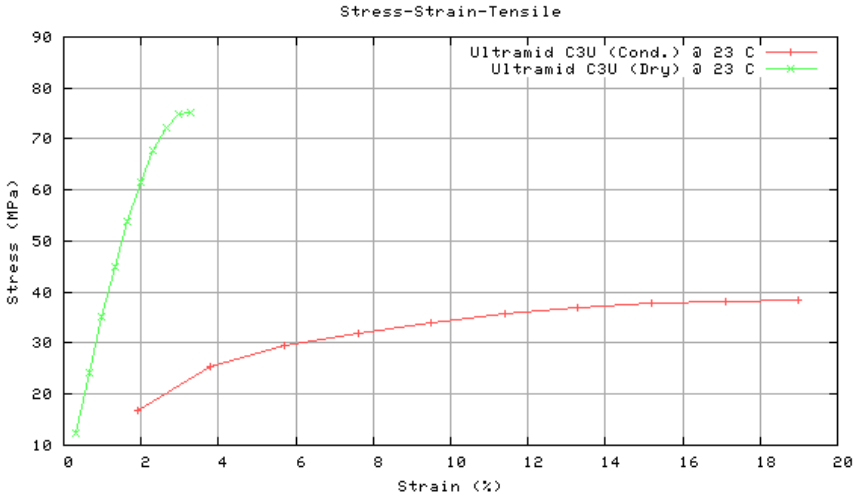

Figure 2 : Courbe contrainte/déformation, en traction à 23°C, pour un Polyamide 66/6 (Ultramid® C3U de BASF) sec (vert) et après conditionnement 50% HR (rouge) [http://iwww.plasticsportal.com/]

b) Le renfort en fibres de verres tissées

Les renforts tissés sont constitués de torons de fibres entremêlées suivant un motif choisi afin de constituer une structure complexe. Les torons dans la direction principale du tissage sont nommés torons du sens chaîne, alors que ceux perpendiculaires à cette direction sont nommés torons du sens chaine.

L'un des avantages notable du renfort tissé est de limiter la propagation de délaminage [1]. Ce type d'endommagement est l'un des mécanismes les plus critiques, pouvant de plus apparaitre lors de sollicitations par impact. Ce choix de renfort peut donc augmenter la durée de vie du composite de manière significative après un choc à basse vélocité imprévus. Par ailleurs, le renfort tissé va également permettre, contrairement à un renfort

unidirectionnel, un meilleur équilibre des propriétés mécaniques dans le plan du renfort. Néanmoins, ce type de renfort va entrainer une diminution, par rapport au renfort unidirectionnel, de la résistance maximale ainsi que du module élastique lors de sollicitation suivant l'axe des fibres [2], [3].

Les composites utilisant ce type de renfort sont connus pour voir apparaitre des mécanismes d'endommagements très spécifiques aux types de sollicitations considérés. Une étude des mécanismes susceptibles d'apparaitre lors de sollicitions en traction, compression et flexion, menée par Karakaya et al. [2] a mis en avant l'influence du type de sollicitation. Des échantillons orientés suivant le sens chaine ou orientés à 45° de celui-ci ont été considérés; ceux-ci étant évidemment les cas critiques lors de sollicitation en traction dans le plan du composite. Ces mécanismes seront discutés plus en détail, pour le composite de l'étude, dans la partie dédiée à son étude microscopique pour le cas de la sollicitation en traction d'échantillons orientés suivant le sens chaine et orientés à 45° de celui-ci.

3) Caractérisation du comportement mécanique du composite étudié lors de sollicitations monotone et cyclique en traction

Cette partie est dédiée à l'étude de la réponse mécanique du composite polyamide 66/6|fibres de verre tissées lors de sollicitations en traction monotone et cyclique. Deux configurations d'échantillons ont été considérées. Pour la première configuration les échantillons sont orientés suivant le sens chaine et pour la seconde les échantillons sont orientés à 45° du sens chaine. Les éprouvettes sont des rectangles de 150 x 45 x 1.5 mm découpés par jet d'eau. Les deux configurations d'échantillons sont représentées sur la Figure 3.

Avant les essais, les éprouvettes sont conditionnées dans une étuve humide *Memmert HCP256* à une humidité relative de 50 % et une température de 70°C. Une humidité relative de 50 % pour les essais sur les matériaux sensibles aux RH est privilégiée par les

normes (ISO-527) lorsqu'aucune autre précaution n'est nécessaire. Une température de 70°C permet d'atteindre l'équilibre du taux d'humidité dans l'échantillon. Enfin, tous les essais sont réalisés sur une machine de traction « Z50 » de *Zwick Roell Gruppe* à température ambiante. Les essais sont réalisés à une vitesse de déformation de 10^{-4} s^{-1}, sauf mention contraire. Les déplacements sont mesurés à l'aide de 4 outils de mesures. Un capteur LVDT (Linear Variable Differential Transformer), une caméra pour des mesures par corrélation d'image, un extensomètre *Epsilon Technology corp* (Model: 3542-025M-010-ST) et la mesure du déplacement de la traverse. Seules les mesures par extensomètre et corrélation d'image sont indiqués ici. Pour plus d'information, merci de se référer au manuscrit en anglais. Les essais sont répétés trois fois par configurations d'échantillons afin de valider la répétabilité de l'essai. Les modules d'élasticité sont mesurés d'après la norme ISO-527-1 nécessitant la mesure par régression linéaire entre ε_1 = 0.05% et ε_2 = 0.25%.

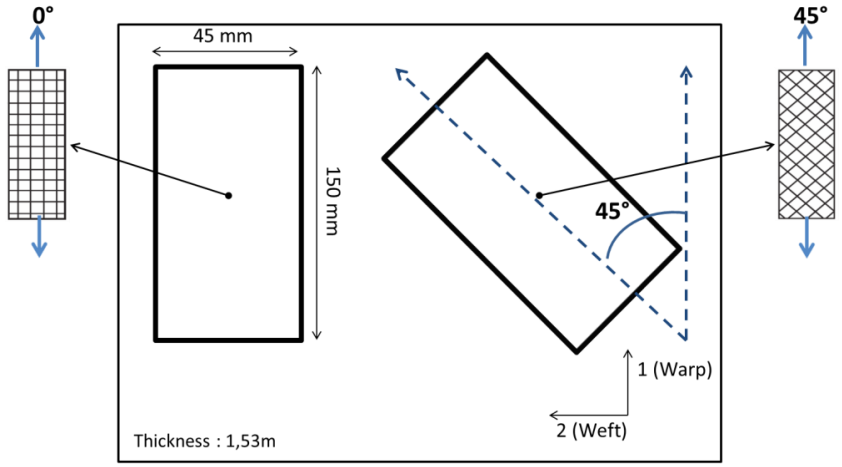

Figure 3 : Position des éprouvettes orientées à 0° et 45° par rapport au sens chaine (direction du sens de l'écoulement) pour la plaque en composite.

Pour les échantillons orientés suivant l'axe de trame, le comportement observé est linéaire fragile (Figure 4). Tandis que pour les échantillons dans la configuration 45°, on peut noter un comportement non linéaire ductile, principalement dû au caractère viscoélastique de la matrice polyamide 66/6 (Figure 5). Il faut noter que comme l'extensomètre ne peut dépasser une déformation de 10%, trois essais ont été effectués avec l'extensomètre seul sans atteindre la rupture de l'échantillon. Le déplacement a été mesuré

avec la caméra, pour la corrélation d'image, sur trois autres échantillons chargés jusqu'à atteindre la rupture. Les principaux résultats sont résumés dans le Tableau 2 pour les deux configurations. Ces résultats concernent le module d'élasticité ainsi que la résistance maximale en traction moyennés sur tous les essais. Le calcul de cette moyenne est possible car comme visible sur la Figure 4 et Figure 5, les mesures par corrélation d'image et extensomètre présentent une très bonne reproductibilité.

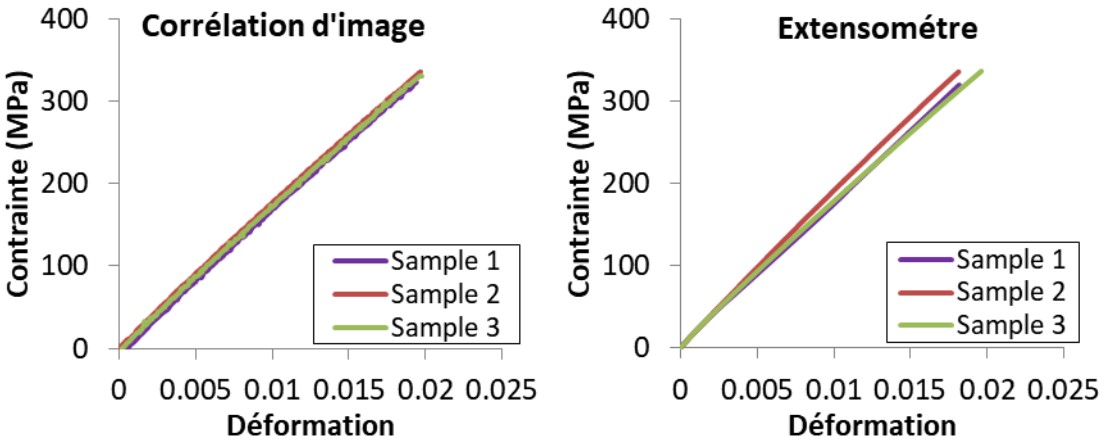

Figure 4 : Réponses contrainte/déformation obtenues par corrélation d'image (Gauche) et extensomètre (Droite) sur trois échantillons dans la configuration 0°.

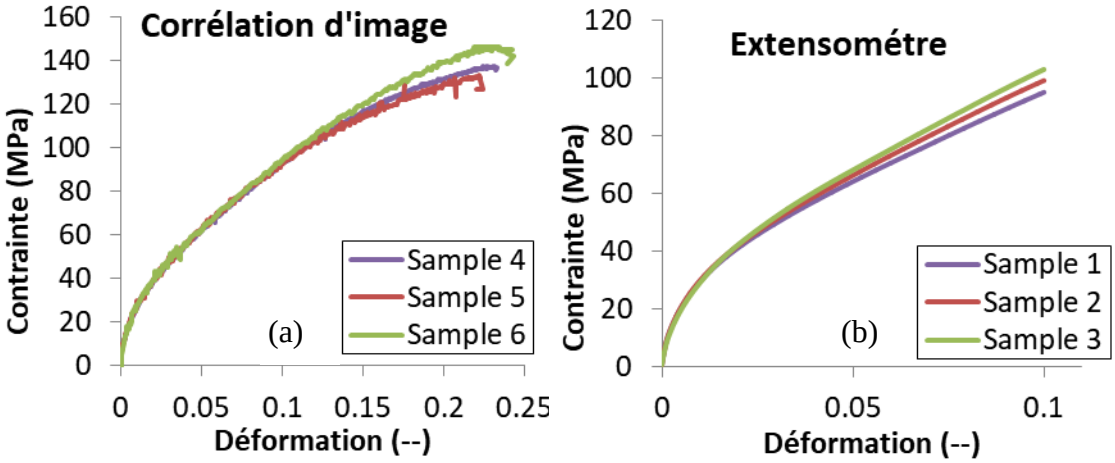

Figure 5 : Réponses contrainte/déformation obtenues par corrélation d'image (Gauche) et extensomètre (Droite) sur trois échantillons dans la configuration 45°.

	Extensomètre (0°)	**DIC (0°)**	**Extensomètre (45°)**	**DIC (45°)**
Module de Young moyen	18,8 GPa	18,3 GPa	3,7 GPa	3,4 GPa
Ecart type	0,4546	0,2160	0,3514	0,3300
ε_f moyen	0,0190	0,0191	--	0,234
Ecart type	0,0009	0,00045	--	0,0076

Tableau 2 : Résumé des résultats des essais de traction sur les échantillons dans la configuration (0°) et (45°)

A l'aide des résultats de corrélation d'image, les champs de déformation dans le plan du composite ont pu être mesurés pour les deux configurations d'échantillons. En observant le champ ε_{11} (avec « 1 » la direction de chargement) juste avant la ruine de l'échantillon sur la Figure 6-a, on peut remarquer que celui-ci reste relativement homogène pour la configuration 0°. Les champs de déformation ε_{22} et ε_{12} n'évoluent presque pas. En revanche, pour la configuration 45°, tous les champs du plan évoluent de façon significative. Des efforts de cisaillement sont clairement induits sur la partie centrale de l'éprouvette. Cette zone correspond à la zone en forme de losange visible sur la Figure 6-b. Dans cette zone, les fibres vont avoir tendance à se réorienter suivant la direction de chargement. On peut remarquer des zones avec des craquelures où le calcul de corrélation ne s'est pas fait correctement. Ces craquelures apparaissent généralement lorsque l'angle de déformation maximal a été localement atteint. Cet angle dépend notamment du motif de tissage utilisé et permet d'obtenir des informations sur les propriétés de cisaillement dans le plan du composite. Une étude relativement complète de ces essais, permettant l'extraction des propriétés de cisaillement des composites tissés, a été réalisée par Boisse et al. [4].

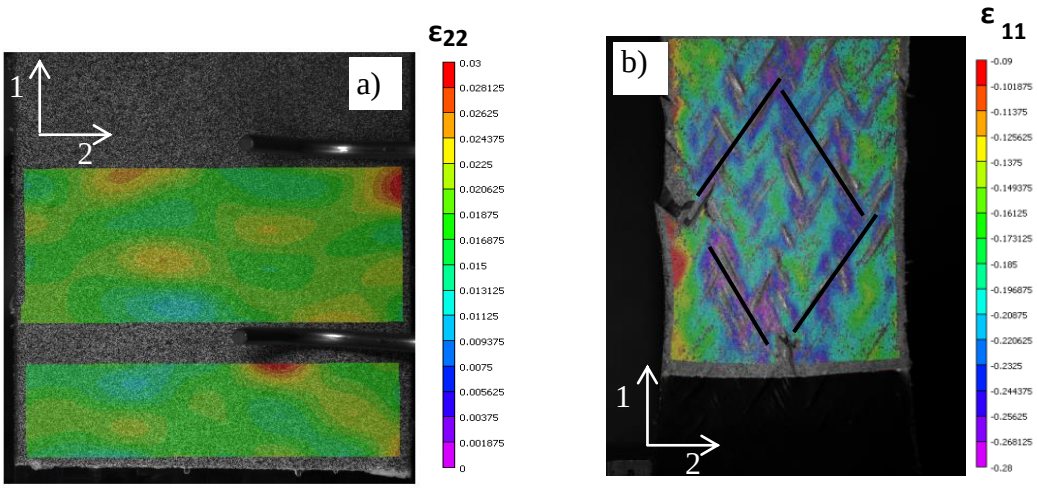

Figure 6 : (a) Champs de déformation ε_{11} pour un échantillon dans la configuration 0°. (b) Champs de déformation ε_{22} pour un échantillon dans la configuration 45°. Les deux champs sont calculés peu avant la ruine.

A présent, les deux configurations d'échantillons sont soumises à des sollicitations cycliques incrémentales de 20 MPa en traction. Afin de pouvoir solliciter les échantillons jusqu'à rupture, la mesure des déplacements a été effectuée par corrélation d'image pour les deux configurations. Ces essais ont principalement pour but de mesurer l'évolution de l'endommagement avec l'augmentation du chargement. L'endommagement est estimé ici par réduction du module élastique en suivant la procédure décrite par Ladeveze et al. dans [5]. Il est calculé à l'aide de : $D = 1 - \frac{E_n}{E_0}$, avec E_n le module de décharge pour le niéme cycle mesuré par régression linéaire comme indiqué sur la Figure 7 et E_0 le module de Young mesuré lors du premier cycle. L'évolution de l'endommagement obtenu pour les deux configurations d'échantillons étudiés est visible sur la Figure 8. L'endommagement induit lors de sollicitations hors axes des fibres est alors nettement plus important que lors de sollicitions suivant le sens chaine. Il atteint en effet une valeur de 0.53 pour la configuration 45° alors qu'il ne dépasse pas les 0.1 pour l'autre configuration. Cette première estimation de l'endommagement servira de point de comparaison pour toutes les autres méthodes d'évaluation de l'endommagement considérées par la suite, notamment les méthodes ultrasonores.

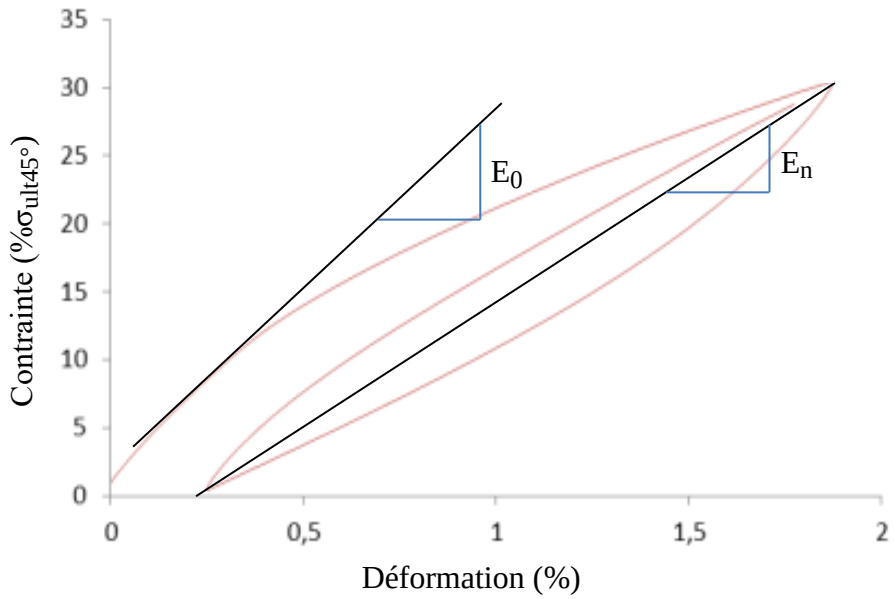

Figure 7 : Mesure des modules E_0 et E_n sur une courbe charge/décharge.

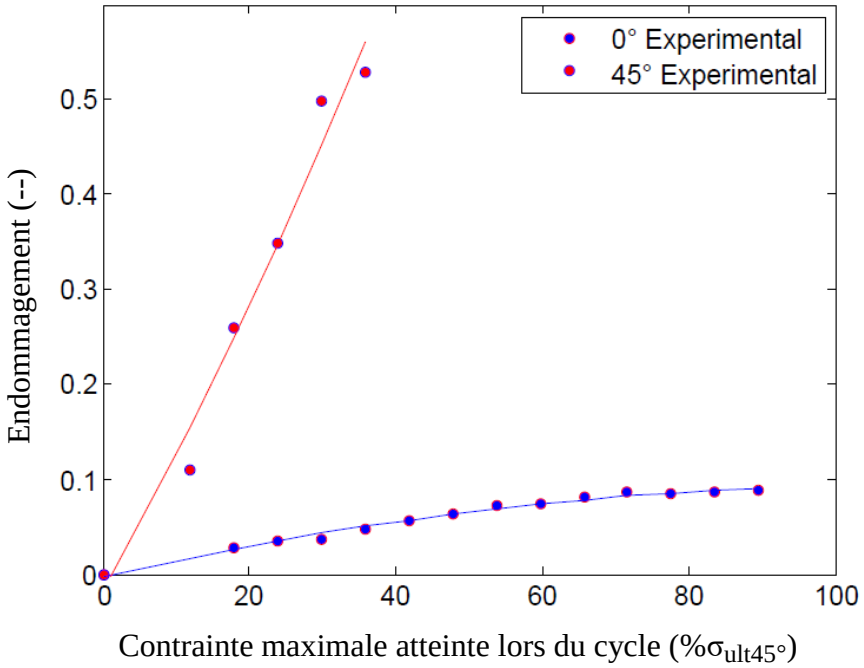

Figure 8 : Comparaison de l'évolution de la réduction du module d'Young lors d'essais cycliques incrémentaux en traction pour des échantillons dans la configuration 0° et 45°.

4) Etude des mécanismes d'endommagement : analyses quantitatives et qualitatives

Comme évoqué précédemment, plusieurs mécanismes d'endommagement sont susceptibles d'apparaitre sur les composites tissés. Ils vont de plus être extrêmement dépendants du type de sollicitation que la pièce est susceptible de rencontrer durant sa vie en service. Afin de caractériser efficacement l'endommagement du polyamide 66/6 renforcé de fibres de verre tissées, il est nécessaire de considérer différents cas de sollicitation mécanique. Ici nous considérons le cas de chargement en traction pour les deux configurations d'échantillons évoquées précédemment.

Pour ces deux cas de chargements, le premier mécanisme d'endommagement observé sera la décohésion fibre/matrice. Ce dernier a été mis en avant lors d'essais de traction in-situ au Microscope Electronique à Balayage (MEB). On peut voir sur la Figure 9-c que ce dernier s'est initié pour des valeurs de chargement entre 66 N et 120 N. Cette décohésion fibres/matrice va ensuite se propager sous forme de fissure suivant la direction transverse à la direction de chargement.

Les autres mécanismes d'endommagement sont analysés à l'aide d'un tomographe à rayon X EasyTom (Nano) conçu par *RX solutions*. Des échantillons orientés à 0° et 45° du sens chaine, préalablement chargés en traction à des niveaux de contrainte définis, sont tous observés. Un échantillon resté intact est également observé pour chaque configuration. Au total 6 échantillons dans la configuration 0° et 4 échantillons dans la configuration 45° sont considérés. Pour information, ces échantillons seront également considérés pour les parties suivantes. Les valeurs de chargements sont indiquées par des cercles rouges sur la Figure 10 et résumées dans le Tableau 3.

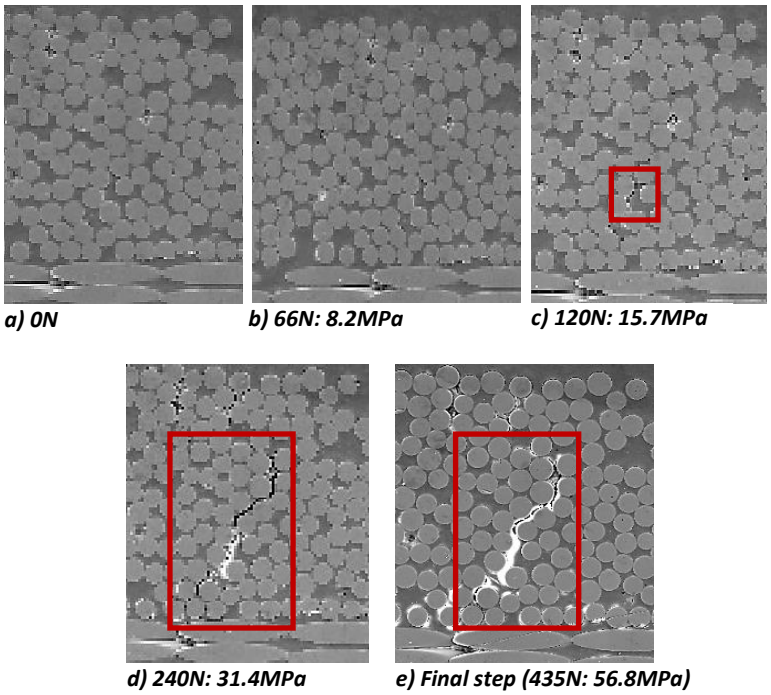

Figure 9: Images MEB lors d'essais de traction in-situ pour différents niveaux de changements appliqués suivant l'axe des fibres

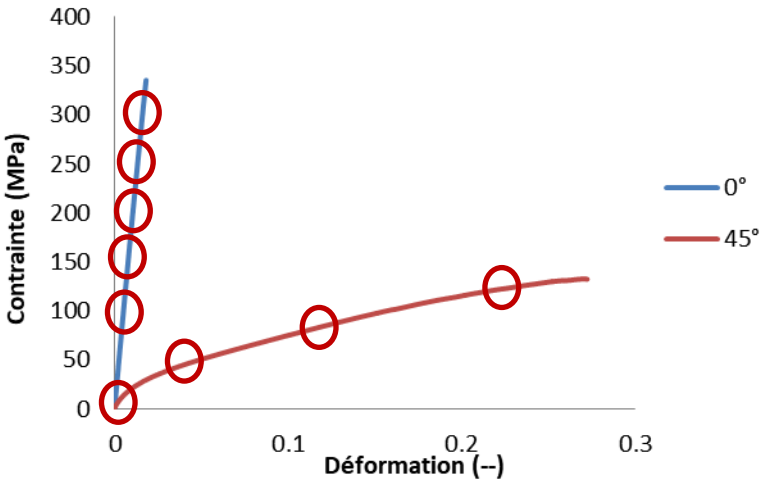

Figure 10 : Courbes contrainte/déformation typiques du polyamide 66/6 renforcé de fibres de verre tissées dans la configuration 0° et 45°. Les cercles rouges indiquent le niveau de contrainte et de déformation pour lesquels les essais de traction (réalisés sur différents échantillons) ont été interompus comme resumé dans le Tableau 3.

Echantillon	**1**	**2**	**3**	**4**	**5**	**6**
Configuration	0°	0°	0°	0°	0°	0°
Chargement normalisé	0 $\%\boldsymbol{\sigma}_{UTS0°}$	30,8 $\%\boldsymbol{\sigma}_{UTS0°}$	46,3 $\%\boldsymbol{\sigma}_{UTS0°}$	61,7 $\%\boldsymbol{\sigma}_{UTS0°}$	77,2 $\%\boldsymbol{\sigma}_{UTS0°}$	92,6 $\%\boldsymbol{\sigma}_{UTS0°}$
Déformation	0	0,005	0,007	0,010	0,013	0,016

Echantillon	**7**	**8**	**9**	**10**
Configuration	45°	45°	45°	45°
Chargement normalisé	0 $\%\boldsymbol{\sigma}_{UTS45°}$	30,5 $\%\boldsymbol{\sigma}_{UTS45°}$	61,1 $\%\boldsymbol{\sigma}_{UTS45°}$	91,6 $\%\boldsymbol{\sigma}_{UTS45°}$
Déformation	0	0,021	0,083	0,162

Tableau 3 : Echantillons observés et leurs chargements fixés associés

Les mécanismes d'endommagement observés sont résumés sur la Figure 11 pour les deux orientations d'échantillons. Pour ceux orientés suivant le sens chaine, on remarque que le nombre de fissures transverses augmente avec le chargement. Des zones de vides au bord des torons transverses sont également clairement visibles. Pour les valeurs de chargement les plus importantes, le sens de propagation des fissures transverses peuvent bifurquer et se mettre à longer les torons longitudinaux. Cela se produit généralement une fois que la fissure transverse s'est propagée jusqu'au bout du toron transverse. Il requiert alors généralement moins d'énergie à la fissure de bifurquer plutôt que de continuer et de casser les fibres du toron longitudinal. On appelle ce mécanisme le méta-délaminage.

Pour les échantillons orientés à 45° du sens chaine, des mécanismes d'endommagement supplémentaires ont été observés. Lorsque l'effort de chargement a atteint 61 %$\boldsymbol{\sigma_{UTS45°}}$, des micro-flambements de fibres ainsi que quelques ruptures de fibres sont visibles. Ces endommagements sont dus à l'effet de réorientation des fibres mentionné plus haut. De plus, du délaminage peut être induit notamment près des bords des échantillons.

La taille caractéristique de ces mécanismes d'endommagement a été mesurée sur les différents échantillons. Il a été remarqué que les mécanismes d'endommagement les plus notables apparaissent sur les échantillons dans la configuration 45°. Il s'agit du micro-flambement des fibres ainsi que du pseudo-délaminage ayant une taille caractéristique de 200 µm environ. Pour les échantillons dans la configuration 0°, les plus grands mécanismes d'endommagements observés ont une taille caractéristique ne dépassant pas les 50 µm environ.

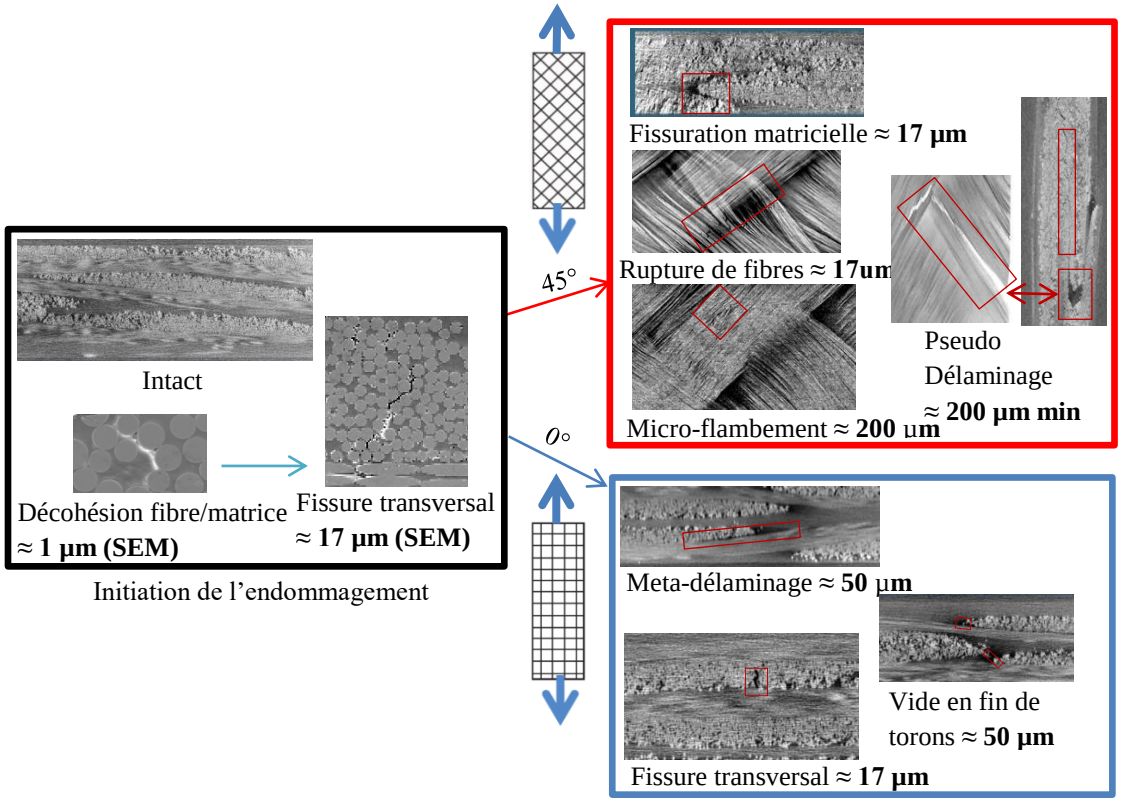

Figure 11 : Récapitulatif des mécanismes d'endommagement et leurs tailles caractéristiques associées pour les échantillons dans la configuration 0° and 45°

A l'aide d'un seuillage par niveau de gris, l'évolution de la fraction volumique de vides a ensuite été quantifiée. En effet, les vides vont apparaitre clairement en noir sur les volumes reconstitués par tomographie et peuvent être clairement séparés du reste du matériau. Comme illustré sur la Figure 12, le taux de vides va atteindre des valeurs nettement plus importantes avant la ruine sur les échantillons en configurations 45°. Il part en effet d'une valeur de 0.59 % pour un échantillon intact jusqu'à atteindre une valeur de 5.51% ; tandis qu'il est compris entre 0.59 % et 1.56 % pour l'ensemble des échantillons orientés suivant le sens chaine. Ce résultat est en accord avec l'estimation de l'endommagement obtenue par réduction du module élastique.

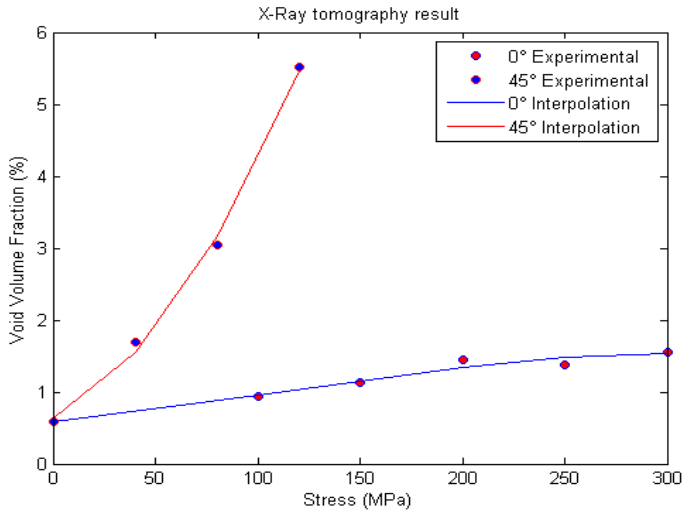

Figure 12 : Evolution de la fraction volumique de vides obtenue par tomographie aux rayons X pour des échantillons précédemment endommagées suivant les valeurs de chargement en traction.

5) Méthodes ultrasonores de Contrôle Non Destructif (CND)

Différentes méthodes ultrasonores ont été envisagées afin d'évaluer l'endommagement induit sur les échantillons sollicités en traction. La technique utilisée le plus couramment dans l'industrie est l'imagerie C-scan des échantillons en transmission et réflexion. Des

essais ont été effectués sur les échantillons dans la configuration 0° et 45° observés par tomographie à rayon X. Mais aucun endommagement n'a pu être clairement détecté sur les échantillons dans la configuration 0° comme montré sur la Figure 13-a. Comme vu précédemment, les endommagements ici vont être de taille caractéristique très faible dans cette configuration. En revanche, pour l'autre configuration, des zones d'endommagement très nettes ont pu être imagées. Elles ont été comparées avec la tomographie à rayon X et correspondent en fait à des flambements de fibres ainsi qu'à du délaminage local. D'autres méthodes ont été alors envisagées pour évaluer l'importance des microfissurations induites sur les échantillons dans la configuration 0°.

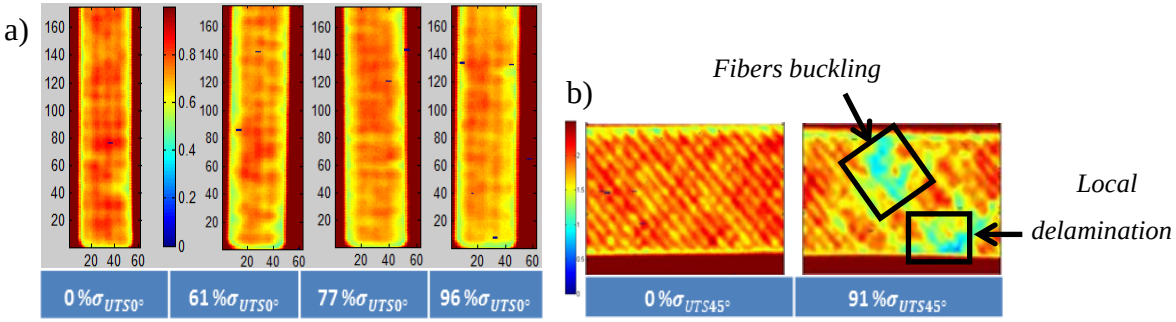

Figure 13 : Essai C-scans préliminaires sur le composite polyamide 66/6 renforcé avec des fibres de verre tissée chargé en traction à différents niveaux. (a): Echantillons en configuration 0°; (b): Echantillons en configuration 45°. Pour ces derniers,de large zones d'endommagement sont clairement visible.

a) Détermination du tenseur de rigidité par mesure des vitesses de propagation ultrasonore

Cette première méthode vise à obtenir le tenseur de rigidité d'un matériau en mesurant la vitesse de propagation des ondes de volume dans différentes directions et pour différents plans du matériau. En effet, la vitesse de propagation des ondes de volume dans une direction donnée est reliée au tenseur de rigidité C_{ijkl} par l'équation de Christoffel : $(C_{ijkl}n_k n_j - \rho v^2 \delta_{ij})U_l = 0$. Les vitesses mesurées sont ensuite utilisées dans un

algorithme d'optimisation qui permettra d'avoir les différentes composantes du tenseur. Tous les composites préalablement chargés en traction ont été analysés à l'aide de cette méthode. Le composite étudié ayant un comportement élastique orthotrope, neuf composantes sont nécessaires pour obtenir un tenseur de rigidité complet. Des mesures dans les trois plans principaux du composite sont alors nécessaires. Ce sont les plans 1-2, 1-3 et 2-3 visibles sur la Figure 14. Cependant, dans notre cas, l'épaisseur du composite est trop faible les ondes se propageant dans le plan 1-2 ne seront donc pas des ondes de volumes mais des ondes guidées. Ces ondes guidées sont reliées aux propriétés de rigidité par d'autres systèmes d'équation. En conséquence, les mesures réalisées dans les plans 1-3 et 2-3 prennent en compte la propagation des ondes de volume sont liées à C_{ijkl} par l'équation de Christoffel alors que les mesures dans le plan 1-2 sont reliées à C_{ijkl} par des équations plus complexes. Ceci est pris en compte lors du calcul du tenseur de rigidité par optimisation.

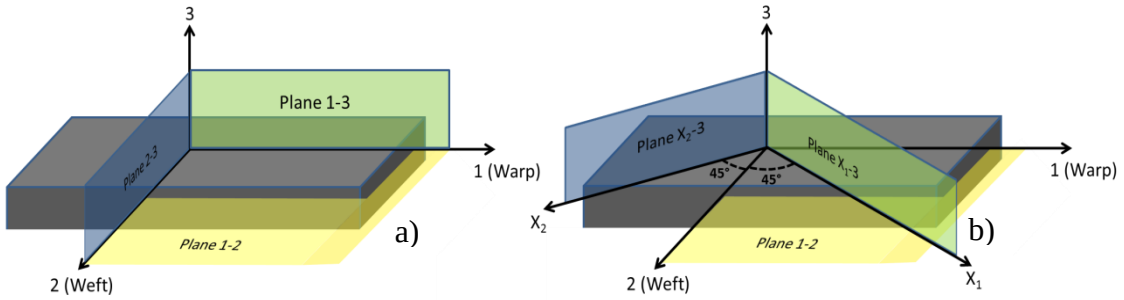

Figure 14 : Schéma représentatif des différents plans de propagation des ondes de volume (a) Plans de propagation pour la configuration 0° (b) Plans de propagation pour la configuration 45°

Des essais sur des échantillons non endommagés orientés suivant 0° et à 45° du sens chaine ont été réalisés. Des mesures dans les trois plans principaux ont pu être effectuées. Afin d'initialiser l'algorithme, une première estimation du tenseur de rigidité est réalisée par homogénéisation périodique avec l'aide de Francis Praud. Les tenseurs obtenus avec optimisation sont indiqués avec les deux premières estimations dans le Tableau 4.

		C_{11}	C_{12}	C_{13}	C_{22}	C_{23}	C_{33}	C_{44}	C_{55}	C_{66}
Numérique		20	2,1	1,5	20	1,5	4,5	2,3	1,3	1,3
Expérimentale	0°	22,16 (0,2)	2,6 (0,15)	1,48 (0,76)	21,75 (0,08)	1,45 (0,17)	4,13 (0,07)	2,33 (0,09)	1,61 (0,21)	1,42 (0,12)
Numérique		13,35	8,75	1,5	13,35	1,5	4,5	8,95	1,3	1,3
Expérimentale	45°	14,6 (0,43)	6,0 (0,29)	1,5 (0,645)	13,5 (0,184)	1,4 (0,223)	4,2 (0,248)	6,7 (0,118)	1,7 (0,237)	1,6 (0,31)

Tableau 4 : Tenseurs de rigidité obtenus pour le matériau composite étudié par homogénéisation périodique analytique et mesure ultrasonore pour les configurations 0° et 45°. L'intervalle de confiance pour chaque composante est indiqué entre parenthèse.

Les différents échantillons endommagés sont ensuite analysés à l'aide de la même méthode. Cependant, à cause de la petite largeur de l'éprouvette, des mesures seulement suivant dans les plans 1-2 et 1-3 ont pu être effectués. Cela entraine que seuls 7 des 9 composantes du tenseur de rigidité ont pu être obtenus. Pour le composite orienté à 45° du sens chaine, le plan 1-3 n'est plus un plan principal. Lorsque l'échantillon est sollicité en traction, la symétrie d'élasticité va être perdue à cause du mode de propagation des fissures pour cette configuration. Nous devons alors considérer 13 composantes de rigidité pour correctement prévoir l'évolution du comportement du composite. Les composantes C_{56}, C_{14}, C_{24} et C_{13} sont alors ajoutées. On peut noter sur la Figure 15 que lorsque les échantillons dans la configuration 0° sont sollicités en traction, ce sont principalement les composantes fonctions de la direction de chargement qui vont diminuer, c'est-à-dire C_{11}, C_{12}, C_{13}. Une relative diminution de C_{55} est également notable. En revanche, les autres composantes évoluent peu avec le niveau de chargement en traction.

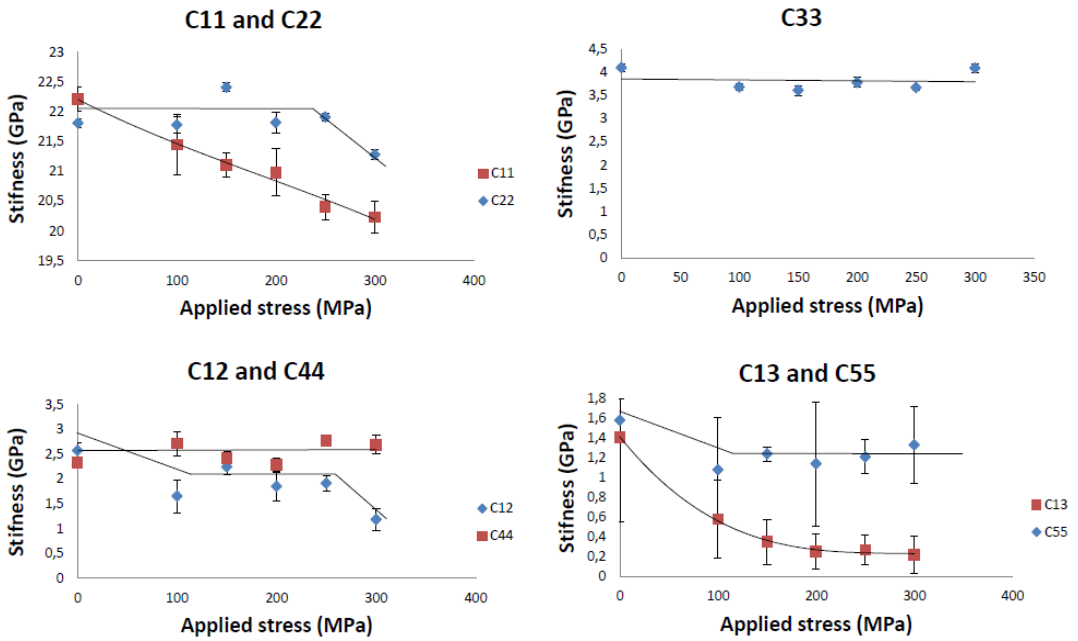

Figure 15 : Evolution de sept des constantes de rigidité en fonction du chargement, pour différents échantillons orientés à 0°.

Pour les échantillons orientés à 45°, un autre schéma d'évolution de l'endommagement est noté. Comme présenté sur la Figure 16 les composantes de cisaillement C_{44} ainsi que les composantes C_{11}, C_{22} et C_{12} sont les composantes les plus impactées par le chargement. Ce sont les composantes pilotant le comportement élastique du composite dans le plan. Ce résultat est en accord avec les observations faites avec la corrélation d'image. On pouvait en effet remarquer que les champs de déformation ε_{11}, ε_{22} et ε_{12} évoluaient de façon non nuls. Cependant on peut noter une incertitude importante, sur les nouveaux paramètres introduits. En effet, le nombre de mesures est clairement insuffisant pour proposer une correcte identification de ces composantes additionnelles. Des mesures dans un plan supplémentaire auraient pu permettre une incertitude moindre.

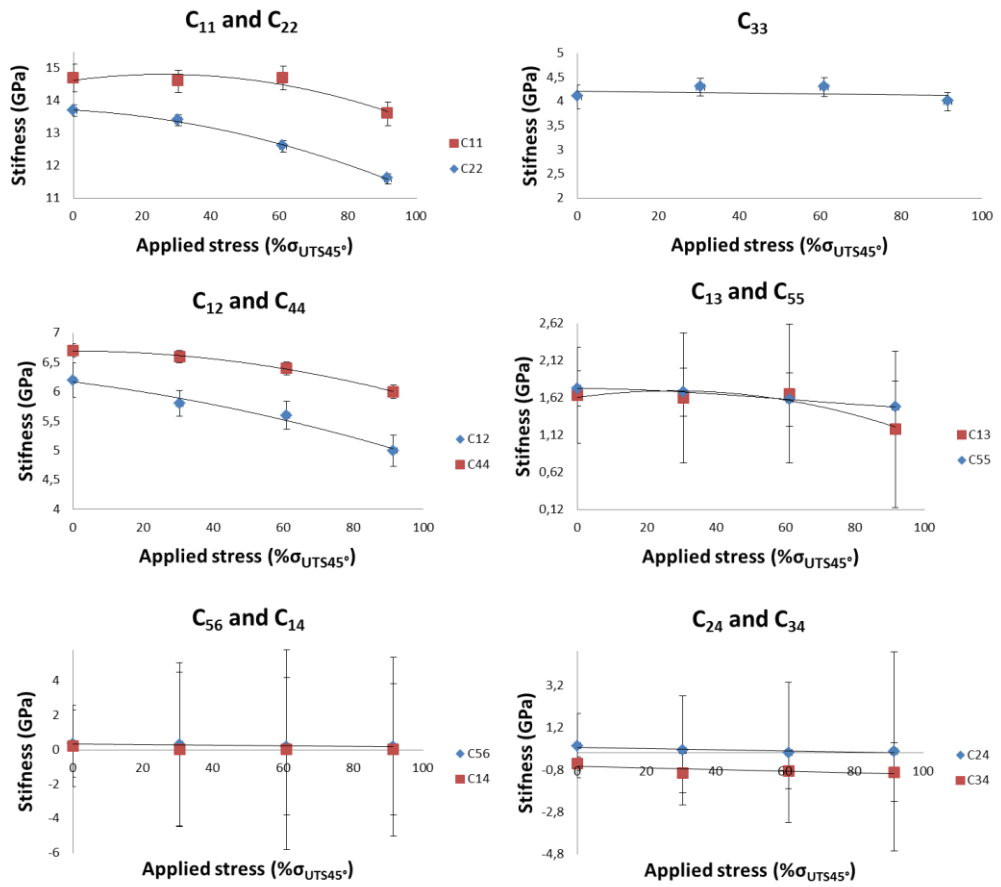

Figure 16 : Evolution de onze des constantes de rigidité en fonction du chargement pour différents échantillons orientés à 45°.

Ensuite, deux indicateurs d'endommagement ont été proposés. Le premier est basé sur le calcul de la norme du tenseur de rigidité obtenu par mesures ultrasonores ; tandis que le deuxième est basé sur le calcul du déphasage du signal pour toutes les directions de propagation considérées. La prise en compte de mesures à différents angles d'incidence permet d'évaluer l'évolution anisotrope de l'endommagement. L'évolution de ces indicateurs est tracée respectivement sur la Figure 17-c et Figure 17-d. Ces derniers retranscrivent une évolution plus importante de l'endommagement pour la configuration 45° que pour la configuration 0°. Ce qui est en accord avec l'estimation de l'endommagement obtenue lors des essais de traction et de tomographie à rayon X. Cependant, la différence d'évolution de l'endommagement entre les deux configurations

pour l'indicateur basé sur le décalage des signaux est plus proche de ces premières estimations de l'endommagement.

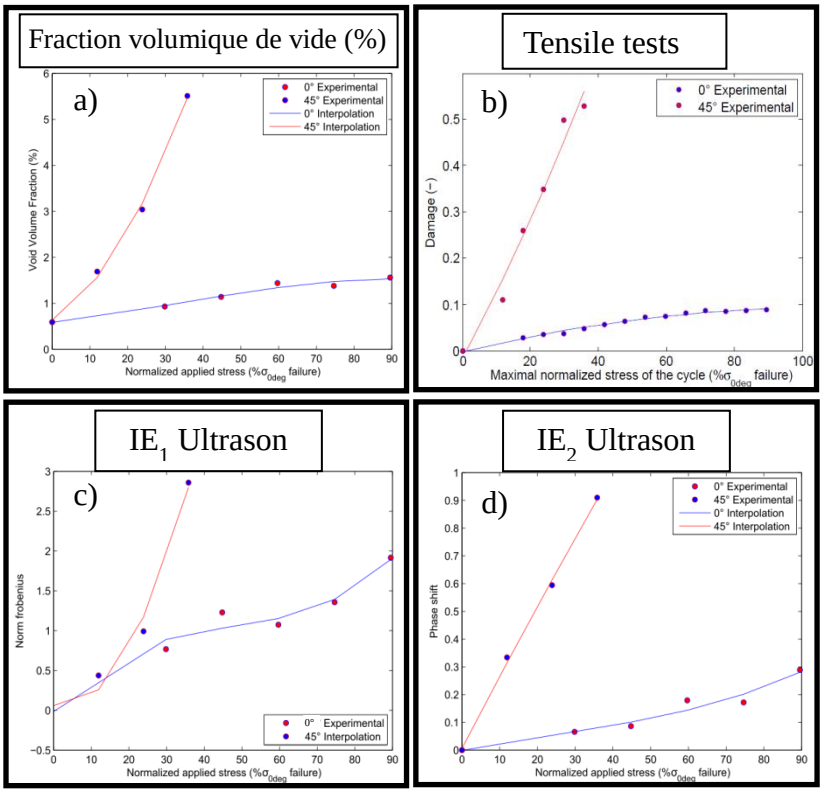

Figure 17 : Evolution des différents indicateurs d'endommagement utilisés jusqu'ici. a) Fractions volumiques de vides obtenues par tomographie à rayons X. b) Réduction du module élastique. c) Norme de Frobenius du tenseur de rigidité obtenue par mesure ultrasonore. d) Déphasage des signaux ultrasonores utilisé pour le calcul du tenseur de rigidité

b) Mesures par ondes de Lamb guidées

Les ondes guidées ont pour avantage de pouvoir analyser une grande surface d'une pièce en une seule mesure. De plus, l'accès à une seule surface de la pièce est nécessaire ce qui permet d'éviter de démonter entièrement une pièce pour la contrôler. Cette méthode est

plus simple à mettre en place que la méthode décrite précédemment. Deux transducteurs sont utilisés en transmission, l'émetteur est fixé alors que le receveur est attaché au bras d'un robot afin de contrôler son déplacement. Un burst de 5 cycles de sinus à 500 KHz est généré par l'émetteur. La distance entre les deux transducteurs variera entre 4.25 et 7.25 cm. Des signaux sont alors enregistrés tous les 0.5 cm. Le montage expérimental est renseigné sur la Figure 18.

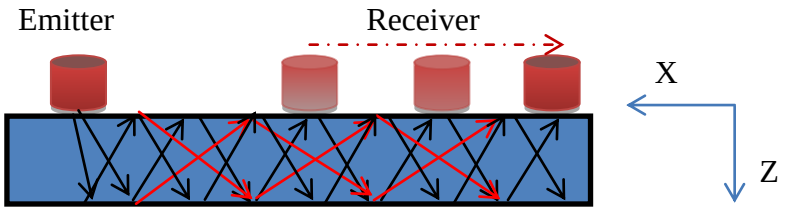

Figure 18 : Montage expérimental pour la mesure des modes d'ondes guidées

Des échantillons intacts de référence sont analysés en premier lieu afin de déterminer quels modes se propagent suivant la configuration. Une analyse des spectrogrammes des différents signaux enregistrés sur les deux configurations d'échantillons a tout d'abord été menée. On peut remarquer, sur la Figure 19-a, qu'un seul mode semble se propager dans l'échantillon dans la configuration 0°, il apparait pour une fréquence de 500 KHz. En revanche, deux modes sont observables sur les spectrogrammes des échantillons dans la configuration 45° en Figure 19-b. Ils apparaissent respectivement pour une fréquence de 500 KHz et 250 KHz.

Ensuite, une transformée de Fourier 2D est appliquée sur les signaux obtenus pour les deux échantillons non endommagés. Cette transformée s'effectue à la fois dans le domaine temporel et dans le domaine spatial. Les figures résultantes sont donc affichées dans un graphe fréquence (MHz)/nombre d'onde (mm^{-1}) pour respectivement l'échantillon dans la configuration 0° (Figure 20) et 45° (Figure 21). Deux ensembles de modes obtenus à l'aide du logiciel *Disperse*, en utilisant deux tenseurs d'élasticité différents, ont été considérés. Ainsi, pour les modes en ligne continue, le tenseur utilisé a été calculé par homogénéisation périodique avec l'aide de Francis Praud. Pour les modes en ligne pointillé, le tenseur utilisé

est celui obtenu par mesure ultrasonore à l'aide de la méthode présentée dans la section précédente.

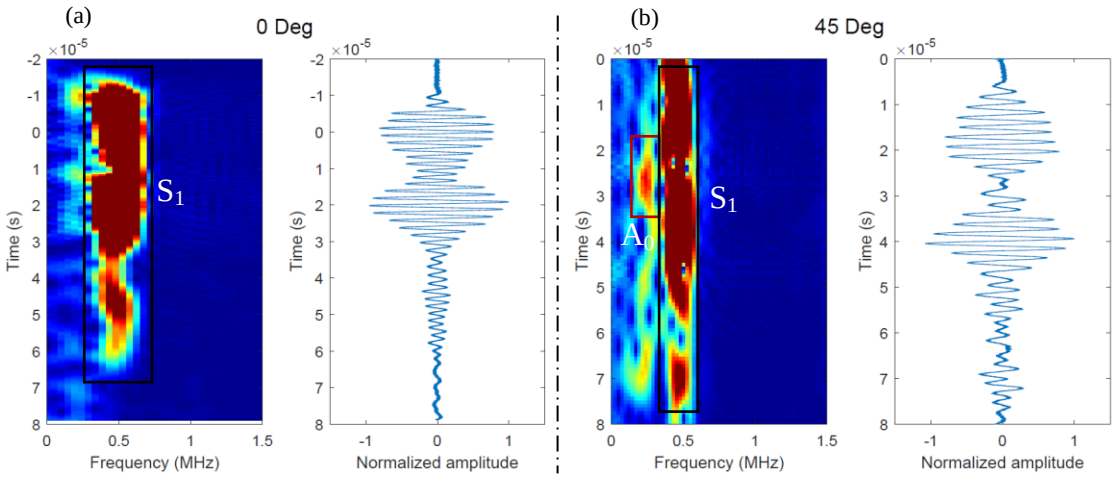

Figure 19 : Spectrogramme d'un signal transmis dans un échantillon dans (a) la configuration 0° et (b) la configuration 45 ° avec le signal temporel correspondant

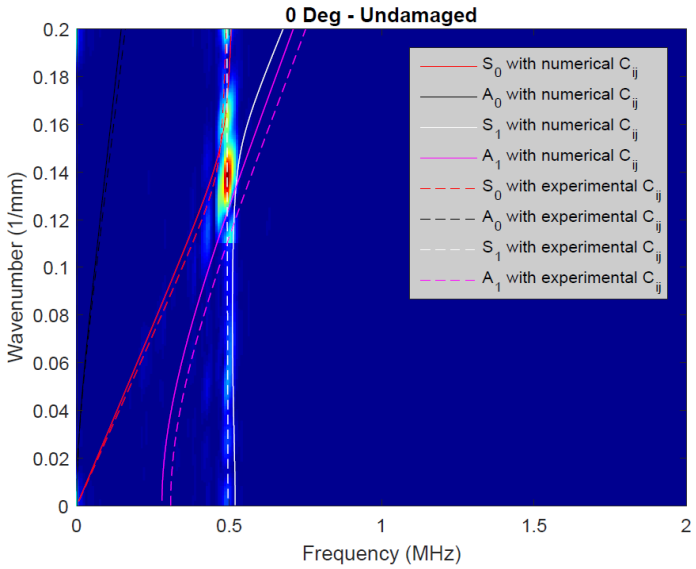

Figure 20 : Transformée de Fourier 2D pour un échantillon intact dans la configuration 0° avec les modes S_0, A_0, S_1 et A_1. Le tenseur de rigidité obtenu par homogénéisation périodique a été utilisé pour les modes en lignes continues. Le tenseur obtenu par mesures ultrasonores, a lui été utilisé pour celles en lignes discontinues.

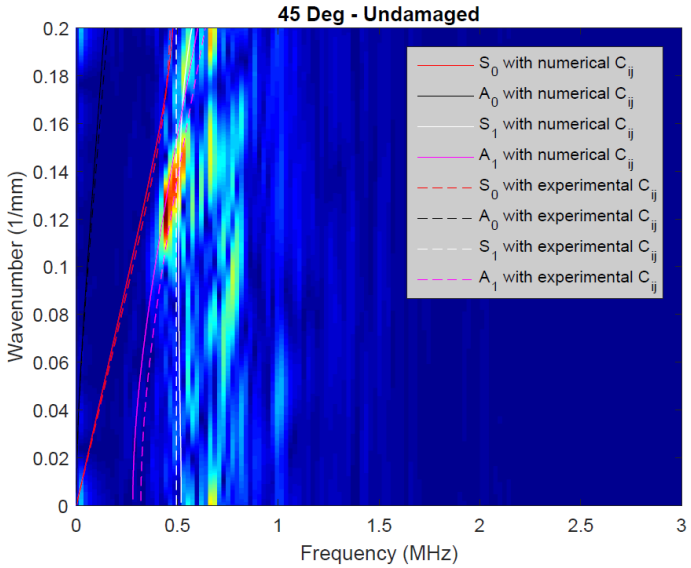

Figure 21 : Transformée de Fourier 2D pour un échantillon intact dans la configuration 45° avec les modes S_0, A_0, S_1 and A_1. Le tenseur de rigidité obtenu par homogénéisation périodique a été utilisé pour les modes en lignes continues. Le tenseur obtenu par mesures ultrasonores, a lui été utilisé pour celles en lignes discontinues.

Pour l'échantillon orienté suivant le sens chaine, le mode observé expérimentalement est très proche de la courbe analytique en pointillé du mode S_1. Cependant, le mode expérimental est également très proche des modes S_0 et A_1, ce qui rend l'identification du mode transmis difficile. La vitesse de phase est alors calculée afin de faciliter cette identification. Pour cela, nous utilisons la méthode dite du « zero-crossing », c'est-à-dire que l'on enregistre les temps pour lesquels le signal passe par zero amplitude pour différentes distances émetteur-receveur. Un exemple d'application de cette méthode est proposé sur la Figure 22-b. La vitesse de phase est ici de 3629 m/s.

Toujours à l'aide du logiciel *Disperse*, les courbes de dispersion fréquences/vitesses de phase ont été tracées sur la Figure 23-a. Comme précédemment, deux ensembles de modes ont été calculés et tracés. Après comparaison avec les courbes de dispersion, le mode expérimentalement observé en configuration 0° est un mode S_1.

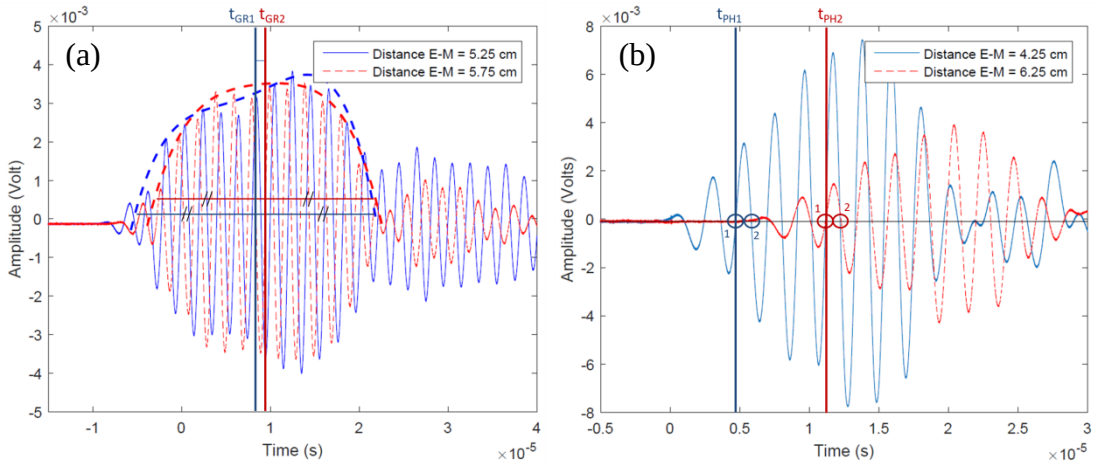

Figure 22 : Deux signaux transmis avec un exemple de mesure des vitesses de (a) groupe et de (b) phase.

Pour l'échantillon en configuration 45°, le mode expérimental apparait entre les modes analytiques A_1 et S_1. La vitesse de phase a ensuite été évaluée à 3272 m/s en se servant de la même méthode que celle citée précédemment. Après comparaison avec les courbes de dispersion numérique, il reste difficile de déterminer le mode avec certitude. Afin de lever cette indétermination, un montage permettant de mesurer le signal arrivant sur la surface inférieure et supérieure de la plaque est mis en place. On s'attend à ce que les signaux mesurés au même endroit sur chaque surface soit en phase, pour un mode symétrique, et en déphasage pour un mode antisymétrique. Il a été observé que pour les deux configurations étudiées, le décalage temporel entre les signaux mesurés sur chacune des faces est très faible. En conséquence, nous faisons l'hypothèse que les modes observés sur les deux configurations sont de même nature. Au vu des informations recueillies jusqu'à présent, les deux modes sont donc des modes S_1.

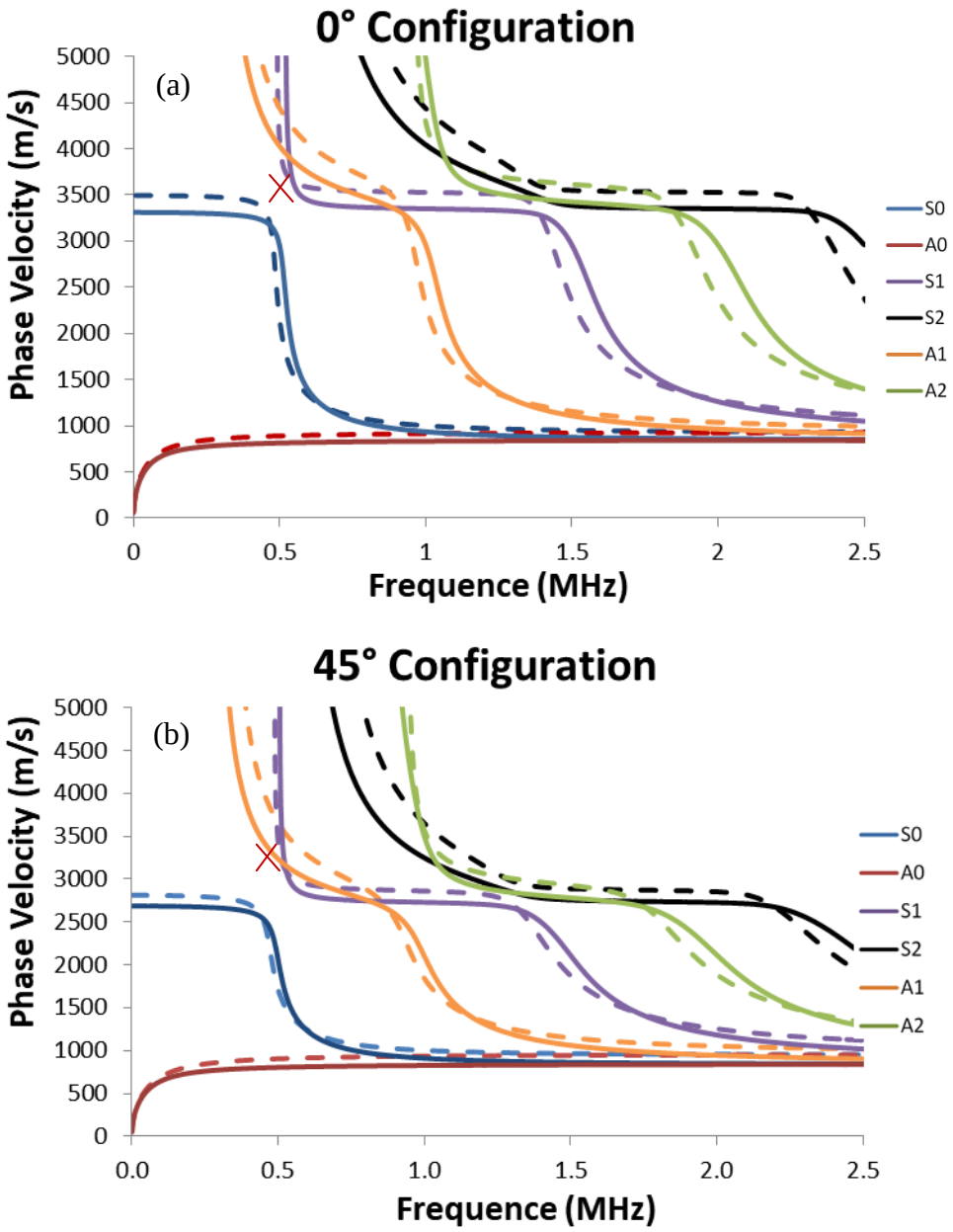

Figure 23 : Courbes de dispersion des vitesses de phase en fonction de la fréquence pour des échantillons dans (a) la configuration 0° et (b) la configuration 45°. La matrice de rigidité, obtenue par homogénéisation périodique, a été utilisée pour les modes représentés par la moyenne des lignes continues. Alors que la matrice de rigidité obtenue par acquisitions ultrasonores a été utilisée pour les lignes discontinues.

Les échantillons endommagés, et étudiés dans les sections précédentes sont ensuite également analysés par ondes guidées suivant la même procédure. L'objectif étant de voir si les endommagements apparaissant dans ces échantillons entraînent un changement dans les modes transmis. Seulement, aucun changement de modes n'a été noté, pour les deux configurations d'échantillons, quel que soit le niveau de chargement considéré. Une autre approche a ensuite été considérée pour évaluer le niveau d'endommagement par ondes guidées. Pour cela, deux autres indicateurs d'endommagement ont été proposés. Le premier prend en compte la moyenne, sur toutes les distances émetteur-receveur considérées, de l'amplitude maximale du signal. Le second est calculé de façon équivalente, mais en prenant en compte l'intégralité du signal au lieu de l'amplitude maximale de celui-ci. Ils sont calculés ainsi :

$$DI_3\ (i) = \frac{1}{n_{max}} * \sum_{i=0}^{n_{max}} Max(x(t))$$

$$DI_4\ (i) = \frac{1}{n_{max}} * \sum_{i=0}^{n_{max}} \int abs(x(t))^2\ dt$$

L'évolution de ces deux indicateurs est tracée sur la Figure 24 pour les deux configurations d'échantillon. Le premier de ces deux indicateurs ne semble pas correctement détecter l'évolution de l'endommagement. Particulièrement pour les échantillons dans la configuration 0°. En effet, de 150 MPa à 250 MPa, l'indicateur décroit de façon continue, ce qui n'est pas en accord avec ce qui été observé dans les sections précédentes. De la même façon, on peut noter que pour l'autre configuration d'échantillon, une décroissance de l'indicateur se produit entre 0 et 40 MPa. L'évolution du second indicateur semble être plus en accord avec les autres indicateurs d'endommagement étudiés jusqu'ici. C'est-à-dire une évolution de l'endommagement avec le niveau de chargement, mais également un niveau d'endommagement maximal atteint plus important pour les échantillons dans la configuration 45°.

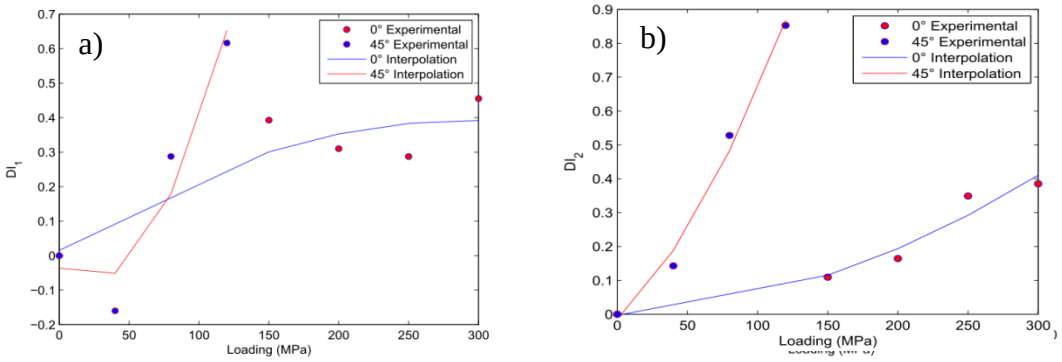

Figure 24 : Comparaison entre les évolutions des deux indicateurs d'endommagement considérés (a) DI_3 et (b) DI_4 pour les deux orientations d'échantillon considérées.

6) Validation sur échantillon impacté par poids tombant

Dans l'industrie automobile, les structures sont dimensionnées en vue de résister le plus possible à des impacts. Cependant, pour la plupart des matériaux composites renforcés par des fibres continues, un impact peut entrainer, même pour des énergies d'impact faibles, l'apparition et la propagation de délaminages. Ce dernier peut entrainer une ruine catastrophique et inattendue de la pièce en composite. Le renfort tissé a pour avantage de réduire la propagation de délaminage, cependant ce type de ruine est toujours possible. Il est donc critique de connaitre le comportement de la pièce lors d'un impact imprévu, mais également de connaitre la capacité des différentes méthodes de contrôle ultrasonore à détecter et quantifier l'endommagement induit par impact.

Cette section est donc dédiée à la validation des méthodes ultrasonores sur structure impactée. Quatre éprouvettes normalisées de 100 x 150 x 1.53 mm ont été impactées à l'aide d'une machine de chute au laboratoire LAMPA d'Angers grâce à l'aide du professeur Laurent Guillaumat. Un impacteur de 16 mm de diamètre et de 1.02 kg a été utilisé. Les énergies d'impact ont été choisies afin de rester dans le domaine des endommagements à peine visibles ou Barely Visible Impact Damage en anglais (BVID). L'énergie d'impact réel et l'énergie absorbée ont été calculées grâce aux courbes

force/déflection par intégration de l'aire sous la courbe. Les informations de l'essai sont indiquées dans le Tableau 5. L'évolution de la force, de la déflection et de l'énergie en fonction du temps sont tracées sur la Figure 25. Il faut noter que lors de l'essai sur l'échantillon impacté d'une hauteur de 2 m, le capteur de déplacement sature. En conséquent, les résultats obtenus à partir de ces courbes doivent être pris avec précaution. Si on exclue ce dernier essai, l'énergie absorbée augmente avec la hauteur d'impact.

Numéro de plaque	**8**	**9**	**7**	**10**
Hauteur de chute (m)	1,00	1,50	1,75	2,00
Energie d'impact attendu (J)	10,00	15,00	17,50	20,00
Energie d'impact mesuré (J)	8,92	14,45	16,36	17,59(*)
Energie absorbée (J)	3,24	6,65	7,73	4,48(*)

Tableau 5 : Hauteur de chute et niveau d'énergie d'impact pour les quatre plaques en composite impactée. Le capteur de déplacement sature pour une hauteur de chute de 2,00 m. Les valeurs avec un (*) doivent être considérées prudemment à cause de cette saturation du capteur

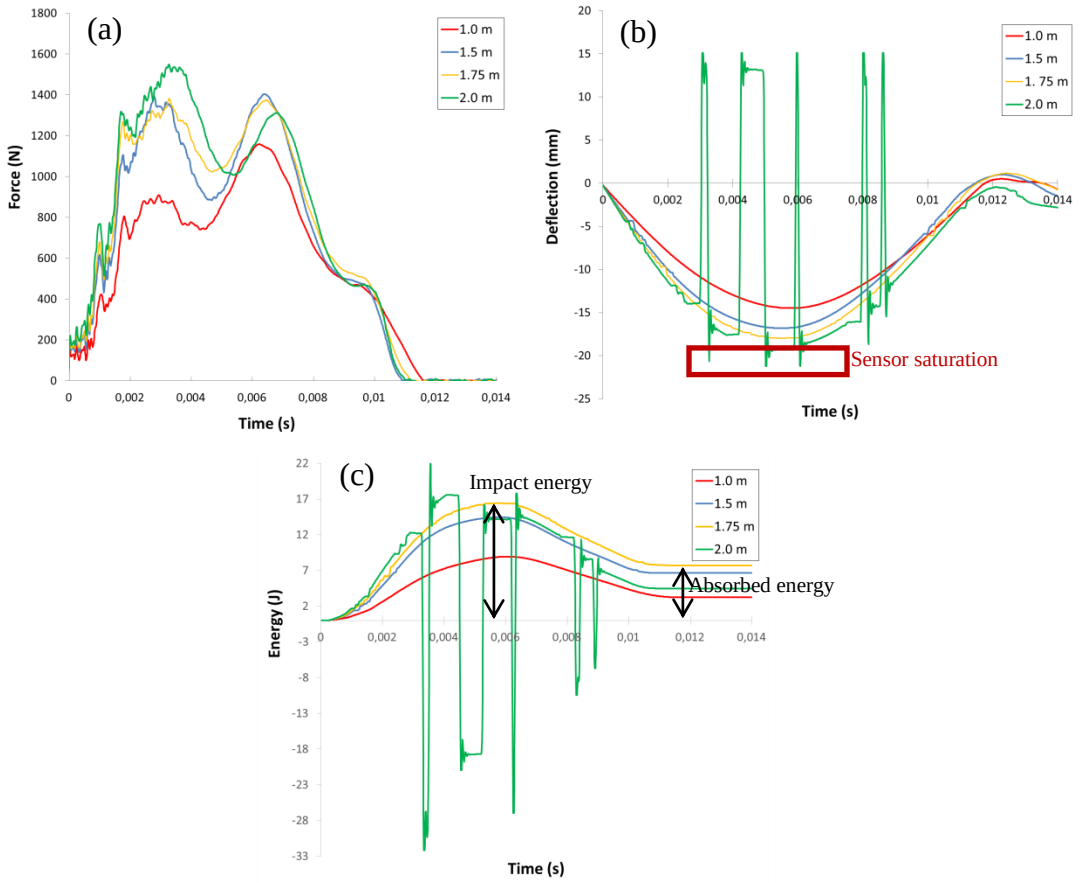

Figure 25 : (a) Coubes force/temps, (b) courbes déplacement/temps et (c) courbes énergie/temps pour les quatre énergies de poids tombant considérées. Le capteur de déplacement sature pour une hauteur de chute de 2.00 M

Après analyse visuelle, on peut remarquer que l'endommagement apparait sur la face non impactée sous la forme de fissures, se propageant suivant la direction longitudinale et transverse. Pour une hauteur de chute de 1 m aucun endommagement n'a été observé ; pour une chute de 1.5 m un endommagement mineur a été induit. Pour une hauteur de 1.75 m et 2.00 m, un endommagement majeur a été généré. La superficie de la zone fissurée est proche pour ces deux hauteurs. Les faces non impactées sont visibles sur la Figure 26.

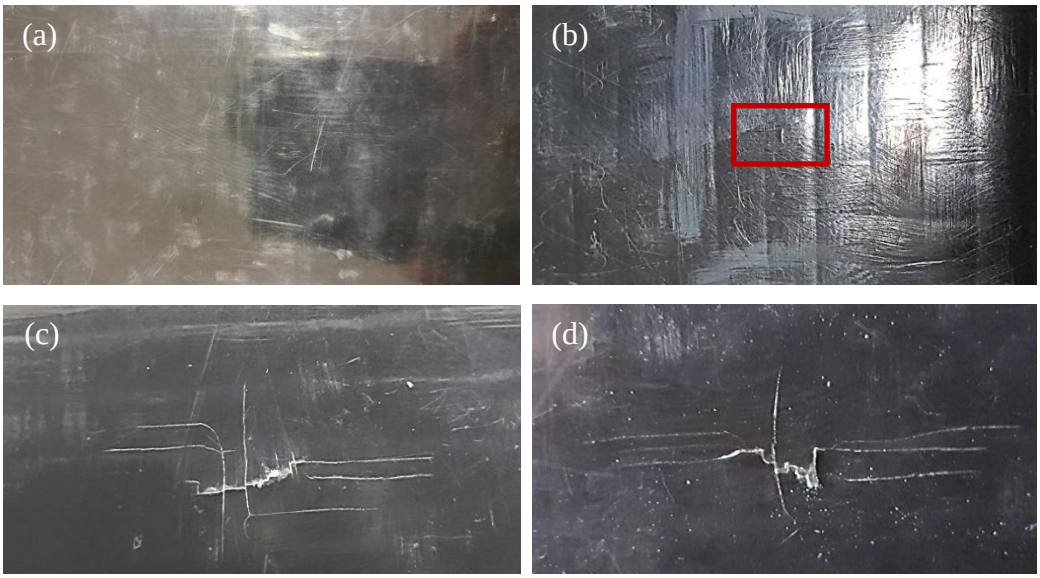

Figure 26 : Faces non-impactée des plaques pour des énergies d'impact de (a) 10 J, (b) 15 J, (c) 17.5 J, et (d) 20 J.

Les quatre plaques ont ensuite été analysées par tomographie à rayon X suivant une procédure équivalente à celle décrite dans la section 4). Cette étude a permis de valider les observations visuelles en termes d'ampleur de l'endommagement induit par l'impact.

Une étude par C-scan ultrasonores en immersion est enfin effectuée sur chacune des plaques. Des essais en réflexion et transmission avec des transducteurs de 10 MHz ont été réalisés. Avec les essais en transmission une zone d'atténuation d'amplitude, correspondant à une zone endommagée, a été imagée sur toutes les plaques sauf celles impactées à 10 J. Les quatre images sont visibles sur la Figure 27. Ensuite, les essais C-scan en réflexion ont permis de caractériser la taille de l'indentation permanente induite par l'impact sur la face impactée. Les indentations permanentes sont souvent utilisées pour estimer la gravité d'un endommagement dû à un impact, particulièrement lorsque l'accès à la face non impactée n'est pas possible. La surface de l'indentation est mesurée grâce aux C-scans représentant le temps d'arrivée du premier pic positif. De plus, comme illustré sur les B-scans de la Figure 28, la profondeur de la déformation permanente est également discernable et peut être mesurée en prenant en compte la vitesse de propagation de l'onde ultrasonore dans

l'eau. Les dimensions des indentations permanentes mesurées sont renseignées dans le Tableau 6 pour chacune des plaques étudiées.

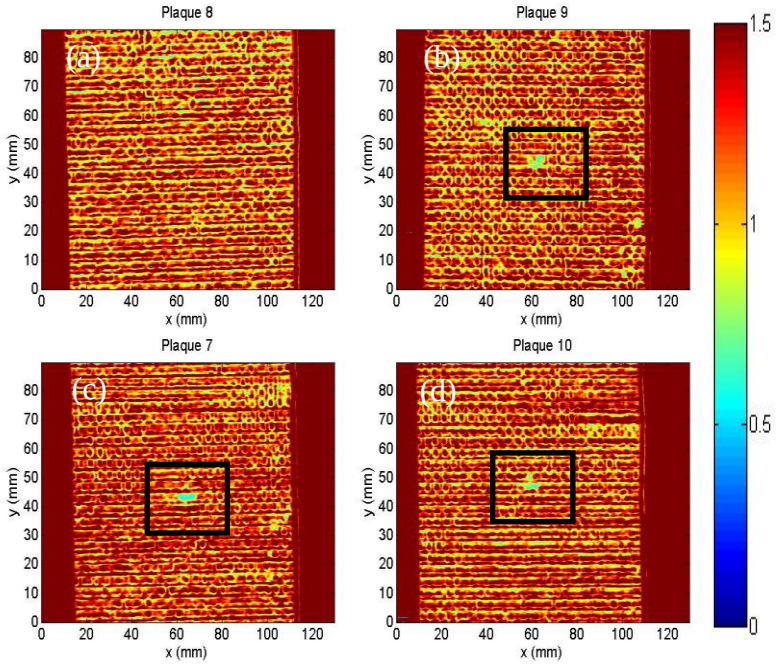

Figure 27 : C-scans ultrasonore en transmission obtenue avec un transducteur de 10 MHz pour les plaques impactée à des niveaux d'énergies de (a) 10, (b) 15, (c) 17.5 et (d) 20 J

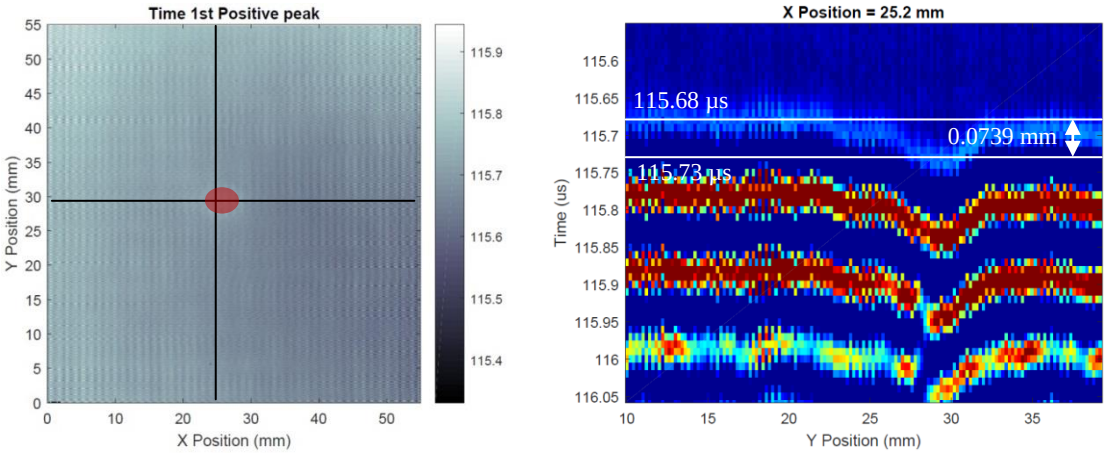

Figure 28 : (a) Carte des temps d'arrivés du premier pic positif de la plaque impactée à 20 J. L'indentation permanente est colorée en rouge (b) Zoom sur un des B-scans de la plaque impactée à 20 J.

On peut remarquer qu'aucune indentation n'a été observée sur la plaque impactée à 10 J. Une marque de 3,2 x 3 x 0,045 mm a été mesurée pour un impact de 15 J. La taille augmente nettement pour l'impact de 17.5 J et passe à 3,8 x 2,8 x 0,088 mm. Elle reste ensuite dans le même ordre de grandeur pour un impact de 20 J, elle a été estimée à 4,2 x 3,6 x 0,074 mm. Cette évolution de la taille de l'indentation permanente est équivalente à celle de la zone endommagée sur la face non impactée. Ainsi, nous pouvons vérifier que l'analyse de l'empreinte de l'indentation permanente peut renseigner sur l'endommagement interne du composite. Bien sûr, d'autres niveaux d'impact devraient être considérés et répétés afin de confirmer cette relation.

Energie d'impact	**10 J**	**15 J**	**17,5 J**	**20 J**
Taille dans le plan (mm) ± 0,2 mm	--	3,2 x 3	3,8 x 2,8	4,2 x 3,6
Profondeur (mm) ± 0,014 mm	--	0,045	0,088	0,074

Tableau 6: Tailles des indentations permanentes mesurées par C-scan ultrasonore en réflexion

Les tenseurs de rigidité des quatre plaques impactées ont ensuite été mesurés à l'aide de la méthode ultrasonore présentée dans la section précédente. Les trois plans principaux des échantillons ont pu être utilisés pour les mesures de vitesse ultrasonore ; celles-ci étant plus grandes que les échantillons sollicités en traction. Les neuf composantes des tenseurs ont pu être identifiées. L'évolution de ces composantes est visible sur la Figure 29, les composantes obtenues sur un échantillon laissé intact sont également renseignées. Après comparaison avec l'évolution des constantes de rigidité obtenue dans la section précédente, on peut noter un schéma de décroissance différent lors de sollicitations par impact. Encore une fois, cette méthode a pu permettre d'évaluer un état d'endommagement dû à un autre type de sollicitions mécaniques. Une décroissance de la plupart des composantes a été observée à partir d'un impact de 17.5 J, à l'exception des composantes C_{12} et C_{44}. Il est

cependant difficile de conclure sur la détectabilité de l'endommagement induit par l'impact de 10 J ou 15 J. En effet, seulement les composantes C_{11} et C_{22}, ainsi que C_{13} dans une moindre mesure, décroissent pour un impact de 15 J. Encore une fois, il faudrait considérer d'autres énergies d'impact autour de 10 – 15 J afin de connaitre le seuil de détectabilité de cette méthode.

Afin de finaliser la validation de cette méthode de détection, les indicateurs d'endommagement utilisés précédemment sont calculés pour toutes les éprouvettes impactées. Pour rappel, le premier indicateur est calculé comme la norme de Frobenius du tenseur de rigidité calculé par mesure ultrasonore des vitesses de propagation. Le second est la moyenne de tous les déphasages entre le signal se propageant dans un échantillon endommagé et le signal se propageant dans un échantillon intact. Ils sont encore une fois nommés DI_1 et DI_2 par la suite. Leur évolution en fonction de l'énergie d'impact est visible sur la Figure 30. On peut noter que les deux indicateurs augmentent avec l'énergie d'impact de façon similaire. Une augmentation est discernable à partir de 15 J, la valeur des deux indicateurs continue d'augmenter nettement pour 17.5 J, puis une augmentation plus importante est notable pour 20 J. Ces observations sont en corrélation avec les résultats obtenus par tomographie à rayons X en terme de gravité de la zone endommagée. En effet, aucun d'endommagement n'a été observé pour une énergie d'impact de 10 J tandis qu'une fissure mineure est apparue pour une énergie d'impact de 15 J et enfin une large zone d'endommagement comparable s'est développée pour 17,5 J et 20 J.

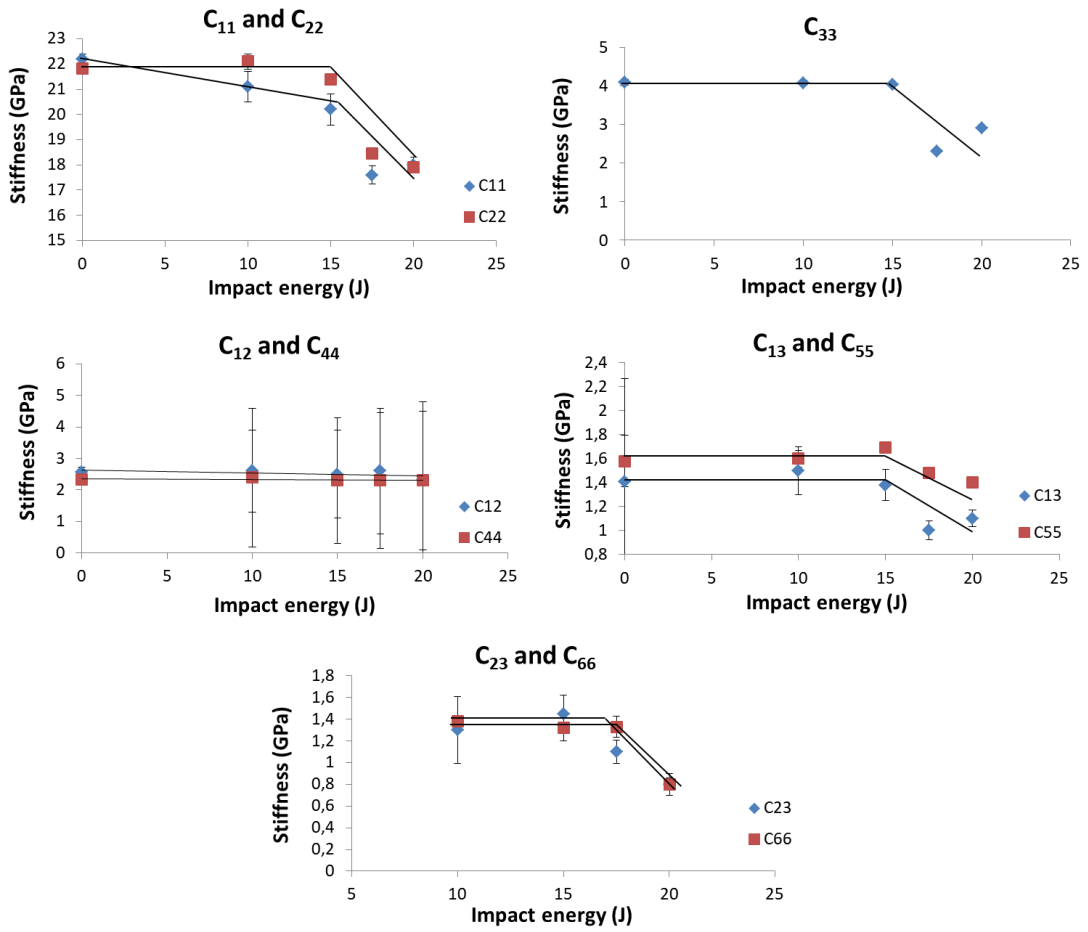

Figure 29 : Evolution des neuf composantes du tenseur de rigidité du matériau composite testé en fonction de l'énergie d'impact.

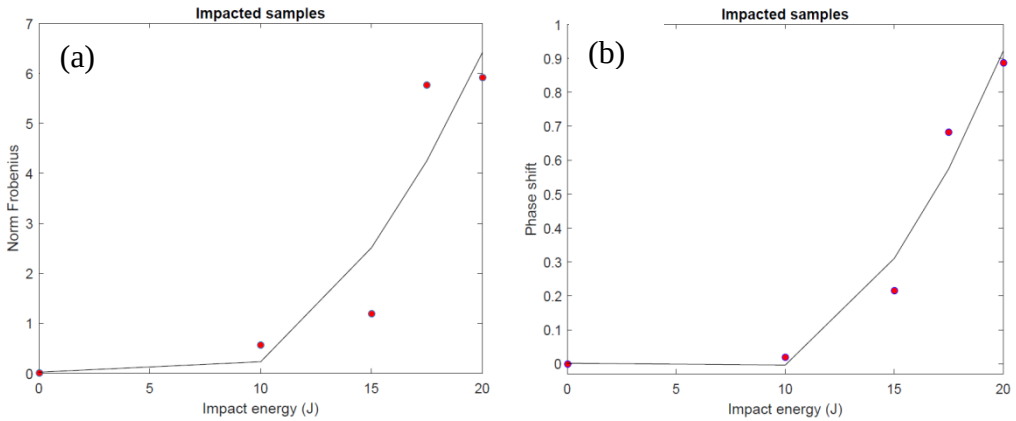

Figure 30 : (a) Evolution de la norme de Frobenius du tenseur de rigidité obtenu par mesures ultrasonores et (b) evolution du déphasage avec l'énergie d'impact

Finalement, des mesures par ondes guidés sont réalisées sur les quatre plaques. Tout d'abord, une mesure ponctuelle est faite en transmission. Deux transducteurs au contact sont placés de chaque côté de la zone impacté, sur la même surface, en étant chacun espacé de 3 cm de cette zone d'impact. Cependant, ici le niveau d'amplitude du signal n'est pas en corrélation avec le niveau d'énergie d'impact. En conséquence, les indicateurs d'endommagement proposé dans la partie précédente ne sont pas validés sur ces essais. Un autre post-traitement a donc été envisagé afin de quantifier le niveau d'endommagement. Le retard du temps d'arrivé du signal, par rapport à un cas de référence, a été alors choisis. Ce dernier est estimé par corrélation-croisé en choisissant la plaque endommagée comme référence. On remarque alors plus le niveau d'énergie d'impact considérés augmente plus le décalage temporel augmente (Figure 31). Les valeurs de décalage temporel obtenues sont également indiquées dans le Tableau 7. De plus, le coefficient de corrélation maximale mesuré reste supérieur à 0.9 quel que soit la plaque étudiés. Ce qui rend sûr les valeurs de décalage temporel obtenus.

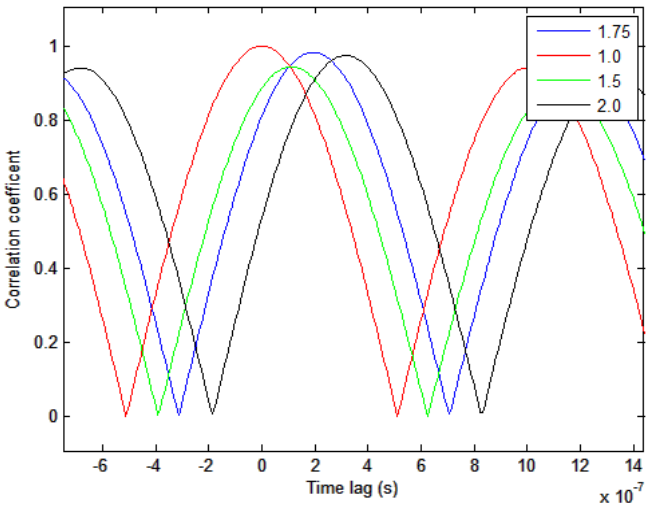

Figure 31 : Résultat de la corrélation croisé effectué sur les quatre plaques impactées

10 J	**15 J**	**17.5 J**	**20 J**
0	1.12e-7	1.92e-7	3.20e-7

Tableau 7 : Décalage temporel mesuré par corrélation croisé sur des signaux mesuré ponctuellement sur les quatre plaques impactées

Afin de valider cette observation, un autre montage expérimentale est mis en place afin d'effectuer cette mesure ponctuelle sur tout l'échantillon. Ainsi, les transducteurs restent séparés de 6 cm mais vont parcourir solidairement une longueur de 70 mm. Seule la plaque impactée à 20 J a été étudiée ici. De la même façon, le coefficient de corrélation ainsi que la valeur de décalage temporel sont estimés pour chaque point de mesure sur la plaque. Les courbes représentant l'évolution du coefficient de corrélation et du décalage temporel en fonction de la position sur la plaque est respectivement tracé sur Figure 171-a et Figure 171-b. Six mesures ont été effectuées afin d'éprouver la répétabilité du montage expérimentale. On peut noter qu'à l'exception d'une mesure (en jaune) toutes les autres mesures présentent des valeurs de coefficient de corrélation au-dessus de 0.9. Ensuite, encore une fois à l'exception d'une mesure (en jaune), une augmentation nette du décalage temporelle est notable autour de -25 mm. Ce qui correspond à l'endroit où le composite a été impacté. Cependant, il faut noter d'importante variation dans les profils de décalage

temporel obtenus selon les mesures effectuées. Cette variation importante a été attribuée à une fluctuation dans la qualité du couplage entre l'échantillon et les transducteurs.

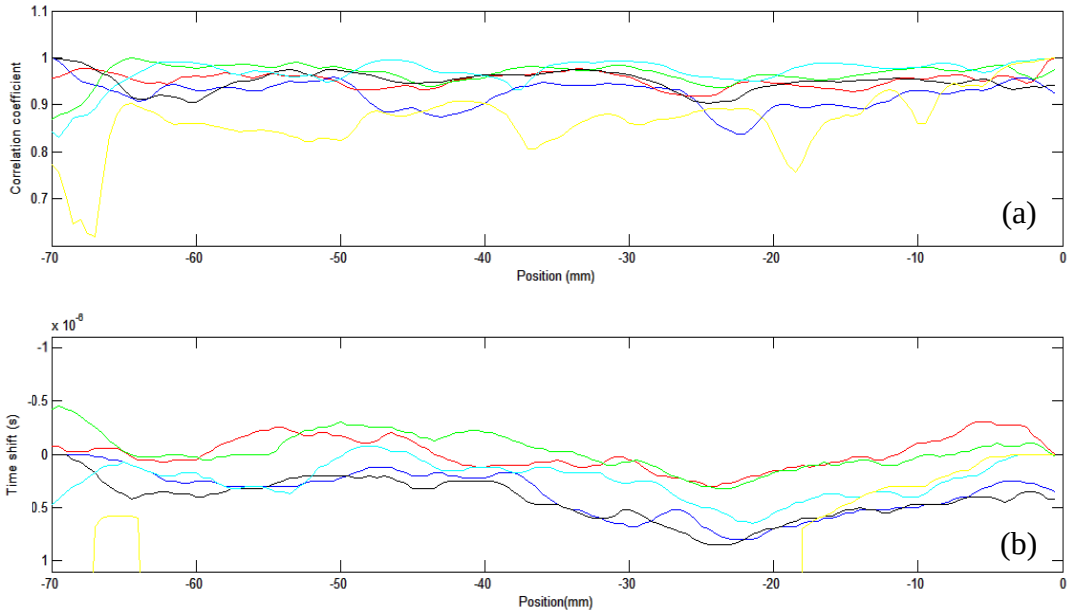

Figure 32 : (a) Evolution du maximum de coefficient de corrélation avec la position des transducteurs. (b) Evolution du décalage temporelle avec la position des transducteurs. Les mesures sont faites sur la plaque impactée à 20 J

7) Conclusion générale et perspectives

Ce travail de thèse avait deux objectifs principaux, tout d'abord étudier l'évolution de l'endommagement d'un composite à base polyamide 66/6 renforcé par un sergé 2,2 de fibre de verre. Ce matériau a été développé par Dupont de Nemours et le groupe PSA en vue de remplacer une partie des pièces métalliques dans les véhicules de série. Ceci doit permettre de réduire le poids du véhicule sans réduire ses performances mécaniques ainsi que sa durée de vie. Ensuite, ce travail visait également à étudier des méthodes de Contrôle Non Destructif (CND) ultrasonore et plus particulièrement leur capacité à quantifier différents

états d'endommagement induit sur des matériaux composite. Ainsi, différentes méthodes de CND ont été étudiées sur des matériaux préalablement endommagés via différents types de sollicitions mécaniques.

Dans un premier temps, le comportement mécanique et les modes d'endommagement lors de sollicitations en traction quasi-statique sont étudiés. Deux orientations d'échantillon ont été considérées : suivant les fibres du sens chaine et orientées à 45° du sens chaine. A l'échelle macroscopique, on note deux réponses bien distinctes. Pour la configuration 0°, une réponse contrainte/déformation linéaire fragile avec un endommagement induit limité. Tandis que pour la configuration 45°, on note une réponse non linéaire ductile avec une augmentation nette de l'endommagement. L'évolution de l'endommagement a été ici estimée par réduction du module élastique. Les champs de déformation, obtenus par corrélation d'image, montrent de plus que pour la configuration 0° la sollicitation en traction entraine majoritairement une déformation uniforme suivant la direction de chargement. Pour la configuration 45°, on observe d'abord également une augmentation progressive de la déformation suivant l'axe de chargement puis un couplage entre le cisaillement plan et la traction. Cette réponse est en fait induite par un effet de réorientation des fibres le long de la direction de chargement. Cette différence de réponse mécanique entraîne également différents mécanismes de rupture. C'est-à-dire une fissure droite et net pour les échantillons en configuration 0° et une fissure en escalier avec du délaminage visible sur les tranches des échantillons en configuration 45°.

Les mécanismes d'endommagement entrainant la ruine ont ensuite été étudiés à l'échelle microscopique. L'initiation de l'endommagement par décohésion fibre/matrice a été tout d'abord observée lors d'essais de traction in-situ au Microscope Electronique à Balayage (MEB). Les autres mécanismes ont dû être observés au tomographe à rayons X suite à différentes difficultés lors des essais MEB. Des échantillons en configuration 0° et 45° ont été observés. Un schéma d'endommagement différent a été noté pour chacune des configurations. Pour la configuration 0°, des mécanismes d'endommagement principalement de faible taille caractéristique ont été observés. En revanche pour

l'orientation 45°, on a pu noter des endommagements de grandes tailles, principalement du flambage de fibres et du pseudo-délaminage. Cette différence de mécanismes entraine une évolution de l'endommagement global distincte. Cette dernière a été estimée par mesure du taux volumique de vides sur les reconstructions 3D des échantillons endommagés. Son évolution en fonction du chargement appliqué présente une évolution similaire à celle de la réduction du module élastique.

Différentes méthodes de Contrôle Non Destructif (CND) basées sur les ultrasons ont ensuite été étudiées. Tout d'abord, des C-scans ultrasonores d'échantillons en configuration 0° et 45° ont été faits. Les échantillons ont été préalablement endommagés en traction à différents niveaux de chargement. Seuls les endommagements macroscopiques apparaissant sur les échantillons en configuration 45° ont pu être imagés. La méthode de calcul des constantes de rigidité par mesure des vitesses de phase a alors été considérée. Grace à cette méthode, l'évolution anisotrope de l'endommagement, après chargement en traction, a pu être observée. Cette évolution est par ailleurs très dissemblable pour les deux configurations et est en accord avec l'évolution des champs de déformation mesurée par corrélation d'image. C'est-à-dire une décroissance des composantes de rigidité dépendant de la direction de chargement pour la configuration 0° et une décroissance de tous les composantes du plan du tissage, y compris le cisaillement plan, pour la configuration 45°. Deux indicateurs d'endommagement basés sur les mesures précédentes ont par la suite été proposés. Le premier est la norme de Frobenius du tenseur de rigidité obtenu et le deuxième est la moyenne, sur tous les plan principaux utilisés, du déphase du signal mesuré par rapport à un signal obtenu sur un matériau sain. Leur évolution, surtout pour le deuxième, est proche de ce qui a été observé grâce aux essais de tomographie et de traction. Les ondes guidées ont ensuite été utilisées pour inspecter les mêmes échantillons. Les modes transmis ont tout d'abord été analysés pour différents cas d'endommagement, mais aucun changement dans la nature des modes transmis n'a été observé quel que soit le niveau de chargement et la configuration des échantillons. D'autres indicateurs ont alors été proposés comme l'énergie du signal transmis. L'évolution de ce dernier est bien en accord avec les autres méthodes d'estimation de l'endommagement utilisées jusqu'ici et indique une

évolution plus importante de l'endommagement avant la ruine pour un échantillon en configuration 45° que pour l'autre configuration.

Enfin, une étude de validation des méthodes proposées grâce à des essais d'impact par poids tombant sur des échantillons est proposée. Différents niveaux d'impact ont été utilisés tout en essayant de rester dans le domaine des endommagements à peine visibles. Il a été montré, par observation visuelle et tomographie à rayon X, que l'endommagement induit augmente avec l'énergie d'impact. L'indentation permanente a été mesurée par pulse-écho ultrasonore sur les quatre plaques. Sa taille augmente également avec l'énergie d'impact ce qui en fait également un bon indicateur de l'endommagement interne induit. La méthode de mesure du tenseur de rigidité a pu détecter une évolution de l'endommagement dès 17.5 J. A partir de ce niveau d'énergie, l'ensemble des composantes diminue, à l'exception de C_{12} et $C_{44,}$ avec l'augmentation du niveau d'énergie. L'indicateur d'endommagement du déphasage augmente lui de façon nette dès 15 J. Enfin, comme l'indicateur d'endommagement basé sur l'amplitude du signal transmis n'a pas pu caractériser l'endommagement induit par impact, une autre méthode de traitement a été considérée. Le décalage temporel a alors été estimé par corrélation croisée et a montré une évolution fonction de l'énergie d'impact. La localisation de l'endommagement a pu être détectée lors de scan effectué sur toute une plaque. Cependant, le montage expérimental, dans son état actuel, présente de larges variations dans les mesures effectuées. Ces variations sont actuellement attribuées à une mauvaise qualité de couplage entre les transducteurs et l'échantillon.

Part II: Damage detection in PA 66/6|Glass woven fabric composite material using ultrasonic techniques towards durability prediction of automotive parts

I) Introduction

Contents

1) Context.....46

2) Objectives and research orientations 50

1) Context

During the last decades, interests and resource efficiency granted to $C0_2$ reduction in automotive vehicle via mass reduction have considerably increased. This is easily explained by the rise of more and more stringent European requirements about car's greenhouse gas emission. Indeed, the European Union required the new average passenger cars to emit less than 130 g $C0_2$/km in 2015 and less than 95 g $C0_2$/km by 2020. Automotive industries in the United States as well as in China also have their own $C0_2$ emission requirement (Figure 33). This makes the car light weighting an international concern which actually involves many industries and research unit. In addition, data from automotive Original Equipment Manufacturers (OEM) shows that "more than 1/3 of the fuel consumption in a fossil fuel-powered vehicle is dependent on mass" [6].

Because of their low density and their relatively high mechanical properties (compared to metallic parts usually used in the automotive industry), polymer based composite material has been quickly considered as a really remarkable solution for the light weighting of next generation cars. The weight percent of plastic materials in large series cars is about 15-20 % nowadays. This percent has slowly increased since the 60's, where it reached 6%, and stabilize around 15-20% since the 2000's [7], [8]. However, because of the previously discussed new European requirements, this percent is set to grow during the next ten years.

Specialists in the French automotive field claim that it will reach 30% before 2020 [9], [10].

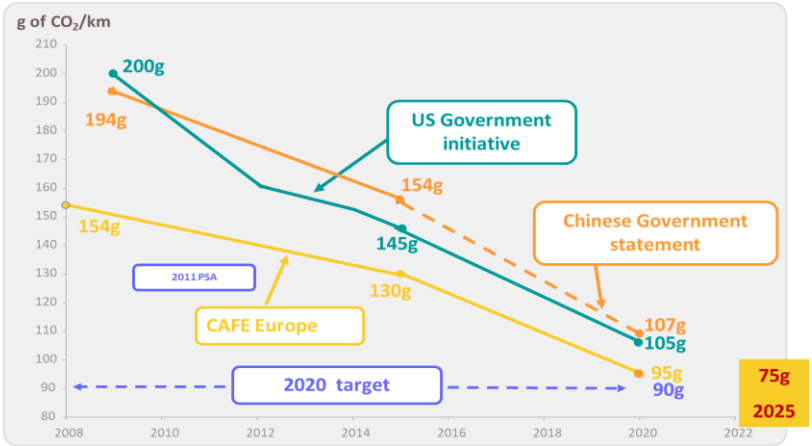

Figure 33 : Required reduction of $C0_2$ emission for large scale produced cars in different countries over years [Groupe PSA]

As a consequence, all the forecasts predict a continuation in the growth of composites parts in the automotive industry (As shown in Figure 34). Two main parts on the vehicle were investigated, the one near the motor that need to withstand high temperature and the one that meant to be used to increase the vehicle's structural performance. As an example, DuPont De Nemours and Groupe PSA manufactured a side-intrusion beam using Vizilon$_{TM}$ woven glass fiber composite in 2013. They showed that a reduction of 40% of weight was achieved in comparison with the ultra-high strength steel previously used. They also showed that DuPont's composite manages to absorb more energy than metals in case of impact. The resistance of automotive part submitted to crash events is of course a key point in the design of automotive structure [6]. Their higher fatigue resistance properties compared to traditional metallic materials is also one of the major reasons of the use of composite materials for structural parts in the automotive industries.

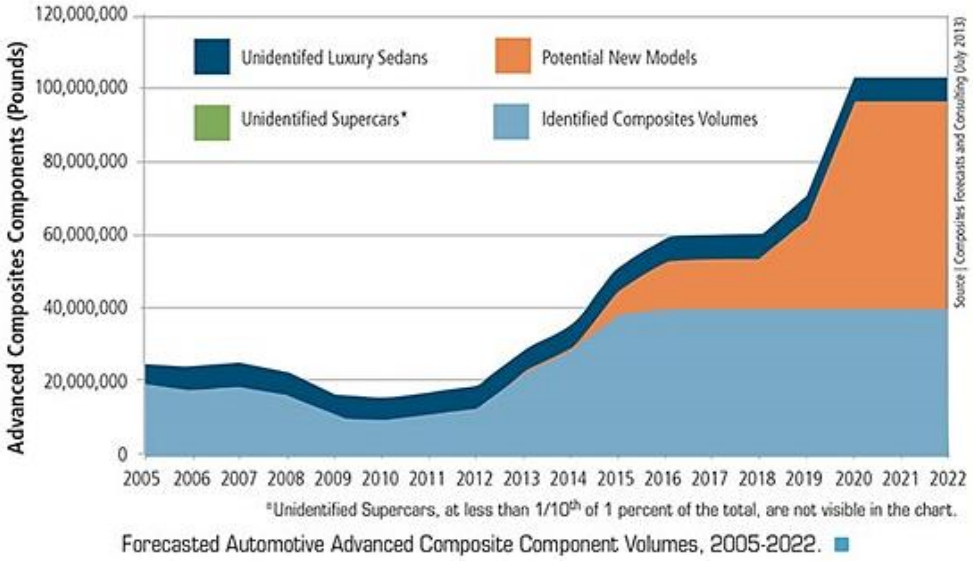

Figure 34 : Forecast volumes of advanced composites components in the automotive industry [Composites, Forecasts and Consulting]

In the opposite of the aeronautic industry, where the composite material made an important breakthrough in the beginning of the 2000's, the automotive industry needs to fulfill several specific requirements such as: relatively low production cost and fast manufacturing cycle per unit, large volume production, specific surface finishing,… [11]. If the innovated manufacture procedures are currently developed to satisfy those conditions Groupe PSA still requires a nondestructive evaluation (NDE) method that can control the automotive part at the end of the production line or during the component life cycle. One does not want to have a critical amount of damage developed during the shaping process of the composite parts. This NDE method should be able to be used on site, fast and reliable. Its final aim is to be also specifically used in car repair shop to control composite parts that may have been damaged after an unexpected impact. Because it is a long time being performed and well documented technique, it has been chosen to use ultrasonic testing methods to investigate the damage state of a composite part and its subsequent damage tolerance. These are used in the industry on multiple types of materials such as metallic material, polymer based material … They can be used either as a tool to characterize sample's thickness, surface treatment, obtain their mechanical properties and, of course, for

characterizing defects and induced damage in materials [12]–[14]. As a consequence of this large application range, there is a lot of NDE techniques based on ultrasound that are investigated in the literature, as it will be discussed in detail in the literature review of the manuscript. They also have the advantages of being relatively inexpensive and easy to set-up on site or being portable.

The study will focus on a thermoplastic matrix based glass fibers reinforced composite produced by DuPont De Nemours meant to be used for structural application. Specifically, it is a polyamide 66/6 based composite reinforced with woven glass fibers. This material is named Vizilon$_{TM}$ SB63G1-T1.5-S3 by their manufacturers. Preliminary works have been performed in 2012 by members of the OpenLab “Materials and Processes”. It was shown that ultrasonic imaging methods can detect large damage appearance induced in this woven composite. However, it was not possible to image the early stages of damage evolution and accumulation.

The present research is taking place in the framework of the OpenLab PSA “Materials and Processes” and was funded by Groupe PSA. This OpenLab involves three academic partners: Arts et Métiers ParisTech, The UMI Georgia Tech-CNRS (UMI 2958) located in Metz and the Luxembourg Institute of Science and Technology (LIST). The letter of intent has been signed by all the partners on May 19th of 2011. The objectives of these OpenLabs is to allow Groupe PSA “to remain on the leading edge of automotive products and services” and “to strengthen its scientific partnerships with the world’s most advanced scientific key Labs”. More specifically, the present thesis subject is a partnership between Georgia Tech Lorraine, les ENSAM-Arts et Métiers ParisTech and Groupe PSA. The research was undertaken in the LEM3-UMR CNRS 7239 and the LUNE laboratories, respectively located in the ENSAM-Arts et Métiers campus and the Georgia Tech Lorraine campus both in Metz.

2) Objectives and research orientations

In 2013, first investigations underwent in the framework of the OpenLab Materials and processes on Vizilon$_{TM}$ SB63G1-T1.5-S3 showed that critical damage can be detected in this composite material. However, the final goal of Groupe PSA is to develop a NDE ultrasonic tool to detect and quantify damage of automotive parts. With this tool a technician should be able to determine if the parts can still be used or if they need to be replaced or repaired. In order to achieve this objective, different damage indicators based on the ultrasonic measurement have to be developed and validated on damaged structure. Then, various fatigue tests can be performed on either the structural parts or a car prototype in order to predict the performance and durability of those structures.

However, before developing this NDE tool, one needs to compile a lot of information on the damage development scheme of the polyamide 66/6 based composite reinforced by woven glass fabrics. Data on damage mechanisms, their chronology of appearance, the influence of the loading nature and path, etc are required. Its mechanical behavior and the related damage effects should also be completely known. Two sample configurations, which are oriented at 0° and 45° from the warp direction, were chosen to be considered for the present study. They obviously are the limiting case of the composite mechanical behavior under tension. Solicitations under low velocity impact were also taken into account because they are considered as event that an automotive part is more likely to undergo during its life in service.

All the samples were investigated after various mechanical solicitations with optical microscopy, Scanning Electronic Microscopy (SEM), X-ray tomography and ultrasonic methods. The ultrasonic apparatuses are actually located at the LUNE laboratory of Georgia Tech Lorraine whereas all the other apparatus are in the LEM3 laboratories in the ENSAM-Arts et Métiers ParisTech campus of Metz. In order to know their sensitivity to detect damage, several ultrasonic NDT methods were investigated during this project. Indeed, the present project is close to a scoping study, from the ultrasonic point of view.

After a review of the investigated ultrasonic based NDE methods some of them were chosen, based on their respective advantages and accordance with the considered composite material.

The present manuscript will be organized according to the following structures:

The chapter II) will be focused on the description of the VizilonTM SB63G1-T1.5-S3 and its constituents based on the information given by the manufacturer DuPont de Nemours. Firstly, it will be reminded what a composite material is; then the different types of matrix and reinforcement are quickly described. A particular attention will be, of course, given to the woven fabric architecture. Then, more specific information will be given on the polyamide 66/6 and the woven E-glass fiber reinforcement that constitute the studied composite itself.

In the chapter III), the different mechanical tests performed on the DuPont's composite material are described and analyzed in terms of damage and stiffness reduction. These include monotonic and cyclic incremental tensile tests performed on both 0° and 45° configurations. An expected difference in the stress/strain response was observed between the two samples orientations. This was confirmed by measurements of the elastic modulus' evolution during the incremental cyclic tensile tests.

The chapter IV) is devoted to the study of the microstructure of the polyamide 66/6 composite reinforced with woven glass fibers. The global microstructure was first investigated with optical microscope. Then undamaged and damaged samples were analyzed with Scanning Electronic Microscopy (SEM) and X-ray tomography. The different damage mechanisms, that may appear, were observed for both sample configurations. Then, the void volume fraction evolution, as a function of tensile loadings level, is measured by images analysis using the grey level thresholding on the X-ray tomography results for both orientations.

Afterwards, the different samples loaded in tension are analyzed with ultrasonic techniques in chapter V). A literature review, dedicated to the ultrasonic NDE methods to

investigate damage, is proposed in the first subsection. There is a growing interest for most of those methods in the field of polymer based composite materials. In a second subsection it is showed that the classical C-scan methods are not suitable for damage quantification, at the microscale, in the studied composite material. Other techniques were then successfully used on stepwise damaged composites samples. First of all the measurement of stiffness components via ultrasonic transmitted signal is performed. This was successfully used on the samples previously analyzed with X-Ray tomography. Its can give useful information to understand how damage mechanisms occur and alter the stiffness properties of the material. Based on this measurement, a first damage indicator was proposed based on the phase shift at various incidence angles. Then, guided waves investigations were considered for a next subsection. This method was also proved to be effective to detect increasing states of damage. From those experimental results, a second damage indicator that considers the signal energy was proposed.

Finally, the validation of the proposed NDT ultrasonic based methods on composite specimens impacted at different energy level is proposed in chapter VI). The samples were analyzed by X-ray tomography in order to observe the induced damage mechanisms as well as the extent of the damaged areas. The ultrasonic C-scan was then performed, both in reflection and transmission, and useful information was collected. The measurement of stiffness components and guided waves was finally used on those samples in a similar manner as in the previous chapter.

The investigations of two others NDT methods based on ultrasound are presented in two appendixes at the end of the manuscript. Since they are worth mentioning, but are not as much in connection with the main study of this research than the other presented investigations, they are proposed in the appendix section. The first appendix is dedicated to the investigation of non-linear ultrasonic methods of damage evaluation whereas the second appendix is dealing with the use of the coda part (or later arrival part) of the signal to quantify the growth of induced damage. Both methods were presented in the literature review dedicated to ultrasonic based NDE method that can be found in chapter V).

II) Description of the studied composite material: Woven glass reinforced polyamide 66/6

Contents

1) Overview of composite material.....55

a) Matrix Parts 55

b) Reinforcements.....56

2) Components of the studied composite material.....57

a) Glass fibers 58

Woven fabric reinforcements.....60

b) Polyamide 66/6 matrix 64

Sensitivity to moisture absorption 65

Sensitivity to temperature 68

c) Properties of the composite material 70

3) Conclusion 73

The main aim of this first chapter is to introduce the Vizilon$_{TM}$ SB63G1-T1.5-S3, produced by DuPont, which is studied in this thesis manuscript. This composite material is a polyamide 66/6 reinforce by woven glass fibers. First, the advantages of the composite material and its specificities are briefly reminded. Then, a focus on woven composite material and its associated damage mechanisms is proposed. The different components of the composite material chosen by Groupe PSA are then introduced in two further subsections. A discussion on the influence of temperature and moisture content on a polyamide matrix is also going to be proposed. In addition, the final subsection is mostly

dealing with specific information on the studied composite material. Most of these technical data were given by the material's manufacturer DuPont.

1) Overview of composite material

A composite material is made of two or more different constituents that are “mixed” together; the latters can be separate in three categories:

- A matrix, which holds the different parts together and allow the composite to be shaped. It also transfers the mechanical loading to the reinforcement parts.
- Reinforcements, which add rigidity and limit crack propagation in the composite material.
- Additives are often added to the matrix part to enhance its properties, whether in terms of electrical/thermal conductivity or stiffness. This eases a reduction in the composite’s cost by lowering the volume fraction of reinforcement without decreasing its mechanical properties.

The two first mentioned types of constituents will be discussed in the following sections.

a) Matrix Parts

Three classes of matrix can be easily distinguished: Ceramic Matrix Composites (CMC), Metal Matrix Composite (MMC), Organic/Polymer matrix composites. The first two are considered for high temperature application. If the composite will not be submitted to a temperature higher than 300°C during its lifespan of service, the organic matrix composites can be used. They are polymer based matrix and are the most used class of composites in the industry. They are usually considered for low cost parts at high-volume production manufacturing. The material studied in the present manuscript is based on an organic matrix (Polyamide 66/6). Therefore, this class will be highlighted in the present section. The polymer matrices can be split in two families: thermosetting matrix and thermoplastic matrix.

- Thermosetting matrix

They are made by heating, which will induce a curing process due to the presence of a catalyst or hardener. Strong three dimensional bonds will be created between the macromolecules. These bonds will be too strong to allow recycling, or a reshaping, of the parts, contrary to composite parts having a thermoplastic matrix.

- Thermoplastic matrix

The thermoplastic matrices are made via a process of heating/cooling which will lead to the creation of weaker Van Der Waals bonds. This results in a reversible structure that can be reshaped multiple times and therefore can be recycled more efficiency. They can be much easily stored, at higher temperature in particular. The curing time of TP is shorter, so this allows an easier mass production than thermosetting matrix. The last three properties lead the French automotive industry to focus on thermoplastic based composite materials. However, the mechanical properties are much more sensitive to high temperature than thermosetting, exception perhaps for high performance thermoplastic matrices. They are also more sensitive to fatigue damage than thermosets. The matrix polyetherketone (PEEK), polyethersulfone (PES) or polyphenylene sulfide (PPS) and of course the polyamide (PA), that will be discussed in detail further on, can be mentioned as good examples of thermoplastic matrix.

b) Reinforcements

As explained earlier, reinforcements are meant to increase the composite's rigidity strength by slowing down the propagation of cracks. They can be added to the matrix as fibers, aggregates, etc. In the present work, the case of fiber reinforcement will be considered. Mechanical properties of several of the industry's most used fibers are listed in Table 1. Typically, they exhibit highly anisotropic properties. The assumption that the fibers are transversely isotropic is usually made for most of the fibers. For others, in

particular for glass fibers, an isotropic structure is assumed. Whenever available in Table 1, the transverse modulus has been estimated by indirect measurement techniques.

Fiber	E_L	E_T	σ_{rL}	ε_{rL}
Polyaramide HM	120	2,5	2900	1,9
Polyamide 6,6 HT	6		960	20
Carbone HT	230	6	3500	1,5
Glass E (Standard)	73	68	2500	3,5
Glass R (High performance)	86		3300	3,5

Table 1 : Mechanical properties of the most used fibers in composite materials [15]. E_L, E_T: Respectively longitudinal and transverse Young modulus; σ_{rL}, ε_{rL}: Respectively stress and strain to failure.

Fiber reinforcements can be used as small fibers or continuous fibers in the composite material. In the latter case, their length is equivalent to that of the plate. They can be arranged along a unique direction (unidirectional composite), as a woven plain fabric or randomly oriented. This choice is normally made while considering the final application of the composite, its expected solicitations in service, its required shape and the expected performance.

2) Components of the studied composite material

As aforementioned in this chapter, the studied composite material is a polyamide 66/6 based composite reinforced with a 2/2 twill weave glass fiber fabric. The different constituents of the composite will now be introduced. In addition, the properties of the composite itself, the Vizilon$_{TM}$ SB63G1-T1.5-S3, will be discussed.

a) Glass fibers

Various types of glass fibers exist in the industry. One can distinguish A, C, D, E, R, S, etc -glass fibers, among others. Each of these types of glass fibers has its own composition and mechanical, electrical, chemical, etc…, properties. The Table 2 gives the compositions of several of the most used types of glass fibers; whereas the Table 3 gives their mechanical properties. In the studied composite material, the reinforcement is made by E-glass fiber, which is the most commonly used glass fiber in the industry. This is due to its reasonable cost of production and to its satisfactory mechanical properties. The “E” stand for “Electrical-application”, this type of glass fiber is indeed very poor in alkali metals in contrast with the A-glass fiber. Now, the woven fabric is considered and the benefit of this arrangement over unidirectional is explained.

	E-glass w/Boron	E-glass w/o Boron	ECR-glass	S-2 glass	R-glass	Quartz
SiO_2	52-56%	59%	54-62%	64-66%	60-64%	99.9999%
Al_2O_3	12-16%	12.1-13.2%	9-15%	24-26%	17-24%	-
B_2O_3	5-10%	-	-	-	-	-
CaO	16-25%	22-23%	17-25%	-	5-11%	-
MgO	0-5%	3.1-3.4%	0-5%	8-12%	6-12%	-
ZnO	-	-	2.9%	-	-	-
Na_2O	0-1%	0.6-0.6%	1.0%	0-0.1%	0-2%	-
K_2O	trace	0-0.2%	0.2%	-	0-2%	-
TiO_2	0.2-0.5%	0.5-1.5%	2.5%	-	-	-
Zr_2O_3	-	-	-	0-1%	-	-
Li_2O	-	-	-	-	-	-
Fe_2O_3	0.2-0.4%	0.2%	0.1%	0-0.1%	-	-
F_2	0.2-0.7%	0-0.1%	trace	-	-	-

Table 2 : Comparison of various types of glass fiber by mass ratio of the different components

	E-glass	R-glass	HS2,HS4	T-glass	S-1	S-2
Tensile strength (GPa)	1.9-2.5	3.1-3.4	3.1-4.0	4.0-4.2	3.8-4.1	4.3-4.6
Tensile modulus (GPa)	69-80	86-89	82-90	84	85-87	88-91

Table 3 : Mechanical properties of various types of glass fibers (Source: www.compositeswolrd.com)

Woven fabric reinforcements

Woven fabric belongs to the textile fabric family. A graph describing the different textile fabrics in the composite industry is shown in the Figure 35. Here, this section is focused solely on the case of 2D woven fabric.

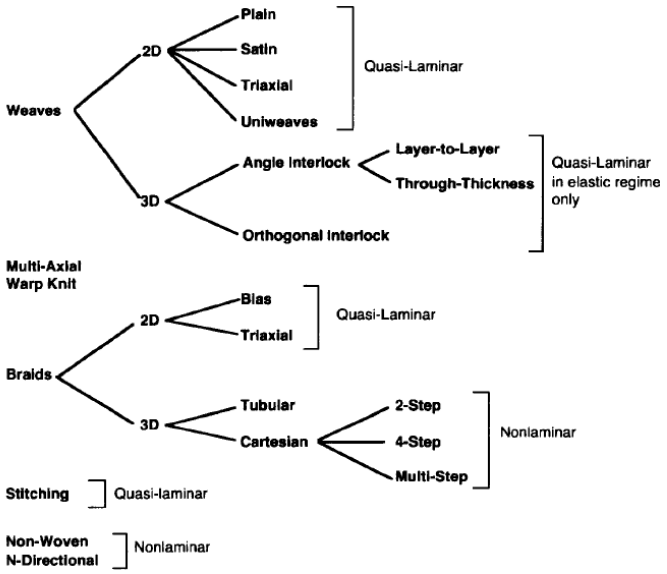

Figure 35 : Representation of the different textile fabrics used in the composite industry [114]

Contrary to unidirectional reinforcement, woven fabric allows a better balance of the mechanical properties, and better resistance to out of plane loading. They also have a better ability to withstand impact and buckling, which is of critical interest for the automotive industry. Nevertheless, they have a lower maximal strength and elastic modulus for a solicitation along the axis of the fibers compared with unidirectional composite [2], [3]. Woven composites are also usually more expensive to produce because of the weaving process of the fabric [15], [16].

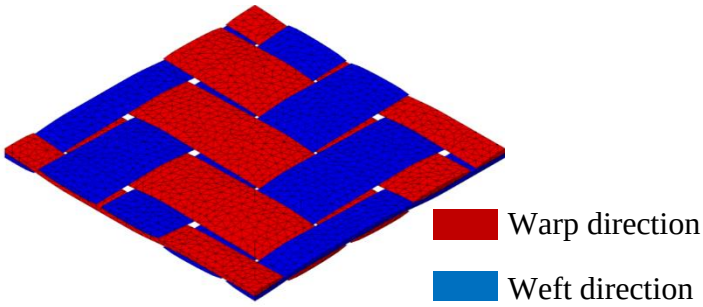

Figure 36 : Meshing of a 2/2 twill weave fabric [115] (Courtesy of Francis Praud)

Woven fabric is made of yarns intertwined together to create a complex structure. The yarns in the longitudinal direction are usually named warp, whereas the ones in the transversal direction are named the weft just as in the textile industry. A representation of a woven fabric with both yarns directions can be observed in Figure 36. Two values are used to define the shape of the woven fabric; this will also define its class:

- n_c indicates that a weft yarn is intertwined with the n_cth warp yarn
- n_t indicates that a warp yarn is intertwined with the n_tth weft yarn

Three different classes of woven fabric can be defined as:

- Taffetas (or plain weave fabric) with the weft and warp yarn intertwined alternatively, which mean $n_c = n_t = 2$. Those are the most stable and stiff fabric, which make them more difficult to be shaped (Figure 37-a).
- Twill with a warp yarn goes up several weft yarns then under a weft yarn with a regular motif. A diagonal motif on the surface of a plate is observed. This is the intermediary class between taffetas and satin (Figure 37-b).
- Satin with a warp yarn goes up several weft yarns then under a weft yarn with a non-regular motif; $n_c = n_t \geq 5$. This is the most flexible woven fabric and it allows the manufacturing of complex parts more easily (Figure 37-c).

These woven fabrics can then be layered as well as classical unidirectional composite material.

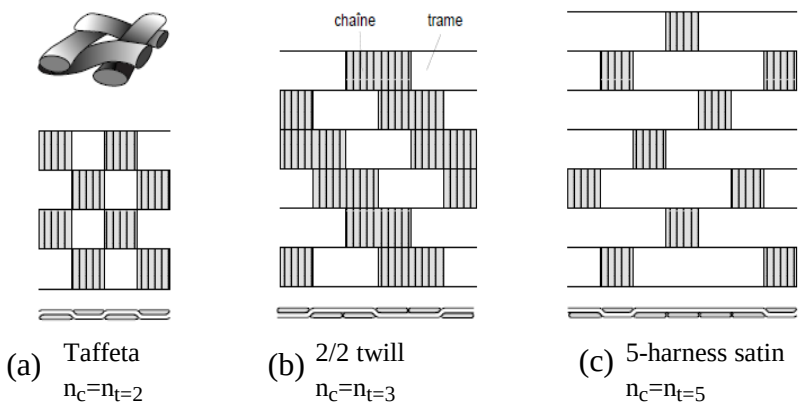

Figure 37 : Schematic representation of the differents woven armor classicaly used in composites material [15]

Compared to a unidirectional reinforcement, the woven reinforcement will suffer a specific damage scheme with specific damage mechanisms. Those mechanisms are classically distinguished into three classes that represent each damage scale:

- Macroscopic scale : Delamination
- Mesoscopic scale : Intra-warp cracks, fiber breakage
- Microscopic scale : inter-warp cracks, Fiber/Matrix debonding

The intra-warp cracks can appear in two configurations. First, transversal cracks can appear parallel to the warp axis along his thickness. Second, longitudinal cracks can appear parallel to the warp axis but along the fabric plane. Karakaya et al. [2], among others, show that these damage mechanisms will be different considering the solicitations and the orientation of the fibers. Tension, bending and compression loading were considered on samples oriented along the warp direction and a 45° direction from the warp axis. Further details about the related damage mechanisms and mechanical behavior can be found in the work by Karakaya [2]. In order to show the change in damage scheme induced by different solicitations, tensile loading at 0° and 45° from the warp directions will now be briefly discussed.

For 0° orientations, fiber/matrix debonding can first be observed. Transversal cracks in the yarns then propagate along the debonded area. When the cracks reach the end of transversal yarns, a deviation of the cracks may occur and induce a longitudinal yarns/matrix debonding. This mechanisms is often named “meta-delamination” [17] and can be observed in Figure 38-a. The failure of the composite is then caused by longitudinal yarn breakage as visible in Figure 38-b. A pull-out of the fibers can consequently be observed [18].

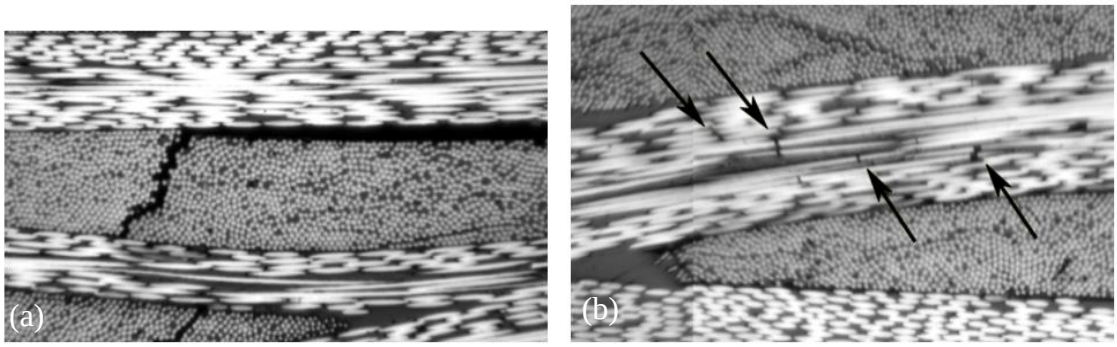

Transversal cracks and associated yarns/matrix debonding Fibers breakage in a longitudinal yarn

Figure 38 : Damage mechanisms in a woven composite loaded in tension along the fibers axis [18]

For 45° orientations, the ductility of the matrix will induce a reorientation of the fibers in the loading direction as illustrated in Figure 39. This phenomenon is induced by plasticization of the matrix near the intertwined area of yarns and is even more pronounced with the matrix’s ductility, temperature and loading velocity [19], [20]. When plastic deformation is no longer possible in the matrix nor the interphase, micro-cracks then appear in the matrix, and propagate along the fibers [20], [21]. This will generally induce delamination in the composite material. Then, shear band localization can be generated and will propagate along the fibers. In the end, the fibers break prior to the final failure of the composite. As shown in Figure 40, the post-failure samples submitted to tensile tests in the 45° orientations may exhibit large amount of delamination.

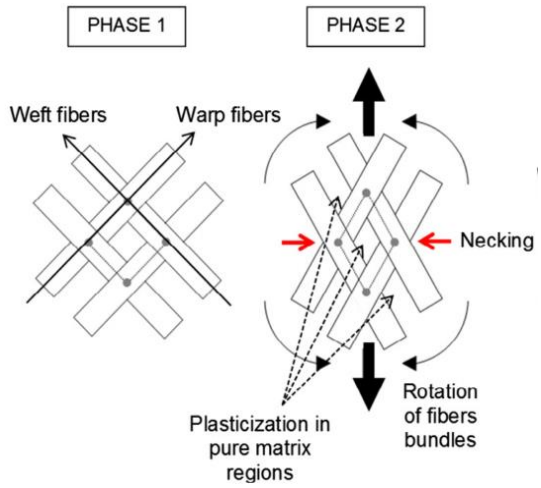

Figure 39 : Fibers rotations during tensile tests on samples oriented at 45° from the warp direction [116]

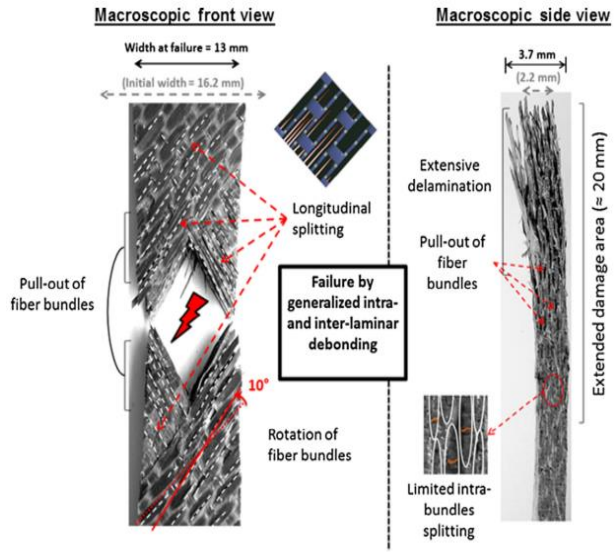

Figure 40 : Post failure damage mechanisms after tensile tests on samples oriented at 45° from the warp direction [116]

During their life cycle, composite parts can be submitted to various solicitations along various orientations. So, it is important to analyze the behavior of the woven composite under these various load cases when the introduction of those materials is considered for a new application.

b) Polyamide 66/6 matrix

Polyamide polymers in general are known for their high strength, abrasion resistance, and resilience. They are however also very sensitive to humidity. The polyamide 66/6 is a copolymer based on polyamide 66 that was developed to obtain a compromise between the polyamide 66 and the polyamide 6.

The polyamide 66 is a thermoplastic polymer made of repeated amid chains. It was first produced by *DuPont De Nemours* in 1935 and then sold as a textile fiber in 1938 (and called Nylon). The polyamide 6, later developed in 1938 by Paul Schlack at *IG Farben*, has a higher resistance to impact and toughness, but lower stiffness properties compared to

polyamide 66. They are more sensitive to humidity, i.e. a higher moisture content, for the same atmospheres conditions [22], [23].

With the polyamide 66/6, the high toughness and impact strength from PA6 can be coupled with the high stiffness from PA66. This is a great advantage for the automotive industry, which can make use of the impact resistance of the polymer without decreasing the stiffness properties to a too large extent. In addition, the copolymer 66/6 can have an enhanced flowability in injection molding which can be helpful during the manufacturing process. Typical properties of polyamide 66/6 are given in Table 4.

Young's modulus (GPa)	1.7*-3.3
Tensile strength (MPa)	45*-80
Elongation at break (%)	5-20*
Melting point (°C)	240
Density (kg/m^3)	1130-1150

Table 4 : Typical properties of polyamide 66/6. The values with a "*" correspond to a conditioned PA66/6 (Source: www.matweb.com)

Sensitivity to moisture absorption

Just as with the other mentioned polyamides, the 66/6 is known to be very sensitive to relative humidity. Indeed, the hydrogen bond between the different amide molecules that make up the polyamide can interact with water molecules. This leads to a weakening of those hydrogen bonds and an increase of the mobility in the polyamide chains of the amorphous network. This is called the plasticizing effect of water. The modification of the molecular structures of the polyamide 66/6 induces important changes in the mechanical behavior of the polymer and an increase of its ductility, as it can be observed in Figure 41. Some authors observed changes in the crystalline phase in the presence of water but this

phenomenon is not clearly understood; nevertheless it remains as a minor effect. The transition temperature will also be affected by the moisture content and will decrease with an increase of the moisture content [24]. When the structure is in service for a relatively long time, the absorbed moisture of the polyamide will not remain as initially, i.e. under dry-as-molded conditions. The mechanical characterization of those materials is therefore, normally, performed in “atmosphere 23” conditions in order to reflect the real material behavior in service. This annotation means 23°C and 50% of relative humidity. However, the moisture absorption rate can be very low at 23°C/50% RH and it can take months to reach moisture equilibrium (Figure 42). As an example, it could take more than a year for a 4 mm thick PA66 if those conditioning conditions are considered [25]. Therefore, it is recommended to condition the sample by considered higher temperature and/or relative humidity before storing the sample in “atmosphere 23” condition. A brief comparison of different standard procedures, as well as useful literature references, can be found in [25].

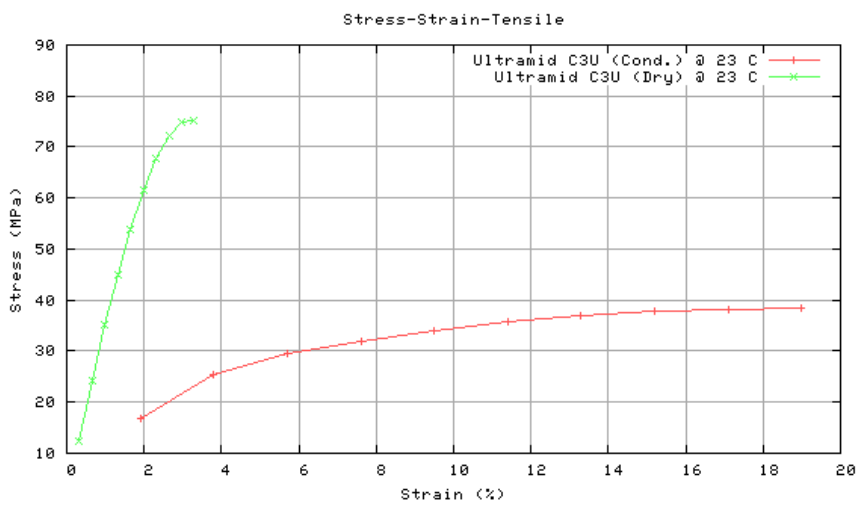

Figure 41 : Stress/strain curve, in tension at 23°C, for a Polyamide 66/6 (Ultramid® C3U from BASF) dry (Green) and after conditionning 50% RH (Red) [http://iwww.plasticsportal.com/]

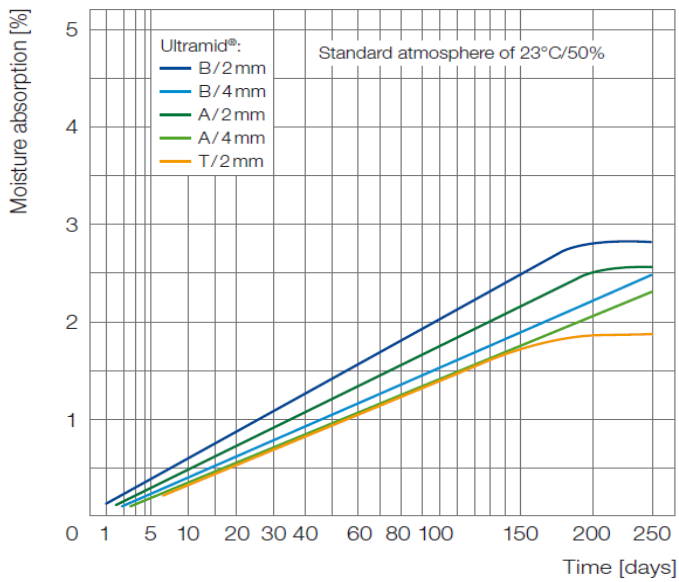

Figure 42 : Moisture absorption function of time for different polyamide and different thickness when conditioning in “atmosphere 23” conditions. The moisture equilibrium for a polyamide 66 (*Ultramid* A) by *BASF* is reached around 2.5% [22]

In the end, the influence of moisture absorption will have a direct effect on the damage mechanisms that can be induced in the reinforced polyamide composite. As an example, the study of Arif et al. [26] on polyamide 66 reinforced with short glass fiber can be mentioned. Their investigation leads to two main results: in one hand, the moisture content will not induce the apparition of pre-damage in the composite. In the other hand damage mechanisms for 0% conditioning conditions and for 50/100% conditioning conditions will be different:

For 0% of relative humidity, the damage mechanisms are:

- Fiber matrix debonding near the end of the fiber
- Brittle matrix cracking and cavitation
- Fiber breakages
- Total failure

For the 50/100 % of relative humidity, the damage mechanisms are :

- Fiber matrix debonding near the end of the fiber

- Local deformation of the matrix near the debonding area
- Ductile matrix cracking (With high matrix deformation bands for the 100%)
- Total failure

Sensitivity to temperature

The polyamide 66/6 is a semi-crystalline polymer, i.e. it has a crystalline and an amorphous phase. The percentage of crystalline phase will differ for each polymer, for example, polyamide 6 and polyamide 66 will have a typical crystalline rate of 35–45% [27]. It can be noted that the mix of polyamide monomers to obtain polyamide copolymers usually leads to a decrease of the crystalline rate. For a semi-crystalline polymer, two important temperatures can be distinguished: the melting point T_m and, in addition to fully amorphous polymer, a vitreous transition temperature T_g. As for moisture, an increase of temperature will lead to an increase of the polymer ductility and a decrease of its strength. In the Figure 43, one can clearly see that when the Young's modulus decrease when increasing the temperature, with an important drop at transition temperature. Those are also caused by an increase of the mobility of chains from the amorphous network. This increase is caused by a breakage of some weak links [28]. In addition to moisture, the temperature will have a plasticizing effect on the crystalline phase. If on the other hand the temperature decreases, the intra-lamellar slip will be reduced and the density of stored energy will increase. This will induce a localization of deformation and a more brittle global behavior [29].

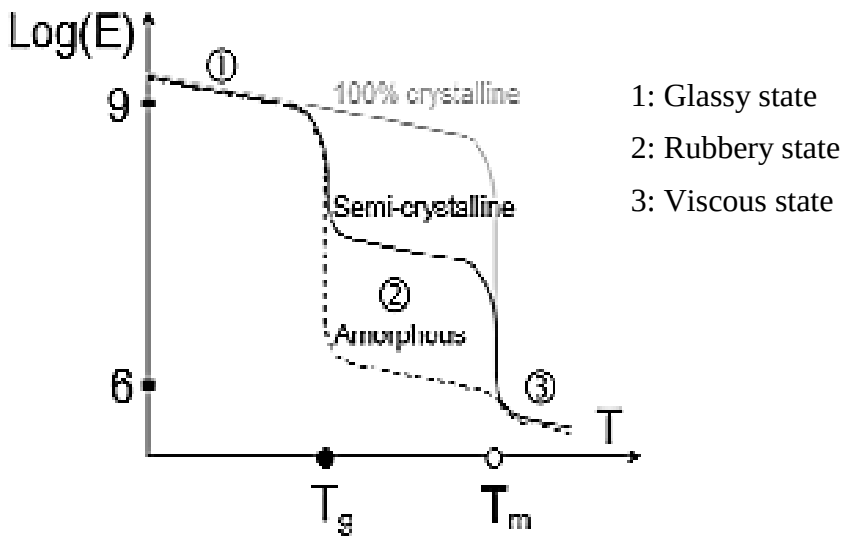

Figure 43 : Young's modulus of classical polymers as function of their temperature and crystallinity [117]

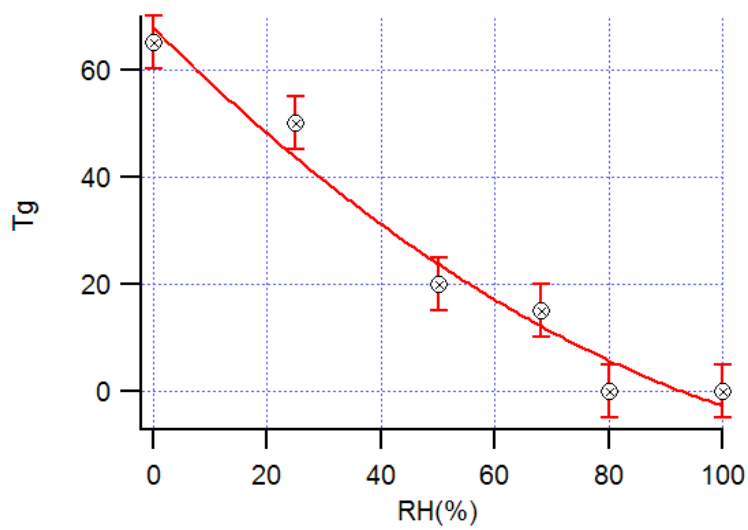

Figure 44 : Evolution of the vitreous transition temperature T_g with the relative humidity (Courtesy of Solvay).

Some studies focused on the specific case of the combined influence of temperature and moisture on the mechanical response. It was observed and discussed in [25], on a polyamide 6, that the combination of both conditions does not necessarily increases the

ductility but only decreases the maximal strength. Indeed, Miri et al. [30] in another investigation of nylon 6 show that the real critical parameter will be the gap of the considered temperature with the vitreous transition temperature of the polymer in its current state. An experimental investigation, done by Launay [24], verified this hypothesis on a short glass fiber reinforced polyamide 66 composite. As the vitreous transition temperature decreases with the relative humidity, its evolution for a polyamide 66 is visible in Figure 44 for completeness purpose.

c) Properties of the composite material

The final automotive part is manufactured by a thermocompression molding process as illustrated in Figure 45. It consists of a balanced 2/2 twill weave glass fabric reinforced co-polyamide 66/6, with three plies, of 1.53 mm thick in total. In this process, the required number of woven fiber plies and polyamide 66/6 films are stack together. This stacking is then pressed and heated into the final shape. This process allows a high-volume production of the parts, which is a critical factor for the automotive industry, much more than in the aeronautical field for example.

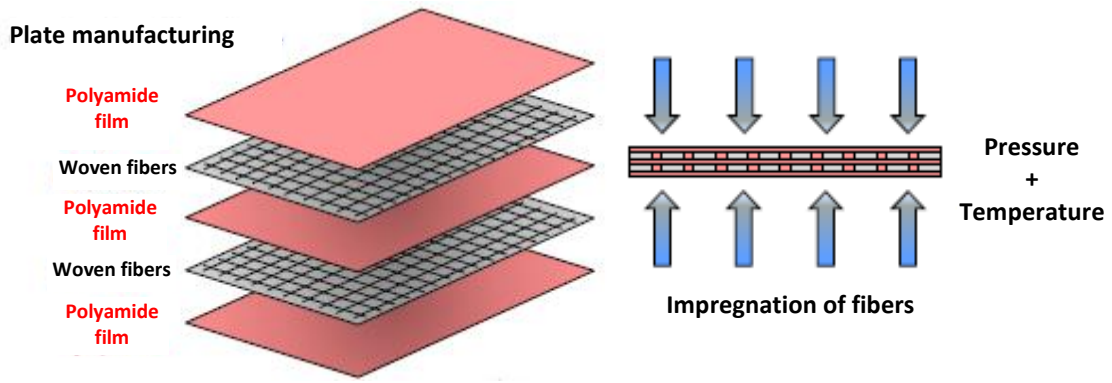

Figure 45 : Compression molding process for a composite of the Vizilon series (Source: DuPont)

An example of RVE of the material is visible in Figure 46-a. This RVE (Representative Volume Elements) is about 16 mm square, this will be important for the choice of the composite samples' dimensions. The overall 3D woven fabric of the studied composite material is shown in Figure 46-b. Those two images were obtained using X-ray tomography acquisitions on PA66/6 reinforced with woven glass fibers. More details about X-ray tomography procedure and acquisitions are proposed in the section IV)-4).

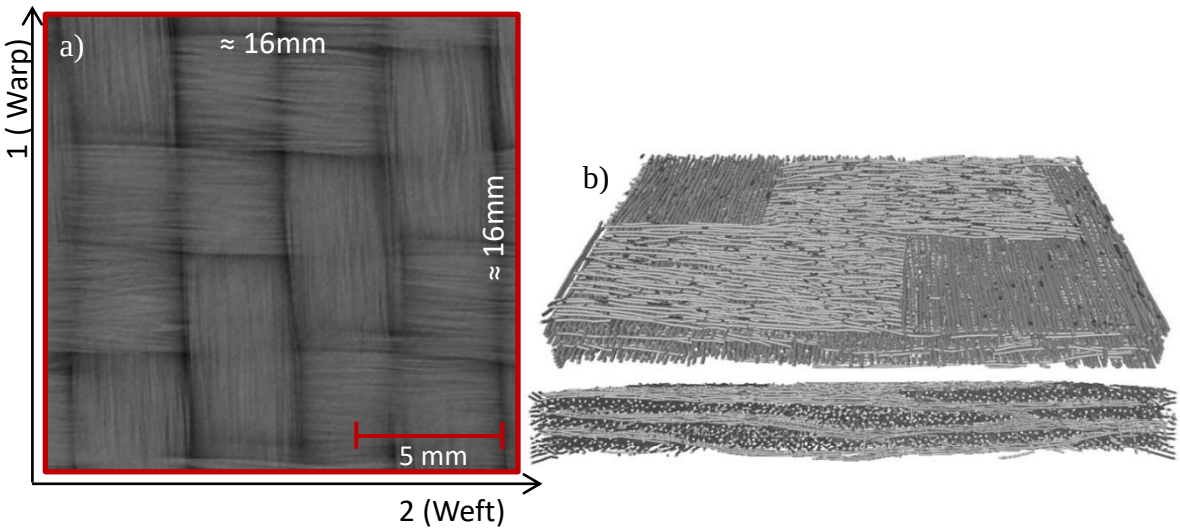

Figure 46 : (a) RVE of the material and (b) 3D representation of the 2/2 twill weave fabric of the Vizilon$_{TM}$ SB63G1-T1.5-S3 obtained by X-ray tomography

As mentioned in the previous part, the woven material has an increased resistance if solicited under impact compared to unidirectional reinforced composites. Indeed, the impact is one of the most critical solicitations that happen on composites because of delaminations that could induce a critical failure of a composite structure. This specific property, among others, made Groupe PSA choose woven material for the next generation cars. In fact, this material is planned to be used as a structural part if the mechanical behavior sustains various criteria. Resistance to impact is one of the most important features that an automotive structure must exhibit. Specific data on this composite are summed-up in Table 5.

This material has a good ductility and a good dissipation before failure. It also exhibits a good compromise between the mechanical properties and the formability, as well as a good ratio between weight and rigidity as summed in Figure 47. It will allow Groupe PSA to design complex automotive parts without reducing strength compared to metallic parts.

Thickness (mm)	≈ 1.53
Void content (%)	< 2
Fiber density (kg/m^3)	1300
Matrix density (kg/m^3)	2500
Composite density (kg/m^3)	1780
Fiber mass fraction (%)	63
Fiber volume fraction (%)	43

Table 5 : Properties of the Vizilon SN63G1-T1.5-S3 (Source: DuPont)

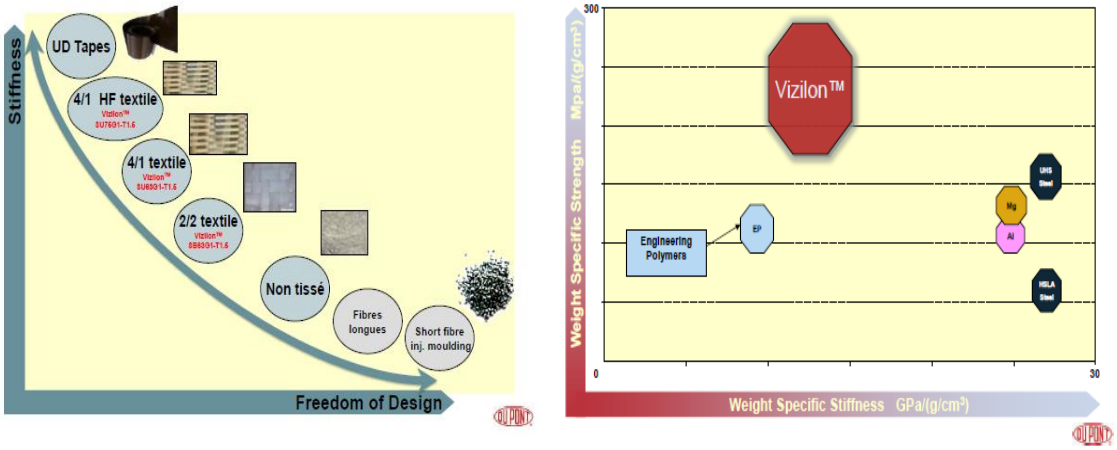

Figure 47: Comparison of the ratio rigidity/formability (Left) and weighted strength/ weighted modulus (right) of the studied composite material with others classically used material: (Source: *DuPont*)

3) Conclusion

For the automotive industry the introduction of a thermoplastic composite reinforced with woven fibers has several advantages. First, the thermoplastic matrix allows both a faster and larger scale manufacturing and easier recycling. In addition, the specific polyamide 66/6 matrix is known to have an important impact resistance and good mechanical properties. Second, the woven reinforcement is known for a larger resistance to impact and delamination. Since the automotive part used to contribute to the vehicle's structural solidity, it must also be able to withstand non-negligible impact solicitations; this choice of constituents is very appealing for structural applications. However, the polyamide matrix used in the Vizilon$_{TM}$ SB63G1-T1.5-S3 is very sensitive to the water uptake. The moisture content will have a direct effect on the development of damage and hence on the mechanical response. In addition, the woven reinforced composite has particular damage schemes, compared to unidirectional reinforced composites, which are influence by the type of solicitation. Therefore, it is important to consider several typical solicitations to characterize the studied composite material behavior and the different associated damage mechanisms. In the end this will permit to test NDE methods on various damage mechanisms. Indeed, since this composite material is planned to be used as a structural part, it may undergo various solicitations during its service life.

II) Description of the studied composite material: Woven glass reinforced polyamide 66/6

III) Characterization of the mechanical behavior of the studied composite material under monotonic and cyclic loading

Contents

1) Description of the experimental procedure 76

2) Monotonic tensile test for the 0° configuration 79

3) Monotonic tensile test for the 45° configuration 82

4) Incremental cyclic tensile test.....88

5) Conclusion 92

Various mechanical tests were performed on the studied composite material to identify its macroscopic mechanical behavior. In the first section, all the information about the tensile tests procedure is described. Then, monotonic tensile tests are performed in order to determine the main mechanical properties, namely: Young modulus, the ultimate strength, the strain to failure etc. Those tests are done on samples oriented at both 0° and 45° from the warp direction. Indeed, as mentioned in the previous chapter, the two orientations are critical cases for tensile test solicitations that, as it is shown, lead to two very different stress/strain responses. Then, incremental cyclic tests are carried out on the two configurations of sample. The evolution of damage, for increasing stress values, is then estimated based on the elastic modulus reduction.

1) Description of the experimental procedure

Because of the influence of the orientation of the woven composite on its mechanical response, two orientations are considered. For the first one, the samples are oriented along the warp direction, for the second, samples are oriented at 45° from the warp directions. It is known that the shape of the tested sample is critical for a correct concentration of stress in the investigated area during tensile test. This area is located in the center of the samples where all the displacement sensors are usually located. Rectangular, tabbed and dogbone samples are the three shapes that are typically used for mechanical investigation of composite materials [26], [31]. Preliminary tests showed that, for monotonic tensile tests on rectangular samples, the final crack always appears in the center of the samples for both configurations. In addition, this shape was found to ensure a homogenous repartition of the strain field in the central zone. Consequently, it was decided to use rectangular samples of 150 mm x 45 mm x 1.5 mm for all the monotonic tensile tests. The width of 45 mm is considered in order to have a sufficient number of representative volume elements (RVE) in this direction. The size of the RVE is a square of about 16 mm as shown in chapter II). This is mandatory in order to have a correct representation of the material behavior during the tests and to avoid unnecessary deformation localization. All the samples were machined using a waterjet cutting machine in order to reduce the apparition of micro-defects near the samples' edges. A representation of the two configurations is shown in Figure 48.

Because of the influence of the relative humidity on the PA66/6 matrix, all the samples were preliminary stored in a humidity oven at 50% of relative humidity until the moisture equilibrium was reached. A humidity conditioning chamber Memmert HCP256 was used for the conditioning. Samples were stored at 50% of relative humidity and 70°C. Those parameters were used by Solvay and DuPont, among others, and based on the NF EN ISO 1110 standard. As discussed in the first part, the 70°C temperature allowed a faster conditioning of the PA66/6 matrix. This value of relative humidity is also recommended by standards (e.g. ISO-527) and is typically used, when a material is known for being sensitive

to relative humidity, except when specific recommendations is required, as was discussed in a previous chapter. The weights of the samples were measured before the conditioning and every two days after storing the samples in the humidity chamber. The moisture equilibrium is considered as reached when the measured weight hardly changes (less than 5%) for three consecutive measurements.

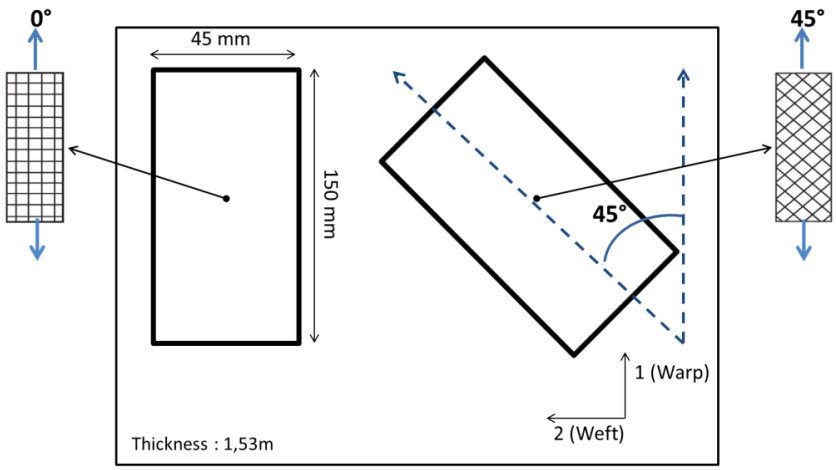

Figure 48 : Position of the samples oriented at 0° and 45° from warp direction (mold flow direction) on the composite plate. The direction “1” is the loading direction in tension.

All the monotonic tensile tests and incremental cyclic tensile tests, described in this section, were done at ambient temperature, with a tensile test machine “Z050” manufactured by Zwick Roell Gruppe compliant with the norm ISO 5893. Except when mentioned, the tensile tests were performed at a constant strain rate of 10^{-4} s^{-1}. An initial gauge length of 65 mm was considered for all tensile tests.

In order to validate the tensile test procedure, various displacement sensors were used for the first tests:

- A Linear Variable Displacement Transformer (LVDT),
- A video camera for Digital Image Correlation (DIC) technique,

- A clip-on extensometer from *Epsilon Technology corp* (Model: 3542-025M-010-ST),
- The measure of the crosshead displacement,

All those displacement sensors can be identified in the experimental set-up depicted in Figure 49. A black and white speckle pattern was applied on the sample surfaces for the DIC acquisitions. A lighting system is also used to enhance the contrast on this surface. An image every 4 secondes was recorded for the 0° configuration. Because the test duration in the 45° configuration is about three times higher, in this case only an image every six secondes was recorded. The obtained images were processed using the Vic2D software in order to obtain an evolution of the strain fields during the loadings as well as the global strain in the loading direction (“1”).

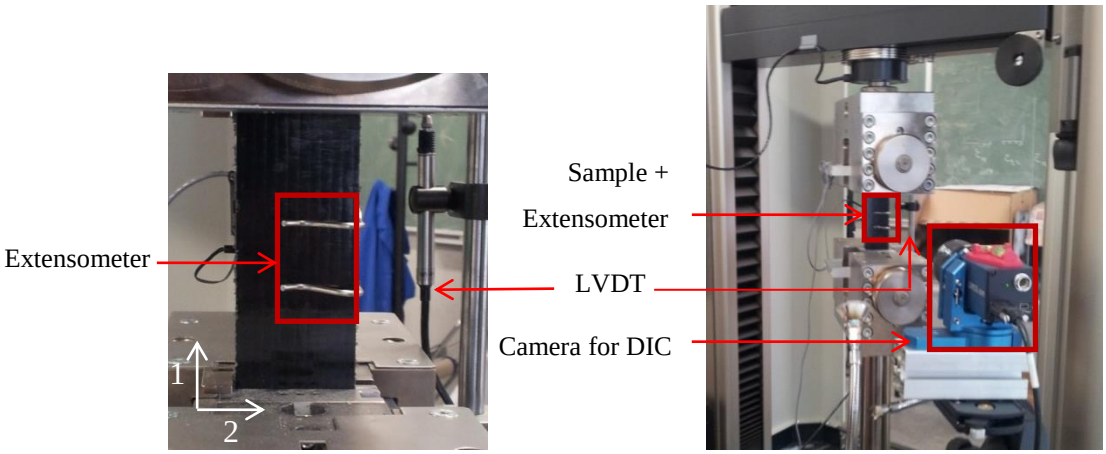

Figure 49 : Experimental set-up of the tensile test with all the displacement measurement sensors

For each orientation, the test is performed three times to assess the repeatability of the tests and the manufacturing process. Thanks to the high repeatability of the observed results compared to other composite materials, it was not necessary to perform five tests as is usually required by common standards. The Young’s modulus is calculated using the

standard ISO-527-1, which recommends calculation of the elastic modulus by linear regression between ε_1 = 0.05% and ε_2 = 0.25%.

2) Monotonic tensile test for the 0° configuration

The stress/train curves for the different displacement sensors are plotted in Figure 50. For the samples oriented at 0° from fiber's axis, one can clearly see a correlation between the extensometer measurement and the DIC method and between the crosshead displacement and the LVDT separately, what is quite expected. Indeed the LVDT is fixed to the jaws and follow their displacement and the extensometer is fixed close to the mapping area that was used for the DIC method.

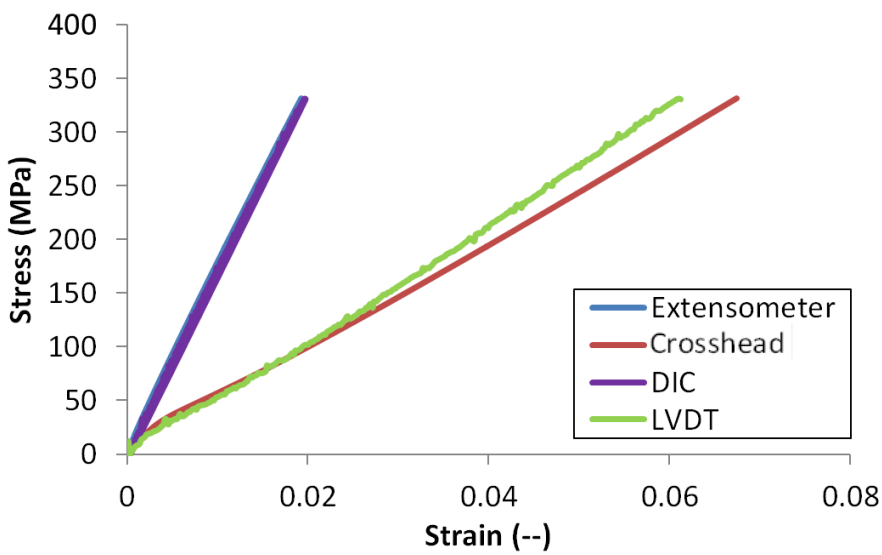

Figure 50 : Stress/Strain curves for one of the samples with fibers oriented at 0° with the four displacement sensors considered

It was chosen to consider as relevant, information that is measured by the extensometer and the DIC, because the other two sensors appear to include, in the obtained results, the response of the jaws. The extensometer and the DIC only measure the response of the material. As mentioned in the procedure's section, only three samples were tested because

of good repeatability of the tests. This result can be observed in Figure 52, for those two mentioned displacement sensor. One can clearly see the repeatability of the present monotonic tensile tests.

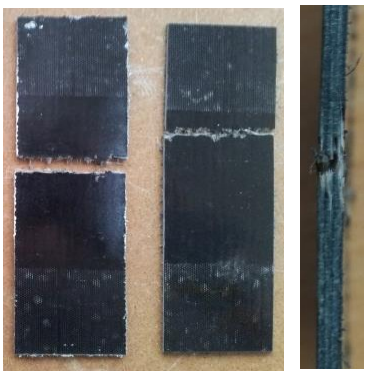

Figure 51 : 0° oriented samples after tensile test until failure

The woven composite material exhibits an almost linear and quasi-brittle behavior during tensile tests along the fiber's axis. However, one can notice a loss of linearity around 120 MPa in Figure 53. As explained by Osada et al. [32], among others, this knee/yield point corresponds generally to the initiation of damage in the woven composite sample. When the failure area is observed in Figure 51, it can be noticed that the crack is running perpendicular to the loading direction, which is due to the fiber's orientation. The crack is very clean and remains located in the failure area. No particular delamination is observed on the edges of the sample.

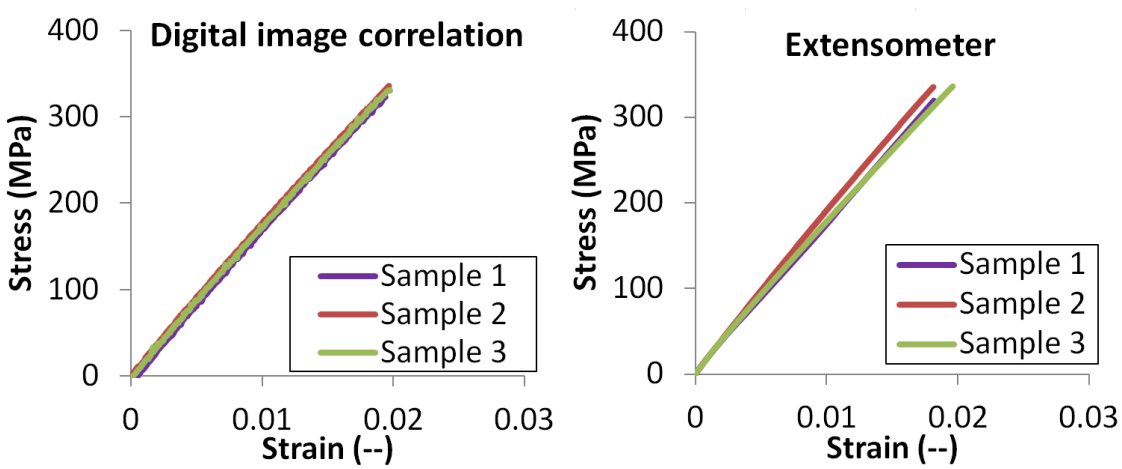

Figure 52 : Stress/Strain curve obtained with DIC (Left) and Extensometer (Right) for the three tested samples oriented at 0° from fiber's axis

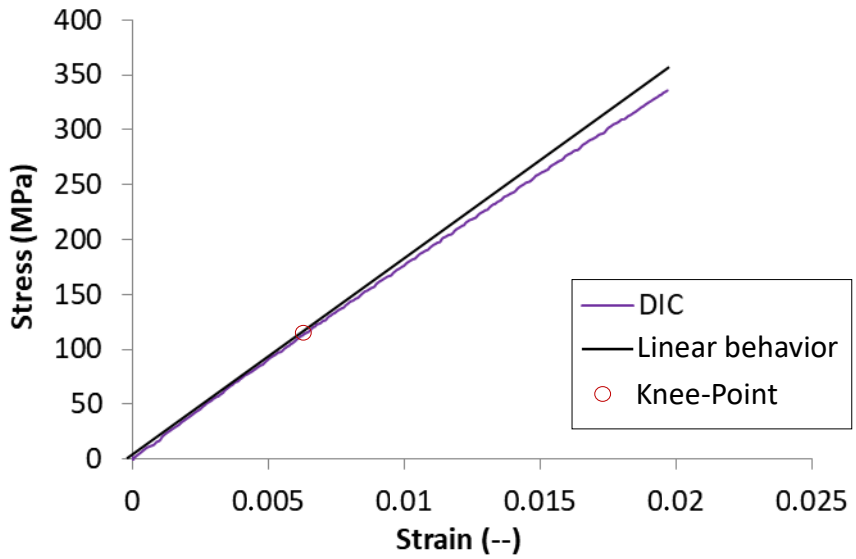

Figure 53 : Nonlinearity point on the stress-strain curve from DIC acquisitions

The most important extracted results are summed-up in the Table 6 below. For each indicated sensor, the mean Young Modulus and the mean strain to failure over the three performed tensile tests is determined. The standard deviation is also computed for these two values. A value of about 18 GPa for the Young modulus can be determined from our tests. And a value of about 0.019 was found for ε_f,. The standard deviations are reasonable for each sensor, so the extensometer and the DIC method can be considered for our next tests. The mean strength to failure over these three tests is around 331 MPa.

On the strain fields obtained with Digital Image Correlation, only the $\boldsymbol{\varepsilon_{11}}$ component is of importance to analyze the macroscopic behavior of the composite. Indeed, one can notice a difference factor of 10 between the $\boldsymbol{\varepsilon_{11}}$ components and the $\boldsymbol{\varepsilon_{22}}$ and $\boldsymbol{\varepsilon_{12}}$ that can be determined with this technique. In Figure 54, the $\boldsymbol{\varepsilon_{11}}$ strain is represented just prior to failure as well as a picture of the sample just after failure. A relative homogenous strain field is observed, on the left picture, with the exception of two strain concentration areas. This is of course expected as the main crack is appearing on the area with the highest strain concentration on the right picture.

	Extensometer	Crosshead	DIC	LVDT
Young modulus (average)	18.8 GPa	8.6 GPa	18.3 GPa	9.7 GPa
Standard deviation	0.4546	0.2170	0.2160	0.0471
Strain to failure ε_f (average)	0.0190	0.0659	0.0191	0.0596
Standard deviation	0.0009	0.0031	0.00045	0.0013

Table 6 : Summary of the results for tensile tests on samples oriented along the fiber's axis

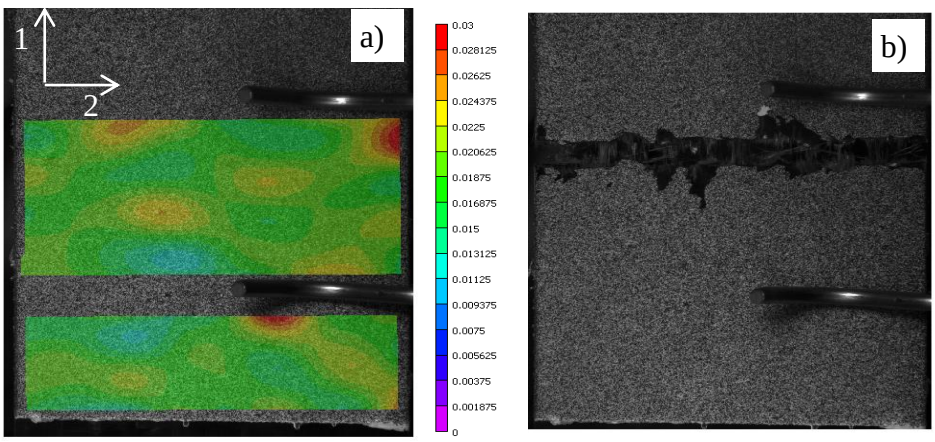

Figure 54 : a): $\boldsymbol{\varepsilon_{11}}$ strain field during tensile tests right before failure. b) : sample right after failure

3) Monotonic tensile test for the 45° configuration

Stress/strain curves obtained for all the four displacement sensors are visible in Figure 56. For off-axis tensile tests, the woven material exhibits a much more non-linear and more ductile behavior than the sample oriented at 0° from the fiber's axis. Here, six samples were used, but the extensometer and the LVDT cannot be used beyond a certain value of displacement to prevent damage. So three samples were submitted to tension until breakage

but only the measurement of the crosshead and resulting from the DIC can be obtained. The resulting stress/strain curves are plotted in Figure 57-a. The other three samples did not exceed 10% of strain; therefore in this case all sensors were used. The stress/strain curves obtained from the extensometer are plotted in Figure 57-b. For the 45° configuration, the same observation can be made from the correlation between the different displacement sensors.

Figure 55 : 45° oriented sample after tensile test until failure

When the failure area visible in Figure 55 is observed, it can be noted that the crack is running at 45° of the loading direction, which is induced by the fabric orientation. The main crack is propagating in stairs shape; lots of delamination can be observed on the side of the sample relatively close to the failure zone.

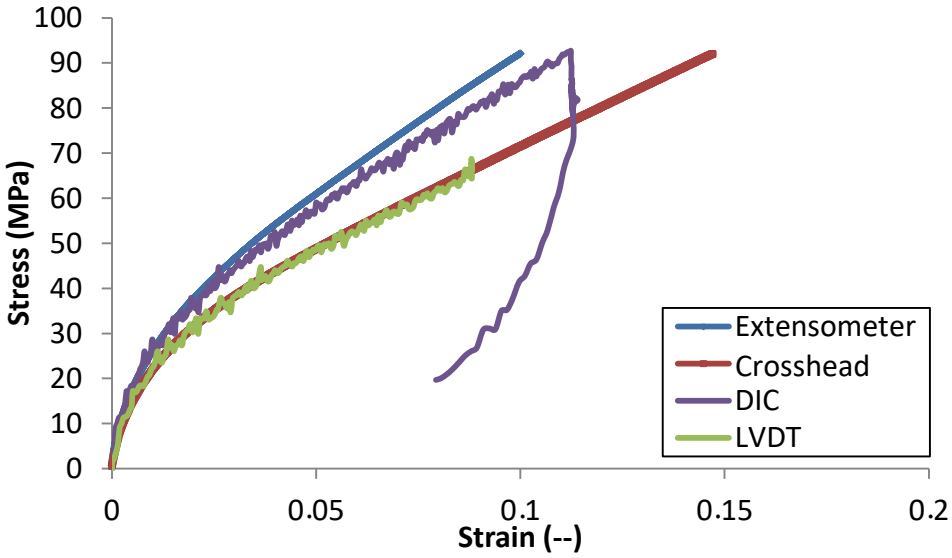

Figure 56 : Stress/Strain curves for the 45° orientation for the entire displacement sensor considered (Here the sample was not solicited until

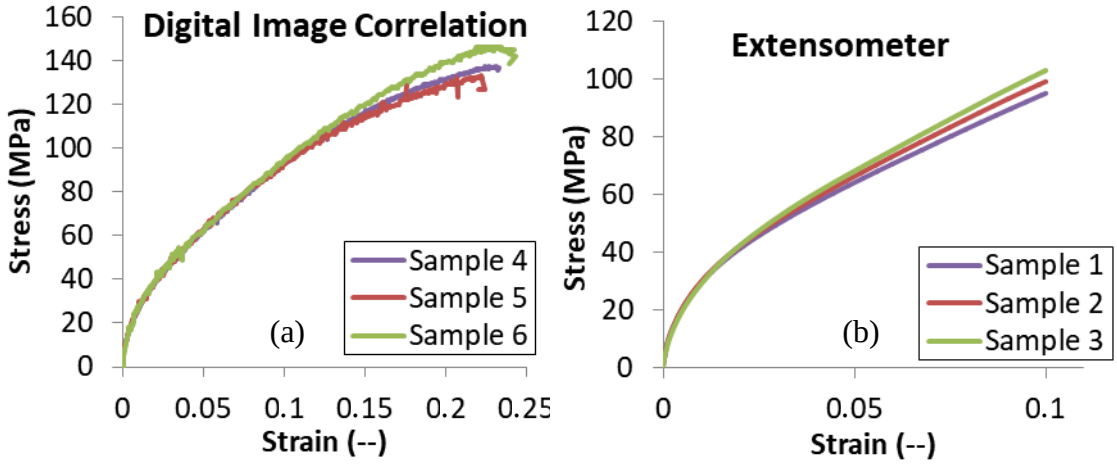

Figure 57 : Stress/Strain curve obtained with DIC (a) and Extensometer (b) for the three tested samples oriented at 45° from fiber's axis

As in the previous subsection, the most important results are summed up in the Table 7. The Young modulus is about 3.5 GPa and the strain to failure ε_f is about 0.23. The deviation for this test is higher when considering the value of Young's modulus. The mean strength to failure is about 134 MPa.

	Extensometer	**Crosshead**	**DIC**	**LVDT**
Young modulus (average)	3.7 GPa	3.5 GPa	3.4 GPa	3.3 GPa
Standard deviation	0.3514	0.2625	0.3300	0.6481
Strain to failure ε_f (average)	--	0.225	0.234	--
Standard deviation	--	0.0052	0.0076	--

Table 7 : Summary of the results for tensile test on samples oriented at 45° from fiber's axis

As for the tests in the 0° configuration, an imaging of the ε_{11}, ε_{22} and ε_{12} strain fields were made. ε_{22} strain field can be observed at the beginning of the tensile tests, at the middle and near the end of the tests close to the final failure on the Figure 58.

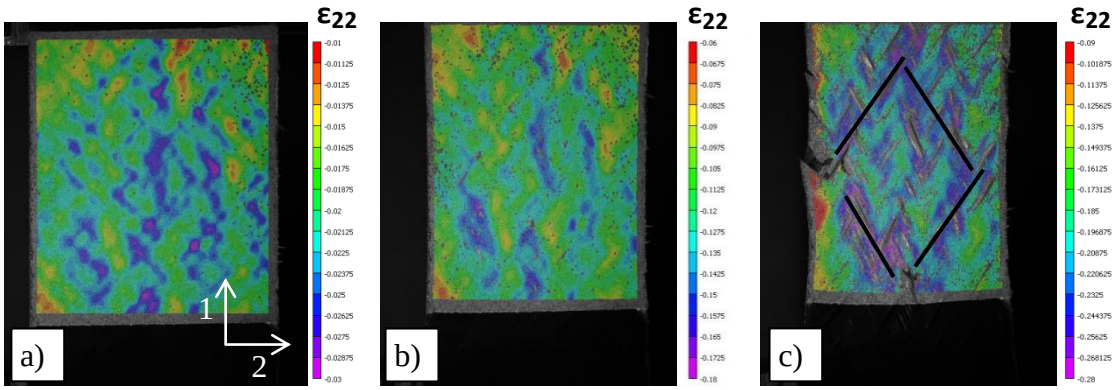

Figure 58 : ε_{22} strain field at the (a) beginning (b) middle (c) end of the test for a sample in the 45° configuration during a tensile test

Three steps leading to failure clearly appear on the DIC results. First, a concentration of strain undoubtedly influenced by the shape of the woven fabric architecture is visible almost everywhere in the investigated surface area. The rotation of the fibers and the resulting necking are noticeable from that point onwards. The strain concentration consequently starts to form the well-known diamond pattern. Those areas are, for this reason, characterized by a displacement along the loading direction, a contraction in the transverse direction and an increasing shearing angle. Those are visible in Figure 60 that depicts the evolution of ε_{11} and ε_{12} strain fields for a high level of tensile stress. Note that, here, the three strain fields have the same order of magnitude. Beyond this point some anomalies (holes or gaps) appear in the correlation results induced by out of plane deformation as seen in the left picture of the Figure 60. They are caused by multiple wrinkling, visible in Figure 59, which occurs when the maximal shear angle (or locking angle) is reached. The appearance of the wringing on woven fabric reinforced composites has been investigated, in particular during the shaping process, as can be found for instance

in [33]. The strain scheme, which is more complex than in the 0° configuration, explains why the tensile test in 45° configuration (or bias-extension test) is still extensively investigated. In addition, this is one of the easiest experiments that can provide information on in-plane shear properties of a given woven reinforced composite. A recent review of the bias-extension test as well as some known experimental and numerical issues that may be undergone with the test, and may lead to unprecise results, can be found in [4].

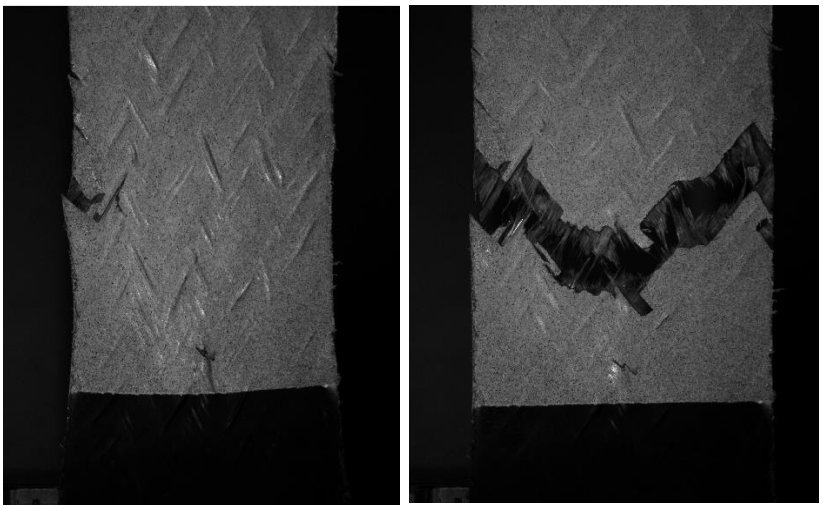

Figure 59 : Tested sample in the 45° configuration just before failure (Left) and after failure (Right) from a tensile test

As a reminder, Figure 61 depicts the stress/strain curve for the two chosen configurations (0° and 45°). The selected configurations made the difference in mechanical behavior very obvious, which is why they have been chosen for the present study. Indeed, they lead to very distinct microstructural behavior, i.e. brittle for the 0° and mostly ductile for the 45°. In addition, the 45° case induces high shearing effect during the tensile loading.

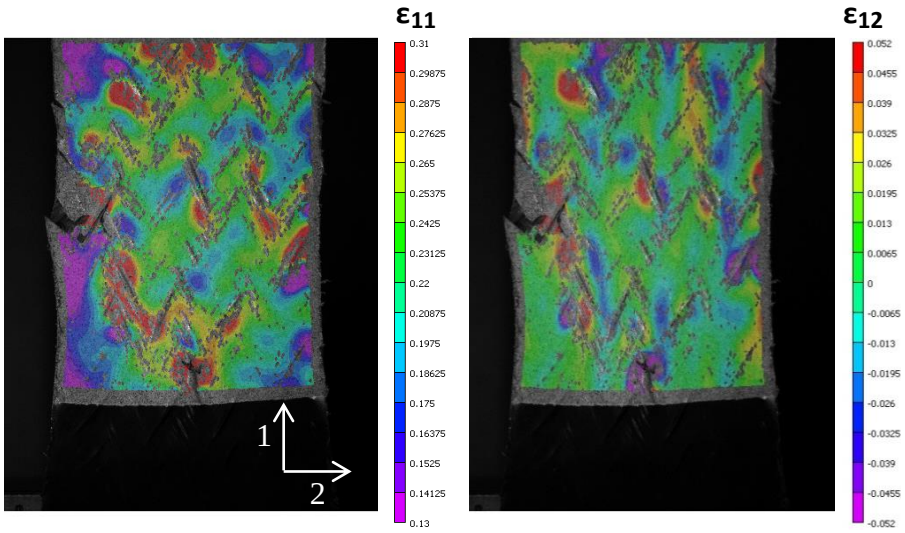

Figure 60 : ε_{11} (Left) and ε_{12} (Right) strain field for the 45° configuration during a tensile test

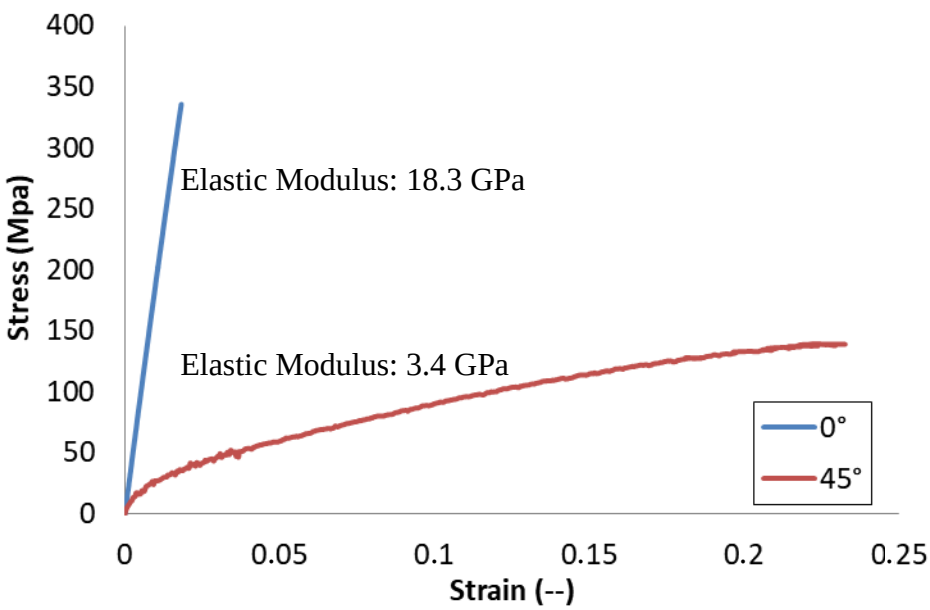

Figure 61 : Comparison between the behavior in the 0° configuration and the 45° configuration. Displacement measured with Digital Image Correlation

4) Incremental cyclic tensile test

The incremental cyclic tensile test will now be described. The tests were, as previously, performed on both orientations (0° and 45°), with a loading increment of 20 MPa until failure. In order to perform the cyclic tensile tests until breakage, even for the samples in the 45° configuration, the digital image correlation (DIC) technique was used in the experiments described in the present section. Recall that, contrary to the DIC technique, the extensometer, which is an alternative displacement sensor used in the previous section, cannot exceed 10% of deformation. This is lower than the maximal deformation of the composite in the 45° configuration and is therefore a limitation. The obtained stress/strain curves for the 0° and 45° configurations can be seen in Figure 62 and Figure 63 respectively. Mechanical responses for monotonic solicitations were also added for the purpose of comparison.

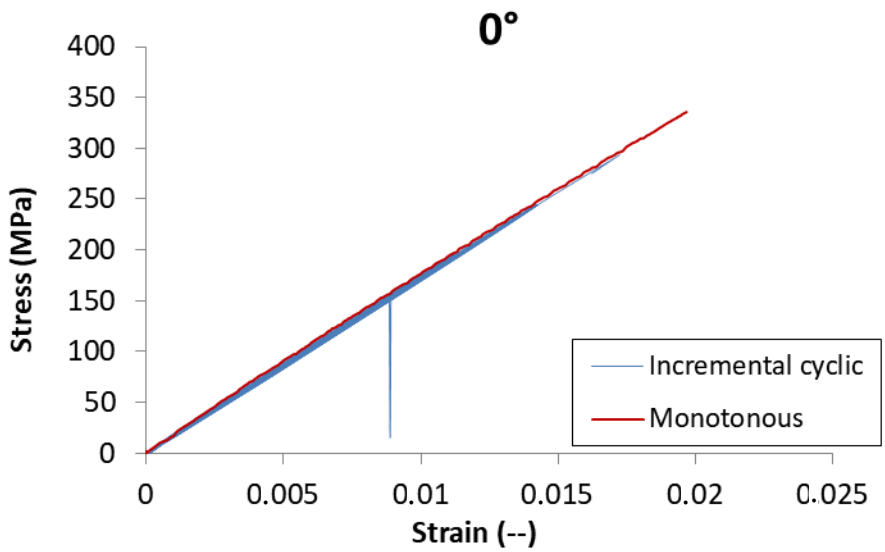

Figure 62 : Monotonic tensile test and incremental (20 MPa) cyclic test for the 0° configuration

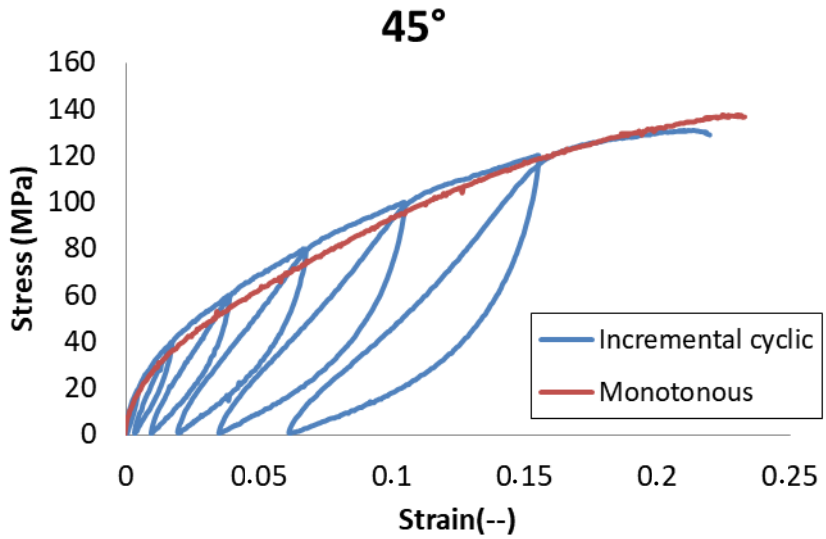

Figure 63: Monotonic tensile test and incremental (20 MPa) cyclic test for the 45° configuration

As a first result, one can verify that the 0° oriented samples behave quasi linearly during the cyclic tensile tests as was observed by Pandita [21], among others. On the other hand, the 45° oriented samples clearly exhibit a visco-elastic damage behavior. An increase of the hysteresis is noted in each cycle. It can be observed that the exhibited behavior is very similar to the monotonic response discussed in the previous subsections. Indeed, for both configurations the two curves are very close, which indicate, for instance, an evolution of the damage state remaining primarily unchanged for this type of solicitations. The evolution of damage was then computed for both orientations as: $D = 1 - \frac{E_n}{E_0}$; Where E_n is the Young's modulus, during the unloading at the cycle under consideration and E_0 is the Young's modulus during the first cycle. The E_0 values are calculated for every sample between 0.2% and 0.4% of strain according to the standard ISO 527. The E_n are calculated after the unloading following the Ladeveze damage measurement procedure [5]. A representation of this procedure can be found in Figure 64. The obtained results for the 0° and the 45° configurations are summed up in the Table 8 and Table 9 respectively. Finally Figure 65 reveals the evolution of damage for the two configurations.

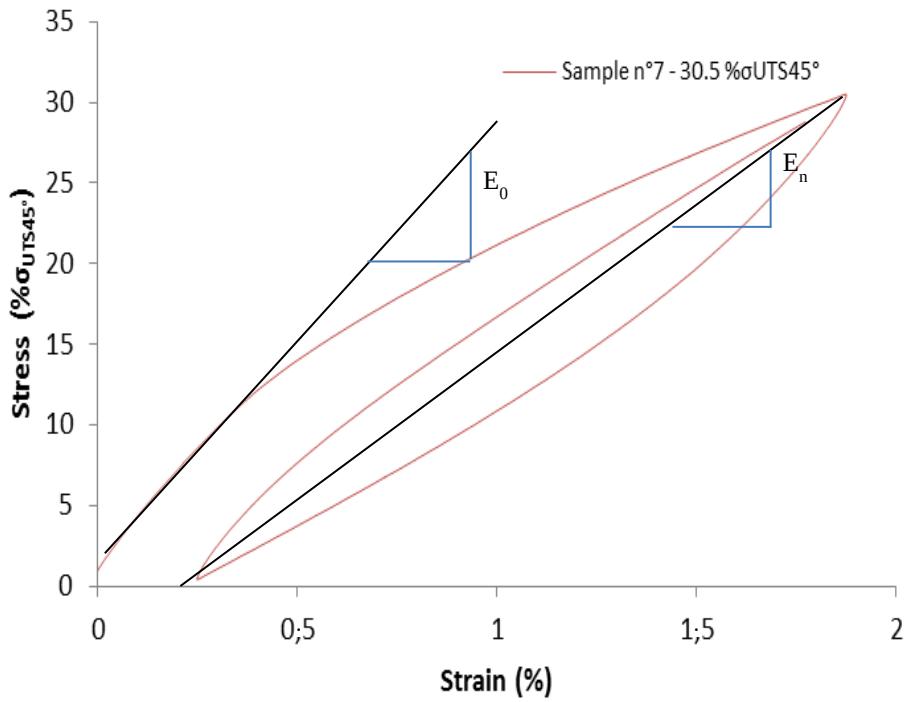

Figure 64 : Measurement of the E_0 and E_n moduli on a loading unloading curve

Maximal stress (MPa)	**0**	**40**	**60**	**80**	**100**	**120**
Modulus (GPa)	3.2	2.84	2.36	2.08	1.6	1.50
Damage (-)	0	0.11	0.26	0.35	0.5	0.53

Table 8 : Elastic modulus and associated damage for each cycle for the sample oriented at 45° from fiber's axis

Maximal stress (MPa)	**0**	**40**	**60**	**80**	**100**	**120**	**140**	**160**	**180**	**200**	**220**	**240**	**260**	**280**
Modulus (GPa)	20.98	20.39	20.26	20.20	20.00	19.80	19.64	19.47	19.42	19.29	19.17	19.18	19.19	19.13
Damage (-)	0	0.028	0.034	0.037	0.046	0.056	0.064	0.071	0.074	0.080	0.086	0.085	0.087	0.088

Table 9 : Elastic modulus and associated damage for each cycle for samples oriented at along the fiber's axis

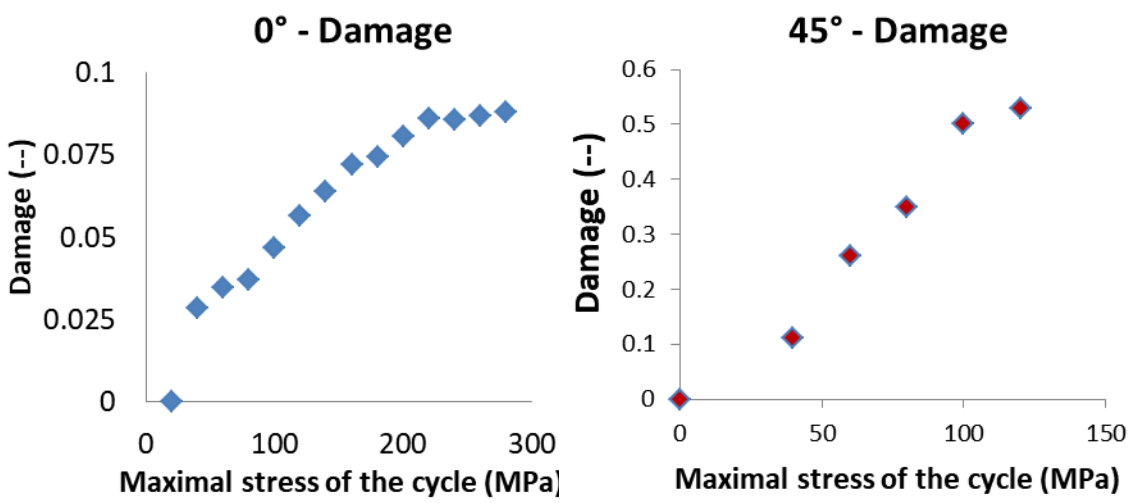

Figure 65 : Evolution of damage function of the maximal stress of the cycle for a 0° (Left) and 45° (Right) oriented sample

The cyclic tensile behavior of the studied PA66/6 reinforced with woven glass fibers is anisotropic. For the samples in the 45° configuration, damage almost reaches a value of 0.53 close to the final failure. However, for the 0° case, it only goes up to 0.1 when close to the final failure.

The Figure 66 depicts a comparison of the damage evolution for the two configurations. This observed anisotropic increase of damage is easily explained by the change in the material response when its orientation varies. Indeed, samples are submitted to tension along the warp direction, the behavior is ruled by the fibers. The behavior is then mostly brittle. However, for samples oriented at 45° from the warp direction, the behavior is ruled by the matrix and is mostly ductile. So this may lead to more matrix micro-cracks development. This will be discussed in the following chapter in which the composite's microstructure will be studied.

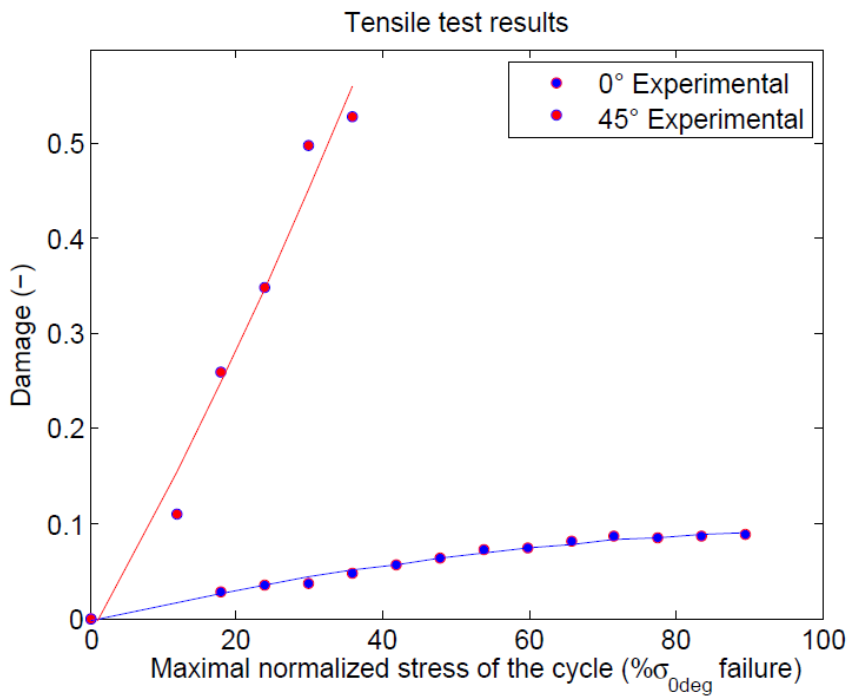

Figure 66 : Comparison of the Young modulus reduction during incremental cyclic test for 0° and 45° oriented samples

5) Conclusion

The mechanical behavior in tension of the PA66/6 reinforced with woven glass fiber was investigated in this chapter. Because of their difference in terms of mechanical

response two configurations were studied. The first one with the warp yarns oriented along the loading direction and the second with those yarns oriented at 45° from the loading direction. The behavior in the first configuration is more linear and brittle whereas it appears more nonlinear and ductile for the 45° configurations. Digital Image Correlation (DIC) results indicate, for the latter, the presence of shear strain in the woven fabric during the loading, as well as fiber re-orientation along the direction of the loading. For the 0° configurations the strain field evolution is mostly governed by elongation along the loading direction (E_{yy}). The damage growth was then estimated by elastic modulus reduction during incremental tensile tests. The results indicate a higher increase of damage for the 45° configurations. Clearly, different samples need investigation at a microscale in order to identify the related damage mechanisms for each considered samples configurations.

IV) Damage mechanisms investigation: quantitative and qualitative analysis

Contents

1) Optical microscopy analysis of undamaged composite.....97

2) Damage initiation.....99

3) Fractography analysis.....102

4) X-ray tomography analysis.....104

a) 0° oriented - Undamaged sample 108

b) 0° oriented - Damaged sample 111

c) 45° oriented – Damaged sample.....113

d) Void volume fraction evolution.....116

5) Conclusion.....117

In the previous chapter, the polyamide 66/6 reinforced by woven glass fibers was investigated at the macroscale; its microstructure is now studied in this chapter. Optical microscopy, Scanning Electron Microscopy (SEM) and X-ray tomography, are used to analyze the composite material at the microscale. An optical microscope is first used to roughly analyze the microstructure of the undamaged composite samples oriented at 0° (warp) and 45° from the warp direction. The presence of initial damage is also investigated. The initiation of damage is then identified with SEM in-situ tensile tests in the 0° configurations exclusively. The different rupture patterns that may appear on the two considered orientations after the failure of the composite are then observed with a SEM.

The last and main subsection of this chapter is dedicated to X-ray tomography analysis. Undamaged samples are first investigated for the purpose of a reference state, and then

composite samples, preliminary loaded in tension at stepwise increasing loading values are analyzed. This allows us to identify the different damage mechanisms and their associated scales. A measurement of the evolution of the void volume fraction is also performed by using a grey level threshold. Both along axis (0°) and off axis (45°) oriented composites specimens are tested as in the previous chapter.

1) Optical microscopy analysis of undamaged composite

The microstructure of the studied composite is observed and analyzed using an optical microscope. Samples with fibers oriented at 0° and 45° were considered, as in the previous chapter, in order to analyze the effect of the reinforcement orientation on the mechanical behavior at the microscopic scale. The edges of both samples were observed and the difference in the microstructure was noted. Rough samples were first cut with a water cooled saw at small velocity to have a clean cut. This cut surface is subsequently polished using an automatic polishing machine *Presi Mecatech* using the following procedure:

Polishing disk	**Time**	**Rotating velocity Tray**	**Rotating velocity Head**
SiC Disk 1200	Until the remaining resins is gone	+250 rpm	- 100 rpm
Ram Disk 9um	10	+200 rpm	- 100 rpm
Ram Disk 6um	10	+200 rpm	- 100 rpm
Ram Disk 3um	20	+200 rpm	- 100 rpm
Ram Disk 1um	20	+200 rpm	- 100 rpm

Table 10 : Polishing procedure

The typical microstructure of the woven composite can be observed for sample in the 0° configuration in Figure 67-a. One can see the longitudinal yarns along the direction of tension and the transversal yarns perpendicular to the direction of tension. Areas rich in resin are observed near the end of some transversal yarns. It will be observed later that the majority of the damage will be located in those areas after mechanical loading.

An average fiber diameter of 17 µm was measured using the optical microscope acquisitions, as visible in Figure 67-c. An average transversal yarn shape factor of 0.065 was found, with a major axis of 3.70 mm and a minor axis of 0.24 mm.

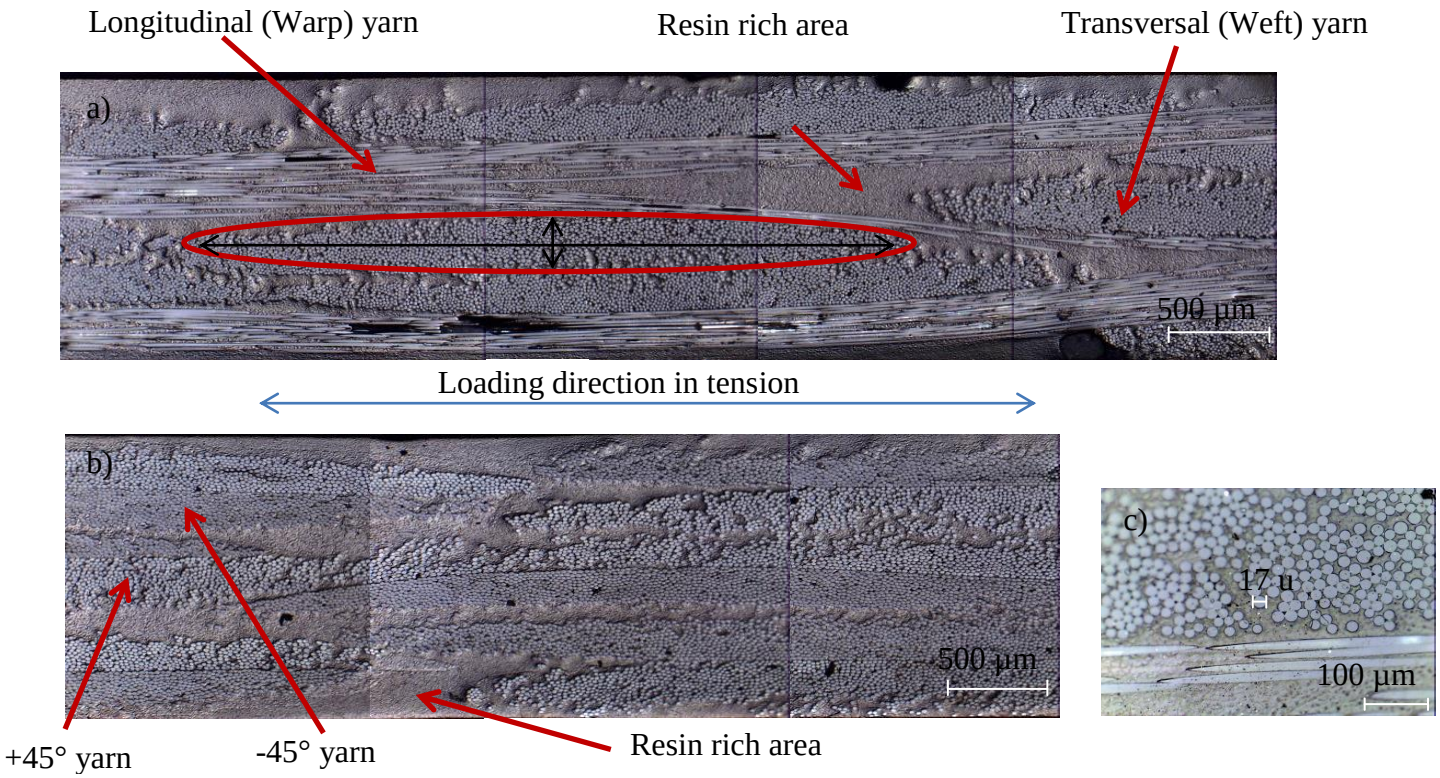

Figure 67: Microstructure observation via optical microscope of the polyamide 66/6 reinforced with woven glass fibers. (a) and (b) depict respectively 0° and 45° configurations. (c) is a magnification on a sample in the 0° configuration

For the samples in the 45° configurations, two classes of yarns are appearing, the +45° yarns and the –45° yarns as visible in Figure 67-b. This corresponds of course respectively to the transversal and longitudinal yarns of a 0° oriented sample. The same areas rich in resin are observed at the end of yarns.

On both observed samples initial damage may be observed. They are essentially located in the transversal yarns in the 0° oriented sample. Fibers/matrix debonding and macro

porosities are the most apparent defects (Figure 68-b and c). Some cracks are also noticed but are very rare in the initial state (Figure 68-a). Some initial defects can be observed in the longitudinal yarns but they may be difficult to quantify because of fibers removal during the samples polishing. Indeed, because of their low diameter, the longitudinal fibers can be easily damaged and even debonded from the matrix during this process. In the 45° oriented sample, the initial damage is essentially located inside the yarns. The rich resin area seems to remain undamaged.

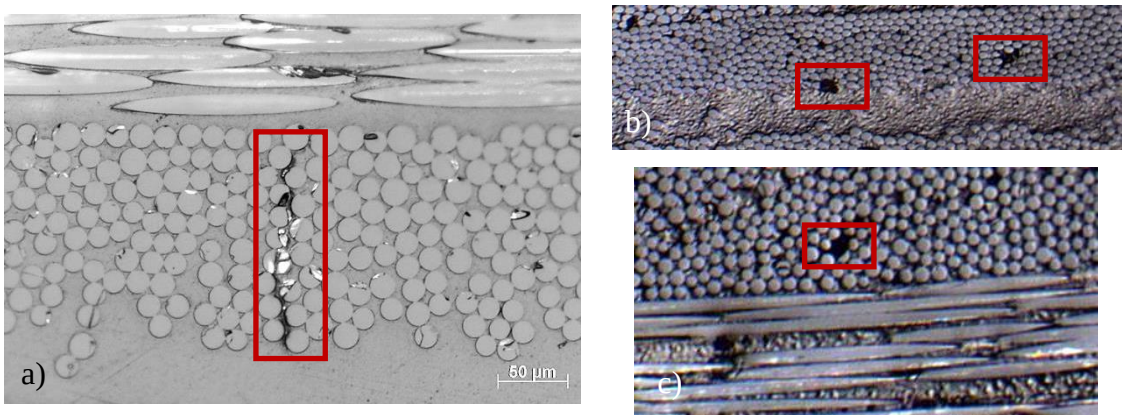

Figure 68 : a) Crack visible in transversal yarns, b) Micro porosities in the 45° configurations c) Micro porosities in the 0° configurations.
All pictures were taken in the initial state prior to any mechanical loading

More information on the initial amount of damage inside the composite is given in the subsection dedicated to X-ray tomography.

2) Damage initiation

The damage initiation and the first appearing damage mechanisms is investigated in this subsection. Scanning Electronic Microscopy (SEM) in-situ tensile tests along the fiber axis were considered. The samples were first cut in 50 mm x 5 mm x 1.53 mm rectangular shape. This geometry is adopted because of the tensile tests machine limitations. However, because of the chosen sample's dimension, the mentioned results should be considered with caution. Indeed, in order to have a homogenized stress concentration, the sample should

contain more than one RVE of the microstructure. The RVE adopted here is a square of 16 mm x 16 mm, but the tested sample is only 5mm width. The samples were then polished using the procedure described in the previous subsection. A coating of gold/palladium is then applied on the samples, in order to increase the imaging quality because of their limited conductivity. Pictures are then taken for different loading values: 120 N, 240 N and 435 N. The microscopic observations are given in Figure 69. Some damage is visible in Figure 69-a before the loading test and is caused mostly by the cutting process and polishing. Knowledge of the reference state is therefore essential in order to avoid wrong assumptions concerning the location and the stress level corresponding to damage initiation. During this experiment, the first apparition of damage was noted starting between 66 N and 120 N, it consists mostly of fiber/matrix debonding in the transversal yarns (Figure 70). The debonding in the samples becomes gradually more important and some cracks begin to appear due to damage propagating along the debonding area (Figure 69-d) between 120 N and 240 N. The loading test continues until 435 N with the accumulation of debonding and cracks in transversal yarns. Nevertheless, the process cannot continue further an applied load beyond 435 N because of breakage of the sample inside the jaws. Because the other appearing damage mechanisms can be more easily observed than fiber/matrix deboning when using X-ray tomography the rest of the damage mechanisms characterization will be performed with this X-ray technique. Though, an observation, using SEM, of fracture surfaces is still proposed in the following subsection.

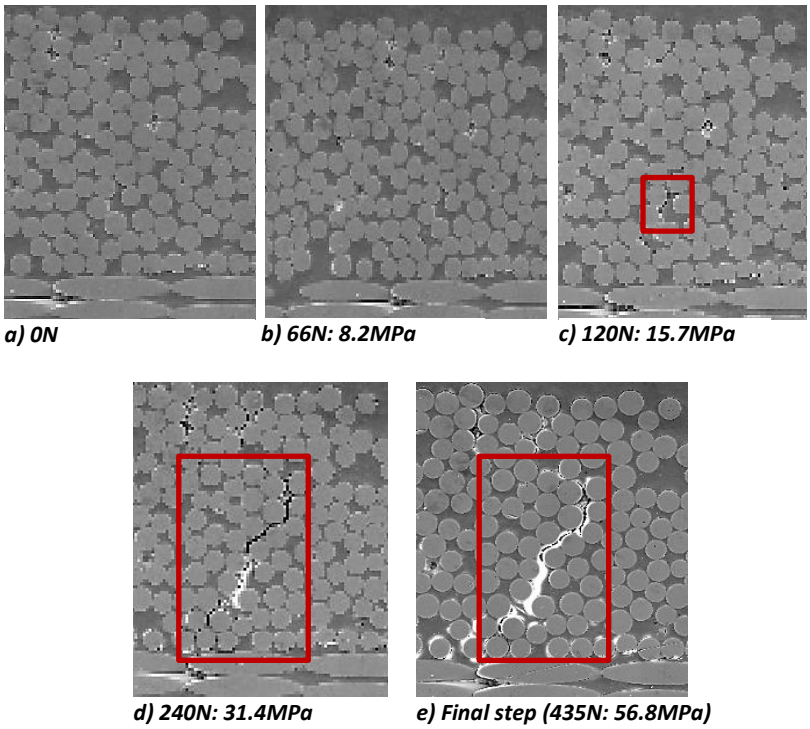

Figure 69 : Transversal yarns during SEM in-situ tensile test for different applied force

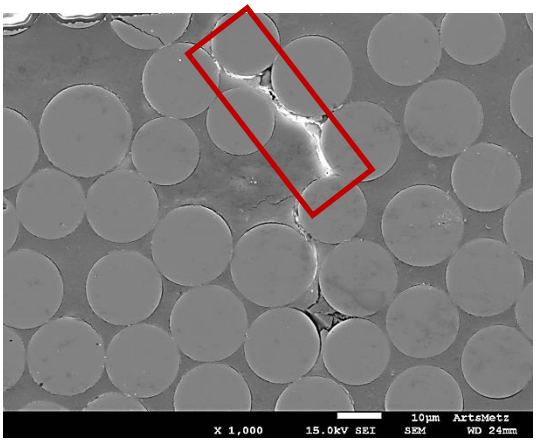

Figure 70 : Fiber/matrix deboning obtained with SEM

3) Fractography analysis

In order to identify the different rupture mechanisms, it has been decided to use fractography of the samples subjected to tensile test until breakage. Composites with fibers at 0° and composites with fibers at 45° with respect to the direction of tension load are examined. The technique can provide a first clear idea about the different mechanisms that lead to failure.

- 0° orientation:

In Figure 71 are represented the different observed rupture mechanism for samples in the 0° configuration. As main mechanisms, cracks in the matrix and also fiber/matrix deboning can be seen in Figure 71-a and b. As observed in Figure 71-c, fiber breakage in the transversal yarns can propagate all along the yarn and leads to a longitudinal fiber/matrix deboning. The mechanism which causes the final failure of the composite is of course longitudinal fibers breakage, visible in Figure 71-d. A pull-out phenomenon can be observed right after the failure as well (Figure 71-f). This indicates a relatively weak fiber/matrix interface.

- 45° orientation:

Fractography images of the samples in the 45° configurations can be found in Figure 72. As shown for the 0° configurations, matrix cracking is observed (Figure 72-b). Some pseudo-delamination can also be noticed in Figure 72-d. The final failure of the composite is again caused by fiber breakage Figure 72-a. Fiber pull-out was observed, in Figure 72-c, to a higher extent than in the 0° configuration. This observation can be explained by the plasticization in the matrix induced by fibers reorientations that could weaken the fibers/matrix interface.

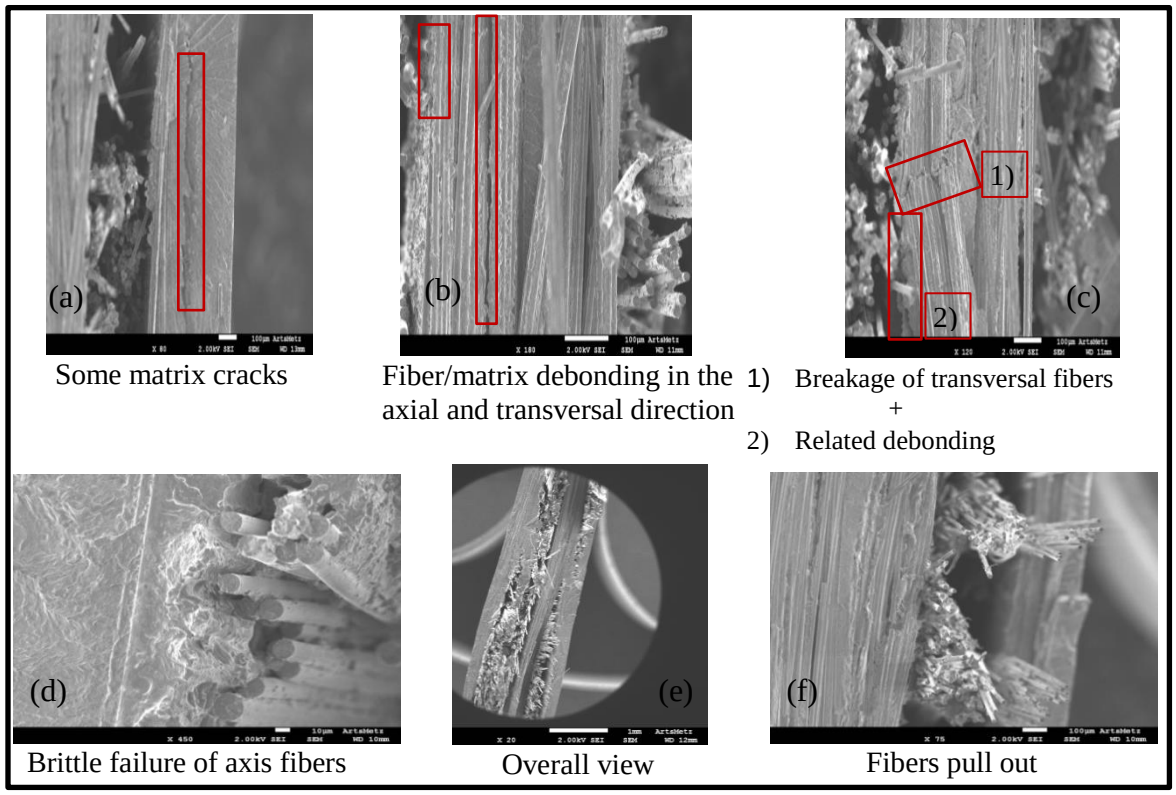

Figure 71 : Rupture mechanisms observed for samples oriented along the fiber axis

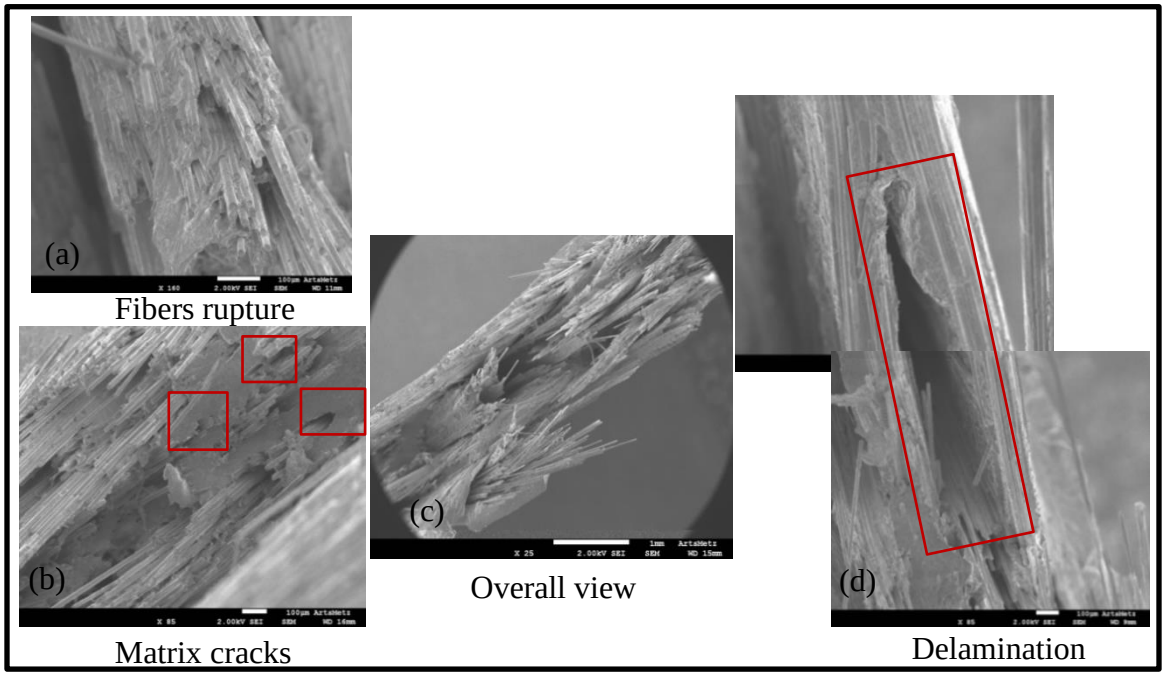

Figure 72 : Rupture mechanisms observed for samples oriented at 45° from fiber axis

With these observations, a number of failure mechanisms can be identified on the two studied orientations. Nevertheless, it is of interest to know the order of appearance of the different mechanisms when a sample is submitted to tension. A more accurate estimation of the typical extent and importance of the observed mechanisms are also necessary for what follows in this thesis. In addition, in order to characterize the sensitivity of a Non Destructive Evaluation method, one of the first tests is to verify the size of the smallest detectable defects, which corresponds to the resolution of the detection technique. X-ray tomography observation will be presented in the next subsection to answer those specific questions.

4) X-ray tomography analysis

An X-ray tomography (EasyTom (Nano) from *RX solutions*) was used to perform a 3D non-destructive analysis. A representation of the basic principle of micro-tomography is shown in Figure 73. X-rays are beamed through the tested sample for different angular positions with respect to a flat panel detector. Images are recorded as a grey level map which is a function of the absorption of X-rays by the material. The *X-Act* software is then used to make a 3D reconstruction of the tested sample. Then, various image processing filters are applied, using the *Avizo* software, on the reconstruction to get rid of noise in the images. First, a median filter is used on the raw images to reduce the major contribution of noise. A despeckle filter is finally applied on the filter images to remove most of the remaining interference noise. The contribution of the two filters can be seen in Figure 74.

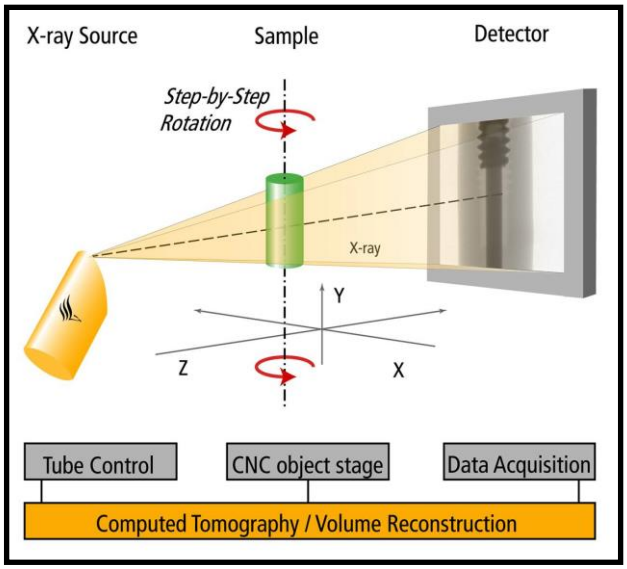

Figure 73 : Principle of the X-Ray tomography techniques [http://www.techmaxasia.com]

In this work, X-ray tomography is used to obtain information about undamaged and damaged (by tensile tests) samples. Acquisitions on 0° oriented samples and samples oriented at 45° from the warp axis have been performed. For both orientations tensile test samples of 150 mm x 45 mm x 1.53 mm were used. The different damage mechanisms, as well as their respective characteristic length, will first be analyzed for both cases. Then, the evolution of the void volume, as function of the loading stress, will be measured by grey level thresholding. Indeed, the matrix, the fibers and the void in the composite have distinctive values of X-Ray absorption and therefore can be easily distinguished; respectively in dark grey, light grey and black as shown in Figure 74.

For the present X-ray tomography acquisitions, the size of the voxel is around 5.5 µm, which is a compromise between the resolution and the size of the investigated area on the sample. The technique allows us to investigate a minimum volume of 16.5 mm x 16.5 mm x 1.5 mm (Figure 75) which is a quite higher than the size of a representative volume element of the studied composite material. It should be recalled that the RVE of the present composite is indeed about 16 mm x 16 mm x 1.5 mm. The parameters of the X-ray tomography are summed up in the Table 11.

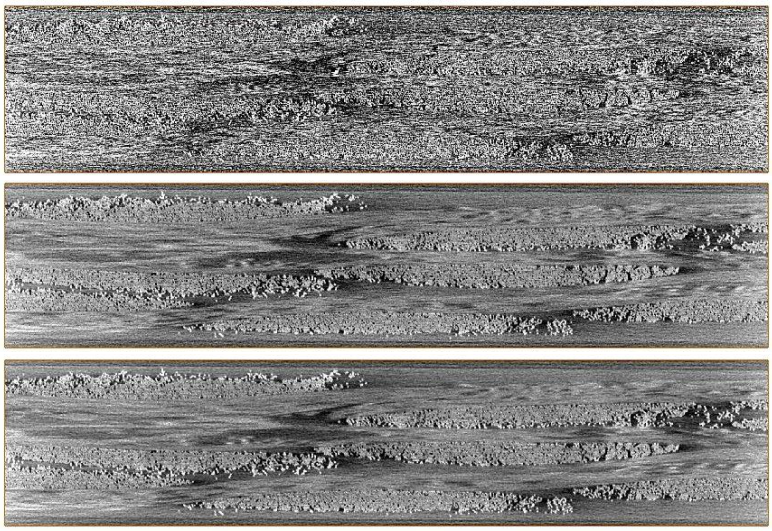

Figure 74 : Slices of an undamaged sample; Top: Raw image, Middle: After a Median filter, Bottom: After a Median filter + a Despeckle filter

Detector resolution	**Exposure**	**Voltage**	**Voxel size**	**Focus to detector (FDD)**	**Focus to Object distance (FOD)**
2320*2336	2 s	90 kV	5,5 µm	670 mm	110 mm

Table 11: X-ray tomography acquisition parameters

It can be seen that some specific X-ray tomography acquisitions were done with a smaller voxel size in order to observe the damage mechanisms more accurately. Those acquisitions were not used in the subsection containing/dealing with the void volume fraction calculation presented at the end of this section.

The composites samples considered here have previously been subjected to an interrupted tensile test at different loading values: 0, 40, 80 and 120 MPa for 45° orientation and 0, 100, 150, 200, 250 and 300 MPa for 0° orientation. The selected stress values are listed in Table 12. The protocol described in the previous chapter, describing tensile tests, was used. Each sample was loaded at a constant strain rate of 10^{-3} until the

defined tensile loading value was reached. They were then unloaded at the same constant strain rate. The chosen loading values are indicated on stress/strain curves previously obtained with tensile test until failure, with red circles in Figure 76.

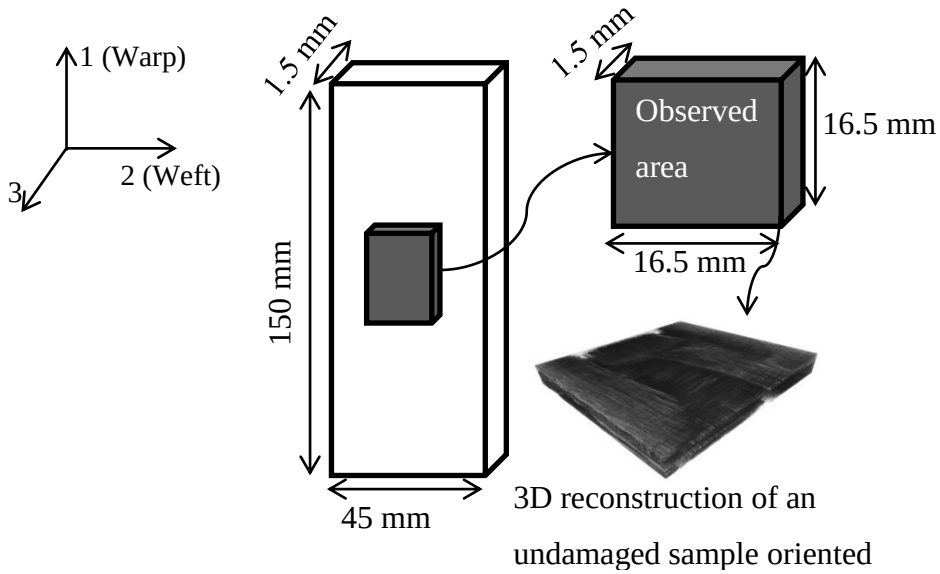

Figure 75 : Schematic representation of the observed area on a polyamide 6,6 /Woven glass fiber samples and the associated 3D reconstruction

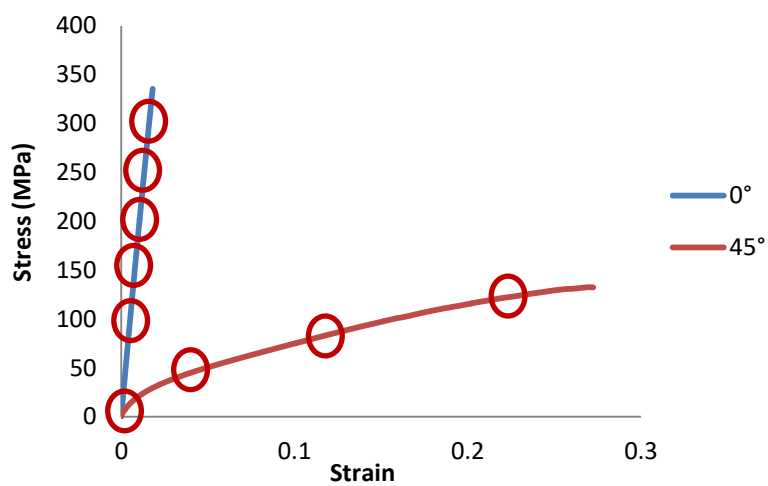

Figure 76 : Typical stress/strain curve of the PA66/6 reinforced with woven glass fiber in the 0° and 45° configurations. The red circles show schematicaly the strain and stress levels where the different tensile tests (performed on several specimens) have been interrupted as summarized in Table 12. Ultrasonic measurements and X-ray tomography investigations are then performed on those specimens

Sample	**1**	**2**	**3**	**4**	**5**	**6**
Configuration	0°	0°	0°	0°	0°	0°
Defined Loading	0 $\%\sigma_{UTS0°}$	30.8 $\%\sigma_{UTS0°}$	46.3 $\%\sigma_{UTS0°}$	61.7 $\%\sigma_{UTS0°}$	77.2 $\%\sigma_{UTS0°}$	92.6 $\%\sigma_{UTS0°}$
Strain	0	0.005	0.007	0.010	0.013	0.016

Sample	**7**	**8**	**9**	**10**
Configuration	45°	45°	45°	45°
Defined Loading	0 $\%\sigma_{UTS45°}$	30.5 $\%\sigma_{UTS45°}$	61.1 $\%\sigma_{UTS45°}$	91.6 $\%\sigma_{UTS45°}$
Strain	0	0.021	0.083	0.162

Table 12 : Samples and their defined tensile loading for 0° and 45° oriented samples

a) 0° oriented - Undamaged sample

As explained in the introduction, an area of 16.5 mm x 16.5 mm x 1.5 mm is observed on a larger sample of 150 mm x 45 mm x 1.5 mm. Samples prior to tensile loading, oriented along and at 45° from the warp direction, will be considered in this subsection.

The three expected plies can be seen in Figure 78, with the three transversal and longitudinal yarns on the slice boxed in red and blue. An estimation of the yarns' size was made based on the obtained sample slice. The yarns in this material have an elliptical shape. Measurements of the major and minor axis were performed on several observed yarns and in several locations in the sample in order to obtain a reliable average value. It is clear that precaution must be taken on what will be considered as "a yarn". Indeed, during the thermo-compression process two yarns, extending in the same direction, can be mixed together. This was not taken into account in the yarns' measurement, only the effect of the

thermo-compression on a sole yarn was considered. Since a 3D representation of the sample is obtained, one can easily follow the propagation of a yarn in the whole reconstructed volume to be sure that only one yarn was measured. All of this can be seen in Figure 77.

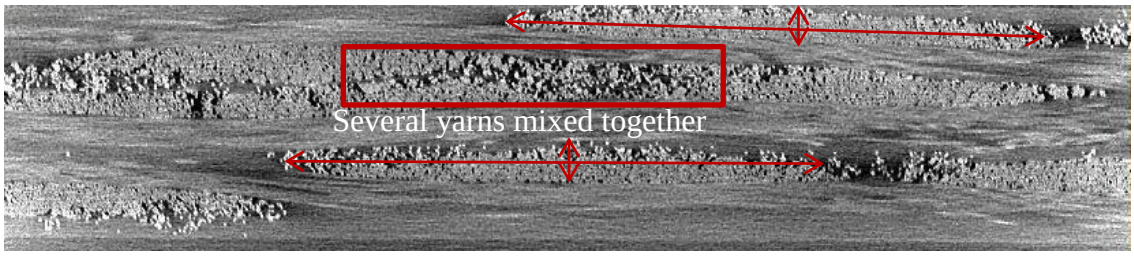

Figure 77 : Transversal (Weft) yarns measurement on a slice of an undamaged sample obtained via X-Ray tomography

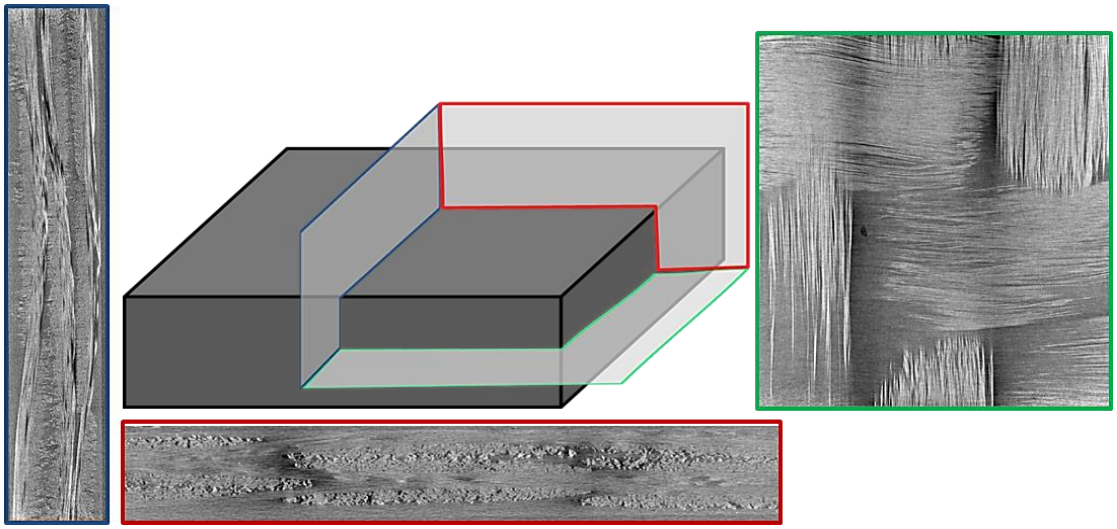

Figure 78 : Slices of the undamaged sample oriented along the fiber axis in different directions before 3D reconstruction

As a result, it appears that the average yarns are ellipses with a minor axis of 0.22 mm and a major axis of 3.6 mm in the weft direction; their minor axis is 0.24 mm and their major axis 3.6 mm in the warp direction. The values are close to those measured on the image obtained with optical microscopy. They will be used in the following chapter to

determine the stiffness matrix of the composite material using a periodic homogenization theory.

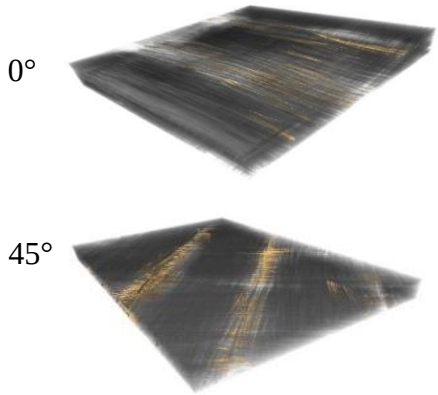

Figure 79 : Three dimensional reconstruction of undamaged samples, in the 0° and 45° configuration, with initial porosity (Yellow)

As mentioned in the introduction, information about the different material present in the tested sample can be extracted from the X-ray tomography acquisitions. Indeed, because of the significantly different X-ray absorption properties of the different constituents of the composite material, estimation of the volume fraction can be performed by grey level thresholding.

First, two constituents, i.e. the fiber and the matrix, are considered for the grey level thresholding. The following first estimation of the volume fraction of each material was obtained. Let's recall that a value of 43% of fiber faction volume was indicated in the data sheet of the composite handed by DuPont, as mentioned in the part II. The measured value of fiber volume fraction is very close to the given value (Table 13).

Matrix volume fraction	**Fiber volume fraction**
57.4 %	42.6 %

Table 13 : Volume fraction of the matrix and fiber on the undamaged sample the 0° configuration

Then, the void is considered as a third constituents and a second grey level thresholding is applied on the undamaged sample. Results are summarized in Table 14. Indeed, as it can be seen in Figure 78, Figure 77 and Figure 79 initial porosities are present in the sample before mechanical solicitation. The porosities appear mostly in the weft yarns near the

yarns' extremity or close to areas where yarns are mixed together during the thermo-compression process.

The fiber volume fraction remains close to the 43% given by DuPont. The measured volume fraction of void is around 0.6% before any mechanical solicitations. Note that in their data sheet, considering the PA 66/6 reinforced with woven glass fibers, DuPont specified that the volume fraction of void is lower than 2%. This is verified on the undamaged samples that have been tested.

Void volume fraction	**Matrix volume fraction**	**Fiber volume fraction**
0.6 %	56.9 %	42.5 %

Table 14 : Volume fraction of the matrix, fiber and void on the undamaged samples in the 0° configuration

b) 0° oriented - Damaged sample

Most of the analysis is done on a sample loaded in tension at 300 MPa along the fiber. A triple constituent grey level thresholding is performed as above. A clear increase of the void area is shown in Figure 80 along the transversal direction (direction of the weft yarn). All the damage mechanisms that were observed are visible in Figure 81. An increase of the number of cracks can be seen on the observed sample compared to the non-loaded composite sample. The main damage mechanisms detected are cracks at the end of yarns, but transversal cracks can also be seen. Some longitudinal cracks appeared as well, but only in the samples loaded at 300 MPa (Figure 81-a). Those are cracks that start from a transversal yarn end and propagate along the nearest longitudinal yarn. This is often called pseudo-delamination in the literature. Nevertheless, it should be expected that some cracks close when the tension on the sample is released. Hence, the number of effective cracks can actually be higher in reality.

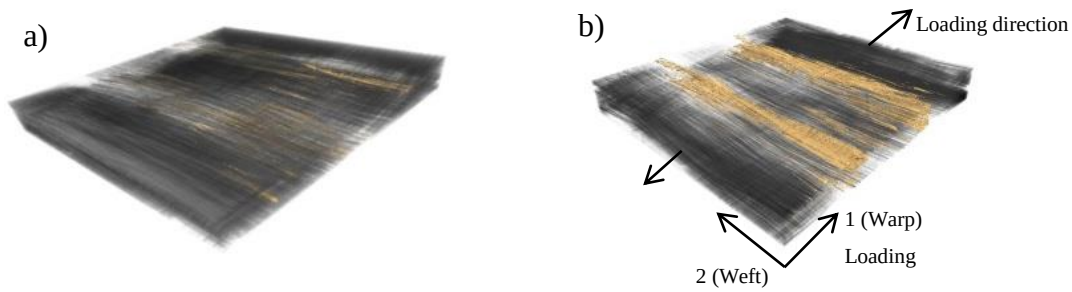

Initial void in an as received sample. The volume void content estimated was 0.5 %

Void and defects (damage) induced by the tension loading at 0°. The volume void content estimated for a stress level of 92.6 %$\sigma_{UTS0°}$ was 1.56 %

Figure 80 : mCT-3D reconstructions of composite samples in the 0° configuration respectively (a) before and (b) after tensile loading at a stress level of 92.6 %$\sigma_{UTS0°}$

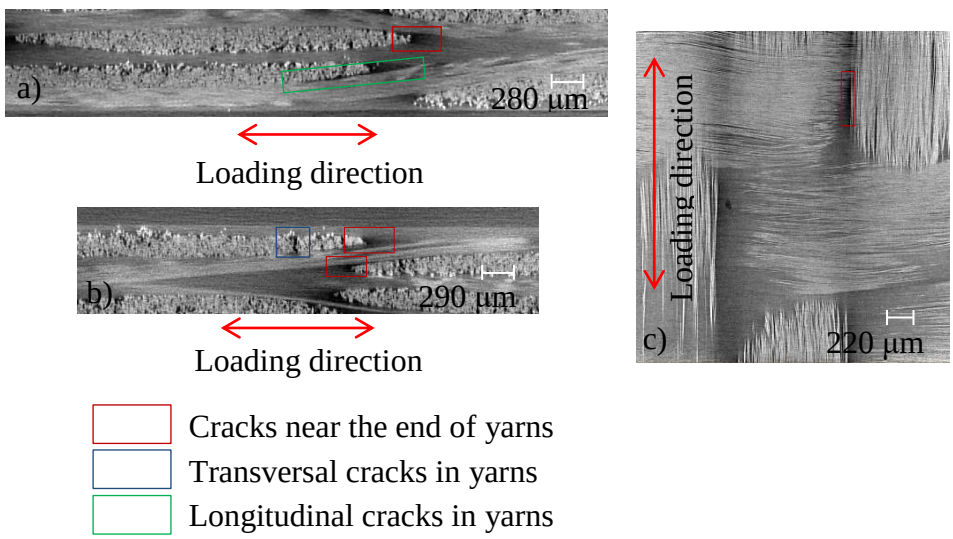

Figure 81 : Slices of the sample loaded at 300 MPa in tension along the warp axis before 3D reconstruction

Characteristic length

Even if they cannot be observed on these tomography results, because of the resolution limited to 5.5 µm, a lot of fiber/matrix deboning happens early on during the tensile loading. They have a typical size of 1 µm (As already observed in the SEM results). As

previously stated the most important damage mechanisms for a woven composite loaded in tension along the axis of the fiber are transversal cracks in the matrix. They have a typical size of 10 µm. The cracks appear as a result of multiple fiber/matrix deboning, locally, in a yarn. They can either grow along the transversal yarns and get stopped by the longitudinal one or propagate along the longitudinal yarn if enough energy is . They can grow all along the transversal yarns, where they are then temporally stopped by the longitudinal yarns. Two damage mechanisms can appear at this stage: pseudo-delamination and fiber breakage. The latter, which is causing the ultimate failure of the composites, has a typical extent of 17 µm (which is the size of the fibers). The pseudo-delamination is a bifurcation of the transversal cracks in the longitudinal direction. The crack then follows the longitudinal yarns. This mechanism has a typical size of 50 µm.

c) 45° oriented – Damaged sample

For the samples oriented at 45° from the fiber axis many other damage mechanisms can be seen in comparison with the previous samples configuration. Indeed, cracks near the end of yarns as well as cracks inside yarns were noticed, just as in the case of samples oriented along the fibers' axis (Figure 82-a and b). However, in addition, fibers breakage (Figure 82-c) and local fiber micro buckling (Figure 82-d) were noticed. These two mechanisms appeared with an onset of 80 MPa loading of the sample, which is significantly early compared with the final stage of sample failure.

The fiber micro buckling is caused by the reorientation of fibers during the loading test. Indeed, as the load increases the angle between the fibers tend to decrease. Then, when the tension is interrupted, the fibers must return to their original place, which is impossible because of the section reduction caused by the Poisson effect. The effect of fiber reorientation during off-axis loading has also been observed by Vieille and al. [19], among others. The mentioned damage mechanisms can be observed in Figure 82. Pseudo-delamination, visible in Figure 83, may also appear locally beyond a stress level of 100 MPa for a loading at 45° from the warp direction. Note that pseudo delamination appears inside a yarns and that delamination appears between two woven fabrics. Finally, it is worth

noting that void area growth occurs along the two fiber direction as shown in Figure 84. This claim is confirmed after comparison with the undamaged sample.

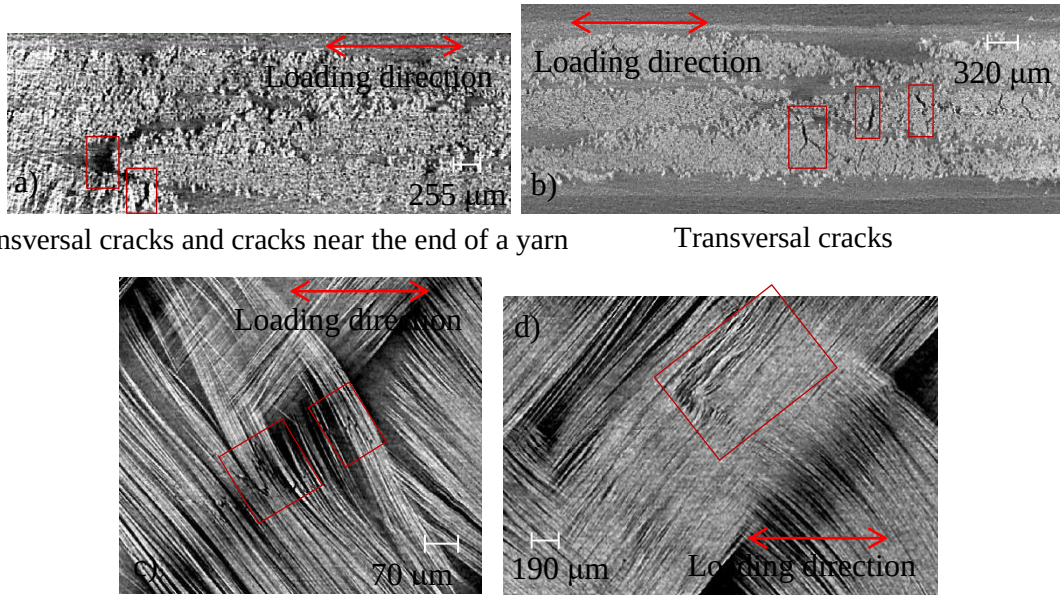

Transversal cracks and cracks near the end of a yarn

Transversal cracks

Fibers breakage

Fibers buckling

Figure 82 : Damage mechanisms observed in woven composite sample loaded in tension at 45° from the warps axis.

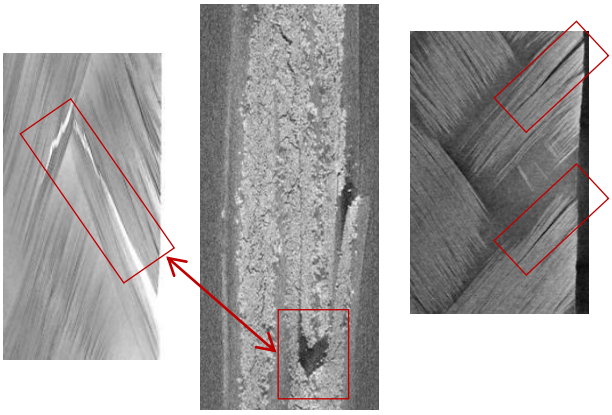

Figure 83 : Pseudo-delamination in a woven composite sample loaded in tension at 45° from the warps axis at a stress level of 120MPa.

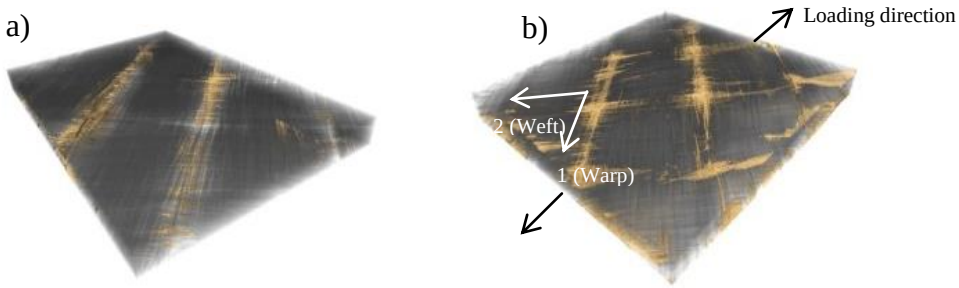

Initial void in an as received sample. The initial volume void content estimated was 0.6 %

Voids and defects (damage) induced by the tension loading at 45°. The volume void content estimated for a stress level of 91.6 %$\sigma_{UTS0°}$ was 5.51 %

Figure 84 : mCT-3D reconstructions of composite samples in the 45° configuration respectively (a) before and (b) after tensil loading at a stress level of 91.6 %$\sigma_{UTS0°}$.

Characteristic length

As for the samples oriented along the fiber axis, the fiber/matrix deboning, transversal cracks and cracks near the yarns' end have a characteristic length of respectively 1 µm, 20 µm and 50 µm. The fiber breakages have a characteristic length of 17 µm. The pseudo-delamination and fibers micro buckling both have a characteristic length of 200 µm which is the largest of the damage mechanisms observed in this woven composite material. The important size of the micro-buckling is explained by the fact that the buckling of numerous fibers is induced which causes local micro-cracks around the fibers. As will be seen in what's next, the last two mechanisms are the only ones visible by C-scan imaging. A summary of all the discussed damage mechanisms, for both 0° and 45° configuration, is presented in Figure 85.

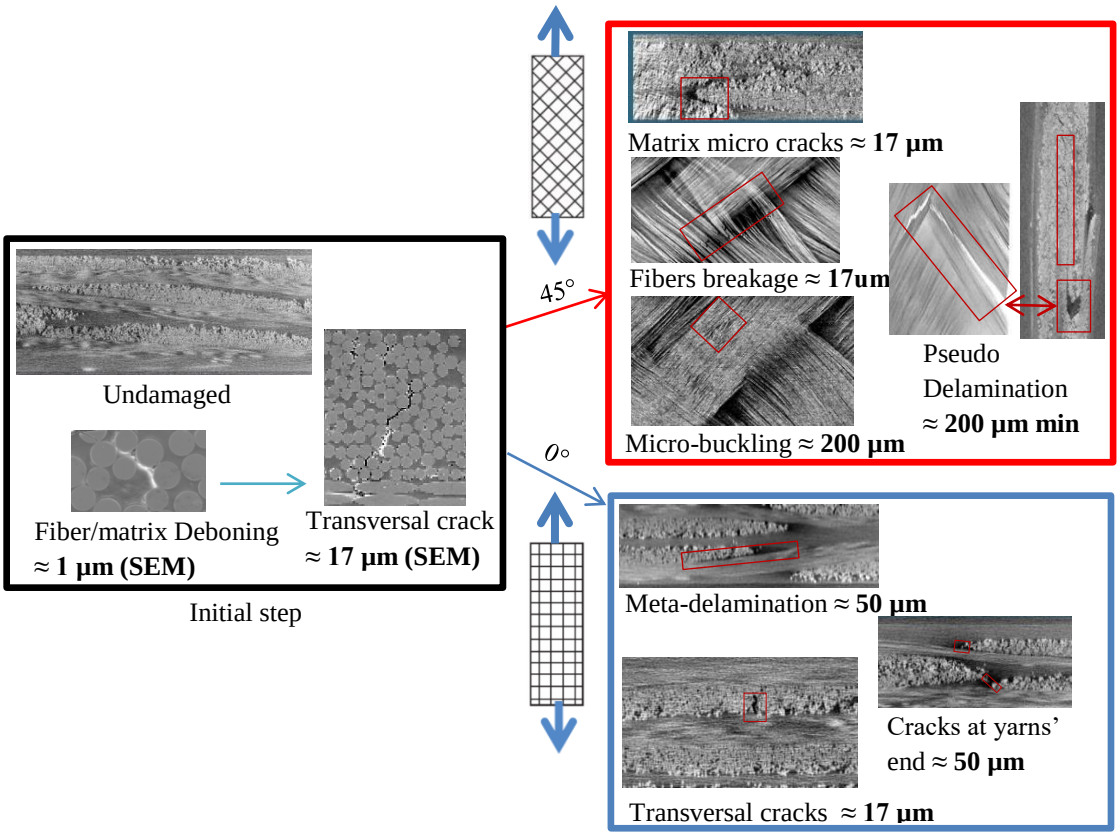

Figure 85 : Summary of the damage mechanisms and their associated typical scale for both 0° and 45° oriented samples.

d) Void volume fraction evolution

In this part, all samples preliminary damaged by interrupted tensile tests are considered. Namely four samples in the 45° configuration and six samples oriented along the yarn axis are investigated. Applying the same procedure described in the introduction, all samples are analyzed with X-Ray tomography. The void volume fractions are evaluated using a grey level thresholding. The measured void volume fraction evolution is plotted in Figure 86 for both studied configurations of samples.

One can clearly observe an important difference between the two orientations. The 45° oriented samples exhibit a more important increase (from 0.59% to 5.51%) of damage

before breakage than the samples in the 0° configuration (increase from 0.59% to 1.56%). The same observation was made from the incremental cyclic tests in section III)-4). As previously discussed this can be reasonably explained by the fact that the polyamide 66/6 matrix, which is very ductile, governs the composite behavior when it is loaded at 45° off the warp direction. As a consequence, when the composite is loaded along the axis of the fibers, the fibers will govern the composite behavior, which means it becomes brittle.

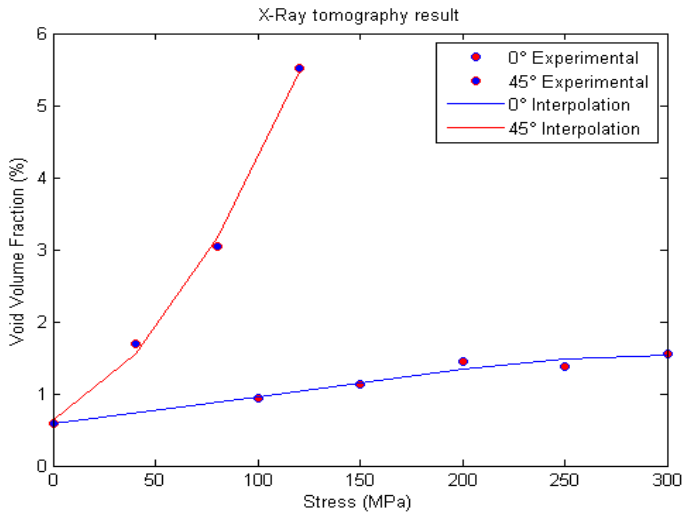

Figure 86 : Void volume fraction evolution obtained with X-ray tomography on previously damaged samples with respect to the tensile loading values.

5) Conclusion

This chapter was dedicated to the analysis of the polyamide 66/6 reinforced by woven glass fiber at the microscale. The use of optical microscopy permits a first observation of the microstructure and the different constituents. The size of the glass fibers and the yarns could be determined. This was also used for the validation of the X-ray acquisition parameters in terms of resolution.

Then, the damage initiation during tensile tests along the fiber axis was analyzed using Scanning Electronic Microscopy (SEM). An observation of fiber deboning was made

starting at 15.7 MPa. The deboning consequently gives rise to matrix cracking propagating along the different fibers of the yarns. Because of experimental issues with the samples during in-situ tensile tests, the analysis of the following events in the damage process was performed using X-Ray tomography. Before continuing with the following subsection, fractography analysis was conducted on samples (in 0° and 45° configurations) broken after tension tests.

As mentioned, X-ray tomography investigation was presented in the third part of this chapter. The different damage mechanisms that may appear in the polyamide 6,6/woven glass fiber composite when it is loaded in tension at 0° or 45° from the fiber axis were observed and discussed. Two distinctive damage schemes were identified for the two orientations. An attention was paid to the typical scale of all the identified damage mechanisms; this is crucial to understand the material damage scheme and validate the different proposed ultrasonic damage detection methods. It was shown that those damage schemes lead to a significant increase of damage for the 45° samples. The observation is in agreement with the elastic modulus reduction measured during increment tensile cyclic tests. It is therefore essential to consider the two orientations in the subsequent study, in order to investigate the sensitivity of the NDT to different damage mechanisms and damage kinematic evolution.

The next chapter will be dedicated to the description of the ultrasonic methods that can be used to detect and to quantify the level of the damage induced in the studied woven composite material undergoing a mechanical loading.

V) Non Destructive Evaluation (NDE) methods based on ultrasound

Contents

1) Review of ultrasonic method of Non Destructive Evaluation (NDE) of damage 122

a) Ultrasonic imaging techniques: transmission and reflection 122

b) Multi angle ultrasonic investigation of material 125

Phase velocities measurement toward stiffness tensor calculation 125

Polar scan method 135

c) Guided waves based testing methods 139

d) Nonlinear acoustic method 146

Nonlinear Resonant Ultrasound Spectroscopy (NRUS) 148

Nonlinear Wave Modulation Spectroscopy (NWMS) 150

Nonlinear Reverberation Spectroscopy (NRS) 153

e) Coda waves in Non-Destructive Testing 154

f) Synthesis of the Non Destructive Evaluation method review 159

2) Ultrasonic C-scan in transmission 160

3) Stiffness tensor components determination 161

a) Description of the experimental procedure and first analysis 162

Preliminary remarks and first results on undamaged samples 162

Experimental procedure for the plane 1-3 and 2-3 164

Experimental procedure for the plane 1-2 166

Preliminary analysis on undamaged samples 167

Investigation of the optimization algorithm robustness to input parameters 173

b) Experimental results: 0° configuration after tensile test 180

c) Experimental results: 45° configuration after tensile test 184

d) Proposed damage indicators 190

4) Guided Lamb waves 195

a) Preliminary investigation on an aluminum plate 196

b) Investigations of the woven glass fiber reinforced polyamide 66/6 samples damaged by tension 199

Analysis of dispersion curves/Lamb waves modes 200

Analysis of signals measured on top/bottom surface of the specimen 206

Investigation of damaged samples 209

Investigation of proposed damage indicators 211

5) Conclusion 215

The objective of this chapter is to present several Non Destructive Evaluation (NDE) techniques based on ultrasonic wave propagation in solid media in order to compare their respective advantages and limitations. The different considered NDE techniques are applied to the polyamide 66/6 reinforced by woven glass fibers damaged samples presented on the previous chapters. The X-ray tomography investigation, from chapter IV), is used as a reference to validate the results from ultrasonic investigation.

In a first section, different ultrasonic NDE techniques are presented with an emphasis on the techniques considered for this project. The majority of those techniques have attracted notable interest by research teams in NDE. Their application on polymer based composites reinforced with fibers is more specifically detailed. All the samples introduced in chapter IV) were analyzed by ultrasonic C-scan, which is described in the second

section. In the third section, the stiffness components measurement by an ultrasonic immersion method and the obtained results is detailed. The method was used on the samples in the 0° and 45° configurations. The evolution, with damage, of the stiffness components identified is then analyzed with regards of the loading level used to introduce an increasing amount of damage. Two damage indicators, based on those results, are then proposed and their relevance is discussed. In a forth section, guided waves were used to evaluate damage. First, an investigation of the transmitted mode for different damage state level is proposed. Then, the evolution of the transmitted signal energy is proposed as another damage indicator. The sensitivity of the different indicators introduced in this chapter is finally discussed.

It is worth mentioning that, in addition to the experimental results discussed in this chapter, investigations on nonlinear acoustics techniques and coda wave interferometry are proposed in the appendix of this manuscript.

1) Review of ultrasonic method of Non Destructive Evaluation (NDE) of damage

Ultrasonic based NDE methods are frequently used to control damage because of various advantages such as their simplicity of implementation and great flexibility. Indeed, ultrasonics can, if needed, be used with only one transducer, e.g. when access to the two sides of a structure is not possible. The method can be used manually in-situ on complex structures with little equipment without reducing efficiency to a significant degree. So, ultrasonic techniques are used either to control structural parts, right after manufacturing and in service, or to validate an assembly [34], [35] for example. On the specific case of composite material, ultrasonic is known to be very effective to detect the most critical damage mechanism in composite material which is the delamination [36]–[38]. In addition, the ultrasonic method can be implemented at a relatively low cost, because of their constant evolution, and does not cause potential health problems like X-ray related techniques for example. This explains why many methods, based on the propagation of ultrasonic waves in material, were developed both in the academic field and in the industry. However, as it was shown in the previous chapter, the damage that can be generated inside the structure can be of very small scale. It may be difficult to detect it with classical industrial imaging technique. Consequently, in this section a review of some ultrasonic methods, that are currently investigated to evaluate damage on material, is proposed. Their application on composite materials will be more specifically discussed.

a) Ultrasonic imaging techniques: transmission and reflection

This class is one of the oldest, and furthermore the most used, of the ultrasonic NDE techniques in the industry. The principle is to scan the whole surface of the structure point by point and to record the ultrasonic signals for each of those points. Information such as the damping (attenuation in amplitude), the velocity, Time of Flight (ToF), etc is then extracted from the acquired signals. The measure can be made on contact or in immersion in water. Two main techniques can be distinguished: the Ultrasonic Pulse Velocity (UPV),

or method in transmission, when two transducers are used and the Ultrasonic Pulse Echo (UPE), or method in reflection, when one transducer is used as emitter and receiver. With the UPE method a defect is detect with the apparition of a new peak on the response signal (Left side of Figure 87). With the UPV method the attenuation of the amplitude is typically considered to identify a defect (Right of Figure 87).

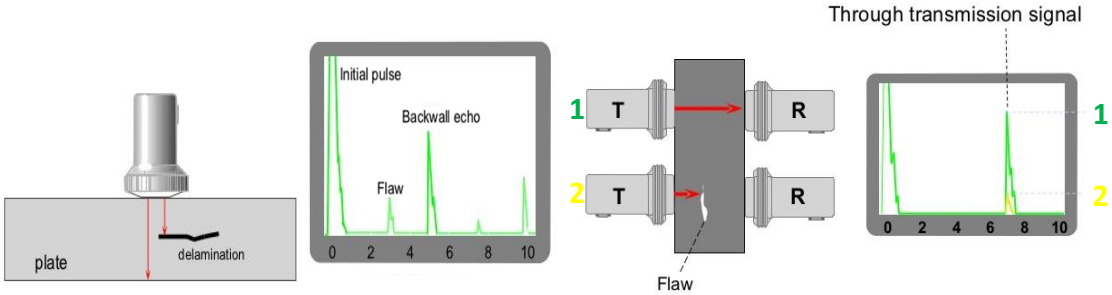

Figure 87 : Left: Ultrasonic Pulse Echo (UPE); Right: Ultrasonic in transmission (UPV) [Krautkramer NDT Ultrasonic Systems]

Nevertheless, different authors [39]–[41], highlight the benefit of using Time of Flight instead of the amplitudes for damage characterization, especially for composite materials. Indeed, Liu and al. [40] specified that for corrugated samples using ToF measurement allowed localizing the defect in the sample but also to characterize vertical geometry. Nevertheless, they showed that measures of amplitude can be more useful for characterization of surface damage. These damages are more dependent of amplitude energy loss. The combination of both analyses can provide more thorough investigation of damage.

When an appropriate time window is used, one can even obtain a 3D representation of the sample (Figure 88). However, the frequency of the emitted pulse has to be carefully taken into account. For example, if a transducer of 5 MHz is used in water, a wavelength of 0.3 mm is obtained, so the sample can be “cut” into 0.3 mm thick slices. If the sample needs to be cut at a lower scale, the interpretation of data must be made with caution. In order to overcome wrong data interpretation and provide better description of the inside damage, different classification and segmentation algorithm could be considered. Note that

ultrasound imaging is often considered as one of the more difficult imaging-techniques to segment [42].

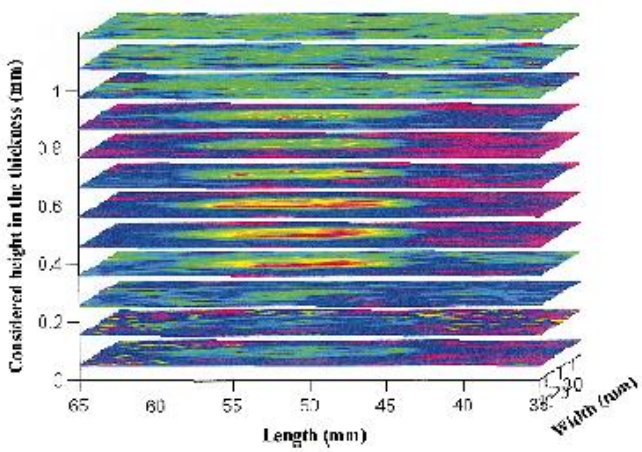

Figure 88 : Examples of C-scan with 12 slices cut on top of each other of a fiber reinforced composites materials damaged by impact [49]

Many studies dealing with the comparison of ultrasonics with other NDE methods are worth mentioning. As an example, Pastor, Garnier and al. [38], [43] propose a comparison of ultrasonic contact testing with infrared (IR) testing. The major advantage of IR is its faster time of control (50 times faster than US). It manages also to detect a defect in a geometric discontinuity region of a sample, which the US testing is not capable of in the report. However, the IR testing had difficulties to detect defects smaller than 6 mm and does not detect an intentionally inserted peel ply. US testing was able to image those defects more efficiently because they appear on flat composite samples. On the other hands, the TeraHertz imaging techniques has proved to be more effective to detect even smaller defects than ultrasound but is slower to process [44]–[46] and does not work for certain materials. It is indeed worth mentioning that, because of its high conductivity, it is very arduous to performed TeraHertz investigation in depth of carbon fibers reinforced composites [47]. The defects that can be detected are typically located on the surface or in the first ply, even though some recent researches performed by Dong et al. in Georgia Tech Lorraine tried to overcome this issue. This investigation was performed in collaboration

with the LEM3 from Metz, which investigated the carbon fibers reinforced composite specimen by means of X-ray tomography in order to provide a validation of the TeraHertz results. A collaborative paper has consequently been submitted for publication.

b) Multi angle ultrasonic investigation of material

Phase velocities measurement toward stiffness tensor calculation

In order to fully characterize the material, Markham [48] presents a method to determine all the stiffness components of a material based on ultrasonic measurements. He applied the method first on a transversely isotropic composite. The method was also successfully used to measure the change in stiffness on composite submitted to different levels of impact [49], [50] and tensile test [51], [52] for example.

The main principle of this method is to measure the velocity of wave propagation at different incidence angles along different principal planes. It can be shown that the velocity of wave propagations trough a solid media is function of the rigidity of the sample. To comply with the laws of physics, three equations must be combined.

First the equation of motion:

$$\frac{\partial \sigma_{ij}}{\partial x_j} = \rho \frac{\partial^2 u_i}{\partial t^2} \tag{V.1}$$

With σ_{ij} : the stress tensor, u_i : the displacement vector, ρ : the material's density

Then, one takes into account the generalized Hooke's law, for linear elastic behavior:

$$\sigma_{ij} = C_{ijkl}\varepsilon_{kl} \tag{V.2}$$

With C_{ijkl} : the fourth order stiffness tensor and ε_{kl} : the strain tensor

Finally the relation between strain and displacement field for small perturbations hypothesis is used:

$$\varepsilon_{ij} = \frac{1}{2}\left(\frac{\partial u_i}{\partial x_j} + \frac{\partial u_j}{\partial x_i}\right) \tag{V.3}$$

After combining the three equations, the following relation is obtained:

$$\frac{\partial C_{ijkl}}{\partial x_j}\frac{\partial u_k}{\partial x_l} + C_{ijkl}\frac{\partial^2 u_k}{\partial x_j \partial x_l} = \rho\frac{\partial^2 u_i}{\partial t^2} \tag{V.4}$$

If the material is considered to be a homogenous media, the stiffness components C_{ijkl} are not function of the local position in the material. Therefore, the spatial derivative of the rigidity matrix is equal to zero. It will be explained later how to experimentally satisfy this assumption. The first term of the previous equation vanishes:

$$C_{ijkl}\frac{\partial^2 u_k}{\partial x_j \partial x_l} = \rho\frac{\partial^2 u_i}{\partial t^2} \tag{V.5}$$

The solution of this equation is now considered for a plane harmonic displacement wave:

$$u_i = U_i e^{\mathrm{i}(k_j x_j - \omega t)} \tag{V.6}$$

With ω: the angular frequency, k: the wave vector, U_i: the wave polarization,

The so called Christoffel‘s equation is consequently defined as follow:

$$(C_{ijkl} n_k n_j - \rho v^2 \delta_{ij}) U_l = 0 \tag{V.7}$$

With $v = \frac{\omega}{k}$, the phase velocity. One can define the Christoffel matrix as:

$$G_{ik} = C_{ijkl} n_k n_j \tag{V.8}$$

The Christoffel's equation can then be rewritten as :

$$(G_{ik} - \rho v^2 \delta_{ij}) U_l = 0 \tag{V.9}$$

With, if a fully anisotropic material is considered:

$$G_{11} = C_{11} n_1^2 + C_{44} n_2^2 + C_{55} n_3^2 + 2C_{14} n_1 n_2 + 2C_{15} n_1 n_3 + 2C_{54} n_2 n_3$$

$$G_{22} = C_{44} n_1^2 + C_{22} n_2^2 + C_{66} n_3^2 + 2C_{24} n_1 n_2 + 2C_{64} n_1 n_3 + 2C_{24} n_2 n_3$$

$$G_{33} = C_{55} n_1^2 + C_{66} n_2^2 + C_{33} n_3^2 + 2C_{65} n_1 n_2 + 2C_{35} n_1 n_3 + 2C_{36} n_2 n_3$$

$$G_{12} = C_{14} n_1^2 + C_{24} n_2^2 + C_{65} n_5^2 + (C_{14} + C_{44)} n_1 n_2 + (C_{16} + C_{54)} n_1 n_3 + (C_{64} + C_{25)} n_2 n_3$$

$$G_{13} = C_{15} n_1^2 + C_{64} n_2^2 + C_{35} n_5^2 + (C_{16} + C_{54)} n_1 n_2 + (C_{13} + C_{55)} n_1 n_3 + (C_{34} + C_{65)} n_2 n_3$$

$$G_{23} = C_{54} n_1^2 + C_{26} n_2^2 + C_{36} n_5^2 + (C_{64} + C_{25)} n_1 n_2 + (C_{34} + C_{65)} n_1 n_3 + (C_{23} + C_{66)} n_2 n_3$$

$$G_{21} = G_{12},\ G_{31} = G_{13},\ G_{32} = G_{23} \tag{V.10}$$

By solving the Christoffel equation as, i.e. by requiring non-trivial solutions, as $det(G_{ik} - \rho v^2 \delta_{ij}) = 0$ it can be shown that a maximum of three wave modes can appear for every propagation direction **n** considered. A representation of the propagation of those modes in a carbon epoxyde is proposed in Figure 89. This figure represents the slowness curves (the inverse of phase velocity) that exhibit an inversely proportional functionality to the stiffness properties of the sample in the wave mode propagation direction. This figure is usually used to expose a representation of the material anisotropy.

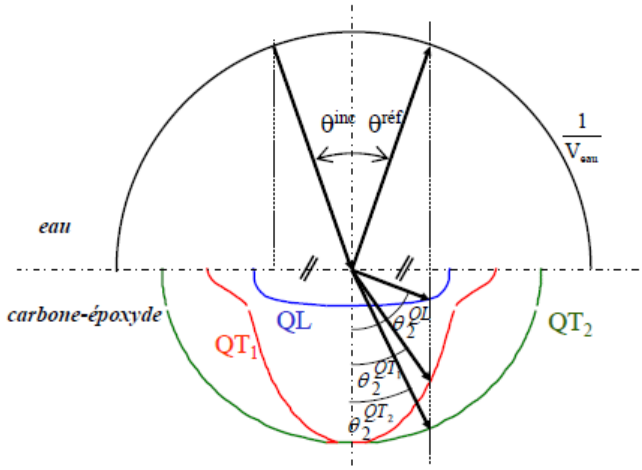

Figure 89 : Slowness curve of the different waves mode that propagate inside a carbon-epoxide composite sample immersed in water [118]

A change in the applied incidence angle can induce a difference of mode conversion of the incident wave. Scanning a range of angles leads to the appearance of the different aforementioned modes; some of them can appear simultaneously for the same incidence angles. The order of apparition of those modes when increasing the incidence angle is depicted in Figure 90. Usually, if the direction of the incident wave is in an axis of symmetry of the material only a quasi-longitudinal mode appears. If **n** is in a plane of symmetry, additionally a quasi-transversal wave appears. Finally, if **n** is in a non-principal plane, an additionally quasi-transversal mode appears [50]. After the 2nd critical angle is reached, only Rayleigh waves (i.e. surface guided waves) can propagate, to some extent, in the sample. The feature of guided waves will be discussed in detail in a further subsection.

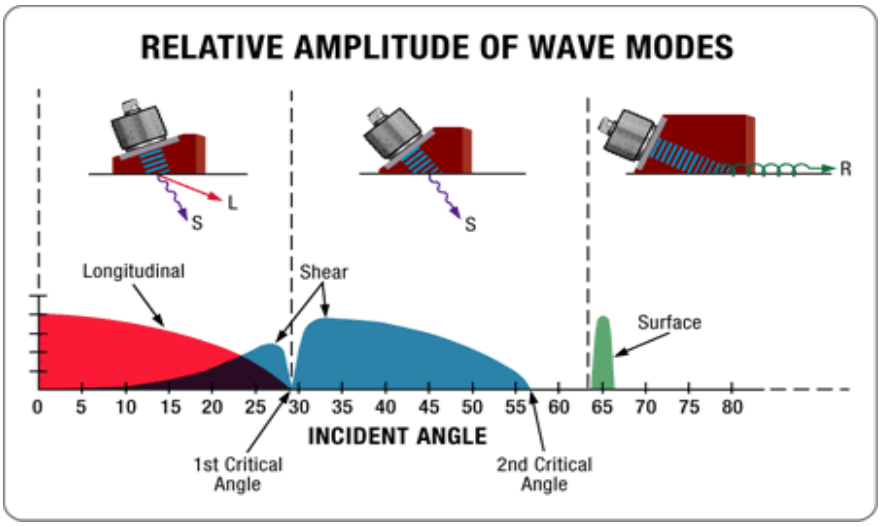

Figure 90 : Schematic representation of the wave mode conversion principle propagating in a plane of symmetry [www.olympus-ims.com]

As previously said, in order to allow the use of Christoffel's equation, the assumption that the material is homogenous is a requirement [53]. So, the frequency of the emitted pulse must be selected in order to have a wavelength larger than the biggest heterogeneity. However, the larger the wavelength, the lower the precision of the result, therefore a trade-off is necessary.

The method can be used with contact transducers or in immersion. In the first case, multiple cube cuttings are needed along its principle orientations [54]. For example, four cuttings are needed to determine all the rigidity constants for an orthotropic material. One cube is cut along the principle axis and the other three are cut at 45° from each of their principle planes. The most obvious problem of this method is the destructive aspect. Indeed, one cannot further analyze the sample in terms of complexes damage scheme, via impact or tensile loading for example.

In the immersion method, the tested sample is put in a liquid (typically water) and the liquid/solid interface permits obtaining, at least, two modes of propagation by varying the angle of incidence. With this method, one can obtain a lot of information with just one

sample and with relatively low number of experimental acquisitions. The measurement of the evolution of the rigidity constants can be done for different damage states. Therefore, in this thesis-study, an immersion ultrasonic system is chosen.

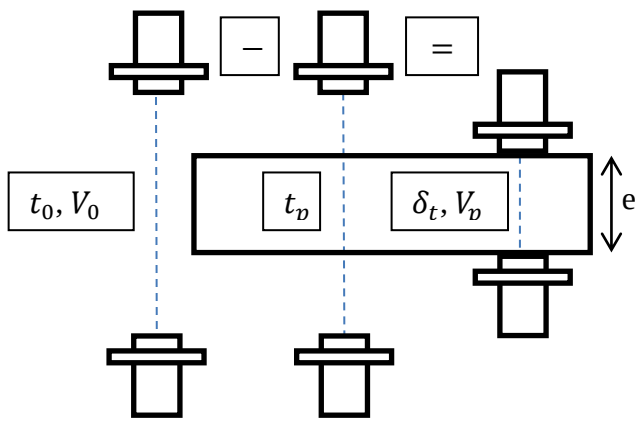

Figure 91 : Schematic representation of the principle of time of flight measurement of the stiffness components measurement in immersion

Experimentally speaking, the difference, named δ_t, between the time of flight of the wave with the sample and without the sample (respectively $t_0$and t_v) is measured. Those different variables are presented in Figure 91. This δ_t is defined as:

$$\delta_t = t_0 - t_p \tag{V.11}$$

$$With\ t_0 = \frac{\mathrm{e} * \cos(\theta_r - \theta_i)}{V_0 * \cos(\theta_r)}\ and\ t_p = \frac{\mathrm{e}}{V_\mathrm{p} * \cos(\theta_r)} \tag{V.12}$$

And e : the sample's size in the principal planes of the propagation direction considered, θ_r : the refraction angle, V_0 and V_p the phase velocity respectively in water and in the considered sample.

$$\frac{\delta_t}{e} = \frac{\cos(\theta_r - \theta_i)}{V_0 * \cos(\theta_r)} - \frac{1}{V_\mathrm{p} * \cos(\theta_r)} \tag{V.13}$$

$$\text{Or}: \cos(\theta_r - \theta_i) = \cos(\theta_r)\cos(\theta_i) + \sin(\theta_r)\sin(\theta_i)$$

$$\frac{\delta_t}{e} = \frac{\cos(\theta_i)}{V_0} + \frac{\sin(\theta_r)\sin(\theta_i)}{V_0 * \cos(\theta_r)} - \frac{1}{V_\mathrm{p} * \cos(\theta_r)} \tag{V.14}$$

$$\text{Or}: \sin(\theta_i) = \frac{\sin(\theta_r) * V_0}{V_\mathrm{p}};\ Snell\ Law \tag{V.15}$$

$$\frac{\delta_t}{e} = \frac{\cos(\theta_i)}{V_0} + \frac{\sin^2(\theta_r) - 1}{V_\mathrm{p} * \cos(\theta_r)} \tag{V.16}$$

In order to get rid of the V_p in equation (V.16), Snell's law is applied:

$$\frac{(\mathrm{V.15})}{(\mathrm{V.16})} \Rightarrow \frac{V_\mathrm{p}}{\cos(\theta_r)} \frac{\sin(\theta_r)}{V_\mathrm{p}} = \frac{\frac{\sin(\theta_i)}{V_0}}{\frac{\cos(\theta_i)}{V_0} - \frac{\delta_t}{e}} \tag{V.17}$$

Eventually, the refraction angle and the velocity of propagation of the wave in the material (named V_p) can be calculated with the following equations:

$$\theta_r = \mathrm{atan}\left(\frac{\sin(\theta_i)}{\cos(\theta_i) - \frac{V_0 \delta_t}{e}}\right) \tag{V.18}$$

$$V_p = \frac{\sin(\theta_r) * V_0}{\sin(\theta_i)} \tag{V.19}$$

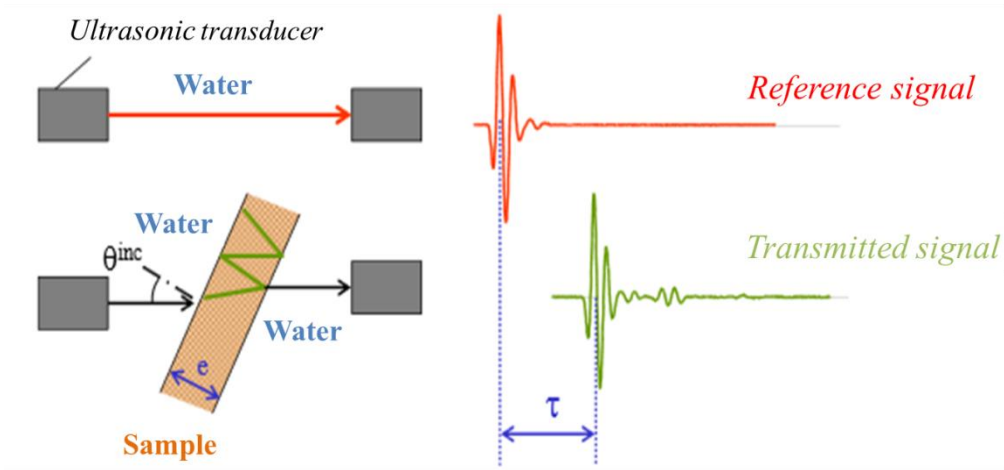

Figure 92 : Schematic representation of the wave velocity measurement method in immersion [Inspired from perso.univ-lemans.fr]

It was shown that the ToF measured with this technique corresponds to the group velocity of the transmitted wave, which is in general different from the phase velocity. This is because the energy flux vector does not coincide necessarily with the wave normal in anisotropic material with oblique incidence. It was later proven, in [55] among others, that for all considered directions and in generally anisotropic materials, the measured ToF is equivalent to a phase delay. Indeed, changes in velocities and travelling paths compensate each other, making it physically correct to use the measured δ_t to estimate phase velocity. This proof will not be detailed here can be found in [56] for example.

In order to extract the full stiffness tensor of a fully anisotropic material (triclinic), measurement in three orthogonal planes of the three waves modes are really advised [57]. Otherwise, large errors in the stiffness components identification may be induced. A lot of experimental measurements are required for similar reason. When an orthotropic material is considered, measurements in three orthogonal planes of the sample are still necessary. But less experimental values are needed and measurement of the three wave modes is not mandatory. Usually, the planes 1-3, 2-3 and 1-2 are used. Indeed, with measurement in the plane 1-3 the components C_{11}, C_{33}, C_{13}, C_{55} can be determined, measurement in the plane

2-3 allow to determine C_{22}, C_{33}, C_{23}, C_{44} and with measurement in the plane 1-3 one can determine the components C_{11}, C_{22}, C_{12}, C_{66}. This is summarized in Figure 93.

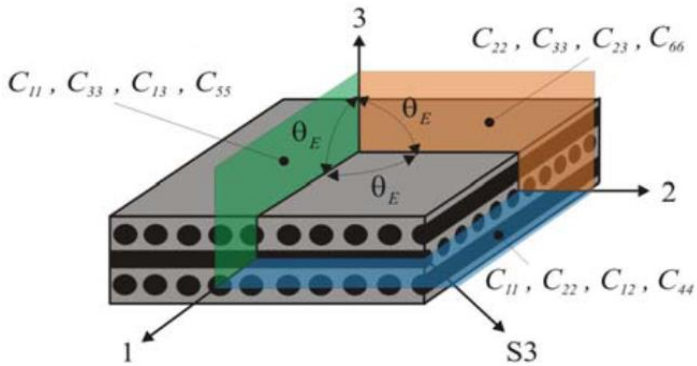

Figure 93 : Figure of the three planes used to compute the nine rigidity constants of an orthotropic material [51]

Some authors [51]–[53] highlight the fact that measurement along the 1-2 plane can be difficult because of the low thickness of a composite material and the possible involvement of guided propagation. So they only used the plane 1-2 and 1-3, which leads to obtaining seven out of nine stiffness constants. There are authors who consider out of plane measurement, usually 45°, in order to obtain the remaining constants. However, Hufenbach [51] precise that out of plane measurement can lead to important wave deviation and false results. So he prefers to consider only in-plane measurement and compute seven rigidity constants.

After the experimental acquisition, the stiffness can consequently be determined by solving the inverse problem of the Christoffel equation. This is typically performed via an optimization approache. Usually, a Levenberg-Marquardt algorithm is use to minimize the square deviation between the analytical and experimental velocities. This optimization problem is set as:

$$F(C_{ij}) = \sum_n [V_{exp} - V_{num}(C_{ij})]^2 \tag{V.20}$$

$$with\ n : the\ number\ of\ experimental\ velocities$$

The numerical velocities are determined by solving the Christoffel equation for a given set of C_{ij}.

Some authors consider a genetic algorithm to solve this problems [58]. This can allow a lower number of experimental data and is less sensitive to the initialization values. However, it requires more time to converge to an optimization solution. Deterministic algorithms, as the Levenberg-Marquardt algorithm, converge more easily and quickly but can lead to stability issues with the algorithm. They are very sensitive to the initial guess, if this guess is too far from the best solution one can find a local minimum instead of the global minimum. As a consequence, in order to initialize the algorithm, a good first estimation of the value of C_{ij} is required.

The values of identified stiffness components will be dependent on this initial guess but also on the number of experimental velocities considered and the number of principal planes investigated. Therefore, it is necessary to estimate a confidence interval, *ci(i)*, for each component of the identified stiffness matrix. It was proposed by Audoin and al. [59] to use the covariance matrix ϕ to obtain statistical information of the deviation from the analytical solutions of the Christoffel equation for each stiffness component. This covariance matrix is calculated as

$$\phi = \frac{\boldsymbol{r}^t * \boldsymbol{r}}{n - m} * [\![([J]]\!]^t * [J])^{-1} \tag{V.21}$$

with: $[J] = \frac{\partial F(C_{ij})}{\partial C_{ij}}$ the Jacobian matrix, **r** is the vector of the residual values i.e. the functional evaluated with the identified solution, n is the number of experimental velocities, m the number of stiffness parameters to identified.

The values of confidence interval can then be extracted from the diagonal terms of the covariance matrix.

$$ci(i) = \sqrt{\phi_{ii}} \tag{V.22}$$

The ultrasonic C-scan, discussed earlier, can give some information about the damage: its location and its size (if the latter is comparable with the wavelength). But it remains difficult to have a good quantification of the damage severity. Recall that increasing damage on a sample induces a decrease of the Young's modulus. This effect can be clearly seen on stress/strain curves of fatigue tests. So the method can be used to compute the stiffness components at several moments of the damage life of the material and to observe their evolutions. This could provide very useful information about the anisotropic properties of the material that could be linked to the microstructure of the tested specimen. The modification of the anisotropy during the damage evolution can be verify and used to developed material damage behavior model.

Polar scan method

The method proposed by Markham requires some long post-processing before having information on the tested sample. Plus, it may be difficult for use in practice because the sample needs to be perfectly aligned in the path of the two transducers. So, another technique, named Polar Scan, was earlier developed to determine the damage with more ease in the composite with an experimental method rather similar [39], [60], [61].

Indeed, with the Polar Scan method a scan of a specific point in the sample is made for all accessible oblique angles of incidence. These angles are usually named ψ and are obtained together with the polar coordinate (θ, ϕ). During the experiment, a pulse wave is emitted and travels through the sample a first time, is then reflected by an acoustic mirror to travel through the sample a second time. This is called the double transmission mode (Right of the Figure 94). For each polar angle, the amplitude is recorded. The acoustic mirror facilitates the technique as normally a sound beam is deviated due to internal scattering and

might miss a transducer placed on the opposite side in reception mode. By having a wide mirror reflecting sound back into the sample sound is actually re-collimated to reach the transducer again which now acts as receiver. A more classical method does not use an acoustic mirror but a second transducer that is used as a receiver as visible on the left of the Figure 94.

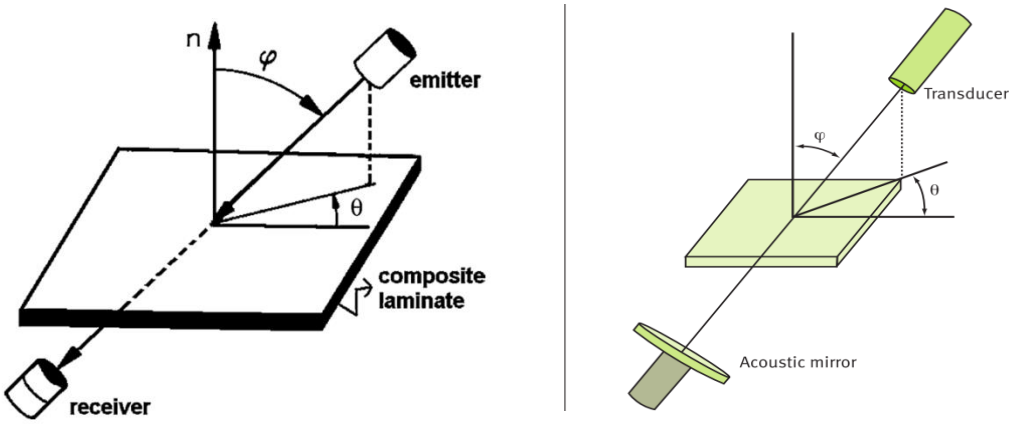

Figure 94 : Left: Polar scan with two transducers in transmission mode [62]; Right: Polar scan with an acoustic mirror [39]

The frequency must be low enough for the composite to be considered as a homogenous material (no fiber detection, no initially present porosity …). As the previous method, information on a homogenized material is obtained. The chosen frequency will be function of the material and his thickness [62]. The amplitudes measured are then plotted on a figure pole. Most of the authors call the resulting figure a local fingerprint of the sample. It was actually shown by numerous authors, [39], [60], [62], that the polar scan method is very useful to determine the fiber direction, the stacking sequence, and the rigidity. Qualitatively, one can see the symmetry of the rigidity very effectively [39]. Polar scan results for an orthotropic material and an isotropic material are respectively plotted on the left and right of the Figure 95 as example.

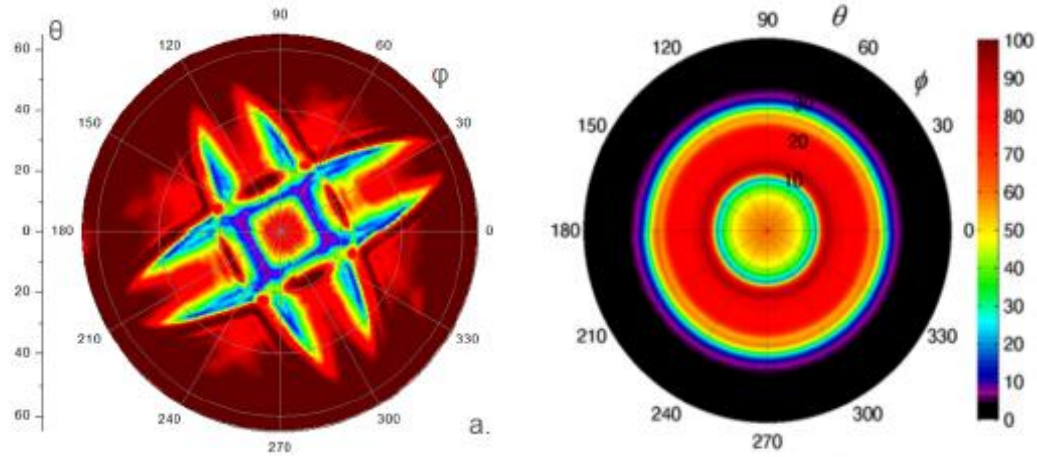

Figure 95 : Left: Pulsed polar scan on a satin weave carbon fabric/PPS laminate [67]; Right: Pole figure for an aluminum sample [119]

On the 2 polar figures, one can easily saw the difference between the rigidity symmetry of the two materials. On the aluminum sample the behavior of the wave is the same in all directions, i.e. the critical angle is the same i.e. the rigidity is the same. On the satin weave composite, the sample exhibit 2 axis of symmetry and can be identify as an orthotropic material. Any change in the material's symmetry, induced by damage or manufacturing issues, can be detected [61]. The resulting pole figure represents in fact the incidence critical angle for which the wave could not travel through the sample anymore. The wave could be either reflected or converted into a surface wave. With the Snell-Descartes law the velocity of propagation is calculated for each polar angle. Then, with the Christoffel equation the rigidity of the material can be obtained with a post-processing technique close to the one describe in the last subsection. Of course since investigation in one principle surface is missing, some of the material's rigidity components may remain undetermined.

The backscattered signal was also proved to be able to give information about damage state and the architecture of composite sample. Following a theoretical study, in transmission, by Declercq et al [63] and further working out ideas of Herbison et al [64]–[66], Kersemans and al. [67] investigate a Carbon/Epoxy [$0°_2$,$90°_2$] and a carbon/epoxy UD using this technique. The surface of the sample was also observed with a microscope and a double through transmission polar scan was also performed. It was observed that even if the

ultrasonically detected mechanical behavior of those two composites is different (Figure 96 b) and Figure 97 b)), the backscattered signal remains unchanged and is in correlation with the observed surface. Indeed, symmetry axis at 0°, 90° (in green) and 30°,150° (in red), detected with the backscattered signal were observed on both samples' surface. They also investigated Glass/Epoxy $[-45°,+45°]_s$ samples before and after shearing loading. On the undamaged sample the expected fiber's orientation were observed with the backscattered signal (Figure 98). On the damaged sample the same symmetry axis could be observed but with a higher amplitude. They recall that for this mechanical solicitation; cracks following the fiber's axis are very expected. Therefore, they state that this technique could be used to estimate the amount of micros-cracks in the material at least on the surface.

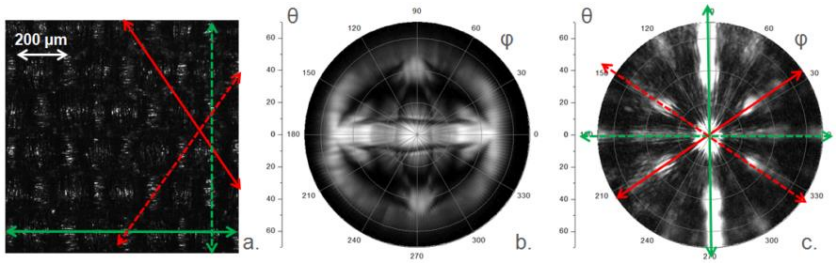

Figure 96 : Carbon/Epoxy $[0°_2,90°_2]$ sample; a) : microscope observation of the surface of the sample; b) Double transmitted signal; c) Backscattered signal [67]

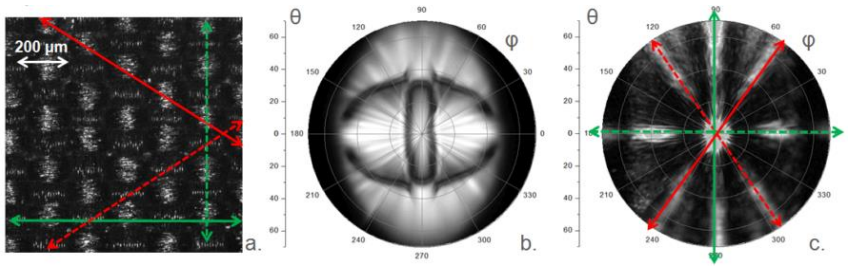

Figure 97 : Carbon/Epoxy UD sample; a) : microscope observation of the surface of the sample; b) Double transmitted signal; c) Backscattered signal [67]

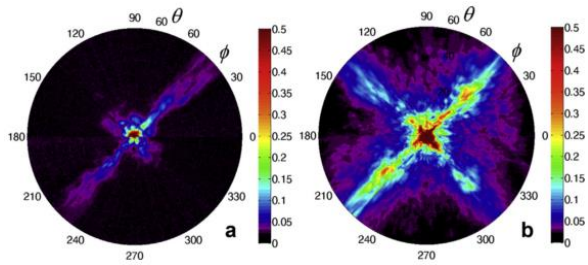

Figure 98 : Backscattered signal on Glass/Epoxy $[-45°,+45°]_s$
; a) :Undamaged; b) Loaded in shear stress at 42.5 MPa [60]

Despite of their presented advantages, the polar scan method, well-established for over a decade, will not be further investigated in detail in the manuscript. Indeed, after preliminary studies the method was not found to be perfectly suitable to investigate the polyamide 66/6 composite reinforced with woven glass fibers considered in this study. This was attributed to the surface of the manufactured composite that is not perfectly flat. In fact, the woven reinforcement induces small perturbation in the sample flatness. In addition, the polar scan method requires a more complicated apparatus that include two axis of rotation which is fine in a laboratory but not necessarily practical in industry and on-site.

c) Guided waves based testing methods

Contrary to bulk waves, the Rayleigh-Lamb wave's motions are bonded to the surface of the plate in which they propagate, this creates the so-called guided wave effects. They can be generated inside the plate when the wavelength of the waves is close or greater than the thickness of the considered sample. Where Rayleigh waves just propagate along a single surface of a plate, Lamb waves exist in the whole plate thickness. Lamb waves will be mostly discussed in the current section.

Lamb waves are the result of longitudinal and shear waves that overlap/superimpose each other. They are known for being dispersive, which means that the velocity of the Lamb waves differs as a function of the frequency. Indeed, when the frequency changes, so does the wavelength. This will induce the appearance of different wave propagation modes

that can be classified as symmetric or antisymmetric modes. Several of these modes may appear at the same time (Left of Figure 99) but with a different velocity of propagation. The representation of the velocity of the different propagating Lamb wave modes as function of frequency is called "dispersions curves". An example of dispersion curves is shown in Figure 100 for aluminum. Dispersion curves are determined by the material characteristics and plate thickness. For an isotropic material, a Lamb mode can be formulated by the characteristic equations as follows [68]:

$$\frac{\tan(qh)}{\tan(ph)} = -\frac{4k^2pq}{(q^2-k^2)} \text{ , for symmetric modes} \tag{V.23}$$

$$\frac{\tan(qh)}{\tan(ph)} = -\frac{(q^2-k^2)}{4k^2pq} \text{ , for antisymmetric modes} \tag{V.24}$$

With: $p^2 = \frac{w^2}{{c_L}^2} - k^2$, $q^2 = \frac{w^2}{{c_t}^2} - k^2$, and $k = \frac{w}{c_p}$, and where, h, k, w, c_L, c_T, and c_p are respectively the plate thickness, the wavenumber, the wave circular frequency, the longitudinal and transverse modes velocities and the phase velocity.

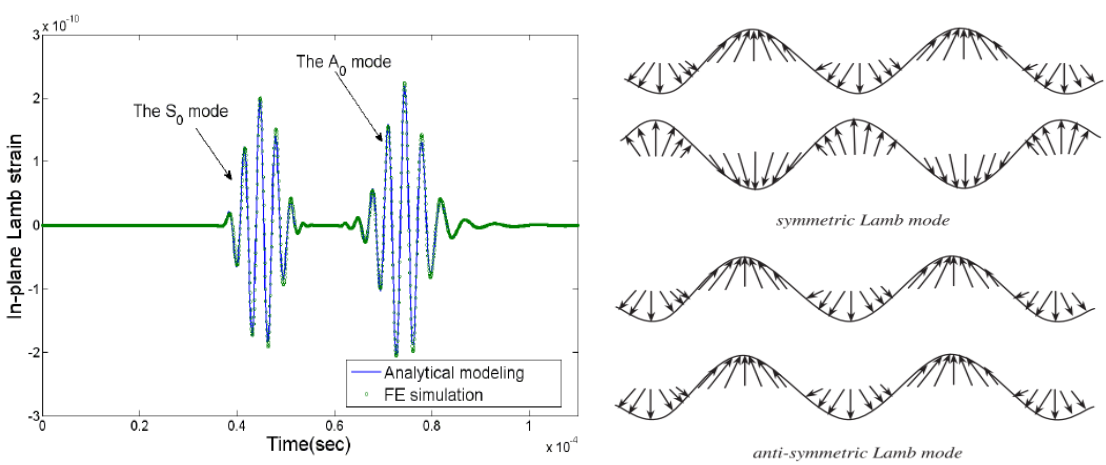

Figure 99 : Left :Signal of Lamb waves from numerical results with a S0 and A0 mode visible [120]

Right : Schematic representation of symmetric and antisymmetric Lamb waves mode [37]

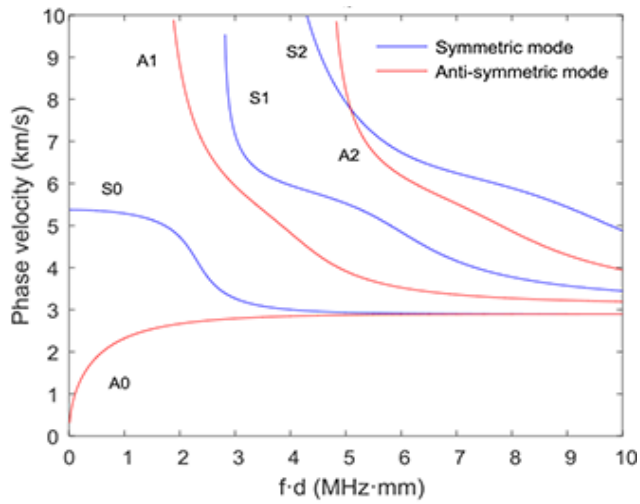

Figure 100 : Typical phase velocity dispersion curves for aluminum

For propagation in an anisotropic medium, the equations are more complicated. Further in the manuscript, guided wave propagation along off-principle planes will be considered. For this reason, the necessary guided wave equations are required for a monoclinic stiffness tensor. The latter is obtained with a rotation along the axis 3 at a chosen angle of the orthotropic stiffness matrix. The wave equations are given by:

$$C_{11}\frac{\partial^2 u_1}{\partial x_1^2}+C_{44}\frac{\partial^2 u_1}{\partial x_2^2}+C_{55}\frac{\partial^2 u_1}{\partial x_3^2}+2C_{14}\frac{\partial^2 u_1}{\partial x_1\partial x_2}+C_{14}\frac{\partial^2 u_2}{\partial x_1^2}+C_{24}\frac{\partial^2 u_2}{\partial x_2^2}$$
$$+C_{56}\frac{\partial^2 u_2}{\partial x_3^2}+(C_{12}+C_{44})\frac{\partial^2 u_2}{\partial x_1\partial x_2}+(C_{13}+C_{55})\frac{\partial^2 u_3}{\partial x_1\partial x_3} \qquad \text{(V.25)}$$
$$+(C_{34}+C_{56})\frac{\partial^2 u_3}{\partial x_2\partial x_3}=\frac{\partial^2 u_1}{\partial t^2}$$

$$C_{14}\frac{\partial^2 u_1}{\partial x_1^2}+C_{24}\frac{\partial^2 u_1}{\partial x_2^2}+C_{56}\frac{\partial^2 u_1}{\partial x_3^2}+(C_{12}+C_{44})\frac{\partial^2 u_2}{\partial x_1\partial x_2}+C_{44}\frac{\partial^2 u_2}{\partial x_1^2}$$
$$+C_{22}\frac{\partial^2 u_2}{\partial x_2^2}+C_{66}\frac{\partial^2 u_2}{\partial x_3^2}+2C_{24}\frac{\partial^2 u_2}{\partial x_1\partial x_2}+(C_{34}+C_{56})\frac{\partial^2 u_3}{\partial x_1\partial x_3} \qquad \text{(V.26)}$$
$$+(C_{23}+C_{66})\frac{\partial^2 u_3}{\partial x_2\partial x_3}=\frac{\partial^2 u_2}{\partial t^2}$$

$$(C_{13}+C_{55})\frac{\partial^2 u_1}{\partial x_1 \partial x_3}+(C_{34}+C_{56})\frac{\partial^2 u_1}{\partial x_2 \partial x_3}+(C_{34}+C_{56})\frac{\partial^2 u_2}{\partial x_1 \partial x_3}$$
$$+(C_{23}+C_{66})\frac{\partial^2 u_2}{\partial x_1 \partial x_2}+C_{55}\frac{\partial^2 u_3}{\partial x_1^2}+C_{66}\frac{\partial^2 u_3}{\partial x_2^2}+C_{33}\frac{\partial^2 u_3}{\partial x_3^2} \qquad \text{(V.27)}$$
$$+2C_{56}\frac{\partial^2 u_3}{\partial x_1 \partial x_2}=\frac{\partial^2 u_3}{\partial t^2}$$

Where C_{ij} are the stiffness components and u_i the displacement vector.

With the listed wave equations, the following guided waves characteristic equations can be obtained:

$$A = D_{11}G_1 \tan(\gamma\alpha_1) - D_{13}G_3 \tan(\gamma\alpha_3) + D_{15}G_5 \tan(\gamma\alpha_5) = 0;\ \text{for the antisymmetric modes} \qquad \text{(V.28)}$$

$$S = D_{11}G_1 \cot(\gamma\alpha_1) - D_{13}G_3 \cot(\gamma\alpha_3) + D_{15}G_5 \cot(\gamma\alpha_5) = 0;\ \text{for the symmetric modes} \qquad \text{(V.29)}$$

Here, $\alpha_{q;q=1,3,5}$ is the solution of the wave equations when the displacement field is of the form: $u_j = U_j e^{i\xi(x_1+\alpha x_3-ct)}$.

With

$$G_1 = D_{23}D_{35} - D_{33}D_{25}$$
$$G_2 = D_{21}D_{35} - D_{31}D_{25}$$
$$G_3 = D_{21}D_{33} - D_{31}D_{23} \qquad \text{(V.30)}$$

And

$$D_{1q} = C_{13} + C_{34}V_q + C_{33}\alpha_q W_q$$
$$D_{2q} = C_{55}(\alpha_q + W_q) + C_{56}\alpha_q W_q$$
$$D_{3q} = C_{56}(\alpha_q + W_q) + C_{66}\alpha_q W_q \tag{V.31}$$

The amplitude ratio V_q and W_q are given by:

$$V_q = \frac{U_{2q}}{U_{1q}} \; and \; W_q = \frac{U_{3q}}{U_{1q}} \tag{V.32}$$

For more details about the guided waves characteristic equations we refer to the book of Nayfeh [69].

Lamb waves are frequently used in the industry to characterize material properties [70], [71], to detect damage in a structure and to locate and to quantify these defects. These waves also have the ability to travel relatively long distances and are therefore frequently used on-site to detect damage in pipelines, for example [36], [37]. They do not require a point by point acquisition, contrary to a C-scan, since all the required information can be obtained via B-scan-like acquisitions. Thanks to Lamb waves, in the industry a single measurement may be sufficient to detect damage. Since it requires access to one side of the sample it is also easier to be used on-site. The simplest application of Lamb waves is to check for generated echoes when damage is encountered.

Nevertheless, many authors [72]–[74] also highlight the strength of an analysis of the dispersions effects of the Lamb waves modes to detect damage. A frequency domain processing is classically done to obtain Lamb wave velocities. Nevertheless, this can be easily performed only when a single wave mode is appearing on the temporal response, or when the different waves are clearly distinguished from each other; clearly not the case in the Figure 101. In the case when multiple Lamb wave modes are detected, a 2D Fourier transform (in time and space) must be applied on the signals [72], [75]. The results are then typically plotted as function of the frequency and the wavenumber. The results typically show distinguishable line patterns, called dispersion curves (Figure 102). The curves can be

used to obtain components of the stiffness tensor of a material by using a methodology similar to the one described in the section V).1).b) but adapted for the guided waves characteristic equations (V.28) and (V.29). Experiment sets-up in immersion [76] or contact [70], [71] for this purpose have been proposed in the literature.

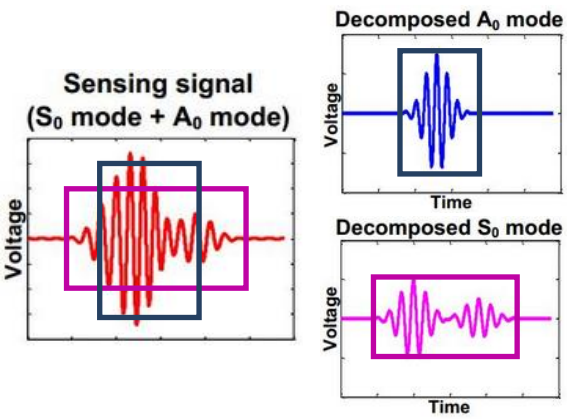

Figure 101 : Decomposition of a Lamb waves signal in A0 and S0 modes [121]

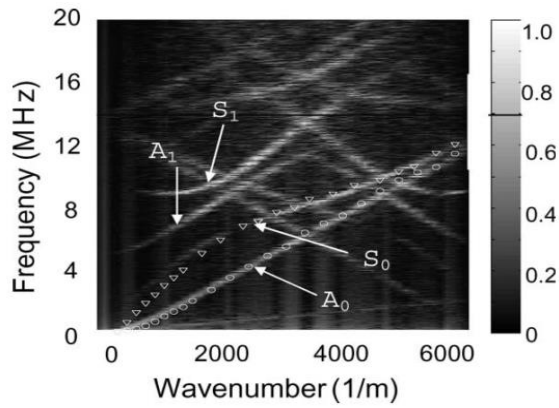

Figure 102 : Results of a 2D-FFT in the wavenumber-frequency

The interaction of Lamb waves with defect may results in a mode conversion effect, as well as a related transmission loss. Indeed, if the defect is considered as an interface, one can easily understand that the incident Lamb waves travelling through the material will undergo an energy re-distribution into multiple Lamb wave's modes. A Lamb mode conversion is for instance clearly shown by Imano et al. [77]. In this study, they considered an aluminum plate with a notch type defect (Figure 103). The three waves observed on the Figure 103-c, were post-processed via a 2D-FFT as shown on the Figure 104. For the incident wave (prior to encountering the defect), only the A0 mode is observed, whereas for the reflected and transmitted waves, S0 and A1 mode appear. Therefore, the A0 mode converts into the S0 and A1 mode in the reported experiment. The authors then propose to consider the amplitude ratio $\frac{S0}{A0}$ for damage quantification.

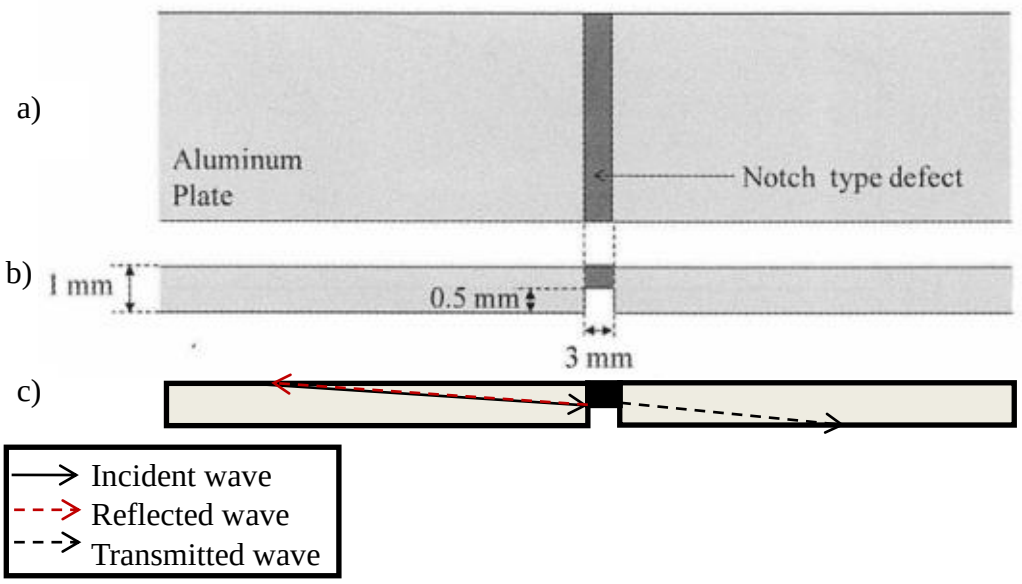

Figure 103 : Schematic representation of the considered aluminum sample with a notch type defect. a) Top observation, b) Side observation, c) Side observation + ultrasonic wave's propagation through the sample (Based on [77])

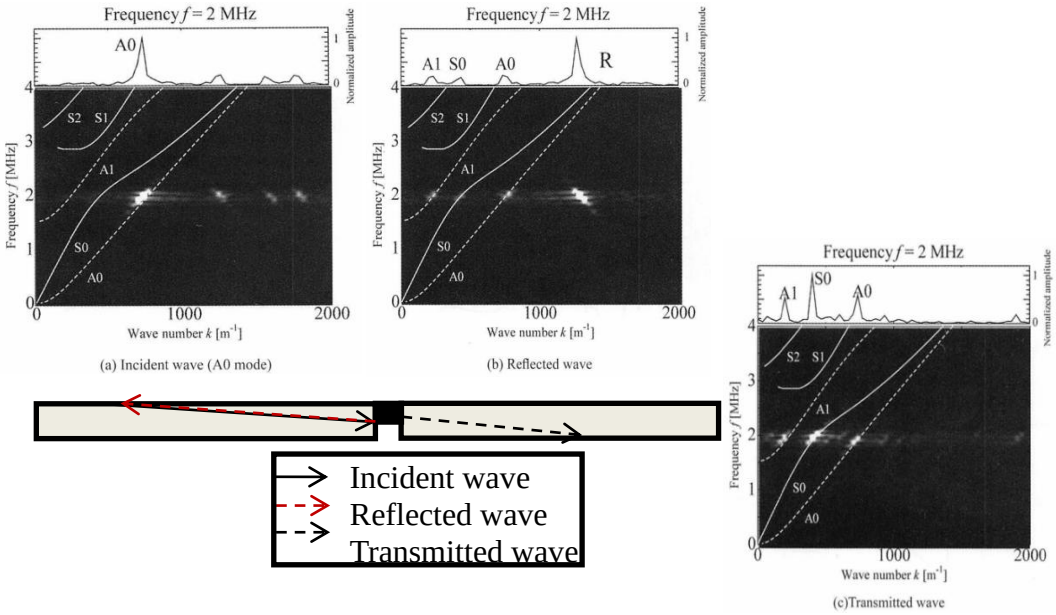

Figure 104 : Side observation of the sample + ultrasonic wave's propagation through the sample. 2D Fourier transform results for the incident, reflected and transmitted wave with the theoretical dispersion curves. (Based on [77])

d) Nonlinear acoustic method

Recently, various experimental researches have been reported on nonlinear acoustic methods and what they can provide to estimate the global damage state of a material [78]–[83]. It was shown that the nonlinearity of the acoustic response increases with increasing damage. Typically, a nonlinear effect will be earlier detected during the degradation of a material than classical linear responses linked to wave velocity, ultrasonic amplitude, rigidity constant, … [83], [84]. The term Nonlinear Elastic Waves Spectroscopy (NEWS) is usually used to name all those methods. As expected with the name of the method, the objective is to investigate the frequency response obtained after a Fourier transform. The acoustic response of the sample can be recorded with a loudspeaker or a laser vibrometer. In his paper Rabe insists on the fact that a laser vibrometer will be much more accurate [80]. The recent literature focuses mostly on applications for composite material (concrete or polymer based composites). Nevertheless the method was also used for characterizing for example the increase of stiffness of metallic alloys by heating treatment [78]. Ostragradsky and Johnson in [85] propose a description of classical nonlinear acoustics that they extend to the study of nonlinear elasticity of rocks and their modeling. The last part of this paper is dedicated to the application of nondestructive evaluation (NDE) of materials. A complementary review of the seminal researched on classical and “non-classical nonlinear acoustics from the 1950’s onwards, can be found in the work of Nizhni Novgorod [86].

If the higher order terms are added into the isotropic elastic equation, a nonlinear description of the elasticity, taking into account hysteresis can be expressed as:

$$\sigma = \int K(\varepsilon, \dot{\varepsilon}) d\varepsilon \tag{V.33}$$

$$K(\varepsilon, \dot{\varepsilon}) = K_0\{1 - \beta\varepsilon - \delta\varepsilon^2 - \alpha[\Delta\epsilon + \varepsilon(t) sign(\dot{\varepsilon}) + \cdots]\} \tag{V.34}$$

With K_0 the linear elastic modulus, β and δ the 2nd and 3st order nonlinear parameter, α the material hysteresis parameter.

Numerous nonlinear acoustic techniques have been developed to measure the material's nonlinearity. Among them two main categories were particularly discussed in the literature : The Nonlinear Wave Modulation Spectroscopy (NWMS) and Nonlinear Resonant Ultrasound Spectroscopy (NRUS) [84]. Another category can be found in the literature : Nonlinear Reverberation Spectroscopy (NRS) [87]. All of these methods can be used in continuous wave mode or in impact mode. In the first case, solicitation is performed using harmonic waves. In the second case, the sample is submitted to an impact investigation. The advantage of using the impact mode is that for a single test, numerous resonance frequencies will be solicited simultaneously [82], [84], [88], which makes the experiment faster. However it has also been shown that the measured resonance frequencies are not perfectly linked to the true physical amplitude in the sample. Because of dynamic effects occuring in the signal, such as a reverberation effect, the real physical amplitude can be hidden when the Fourier transform is applied [82]. Those three NEWS methods will be described in detail further in this section. A graph recalling the three main NEWS methods, with associated references, is seen in Figure 105.

The two first mentioned methods, NRUS and NWMS were investigated in continuous wave mode for three different materials, including the polyamide 66/6 reinforced by woven glass fibers, during the research project discussed in this manuscript. Because a significant share of this work is applied to samples other than this polyamide 66/6 based composite material and because this technique did not successfully evaluated damage in this material, the investigation was not added to the main body of this thesis manuscript but rather in the appendix section 1).

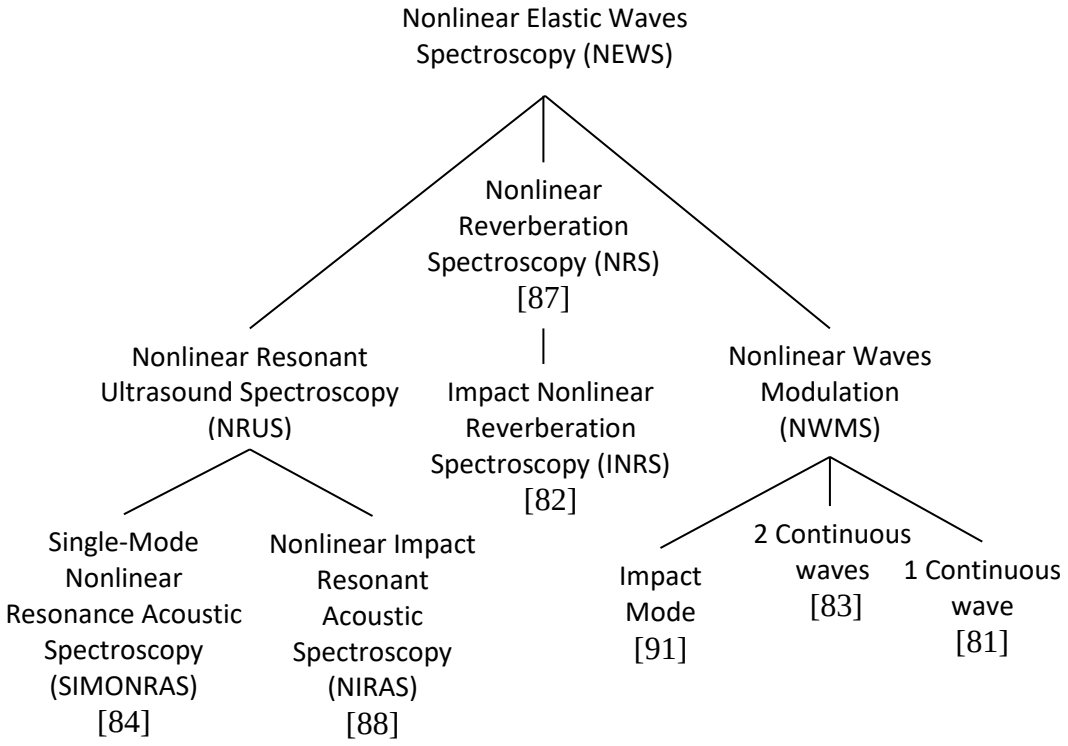

Figure 105 : Schematic representation of the different Nonlinear Elastic Waves Spectroscopy (NEWS) with references for each of them

Nonlinear Resonant Ultrasound Spectroscopy (NRUS)

With this method, the evolution of the resonance frequency with increasing amplitude of the input signal is studied. Indeed, as the damage state in the sample increases, a shift in the resonance frequency is observed in the spectral response with the increase of the amplitude visible as seen in the Figure 106. On this figure, the various plots on each graph correspond to different input amplitudes. On the left a graph for an undamaged sample is plotted and on the right is a graph for a damaged one. As mentioned earlier, this method can be used in continuous mode, named Single Mode Nonlinear Resonance Acoustic Spectroscopy (SIMONRAS), or in impact mode, named Nonlinear Impact Resonance Acoustic Spectroscopy (NIRAS).

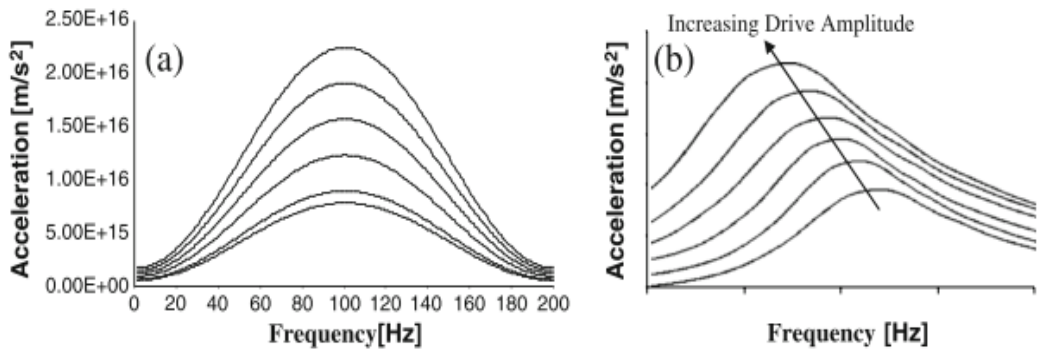

Figure 106 : Schematic spectrum that can be obtain with the NRUS method for an undamaged (left) and damaged (right) sample [83]

It can be shown that the slope of the resonance frequency shift is a function of α, the hysteresis parameter [89]. If the equation of $K(\varepsilon, \dot{\varepsilon})$ described earlier is inserted into the wave equation with β and δ equal to zero and if the nonlinear contribution to the wave solution is computed one can find three relations:

$$\frac{f_0 - f}{f_0} = C_1 * \Delta\varepsilon \tag{V.35}$$

a linear decrease of the resonance frequency for increasing strain levels

$$\Delta\varepsilon = C_2 * \varepsilon^2 \tag{V.36}$$

a quadratic amplitude dependence of the third harmonic the amplitude of the fundamental/resonance frequency, and

$$\frac{\xi - \xi_0}{\xi_0} = C_3 * \Delta\varepsilon \tag{V.37}$$

a linear increase of the modal damping ratio (decrease of the quality factor Q) with the increase of the amplitude, where all the C_i coefficients are function of the α parameter. In other words, any change of the coefficient induces a change in the α parameter. The first relation is considered for this Nonlinear Resonant Ultrasound Spectroscopy method.

Nonlinear Wave Modulation Spectroscopy (NWMS)

The other of the two mainly used nonlinear acoustic methods is the so-called Nonlinear Wave Modulation Spectroscopy. As with the previous method, the NWMS has been used in impact mode (for example : [84], [90]) and continuous mode (for example : [83], [91]). The same observation can be made for the benefits and disadvantages of both methods. Here, the sample is submitted to either two continuous waves, in continuous mode, or one continuous wave and an impact solicitation in impact mode. One of the waves should have a low frequency and the other one a higher frequency. It is often considered that the difference of the two input signals' frequency should be lower than the lowest selected frequency. In impact mode, the impact hammer is used to cover the lower frequency. Aymerich and all [92] used a flexural vibration wave to cover this lower frequency.

When the sample is undamaged, one should observe only peaks that correspond to the input frequency, with of course a decrease of the amplitude. However, when the sample is damaged, various other peaks will appear on the spectrum (Figure 107). They correspond to harmonics of the input frequencies and appear at values of n* f_i, with n: an integer. Modulation between the input frequencies also appear at values of f1 +/- n*f2, they are called sidebands: The amplitude of these new peaks should increase with an increase of the damage in the sample. Specifically, the sidebands' amplitudes can be related to the nonlinear parameter α, β, δ [91] :

	Frequencies	Amplitude
1st order Inter-modulation	f_2 +/- f_1	β*A_1*A_2
2nd order Inter-modulation	f_2 +/- 2*f_1	α*A_1*A_2
2nd order Inter-modulation (For a material with dynamic hysteresis)	f_2 +/- 2*f_1	$C_{\beta\delta}$*$(A_1)^2$*A_2

Table 15 : Relation the nonlinear parameter with the sidebands amplitude and relation of the sidebands frequencies with the input frequencies

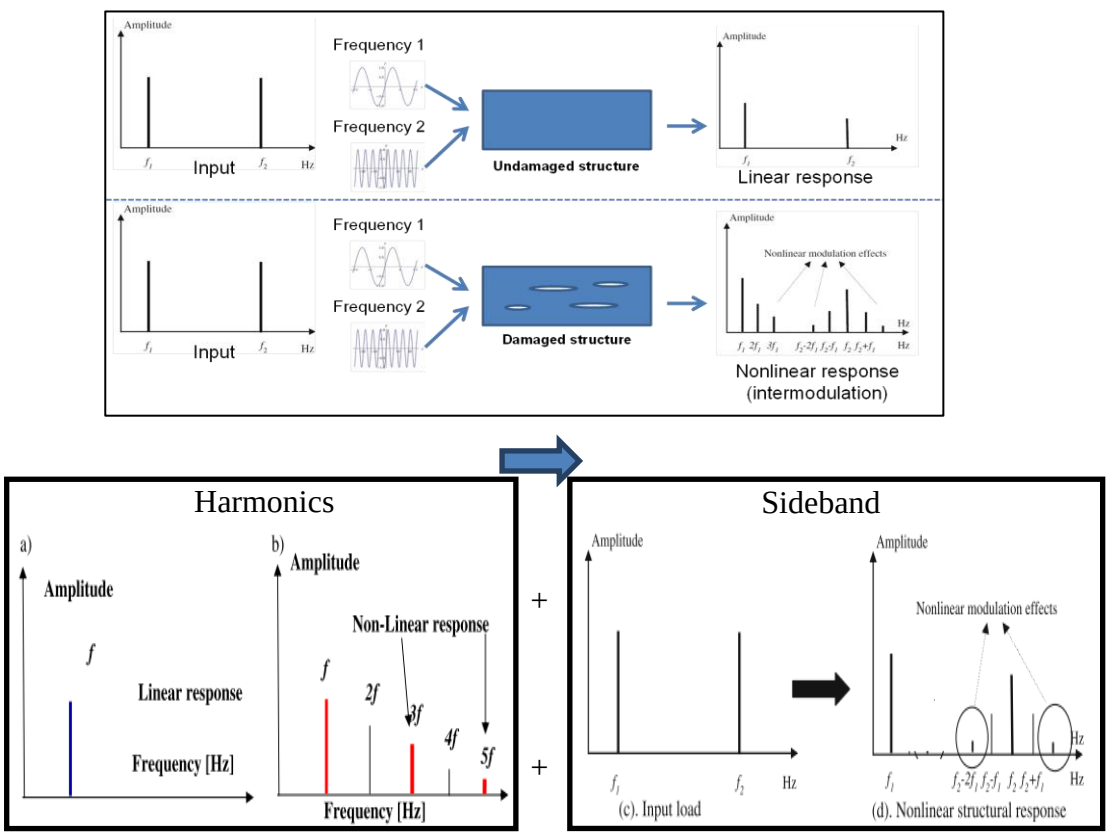

Figure 107 : Schematic representation of the principle of the NWMS technique: spectral analysis of the nonlinear acoustic response of a damaged sample caused by apparition of harmonics and sidebands (Based on [108])

Different damage indicators were proposed for this Nonlinear Wave Modulation Spectroscopy method:

- An indicator based on the energy of the spectrum

$$\alpha \propto \frac{\int E_{HF}^{Received}}{\int E_{HF}^{Emitted} * \int E_{BF}^{Emitted}} \quad (V.38)$$

Avec : $E_{HF}^{Received}$: The energy of the received signal sidebands

$E_{HF/BF}^{Emitted}$: The energy of the emitted signals at high and low frequencies.

- An indicator based on the first order non linearity

$$\beta \propto \frac{A_2}{(A_1)^2} \quad (V.39)$$

Avec : A1 : The amplitude of the fundamental frequency

A2 : The amplitude of the first harmonic

- An indicator K based on the distortion of the response spectrum [93]. Indeed, in the field of audio sound this kind of parameter is used to characterize the quality of an audio amplifier.

$$K = \sqrt{\frac{(A_2)^2 + (A_3)^2 + \cdots}{(A_1)^2 + (A_2)^2 + (A_3)^2 + \cdots}} * 100 \quad (V.40)$$

Avec : A_1 : L'amplitude de fréquence d'excitation fondamentale

A_i : L'amplitude de la (i-éme-1) harmonique

Nonlinear Reverberation Spectroscopy (NRS)

This nonlinear acoustic method studies the reverberation response of a material after the nonlinear input signal is turned off. This method was first introduced by Van Abeele in [87] to compare with the previously discussed SIMONRAS method. They considered that a linear viscous equation can describe the damping of its studied reinforced concrete:

$$x(t) = Xe^{-\xi\omega t}\sin(\omega t - \varphi) \qquad \text{(V.41)}$$

With $\omega = 2\pi f$: the angular frequency, X: the initial amplitude, f: the response frequency, ξ: the modal damping ratio, φ : the phase.

For this method, a curve fitting type identification of those last four parameters is performed on experimental results. They were obtained by vibration signal acquisitions when the input signal is turned off. As it was explained previously, the attenuation depends of the amplitude because of hysteresis effect. So in order to avoid measurement interpretation mistakes, several starting amplitude must be considered. As for the two previous introduced nonlinear acoustic techniques, a continuous wave mode [87] and an impact mode was developed [82]. In the first case, an acquisition is made for each starting amplitude selected and an identification of the four parameters is performed each time. In the impact mode case, Dahlen [82] et al proposed a method that required only one acquisition and tested it by investigating a concrete sample with increasing damage.

Graphs showing the frequency and the modal damping ratio as function of the amplitude are then usually plotted to indicate the increase of the nonlinear effect and therefore the damage growth inside the studied material. This increase is particularly visible on the results of Dahlen et al in Figure 108 for both frequency shift and damping ratio. They also plot results of frequency shifts from NIRAS tests in black on the same figure. However, this was not especially relevant for a direct comparison because NIRAS's results are actually plotted as function of the signal peak amplitude whereas INRS's results are

plotted as function of the acceleration in the z-direction previously computed in COMSOL and matching the experimental set-up. However, they show that both methods detect an increase in the damage state.

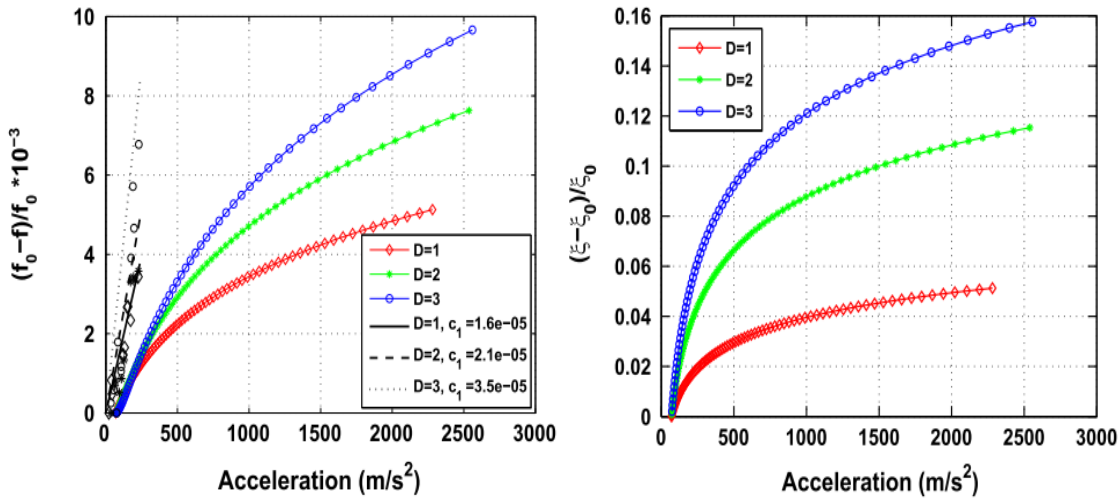

Figure 108 : Numerical results obtained after identification of the attenuation model parameters for concrete

Left : Normalized frequency versus amplitude for samples damaged at different level + results from NIRAS tests performed on the same material, Right : Normalized Modal Damping Ratio versus amplitude for samples damaged at different level [82]

e) Coda waves in Non-Destructive Testing

The investigation of Coda Waves appeared earlier in the field of seismology, they refer to the late arrivals of a response signal. They are the result of multiple wave scattering and act as a fingerprint of the heterogeneity of a seismic wave. As an example, the wave attenuation induced by the scattering process, in addition to the initial absorption effect, has been studied. A review of those studies can be found in [94].

This technique was later considered for nondestructive evaluation of materials, especially of concrete structures. It was extensively demonstrated that the waves are very

sensitive to the weakest change in the material microstructure, such as micro-cracks [95], thermal changes [96], etc . A particular attention must be paid to the input frequency. Indeed, the mesoscopic range of ultrasonic wavelength or the multiple scattering regimes must be considered in order to have a fully reproducible Coda waves propagation (Figure 109). In this regime, the wavelength of the input signal is shorter than the smallest heterogeneity in the considered material. In concrete, this heterogeneity is assumed to be around one centimeter, therefore a frequency range of 150 kHz to 1 MHz is typically considered.

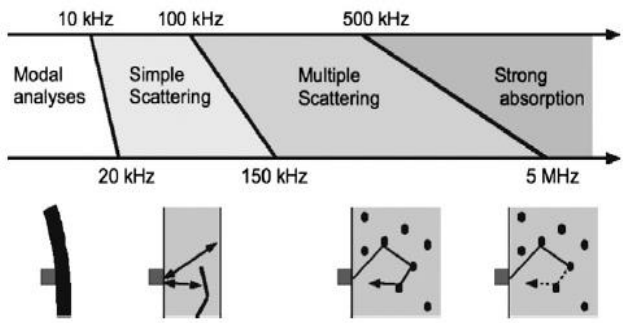

Figure 109 : Schematic representation of the different wave propagation regime [122]

In composite materials however, the considered heterogeneity could be that of full yarns or at a smaller scale the fibers themselves. They have a characteristic size respectively of 0.5 mm and 15 µm, which corresponds to frequencies of 7 MHz and 250 MHz. Because of the attenuation effect it is hard to consider very high frequencies in composite materials. However, papers publish by Livings and al. [96], [97] demonstrate that the acoustic signature of the material is sensitive to small changes in the material for a 1 MHz input emission. One of the major current issues is the lack of sufficiently accurate theoretical work or comparative data. Indeed, the application of the coda wave technique in polymer-based composites is a recent development.

During this research project, coda wave interferometry has been investigated on a woven carbon fiber reinforced polyphenylene sulfide based composite material. Carbon fiber reinforced composite samples were preferred over glass fiber reinforced ones because

of the lower ultrasonic wave attenuation [98]. One of the objectives of this research project is to investigate several ultrasonic NDE methods on composite materials and to try to compare pros and cons. As a consequence, a discussion of this investigation is added in the appendix section 2).

Because Coda waves involve waves that have been scattered multiple times in the structure, the investigation mostly focuses on the late arrival signal, retarded with respect to the initial received signal. As it can be seen on the Figure 110 no difference between the early wave packets of a reference signal and a disturbed one can be observed. However, there appears a phase shift for late wave packets. The main purpose of a Coda wave interferometry study is to measure, based on the observed phase shift, a the relative velocity change induced by a change in the heterogeneity of a material. In order to extract this information, four main waveform comparison techniques can be used. A comparison of those four techniques can be found in [99] and are briefly mentioned below.

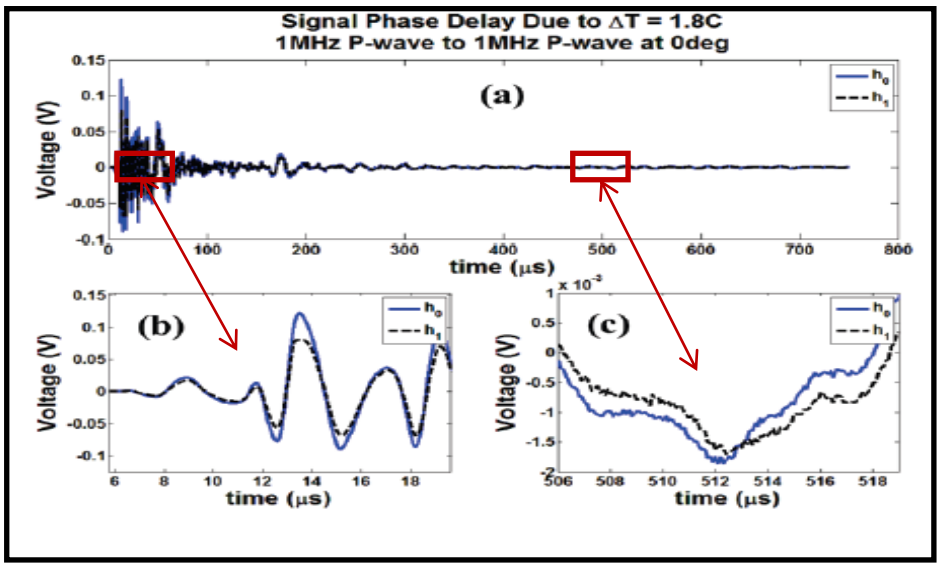

Figure 110 : Signal waveforms collected on a CRFP composite before (h0) and after (h1) an increase of temperature [96]

- The moving window cross-correlation technique

Both the reference signal (without damage) and the perturbed signal (with damage) are cut in time window of length 2*t_w. The perturbed signal is then shifted by a value τ. The correlation coefficient R is computed for every considered τ and for every window.

$$R_{xy}(\tau) = \frac{\sum_{i=t_{c-t_w}}^{t_{c+t_w}} (x_{i+\tau})(y_i{}^*)}{\sqrt{\sum_{i=t_{c-t_w}}^{t_{c+t_w}} (x_{i+\tau})^2} \sqrt{\sum_{i=t_{c-t_w}}^{t_{c+t_w}} (y_i)^2}} \qquad \text{(V.42)}$$

The τ value for which the R coefficient is the highest, frequently named τ_{max} , is then stored for every window. If the change in the signal is only due to small perturbations, such as temperature or minor damage, the evolution of the velocity is constant, as if it's due to a stiffness reduction. This means that $\partial v/v$ is equal to a constant α. It can also be shown that if dv<<v, one can obtain $\partial v/v = \partial t/t$. Since τ_{max} , represents actually dt, α can be measured by plotting τ_{max} function of the central time of the corresponding window. Then by applying a linear regression on this plot, the α's value is directly obtained. Of course, this implies a small perturbation in the signal.

- The moving window cross-spectrum technique

For this technique, the analysis is performed in the frequency domain. First, the cross spectrum between the windowed reference signal, y, and the windowed disturbed one, x, is calculated with:

$$S_{12}(t_c, f) = X(t_c, f)Y^*(t_c, f) \qquad \text{(V.43)}$$

With, X and Y the Fourier transform of respectively x and y and * indicate the complex conjugate

The phase spectrum of the cross spectrum is then calculated. The time delay τ can then be obtained by fitting a line to the phase spectrum.

- The stretching technique

As the name implies, the signal waveform is here stretched by a stretching coefficient $\varepsilon = -\partial v/v$. Indeed, a uniform velocity change in a waveform induces a change closer to a compression or stretching of a signal. This technique could therefore give more stable and accurate results. The stretched signal is calculated as:

$$x_{str}(t) = x(t[1+\varepsilon]) \tag{V.44}$$

The correlation coefficient is then calculated with:

$$R_{xy}(\varepsilon) = \frac{\sum_t x_{str}(t)x(t)}{\sqrt{\sum_t x_{str}(t)^2}\sqrt{\sum_t x(t)^2}} \tag{V.45}$$

- The moving window stretching technique

This technique is similar to the stretching technique but is used for several windowed signals. This technique was proposed in order to increase the stability and the accuracy of the correlation. The relative velocity change $\partial v/v$ is then calculated as an average over all the considered windows.

They are several quantities that have consequently been considered as damage indicators in previous publication such as: the time delay, the peak coherence, the

difference between the maximum and the mean of the cross correlation coefficient, etc. As mentioned before, the coda wave interferometry technique can be conveniently used to measure temperature changes of a material. However, when this technique is considered for non-destructive damage detection, the temporal change of the signal can be caused, in addition to the present damage, by environmental change. One must therefore be very cautious of this issue. Different methods were considered to separate both effects on the resulting signal. For example, Michaels and al. [100] analyzed both the temporal change and the correlation coefficient (or peak coherence) of sample submitted to temperature change, drilling and both. The peak coherence is the maximum of the absolute value of $R_{xy}(\tau)$. They show that when the temperature changes, the delay change linearly as a function of time and the remaining correlation coefficient decreases a slightly function of time (from 1 to 0.75). However, after drilling, the remaining correlation coefficient drops more significantly (from 1 to 0.4). Zhang and al [101], proposed to consider two samples for the Coda Waves Interferometry tests. One is submitted to environmental change and damage growth and the other is submitted to environmental change only.

f) Synthesis of the Non Destructive Evaluation method review

Based on this review, it was decided to investigate the composite specimens presented in section IV)-4) first by using ultrasonic C-scan as a common reference in industry. Then, the method aimed at calculating the stiffness components through phase velocity measurements is considered. Indeed, it could provide a complete description of the anisotropic evolution of damage in the samples. This is of critical interest to link the effect of the mechanical solicitation to the residual properties of the investigated specimens. It can consequently quantify the severity of the induced damage.

Then, its convenience for on-site implementation, as well as the capability to analyze large structures, convinced to more deeply investigate guided wave based methods, which could, by using the direct analysis of the transmitted waves or the investigation of the dispersive wave modes, give a clear and practical estimation of the damage level.

Compared to the first mentioned method, it can be used without an optimization procedure and can consequently provide results more quickly to an NDT specialist.

The aforementioned nonlinear acoustics based methods and Coda Waves Interferometry have been investigated during this project. However, they were not used for specific analysis of induced damage in samples of polyamide 66/6 reinforced by woven glass fibers but rather in other composites, reinforced with woven fibers. For this reason the investigations dedicated to those two methods are presented in the appendix and may be considered as complementary results to the main body of this thesis.

2) Ultrasonic C-scan in transmission

Ultrasonic imaging was performed on all tested samples to investigate the overall damage state of the samples cut at 0° and 45°. Classical ultrasonic 2D C-scans in transmission were performed using a 5 MHz frequency transducer, the maximal amplitude of the ultrasonic signal is measured and recorded at each point of the scanned area with a spatial resolution of 0.5 mm. It is then plotted in Figure 111 for both considered sample configurations. It is worth noting that the values reported in this figure are the actual values of the ultrasound amplitude's signal without any normalization.

As illustrated in Figure 111-a related to the samples tested at 0° from the warp direction, the attenuation of the ultrasound amplitude's signal remains low and a very slight difference, if any, was noticed when increasing the applied stress level from 0 to 92.6% $\boldsymbol{\sigma_{UTS0°}}$. For the sample in 45°, the Figure 111-b shows the evolution of amplitude attenuation (C-scan images) between the unloaded state and the ultimate state level prior failure (92.6% $\boldsymbol{\sigma_{UTS45°}}$). Two damage zones were actually observed macroscopically and the related high attenuations in the signals were associated to the fibers buckling and the local delamination. In addition, the low signal attenuations observed at the border of the samples were clearly induced by a well-known border effect and were not caused by the mechanically induced damage.

As a partial result, one may already conclude that the classical ultrasonic C-scan imaging, as applied in this study, is only suitable for detecting the macroscopic damage in tested composite samples. It appears as a method which is neither reliable nor accurate for the detection of microscopic damage and the related stiffness reduction in the samples.

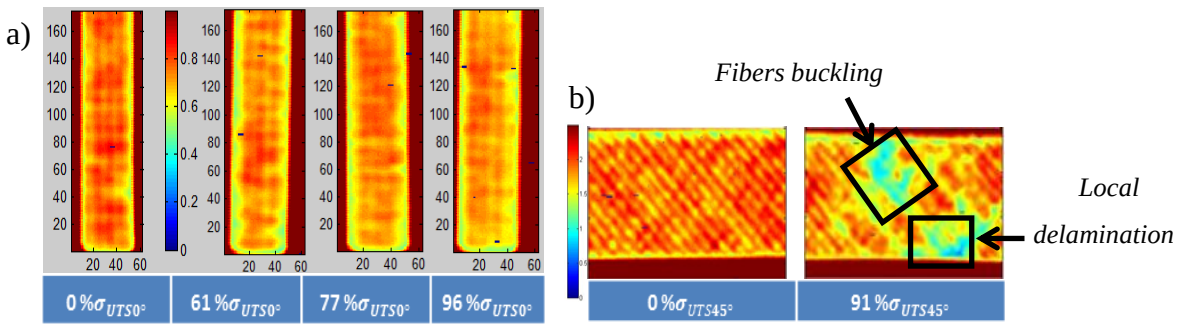

Figure 111 : Preliminary C-scan results on 2/2 twill weave fabric reinforced polyamide composite previously loaded in tension with different amplitude. (a): Samples in 0° configuration ; (b): Samples in 45° configuration. For the latter, besides the large damage zones, one can easily distinguish the 45° orientation of the yarns.

3) Stiffness tensor components determination

This section is dedicated to the application of the stiffness components measurement method on the studied composite. The experimental procedure is discussed in a first subsection. This include a quick analysis of the capability of the Levenberg-Marquard algorithm to find the correct stiffness tensor as well as first results obtained on bigger undamaged plates in 0° and 45° configurations. Then, the evolution of the tensor when samples are submitted to increasing tensile stress level is analyzed for both configurations. Finally, proposed scalar damaged indicators are used, in a final subsection, to quantify the global state based on the results obtained in this section.

a) Description of the experimental procedure and first analysis

Preliminary remarks and first results on undamaged samples

Here, two samples of 150*100*1.53 mm are first investigated in the condition as they have been received. The first sample is in a 0° configuration whereas the second is in the 45° configuration. The principle of this method was presented in section V)-1)-b). Recall that the objective is to compute the stiffness components of a given sample by recording the time of flight while varying the angle of incidence. More precisely, the difference between the TOF with the sample and without the sample (only in water) is measured. For an orthotropic sample, measurements must be done on three principle planes to obtain the nine stiffness components. However, here, two principle planes were considered for the Markham's method that considered bulk waves in transmission. Indeed, the tested sample is too thin, therefore in the 1-2 plane the involved waves are actually guided waves. They are described by other sets of equations that can be found in section V)-1)-c). The experimental set-up must be changed accordingly to generate and measure the phase velocities. For the samples in the 45° configurations, the ultrasonic wave will not propagate in the plane 1-3 and 2-3 but in planes named X_1-3 and X_2-3 respectively oriented at 45° from the two aforementioned planes. The considered propagation planes are indicated in Figure 112-a and b for respectively the 0° and 45° configuration.

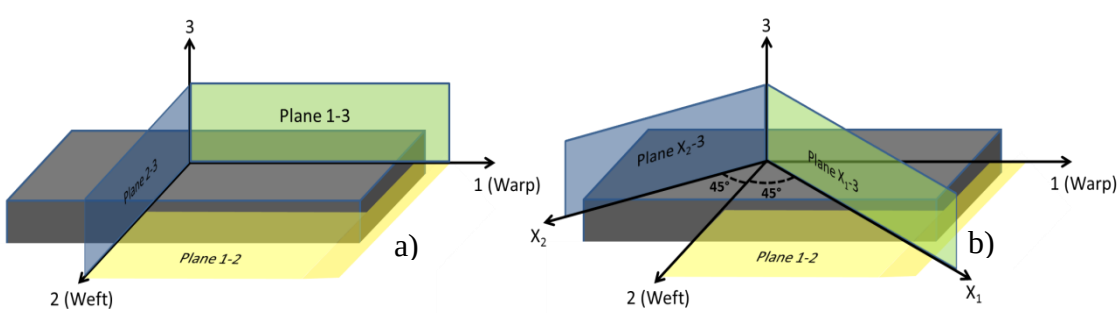

Figure 112 : Schematic representation of the different propagation planes of ultrasonic waves. (a) Propagation planes in the 0° configuration, (b) Propagation planes in the 45° configuration.

All the acquisitions were done at Georgia Tech Lorraine using a customer-designed immersion scanner, visible in Figure 113, fabricated by *Inspection Technology Europe BV*. The pulse is emitted by a dual pulser-receiver DPR500 made by *JSR ultrasonics*. The experimental data are acquired with *Winspect* software and are post-processed in *Matlab*. Two immersion *Panasonic* transducers with a central frequency of 2.25MHz are used in order to satisfy the homogenous media hypothesis. The shape and the spectrum of the emitted pulse are represented on the Figure 114. It can be noted that the actual emitted pulse, as is, frequency is 2.1 MHz.

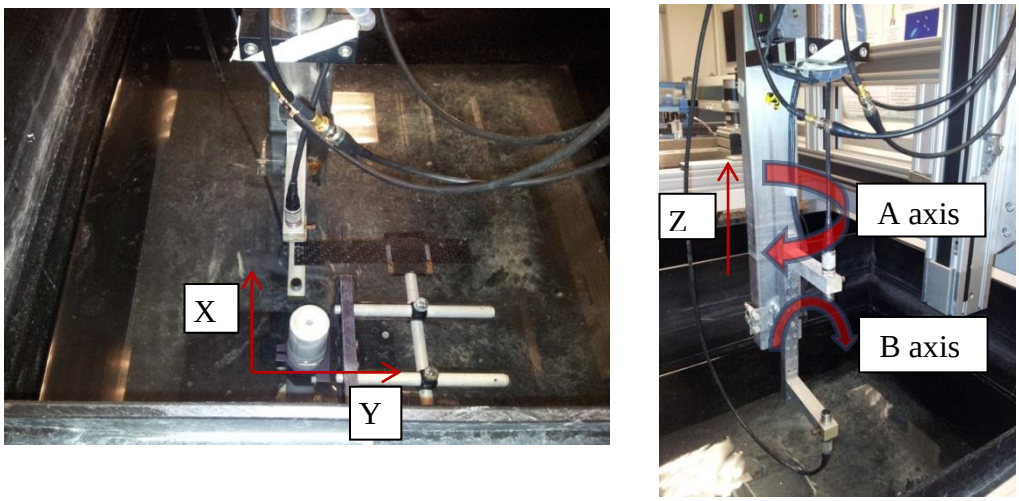

Figure 113 : LUNE lab's 5 axis ultrasonic robot from Inspection Technology

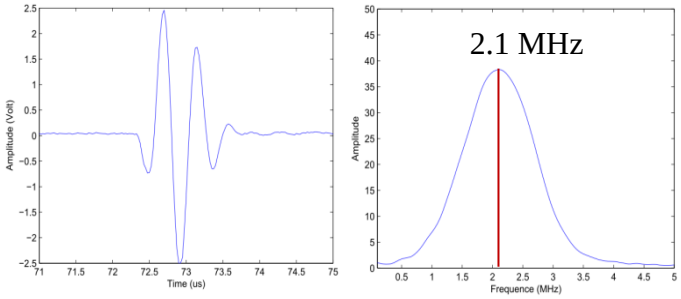

Figure 114 : Emitted pulse shape (Left) and spectrum (Right) for a 2.25MHz centered frequency transducer; The experimentally mesured central frequency is about 2.1 MHz

Experimental procedure for the plane 1-3 and 2-3

Phase velocities measurement in the 1-3 and 2-3 planes were made using the method proposed by Markham. Time of flight measurement in the water without the sample was performed and is used as a reference. The distance between the emitter and the receiver is about 11.6 cm. The wave take about 78.44 us to propagate in the water (Figure 115), it can be easily deduced that the velocity of wave in water is about 1478.8 m/s. This is close to the value that can be found in the literature, which is of 1482.343 m/s in 20°C pure water.

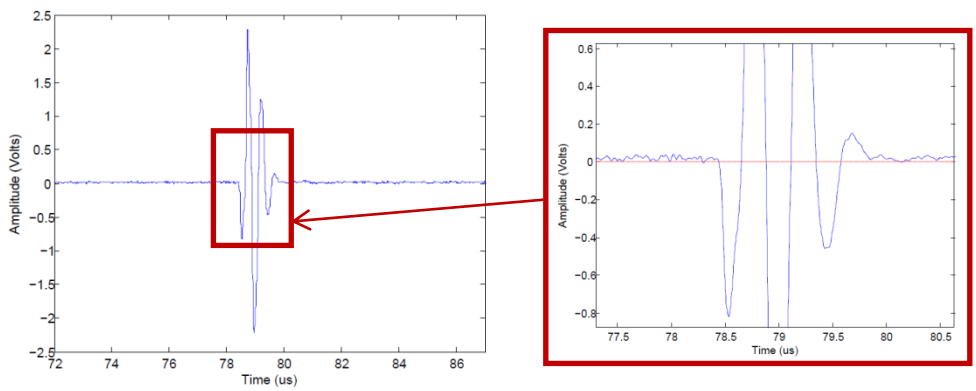

Figure 115 : Response signal of a wave traveling in water (without the

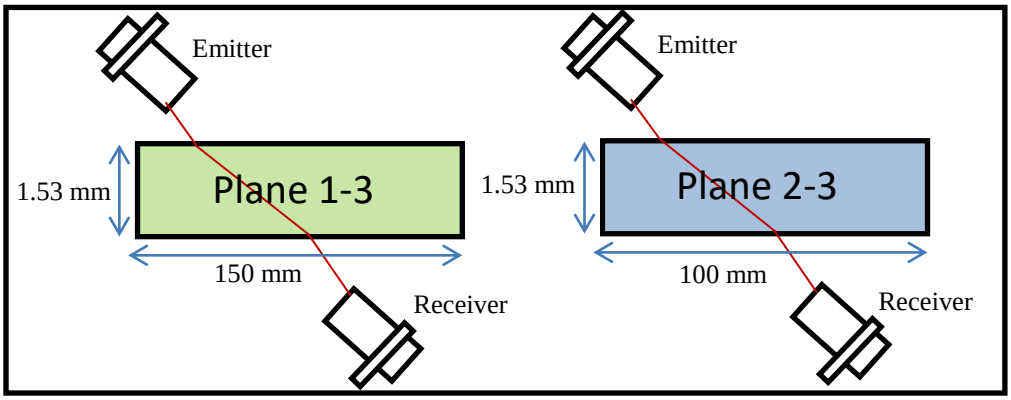

Figure 116 : Schematic representation of the two planes of interest. The plane 1-3 on the left and 2-3 on the right

The sample is then added to the experimental set-up and measurements are made in the planes 1-3 and 2-3 of the sample as depicted in Figure 116. The present subsection (a) will only considered undamaged samples. Note that on both signals, i.e. with and without the sample, the time of flight is actually measured on the first intersection of the signal with the axis of zero amplitude in order to accurately obtain the velocity of the different wave modes. This is easily performed here because of the measured ultrasonic centered on 0 Volts. But when this is not the case, one can measure the time of flight on each first positive peak. This leads to a measured time of flight of 78.65us when the wave travels in water only for a velocity of 1478.8 m/s. This value will be considered for the further stages of the study.

In order to have an accurate computation of the stiffness tensor, a large number of experimental results are necessary. However, wave mode mixing in the recorded signal can make the quasi transversal time of flight measurement difficult. It may possibly lead to inaccurate computation of the mode propagation velocities. In order to be sure of the presence of additional modes, it is necessary to visualize the transmitted signal by varying the incidence angle. This will induce the progressive appearance and disappearance of additional modes. The modes can also be made visible on the spectral response of the transmitted signal. As an example, the transmitted signal and associated spectral response signal after propagating through a pristine composite sample are represented for 0° and 13° angles of incidence in Figure 117. The same information is also plotted on the same figure for a wave propagating only in water for reference purposes. The identified additional quasi transversal mode is circled in red in the 13° incidence angle time signal. This mode also has a visible influence on the spectral response. A full set a quasi-longitudinal and quasi-transversal modes are then acquired for the two chosen principle planes.

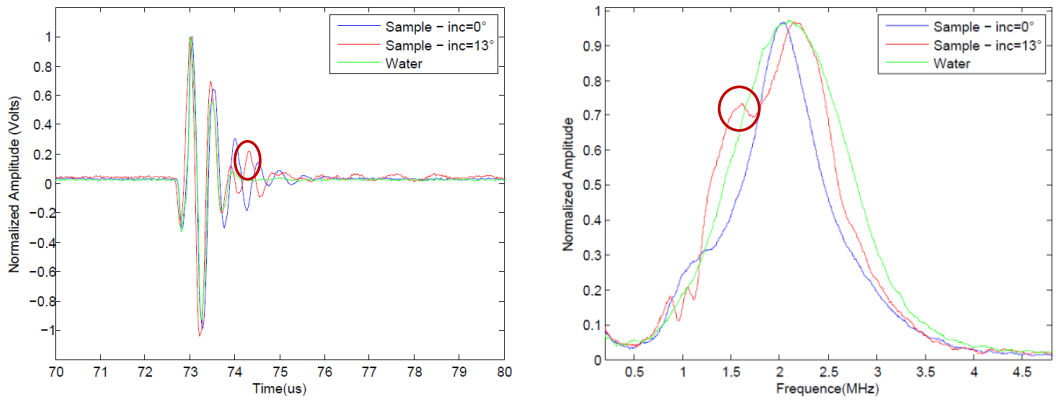

Figure 117 : Transmitted signal (left) and associated spectral response (Right) propagated in an undamaged sample for incidence angle of 0° and 13°. Information for a signal propagated only in water was added for comparison purpose

Then, the velocity of every wave is computed with the following equations explained earlier:

$$\theta_r = \text{atan}\left(\frac{\sin(\theta_i)}{\cos(\theta_i) - \frac{V_0 \delta_t}{e}}\right) \tag{V.46}$$

$$V_p = \frac{\sin(\theta_r) * V_0}{\sin(\theta_i)} \tag{V.47}$$

Experimental procedure for the plane 1-2

Now for measurements in the 1-2 plane of the tested samples an experimental set-up (Visible in Figure 118) in immersion using two transducers in pitch-catch mode, both at a chosen incidence angle, can be used to obtained the phase velocities [76], [102]. For each azimuthal direction of propagation (ψ) in the 1-2 plane, the incidence angle is adjusted to find the same guided wave mode at every acquisition. The phase velocities are then calculated with the use of the Snell's law with $\theta_r = 90°$ i.e.:

$$V_{LWp} = \frac{V_0}{\sin(\theta_i)} \tag{V.48}$$

This experimental set-up is visible in Figure 118.

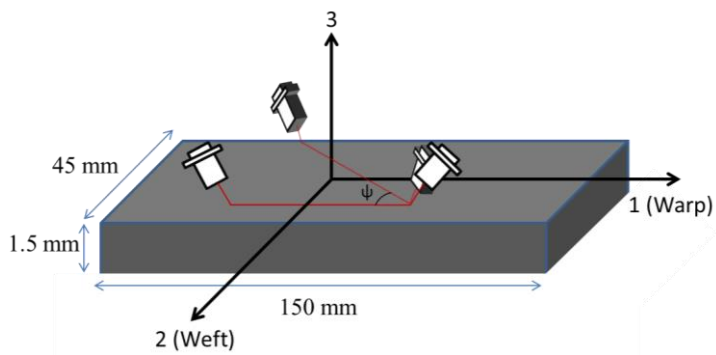

Figure 118 : Experimental set-up for measurement in the plane 1-2

Measurements in those three planes give phase velocities for different propagation directions in the tested sample. All the experimental data are then processed in *Matlab*, through procedures developed for this study, to compute the rigidity constants. The Christoffel equation are used to post-process phase velocities measured in planes 1-3 and 2-3, whereas the guided waves characteristics equations are used to post-process the phase velocities measured in the plane 1-2. The program uses the Levenberg-Marquardt algorithm function available in *Matlab*.

Preliminary analysis on undamaged samples

The algorithm is initialized with an estimation (initial guess) of the stiffness tensor. This must be relatively close to the real solution to avoid local, i.e. false, minima. This is why the complete stiffness tensor of a woven glass fabric/polyamide was computed. The homogenization theory [103] was used on a composite with a woven fabric. The yarns' size used was obtained from the previously discussed microstructural analysis in chapter IV). The computation was performed for a composite oriented along the warp direction. Then the tensor was rotate, along the third axis, at 45° to consider sample oriented at 45° from

warp direction. The numerically computed rigidity components for both 0° and 45° configurations are indicated in the Table 16.

	C_{11}	C_{12}	C_{13}	C_{22}	C_{23}	C_{33}	C_{44}	C_{55}	C_{66}
0° - Stiffness Components (GPa)	20	2.1	1.5	20	1.5	4.5	2.3	1.3	1.3
45° - Stiffness Components (GPa)	13.3	8.7	1.5	13.3	1.5	4.5	8.9	1.3	1.3

Table 16 : Numerical stiffness components for the 0° and 45° configurations obtained by periodic homogenization courtesy of Francis Praud

In order to improve the efficiency and get rid of numerical issues when using the Christoffel equation as is, in the optimization algorithm, it is better to re-write the equation as a cubic equation. The three roots of this cubic equation are then determined with the Cardan's solution of a cubic equation as:

$$\rho {V_L}^2 = 2\sqrt{\frac{\alpha}{3}}\cos\left(\frac{\varphi}{3}\right) - \frac{\alpha}{3} \tag{V.49}$$

$$\rho {V_{T1}}^2 = 2\sqrt{\frac{\alpha}{3}}\cos\left(\frac{\varphi + 2\pi}{3}\right) - \frac{\alpha}{3} \tag{V.50}$$

$$\rho {V_{T2}}^2 = 2\sqrt{\frac{\alpha}{3}}\cos\left(\frac{\varphi - 2\pi}{3}\right) - \frac{\alpha}{3} \tag{V.51}$$

Where

$$\varphi = arcos\left(\frac{-b}{2 * \left(\frac{a}{3}\right)^{\frac{3}{2}}}\right) \tag{V.52}$$

$$a = \frac{\alpha^2}{3} - \beta \tag{V.53}$$

$$b = \gamma - \frac{\alpha\beta}{3} + 2(\frac{\alpha}{2})^3 \quad \text{(V.54)}$$

$$\alpha = -(G_{11} + G_{22} + G_{33}) \quad \text{(V.55)}$$

$$\beta = -({G_{12}}^2 + {G_{13}}^2 + {G_{23}}^2 - G_{11}G_{22} - G_{11}G_{33} - G_{22}G_{33}) = -(G_{11} + G_{22} + G_{33}) \quad \text{(V.56)}$$

A brief study of the relative difference between the results obtained using this velocity computation equations and the resolution of the eigenvalue problem was performed. The case of an orthotropic sample was considered. More specifically, the stiffness matrix considered was previously computed via periodic homogenization as an initial guess for the optimization algorithm. Phase velocities values of QL, QT1 and QT2 were calculated for a set of refraction angles from 0 to 360° both with the resolution of the eigenvalue problem and the Cardan solution of a cubic equation. The averages of the relative difference over the 360° refraction angle were indicated in the table below for each wave mode:

Quasi-Longitudinal	**Quasi-Transversal 1**	**Quasi-Transversal 2**
$3.7*10^{-15}$ %	$5.8*10^{-8}$ %	$5.8*10^{-8}$ %

Table 17: Average relative difference between the two computational methods of the wave mode velocities

It is seen that the two calculation methods give very close results. This validates the use of the Cardan's solution of a cubic problem to compute the numerical values of wave mode phase velocities. Nevertheless, for the reader's information, plots of the relative difference function of the refraction angle can be seen in Figure 119.

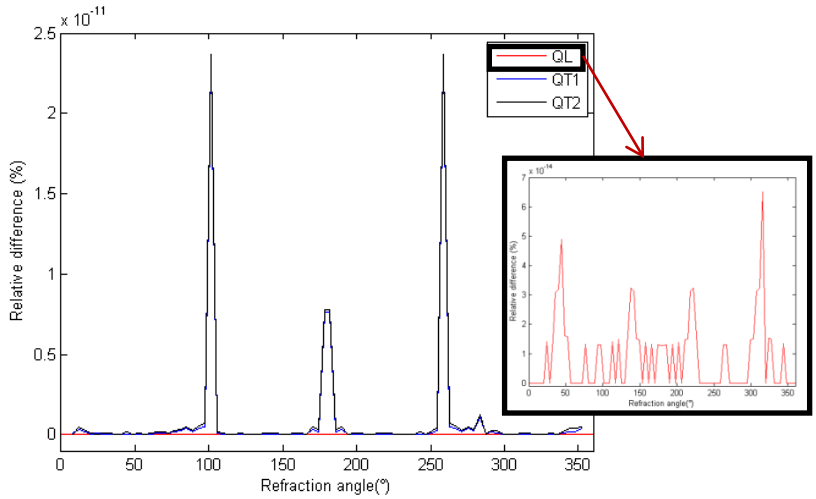

Figure 119 : Relative difference between the velocities values obtains with two considered calculation method

With the computation of velocities for a given plane, one can calculate the associated incidence angle by means of Snell's Law:

$$\theta_i = \mathrm{asin}(\sin(\theta_r) * \frac{V_0}{V_p}) \qquad \text{(V.57)}$$

The evolution of the different phase velocities of acoustic modes and the refraction angles can be plotted as function of the incidence angle. This gives very useful information about the experimental results to be expected. Such figures are also necessary to distinguish the longitudinal mode from a transversal one when the incidence angle is close to the first critical angle (i.e. when the longitudinal mode cannot propagate in the sample).

Numerical results for waves that propagate in the plane (1-3) and (2-3) are represented in Figure 120 and Figure 121 respectively. The stiffness matrix obtained with periodic homogenization theory is still considered. Experimental velocities are also plotted on the same graph to identify the wave modes that propagate function of the incidence angle.

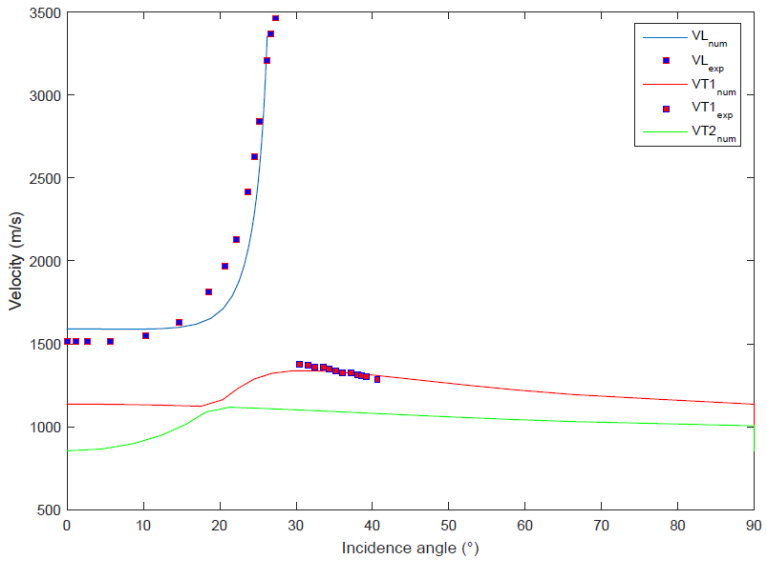

Figure 120 : Comparison of numerically and experimentally determined propagation wave velocities in the plane (1-3). The experimental values are represented by points whereas numerical values are represented in continuous line.

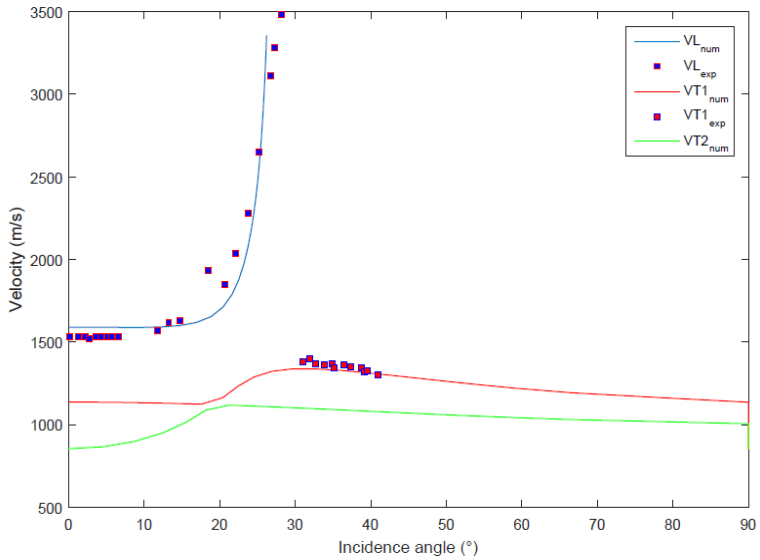

Figure 121 : Comparison of numerically and experimentally determined propagation wave velocities in the plane (2-3). The experimental values are represented by points whereas numerical values are represented in continuous line.

It was found that quasi-longitudinal and quasi-transversal 1 mode velocities were measured in the two planes 1-3 and 2-3. In fact, the experimental velocities exhibit a good correlation with the numerical ones for both modes. This result indicates that the calculated stiffness tensor is a good choice for the initialization of the algorithm.

The dispersion curves of the woven glass fibers reinforced PA66/6 for waves propagating in the 1-2 plane along the fibers axis was computed using the *Disperse* software. They are visible in Figure 122. Those curves are necessary in order to know what mode is propagated in the material for the chosen configuration. The frequency of every recorded signal is carefully measured to compare the experimental results with numerical dispersion curves. The mode S2 was found to propagate in the 1-2 planes. It is worth mentioning that for the considered frequency range, the mode seems to be relatively little dispersive. This made the measurement of the phase velocity and the calculation of the stiffness components easier. Indeed, in order to simplify the optimization procedure, the frequency is fixed to 2.1 MHz, as measured from the frequency spectrum of the propagated signal.

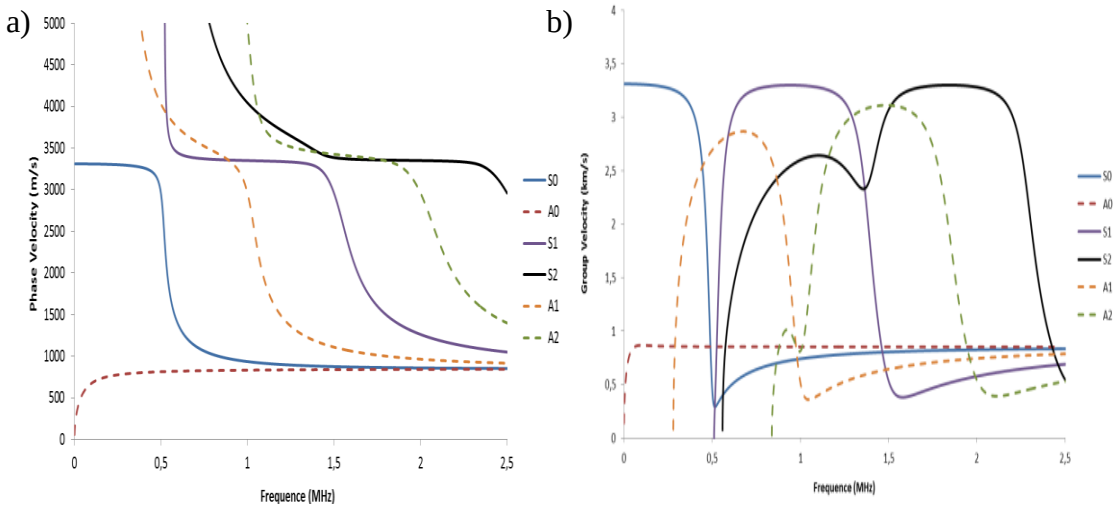

Figure 122 : Dispersion curves computed with the *Disperse software* for guided wave propagation in a 1.53mm thick studied composite along the fibers direction. (a) Phase Velocities, (b): Group Velocities.

Then, the phase velocity of this S2 mode is numerically computed, for the experimentally measured frequencies, as a function of the direction of propagation in the 1-2 plane from 0° to 45° from the warp direction. To do so, the stiffness tensor is rotated along the 3 direction by the angle of the considered propagation direction. This result is plotted in Figure 123 with the experimental velocities measured for the sample in the 0° configuration. As for the acquisitions in plane 1-3 and 2-3, the experimental and numerical phase velocities showed good correlation. The difference in velocity appears as a shift for all the considered angle of propagation. This indicates that the numerical stiffness tensor determined by periodic homogenization is underestimated in comparison with the real sample elastic behavior.

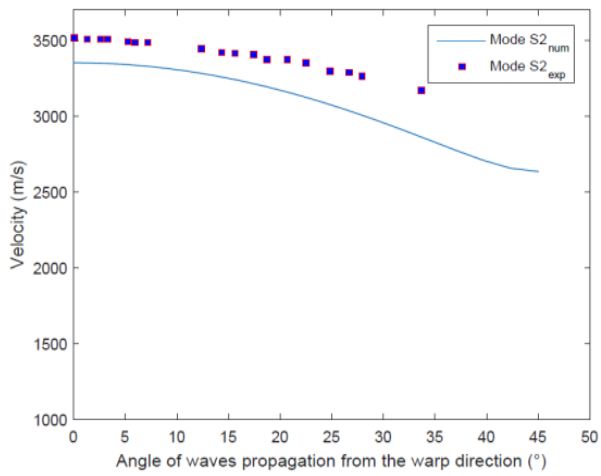

Figure 123 : Comparison between experimental and numerical phase velocities for different propagation direction in the 1-2 plane.

Investigation of the optimization algorithm robustness to input parameters

Before using the optimization algorithm on experimental data, its robustness must be evaluated. The most critical parameters are its sensitivity to the number of experimental input data, the boundary limits of each stiffness constants and the initial guess of the solution. In order to investigate its robustness, a set of simulated ultrasonic wave velocities were calculated. Both the optimized stiffness components and their associated confidence

intervals are given for each set of simulated velocities. As mentioned above, the Christoffel equation (V.9) is used for the plane 1-3 and 2-3 and the guided waves characteristic equations (V.28) and (V.29) are used for the plane 1-2. In a first attempt, the velocities for the 3 wave modes were calculated for refraction angles from 0° to 70°, with a step of 2°, for the 2 main principle planes 1-3 and 2-3. This means 36 values for each wave mode, for those two planes or 216 values in total. In addition, the S2 phase velocities were calculated between 0° and 45°, with a step of 2°, based on the curve visible in Figure 123. As a matter of fact, in this way 23 values were added for the optimization process. The lower and upper bounds of the stiffness components were set to respectively 0.1 GPa and 200 GPa for each component.

As initial guess, the expected stiffness matrix with a perturbation of 20%, 50%, 100%, 200%, 500% and 1000% is considered. The initial guess is then always an orthotropic matrix. The results are summarized in the Table 18. It can be noted that even for large deviation of the initial guess from the expected solution (x10), the accurate solution is always found.

A next attempt was made with an initial guess that is not an orthotropic matrix. First, the initial guess is chosen as 20GPa for each component, and then an isotropic stiffness matrix is considered. The other parameters are unchanged. The initial guess and the resultant optimized components are given in the Table 19. For the first initial guess tested, the algorithm is not even able to start and find a new solution. However, when the isotropic matrix is considered as initial guess, the algorithm is able to find the correct solution. The optimization is then performed with an initial guess that is the isotropic matrix multiply by 10: the algorithm can still find the accurate solution.

	C_{11}	C_{12}	C_{13}	C_{22}	C_{23}	C_{33}	C_{44}	C_{55}	C_{66}
Expected + 20%	20 (0.1e-3)	2.1 (0.2e-3)	1.5 (0.2e-3)	20 (0.1e-3)	1.5 (0.2e-3)	4.5 (0.03e-3)	2.3 (0.04e-3)	1.3 (0.02e-3)	1.3 (0.02e-3)
Expected + 50%	20 (0.3e-3)	2.1 (0.7e-3)	1.5 (0.5e-3)	20 (0.4e-3)	1.5 (0.5e-3)	4.5 (0.1e-3)	2.3 (0.1e-3)	1.3 (0.07e-3)	1.3 (0.08e-3)
Expected + 100%	20 (0.07e-1)	2.1 (0.1e-1)	1.5 (0.1e-1)	20 (0.08e-1)	1.5 (0.1e-1)	4.5 (0.03e-1)	2.3 (0.02e-1)	1.3 (0.01e-1)	1.3 (0.01e-1)
Expected + 200%	20 (0.08e-2)	2.1 (0.1e-2)	1.5 (0.03e-2)	20 (0.02e-2)	1.5 (0.01e-2)	4.5 (0.01e-2)	2.3 (0.08e-2)	1.3 (0.1e-2)	1.3 (0.03e-2)
Expected + 500%	20 (0.09e-3)	2.1 (0.2e-3)	1.5 (0.1e-3)	20 (0.1e-3)	1.5 (0.2e-3)	4.5 (0.03e-3)	2.3 (0.03e-3)	1.3 (0.02e-3)	1.3 (0.02e-3)
Expected + 1000%	20 (0.2e-3)	2.1 (0.4e-3)	1.5 (0.3e-3)	20 (0.2e-3)	1.5 (0.4e-3)	4.5 (0.1e-3)	2.3 (0.7e-4)	1.3 (0.4e-4)	1.3 (0.4e-4)

Table 18 : Identified stiffness components for different orthotropic stiffness tensor as initial guess of the solution. 239 velocity values are used as an input

The algorithm appears to be very reliable in finding accurate solution for various initial guesses; even when the initial values insinuate a different symmetry. Nevertheless, the mentioned first tests are insufficient to evaluate the efficiency of the considered optimization algorithm for values obtained from experiments. Indeed, during experimental acquisitions the time of flight of the quasi-transversal wave mode 2 usually cannot be measured for plane 1-3 and 2-3. In addition, the number of incidence angles that can be considered before wave modes vanish are less important as it can be seen in Figure 120, Figure 121 and Figure 123. A new set of simulated ultrasonic wave velocities is now computed based on the mentioned experimental observations. In order to account for experimental errors during the time of flight measurements, a random perturbation up to 5% is applied on all the new wave velocities. Optimization tests similar to those performed earlier on were then carried out. The obtained optimized stiffness constants and their

associate confidence interval are summarized in the Table 20 and Table 21. The results are the average values over 10 computations.

	C_{11}	C_{12}	C_{13}	C_{22}	C_{23}	C_{33}	C_{44}	C_{55}	C_{66}
Initial guess	20	20	20	20	20	20	20	20	20
Results	20	20	20	20	20	20	20	20	20
	(4.7e-3)	(3.1)	(1.7)	(6.2)	(4.0)	(3.5)	(3.0e-3)	(2.1e-3)	(3.5)
Initial guess	20	2.1	2.1	20	2.1	20	8.9	8.9	8.9
Results	20	2.1	1.5	20	1.5	4.5	2.3	1.3	1.3
	(0.1e-3)	(0.2e-3)	(0.2e-3)	(0.1e-3)	(0.1e-3)	(3e-3)	(3e-4)	(2e-4)	(2e-4)
Initial guess	200	21	21	200	21	200	89	89	89
Results	20	2.1	1.5	20	1.5	4.5	2.3	1.3	1.3
	(0.06e-2)	(0.2e-2)	(0.09e-2)	(0.07e-2)	(0.09e-2)	(0.01e-2)	(0.02e-2)	(0.01e-2)	(0.01e-2)

Table 19 : Identified stiffness components for different isotropic stiffness tensor as initial guess of the solution. 239 velocity values are used as an input

	C_{11}	C_{12}	C_{13}	C_{22}	C_{23}	C_{33}	C_{44}	C_{55}	C_{66}
Expected + 20%	21 (0.1)	1.9 (0.4)	1.5 (0.1)	21 (0.7)	1.7 (0.2)	4.7 (0.04)	2.5 (0.2)	1.3 (0.1)	1.3 (0.1)
Expected + 50%	21 (0.1)	1.8 (0.3)	1.4 (0.1)	20 (0.5)	1.4 (0.1)	4.8 (0.03)	2.4 (0.1)	1.3 (0.09)	1.4 (0.1)
Expected + 100%	21 (0.1)	2.0 (0.3)	1.5 (0.1)	20 (0.5)	1.5 (0.1)	4.7 (0.03)	2.6 (0.1)	1.2 (0.08)	1.5 (0.01)
Expected + 200%	20 (0.2)	1.0 (0.7)	4.2 (1.2)	17 (1)	0.7 (0.2)	4.5 (0.01)	3.4 (0.3)	0.4 (5)	2.7 (0.1)
Expected + 500%	21 (0.1)	2.4 (0.3)	1.5 (0.1)	22 (0.6)	1.5 (0.1)	4.7 (0.03)	2.5 (0.1)	1.5 (0.1)	1.2 (0.1)
Expected + 1000%	21 (0.1)	2.2 (0.4)	1.5 (0.1)	22 (0.6)	1.6 (0.1)	4.7 (0.03)	2.2 (0.1)	1.4 (0.1)	1.2 (0.1)

Table 20 : Identified stiffness components for different orthotropic stiffness tensor as initial guess of the solution. 77 velocity values are used as an input

	C_{11}	C_{12}	C_{13}	C_{22}	C_{23}	C_{33}	C_{44}	C_{55}	C_{66}
Initial guess	20	20	20	20	20	20	20	20	20
Results	20 (3.0e-3)	20 (3.1)	20 (1.4)	20 (6.3)	20 (3.9)	20 (3.6)	20 (3.2e-3)	20 (1.9e-3)	20 (3.2)
Initial guess	20	2.1	2.1	20	2.1	20	8.9	8.9	8.9
Results	21 (0.1)	2.3 (0.4)	1.7 (0.1)	21 (0.7)	1.5 (0.1)	4.7 (0.03)	2.4 (0.2)	1.3 (0.09)	1.4 (0.1)
Initial guess	200	21	21	200	21	200	89	89	89
Results	21 (0.1)	2.2 (0.4)	1.6 (0.1)	20 (0.6)	1.5 (0.2)	4.7 (0.04)	2.6 (0.02	1.3 (0.01)	1.4 (0.01)

Table 21 : Identified stiffness components for different isotropic stiffness tensor as initial guess of the solution. 77 velocity values are used as an input

Even with less simulated input velocities values, the algorithm can still find a stiffness matrix close to the expected solution. The technique is therefore very robust. It is especially relevant that TOF measurements of the modes “quasi-transversal 2” are not necessary to find an appropriate solution. Indeed, this mode cannot be observed during experimental investigations. The major deviation from the exact solution is observed for the components C12 and C44.

Finally, in order to know the influence of experimental noise on the optimization results, different levels of random perturbation is applied on the simulated input velocities values. It is observed that deflection from the expected tensor only appears after 5 % of induced perturbation. A maximum of 11 % deflection is measured for a 15 % perturbation applied on the velocities. On measured time of flight an oscillation effect is noted (Figure 124). It was decided to fit the resulting curves by a fourth order polynomial. Both the experimental data and the interpolate time of flight values are plotted in the Figure 124. Those two sets of data are then used in the optimization algorithm, in order to have an idea of the robustness of this algorithm to experimental uncertainty. After computation, it appears that there is only a maximum of 1.5 % of difference between the rigidity constants obtain with or without fitting the results. So the algorithm is robust enough to compute a proper result despite of this kind of noise in the experimental results. As the oscillation in the time of flight measurements does not induce significant difference to the results it is decided not to smooth the resulting TOF for the further stages of the study.

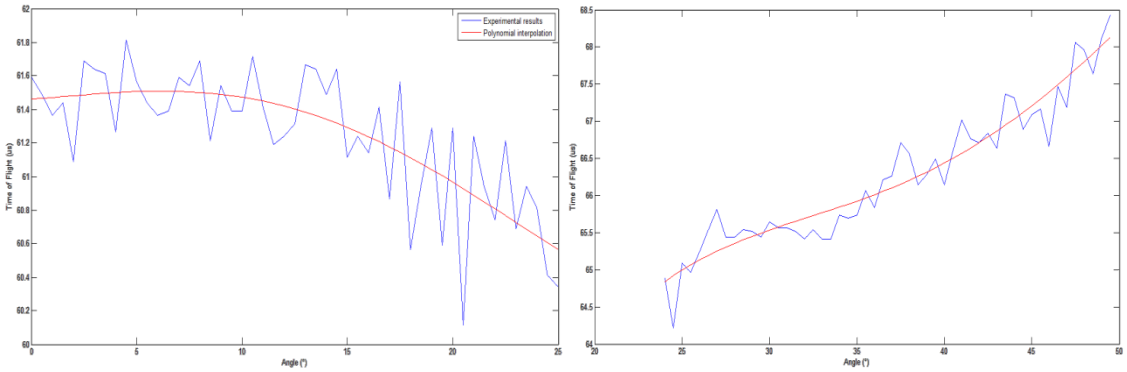

Figure 124 : Time of flight of longitudinal wave (Left) and transversal wave (Right) for all the chosen incidence angles

	C_{11}	C_{12}	C_{13}	C_{22}	C_{23}	C_{33}	C_{44}	C_{55}	C_{66}
Perturbation 5%	21 (0.1)	1.9 (0.4)	1.5 (0.1)	21 (0.7)	1.7 (0.2)	4.7 (0.04)	2.5 (0.2)	1.3 (0.1)	1.3 (0.1)
Perturbation 15%	23.24 (0.4)	2.1 (1.1)	1.7 (0.4)	22.6 (2.1)	1.8 (0.5)	5.2 (0.1)	2.5 (0.3)	1.3 (0.3)	1.5 (0.4)
Perturbation 25%	25.3 (0.6)	1.5 (2.2)	2.5 (0.8)	24.0 (3.4)	1.5 (0.9)	5.5 (0.2)	3.3 (0.9)	1.1 (0.6)	1.9 (0.6)

Table 22 : Identified stiffness components with different level of perturbation on the simulated input velocity values

The stiffness tensors were then computed with this optimization procedure using the experimental velocities measured on the three planes 1-3, 2-3 and 1-2 for both 0° and 45° configuration. As visible in Table 23, the optimized tensors are close to the numerically determined values for both samples orientation. Some discrepancy can be noticed but the symmetry of the material was correctly identified for both material and orders of magnitude were correct. The experimental results for both samples in 0° and at 45° configuration and damaged by tensile tests are described in the next subsection.

		C_{11}	C_{12}	C_{13}	C_{22}	C_{23}	C_{33}	C_{44}	C_{55}	C_{66}
Numerical		20	2.1	1.5	20	1.5	4.5	2.3	1.3	1.3
Experimental	0°	22.16 (0.2)	2.6 (0.15)	1.48 (0.76)	21.75 (0.08)	1.45 (0.17)	4.13 (0.07)	2.33 (0.09)	1.61 (0.21)	1.42 (0.12)
Numerical		13.35	8.75	1.5	13.35	1.5	4.5	8.95	1.3	1.3
Experimental	45°	14.6 (0.43)	6.0 (0.29)	1.5 (0.645)	13.5 (0.184)	1.4 (0.223)	4.2 (0.248)	6.7 (0.118)	1.7 (0.237)	1.6 (0.31)

Table 23 : Stiffness constants of the studied composite material obtained with numerical periodic homogenization method and obtained with the experimental ultrasonic method for 0° and 45° fibers orientation. The confidence interval of each identified stiffness constants is indicated under parenthesis

b) Experimental results: 0° configuration after tensile test

In this part, the results on samples oriented along the warp direction and damaged in tension are discussed. The undamaged sample, which is used as a reference, was presented in the previous subsection. The focus in this part will be placed on the damaged samples. All the tested samples were analyzed with X-ray tomography and studied in the part IV)-4) in order to know the damage level induced by the applied loading. Recall that the 150*45*1.53 mm samples were previously damaged by tensile loading along the axis of the fibers. Five samples were used, each were loaded at different tensile stress levels. As a reminder, the chosen loading levels are indicated in the Figure 125.

Contrary to the subsection on undamaged sample, only two planes (1-3 and 1-2) were used to investigate the damaged samples. Indeed, the width of the sample is too small and only a low number of angular positions can be considered in the plane 2-3. So, the low number of results available in this plane may only induced error on the optimization procedure. Nevertheless, as it was mentioned before, with only two planes tested seven of

the nine stiffness components of an orthotropic sample can be obtained. As a consequence, during the optimization process, the value of C_{23} and C_{66} are fixed, to the values obtained from periodic homogenization, because they cannot be determined without a third testing principle plane. The evolution of the resulting stiffness components are presented in the Table 24 and in Figure 126 for each of the seven computed components.

As first significant results, an important linear decrease of the C_{11} component with increasing the loading is noticed. The same observation was made when the reduction of the elastic modulus with the applied stress obtained in chapter III) is considered. A great fall of the C_{13} parameter is also visible. A smaller decrease of C_{12} and C_{55} is noted. The value of C_{22}, C_{33} and C_{44} does not seem to really vary when compared to the other rigidity components. It can be concluded that the rigidity components that are mostly altered during this mechanical loading are the ones that depend of the loading direction (1), i.e. C_{11}, C_{13} and C_{12}.

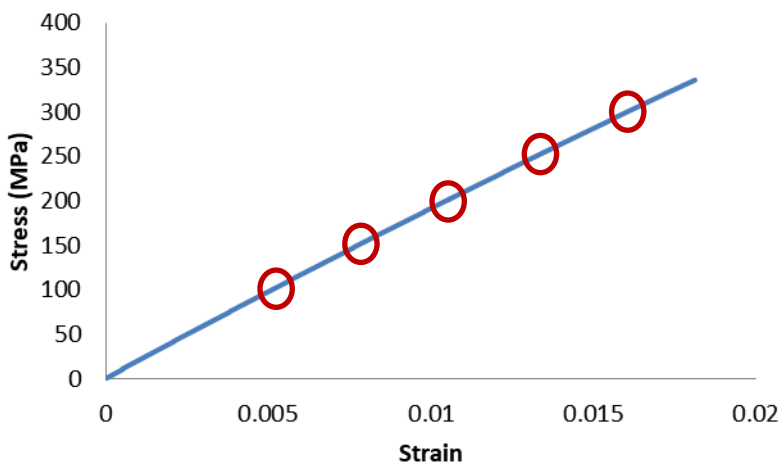

Figure 125 : Stress/strain curve for a tensile test on a 0° oriented sample. The red circles indicate the chosen loading for the five tested samples

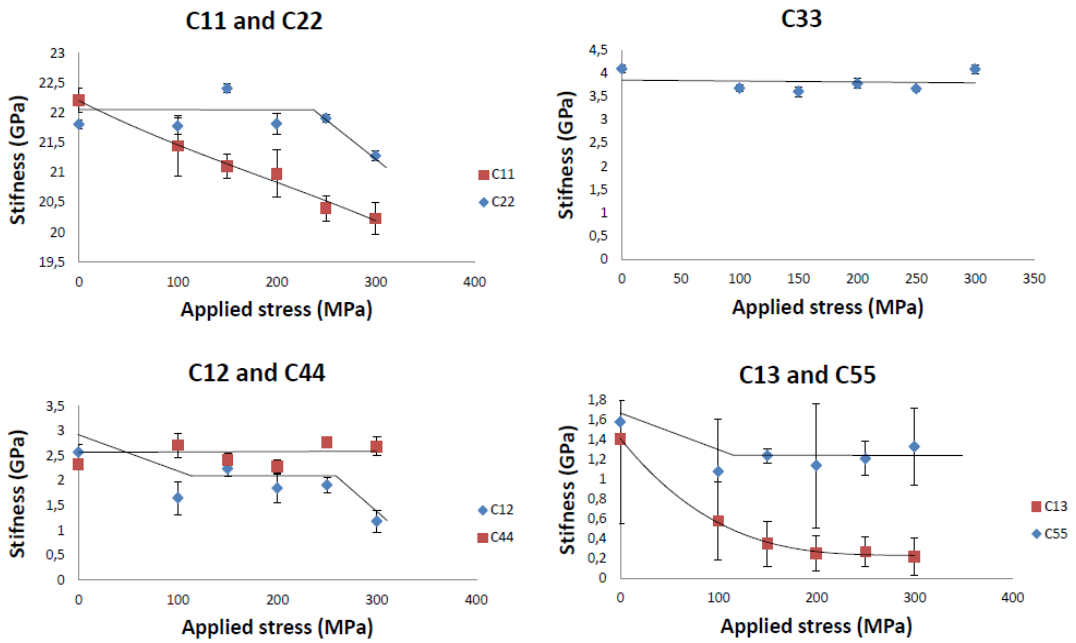

Figure 126 : Evolution of seven of the stiffness components with the increase of the loading for different 0° oriented sample

Applied stress (MPa)	C_{11}	C_{12}	C_{13}	C_{22}	C_{33}	C_{44}	C_{55}
0	22.21	2.57	1.41	21.81	4.10	2.33	1.58
100	21.45	1.65	0.5	21.78	3.68	2.71	1.08
150	21.1	2.24	0.01	22.41	3.61	2.41	1.24
200	20.98	1.85	0.2	21.82	3.78	2.28	1.14
250	20.04	1.91	0.008	21.91	3.67	2.77	1.21
300	20.23	1.18	0.03	21.28	4.09	2.685	1.33

Table 24 : Stiffness components of the studied composite material with an ultrasonic method for various values of loading in tension for samples in the 0° configuration

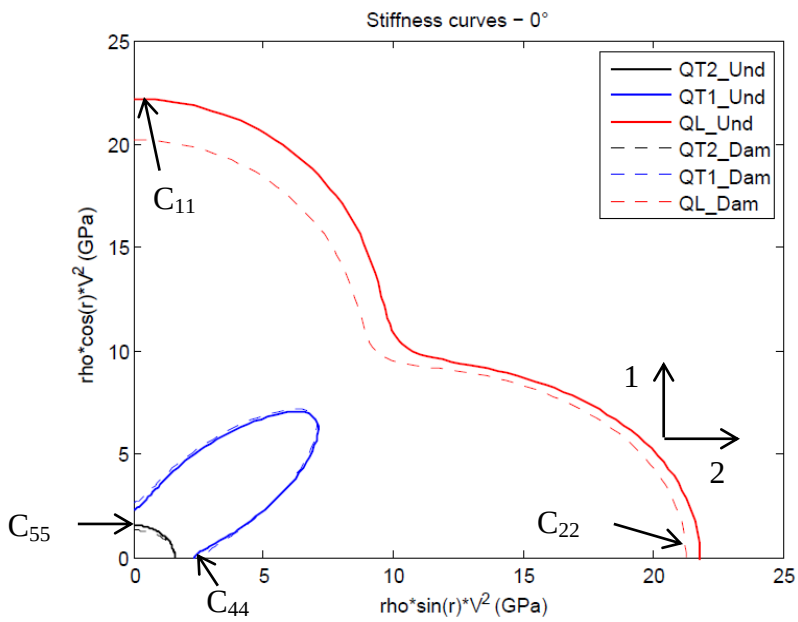

Figure 127 : Stiffness curves for two samples oriented at 0° from the fiber's axis. An undamaged sample and a sample loaded in tension at 300 MPa

Another way to represent the stiffness evolution is to plot the stiffness curves of a tested sample. A full set of velocities (QL, QT1 and QT2) are computed from the identified stiffness matrixes obtained with the optimization procedure. The anisotropy of the considered samples as well as the stiffness components affected by the mechanical solicitation can be more accurately visualized. The results are plot in the [rho*cos(r)*V^2]*[rho*sin(r)*V^2] space. Indeed, if Chrisoffel equation (V.9) is considered it is quickly apparent that the stiffness components are directly formulate in this space. For example, in the principal plane 1-2, for a refraction angle of 0 one have rho*V_L^2=C_{11}, whereas for a refraction angle of 90 rho*V_L^2=C_{22}. Stiffness curves of both the reference and the highest damaged sample (300 MPa), for the principal plane 1-2, can be observed on the Figure 127. Indications of some of the stiffness components that can be extracting from this figure are indicated for each wave mode. The stiffness decreases previously discussed can also be observed of this stiffness curves plot. That is to say, an important decrease of the C_{11} component and a very low decrease of C_{22}, observed from the red stiffness curves.

c) Experimental results: 45° configuration after tensile test

In the 45° configurations, another propagation plane, named X_1-3 is considered. The latter is of course oriented at 45° from the plane 1-3 used in the 0° configuration. Indeed, when the sample is oriented at 45° from the warp direction, the axis of the sample will of course correspond to the axis of the plane X_1-3. The different planes of propagation are illustrated in Figure 128 as a reminder. The X_1-3 plane is not a principal plane of the composite but the axis X_1 remains an axis of symmetry in its undamaged state. The same procedure can then be applied when undamaged. However, when submitted to tension at 45° from the warp direction, the damage induced in the sample can introduce loss in elastic symmetry. This can be provoked by the fiber's reorientations or unexpected micro cracks perpendicular to the loading direction; even though the Figure 84-b indicates that the majority of the damage is appearing along the two fiber axis (i.e. -/+ 45°). Therefore, to describe the elastic behavior of the samples oriented at 45° with respect to the warp direction, thirteen stiffness components are necessary. The Christoffel equation is consequently modified by considering C_{56}, C_{14}, C_{24} and C_{34} components for the stiffness tensor. However, ultrasonic measurements in four planes are needed to have a good estimation of these thirteen stiffness components. Some non-negligible errors may result from this limitation in the number of measurements.

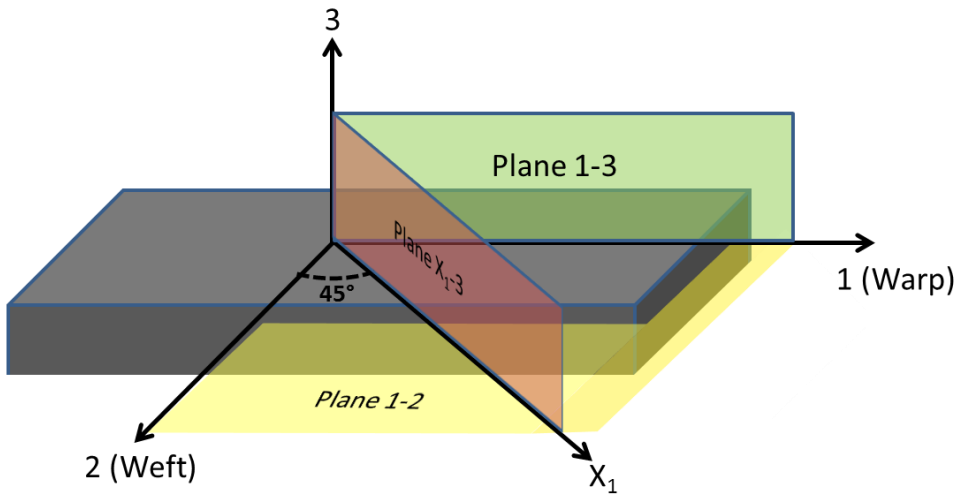

Figure 128 : Schematic representation of the different propagation planes of ultrasonic waves. For samples in the 0° configurations, the planes 1-3 and 1-2 were used. For the samples in the 45° configuration, the plane X_1-3 and 1-2 were used.

As in the previous part, different samples were loaded to different stress levels to induce different damage states originate from the tensile test. After considering the stress to failure (134 MPa) the chosen levels are set to 40, 80 and 120 MPa. They are indicated as a reminder in Figure 129. The important results are presented below, in a similar way to the previous subsection, in Figure 130 and Table 25.

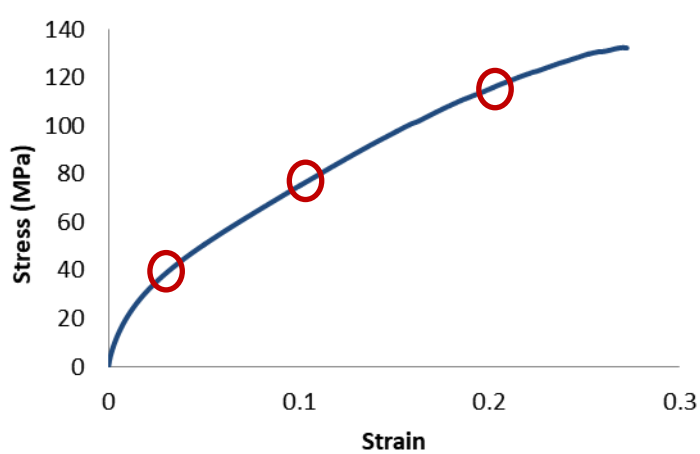

Figure 129 : Stress/strain curve for a tensile test on a 45° oriented sample. The red circles indicate the chosen loading for the three tested

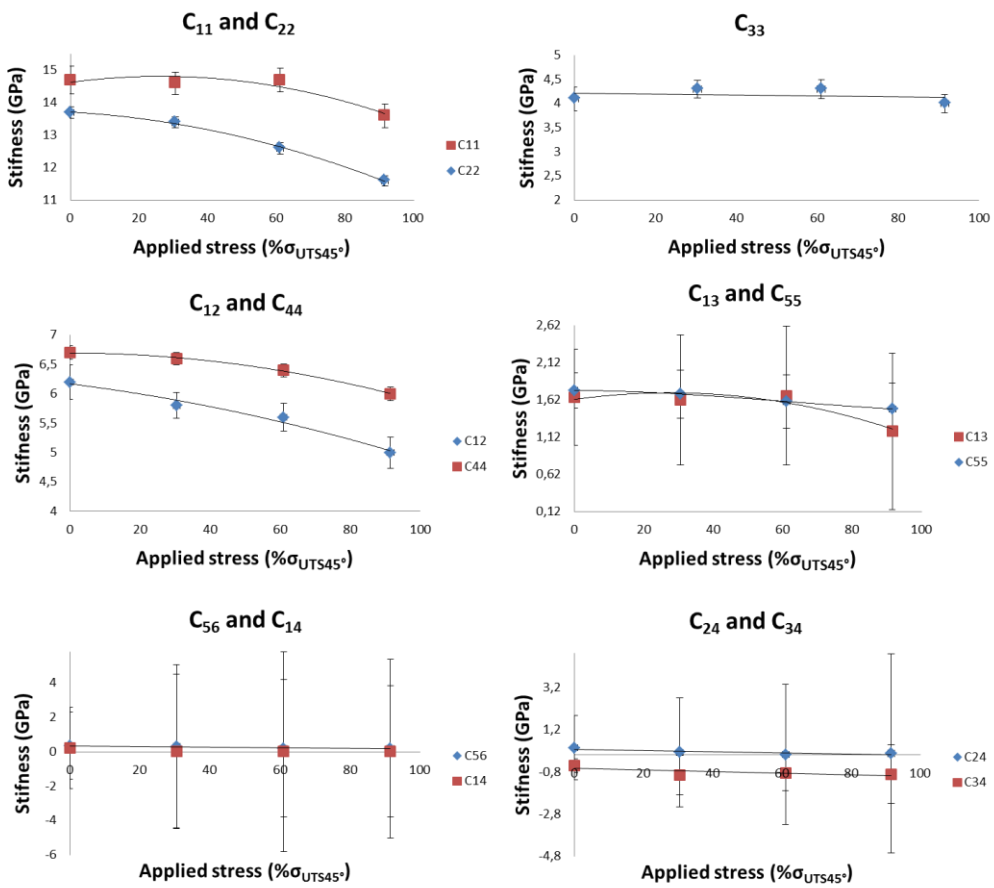

Figure 130 : Evolution of eleven of the rigidity constants with the increase of the loading for different 45° oriented sample with a third order interpolation

A decrease of C_{22}, C_{44} and C_{55} is observed, the value of C_{11} and C_{13} decrease mainly at the last loading step. The value of C_{12} decrease a little and C_{33} can be considered as constant during the tests. More constants clearly decrease to for the 45° oriented sample than the 0° orientation ones but with less amplitude. As expected, the different orientations of the samples lead to a very different evolution of the stiffness constants. Some minor changes can be observed for the C_{56}, C_{14}, C_{24} and C_{34} components. However, the confidence interval is very large when compared to the other stiffness components. This is explained by the lack of measurement in two additional planes as mentioned earlier.

The decrease of the C_{44} component is in agreement with the results from Digital Image Correlation (DIC) from chapter III) and the damage mechanisms observed in the chapter IV). Indeed, recall that a shearing effect was observed on the displacement field obtains with DIC acquisitions. This shearing also induces the fiber buckling noticed on X-ray tomography results.

Applied stress (MPa)	C_{11}	C_{12}	C_{13}	C_{22}	C_{33}	C_{44}	C_{55}	C_{56}	C_{14}	C_{24}	C_{34}
0	14.7	6.2	1.6	13.7	4.1	6.7	1.7	0.35	0.22	0.33	-0.51
40	14.6	5.8	1.6	13.4	4.3	6.6	1.7	0.29	0.02	0.12	-0.96
80	14.7	5.6	1.6	12.6	4.3	6.4	1.6	0.19	0.003	0.009	-0.87
120	13.6	5	0	11.6	4	6	1.5	0.18	0.02	0.07	-0.91

Table 25 : Rigidity constants of the studied composite material with an ultrasonic method for various values of loading in tension for a 45° fiber orientation

As in the previous subsection, the stiffness curves were plotted for two samples subjected to the ultrasonic stiffness measurements method. An undamaged sample and the sample loaded at 120 MPa in tension were considered. The results can be observed on the Figure 131.

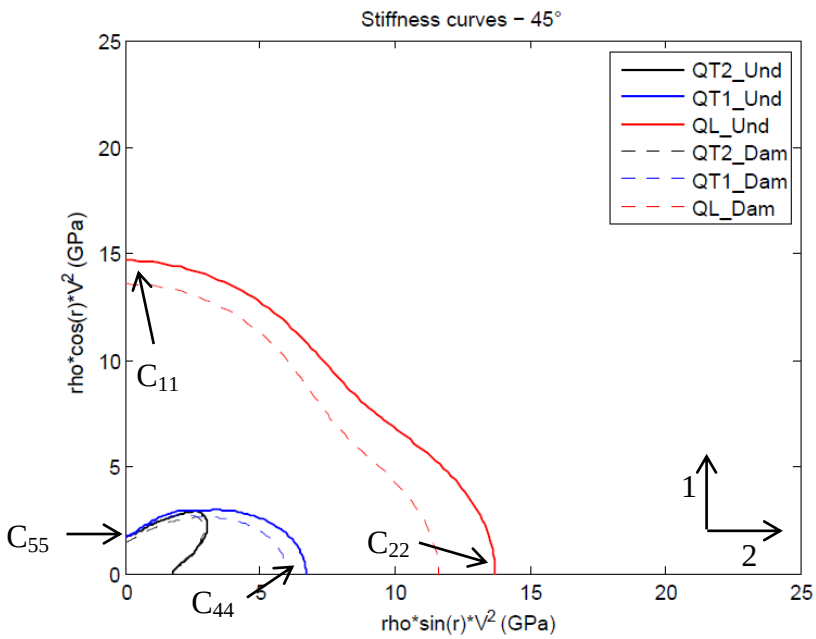

Figure 131 : Stiffness curves for two samples oriented at 45° from the fiber's axis. An undamaged sample and a sample loaded in tension at 120MPa

In order to compute the damage matrices, the macroscopic anisotropic description of damage proposed by El Guerjouma and Baste in [104], and formalized by Baste and Audoin in [105] is considered. This description is based on the continuum damage mechanic approach and considers the elastic tensor as the damage internal variable. The evolution of the stiffness components is considered as an internal variable of damage for this damage model. The latter has advantages because of the following considerations: no assumptions on the material geometry, no specific symmetry class for the material and no specific direction of micro-cracks propagation. In order to remain between 1 and 0, the damage matrix is normalized as follows:

$$D_{ii} = 1 - \frac{C_{ii}}{C_{ii}^{0}},\ i = 1,2,..6 \qquad \text{(V.58)}$$

$$D_{ij} = \frac{C_{ij}^0 - C_{ij}}{C_{ij}^0 + sign(C_{ij}^0 - C_{ij})\sqrt{C_{jj} * C_{ii}}}, i = 1,2,..6, j = 1,2,..6, i \neq j \quad \text{(V.59)}$$

The damage matrix has been calculated for the two samples orientations, this will result in the anisotropic evolution of damage presented in Figure 132. As aforementioned, one can note that the two samples configuration exhibit an evolution of their stiffness components with the damage state induced by increasing the applied stress level different from one another. For the samples in the 0° configuration, the highest evolution is achieved by the components C_{11}, C_{13}, C_{55} and C_{12} to a lesser extent. The other components remain mostly unaltered. However, for the sample in the 45° configuration, almost all components seem to exhibit a noticeable evolution when increasing the applied stress level. It is first worth recalling that the components C_{56}, C_{14}, C_{24}, C_{34}, have an important uncertainty on their values as visible in Figure 130, therefore the associated evolution of damage must be considered with caution. In addition, the evolution of C_{33} and C_{12} remain limited when compared to the other components. At last, the evolution of C_{11}, C_{13}, $C_{22,}$ C_{44} and C_{55} is really remarkable, in particular the last three. In this subsection, it was shown that the ultrasonic method of rigidity constants measurement is very sensitive to the evolution of the damage in the polyamide 66/6 reinforced with woven glass fibers. Another significant result is that damage schemes, different from one another, were observed for the two investigated sample configurations.

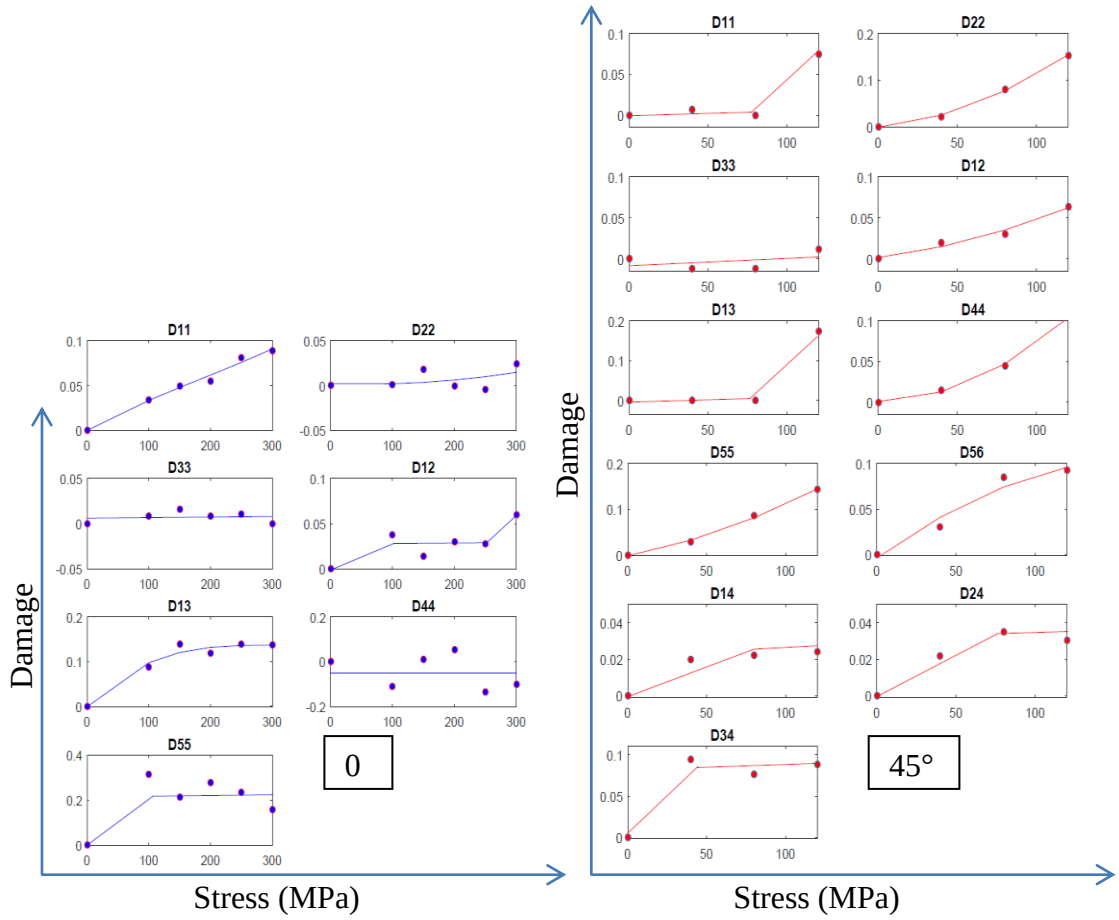

Figure 132 : Damage evolution with stress level of samples oriented at 0° and 45° obtained via ultrasonic measurements

d) Proposed damage indicators

In order to easily estimate the global damage state inside the sample, a damage indicator is needed. The damage indicator should give a first estimation of the damage state from the very raw ultrasonic result. This can help to decide if further tests are required on the composite material to assess the first estimate of the damage state. Therefore, it was proposed to consider a scalar value as a global damage indicator.

In the field of ultrasonic, the attenuation of the amplitude is one of the most used indicators to characterize the damage state. But it was verified firstly that for the C-scan in transmission an indicator based on the amplitude attenuation may not be sensitive enough

to detect the early step of damage. Nevertheless, a quick analysis of the amplitude was done on the raw signals, in order to check the sensitivity of an amplitude based method. The maximum amplitude of the signal was listed for each angle. An oscillation of the amplitude was observed when increasing the stress loading level. The measurement of the amplitude was not a suitable way to evaluate damage for this ultrasonic experimental method. Another indicator used frequently to estimate damage is the shift of the frequency (usually the one with the maximal amplitude), or the evolution of this frequency's amplitude. However, as for the amplitude, the evolution of the frequency with the highest amplitude does not seem to be related to the applied stress levels. Those two tested classical damage indicators do not seem very effective on this case. This can be verified in Figure 133, where the average, over the incidence angles, of the maximum amplitude and of the frequency shift are plotted. The values of the indicators are listed in Table 26 as well. Contrary to what was observed in the part III) and IV) the evolution of the indicator is not related to the applied stress level and therefore not related to the damage state of the tested samples. For this reason another kind of indicator is needed.

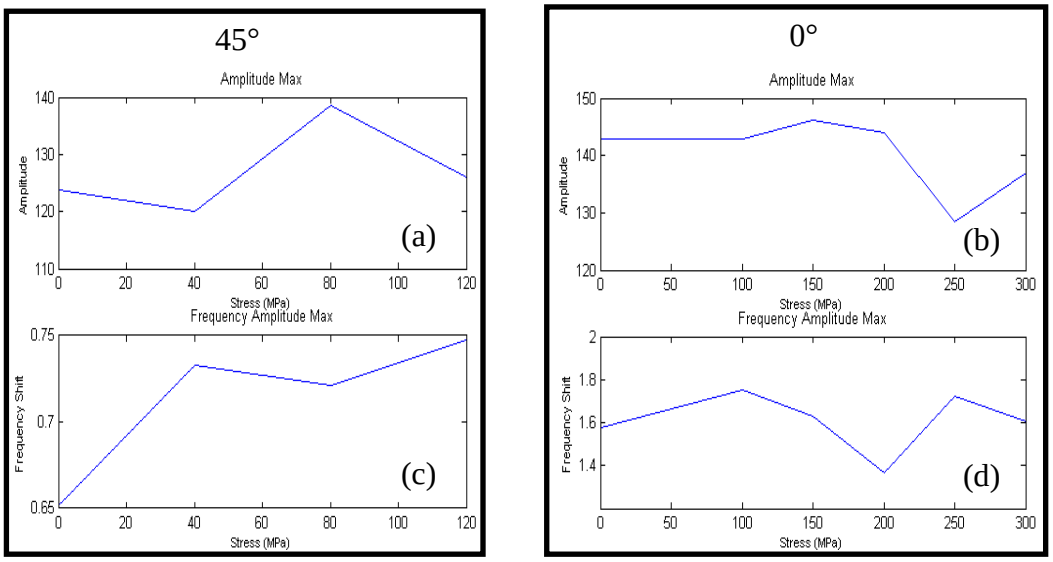

Figure 133 : Evolution of the maximal amplitude for sample in the (a) 0° configuration and (b) 45° configuration. Evolution of the frequency shift for sample in the (c) 0° configuration and (d) 45° configuration.

Applied stress(MPa)	**0**	**100**	**150**	**200**	**250**	**300**
Amplitude 0° (Volts)	0.1	0.082	0.055	0.067	0.068	0.081
Amplitude 26° (Volts)	0.06	0.07	0.047	0.06	0.038	0.056

Table 26 : Maximum amplitude for two fixed angles for all the loading value used

A first proposed scalar damage indicator is based on the reduction of the stiffness components obtained from the last sections. Their reduction is actually mostly linked to the damage state of the tested sample. It is calculated based on the Frobenius norm of the computed stiffness tensor:

$$N_f = \sqrt{trace(C' * C)} \tag{V.60}$$

With C: the stiffness tensor and C': its conjugate transpose.

Taking into account that a proper damage indicator should have a cumulative evolution with the increase of the damage state, the following damage indicator is adopted:

$$DI_1 = abs\big(N_f(C) - N_{f0}(C_0)\big) \tag{V.61}$$

where N_{f0} is the Frobenius norm of an undamaged sample's stiffness matrix and C_0 is the undamaged sample's stiffness matrix. It is recalled that the Frobenius norm actually computes the norm of the eigenvector of the matrix C. This is more convenient for this study compared to the quadratic norm or the largest singular value that does not take into account all the components of the eigenvector.

The resulting evolution of the Frobenius norm is plotted, for the configuration 0° and 45°, in the Figure 134-a and Figure 134-b respectively. The Figure 134-c with the two configurations is plotted for an easy comparison. A global increase of the indicator for both

cases was clearly observed as expected. Furthermore, it was noticed that the indicator increases moderately faster for the 45° than for the 0° configuration. This aspect is consistent with the different response of the samples when submitted to tension, since the behavior is ductile for 45° and brittle for 0°. The propagation of more cracks in the 45° samples was observed by mCT as presented in section 3. The indicator's value of the 45° sample loaded at 91.6% $\boldsymbol{\sigma_{UTS45°}}$ is actually even higher than the corresponding one for the 0° sample loaded at 92.6% $\boldsymbol{\sigma_{UTS0°}}$.

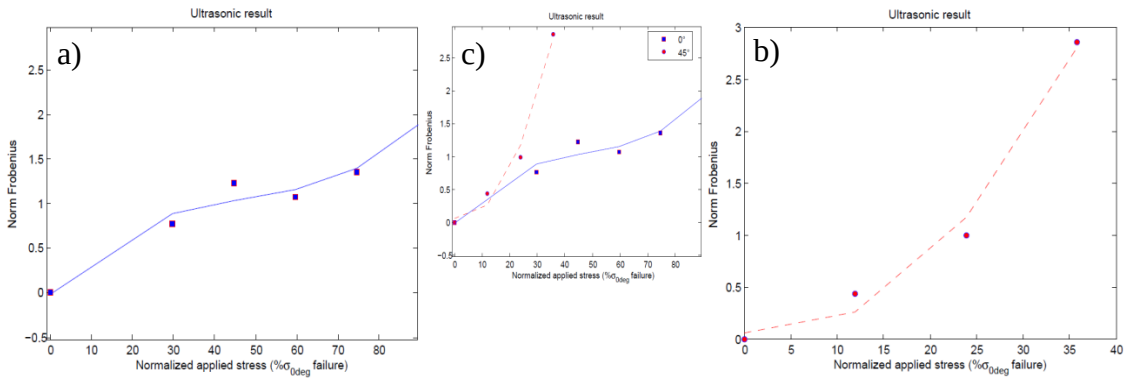

Figure 134 : Evolution of the Frobenius norm of the stiffness matrix for the two configurations of samples (a): 0° and (b) 45° configuration. In (c) both configurations are plotted for comparison purpose.

This second proposed indicator is based on the observation that the phase shift of the signal is sufficiently high when the damage state increases. Indeed, an accurate evolution of stiffness components' reduction was obtained based on the velocity measurement as was discussed in the previous subsection.

One of the least time post-processing consuming indicators is the average phase shift of the signals for different incidence angles:

$$DI_2 = \frac{1}{n} * \sum_{0}^{n_{max}} abs\left(\overline{ph(n)} - \overline{ph_0(n)}\right), \tag{V.62}$$

$$\overline{ph(n)} = \frac{1}{sp} * \sum_t ph(t,n) \tag{V.63}$$

$$ph(t,n) = \operatorname{atan}\left(\frac{Im\left(\widetilde{H(t,n)}\right)}{Real\left(\widetilde{H(t,n)}\right)}\right) = Im\left(Log\left(\widetilde{H(t,n)}\right)\right), \tag{V.64}$$

$$with : n: incidence\ angle\ consider$$

$$sp : sampling\ points\ of\ the\ evaluated\ signal$$

$$\widetilde{H(n)} : Hilbert\ transform\ of the\ response\ signal\ for\ a\ given\ n$$

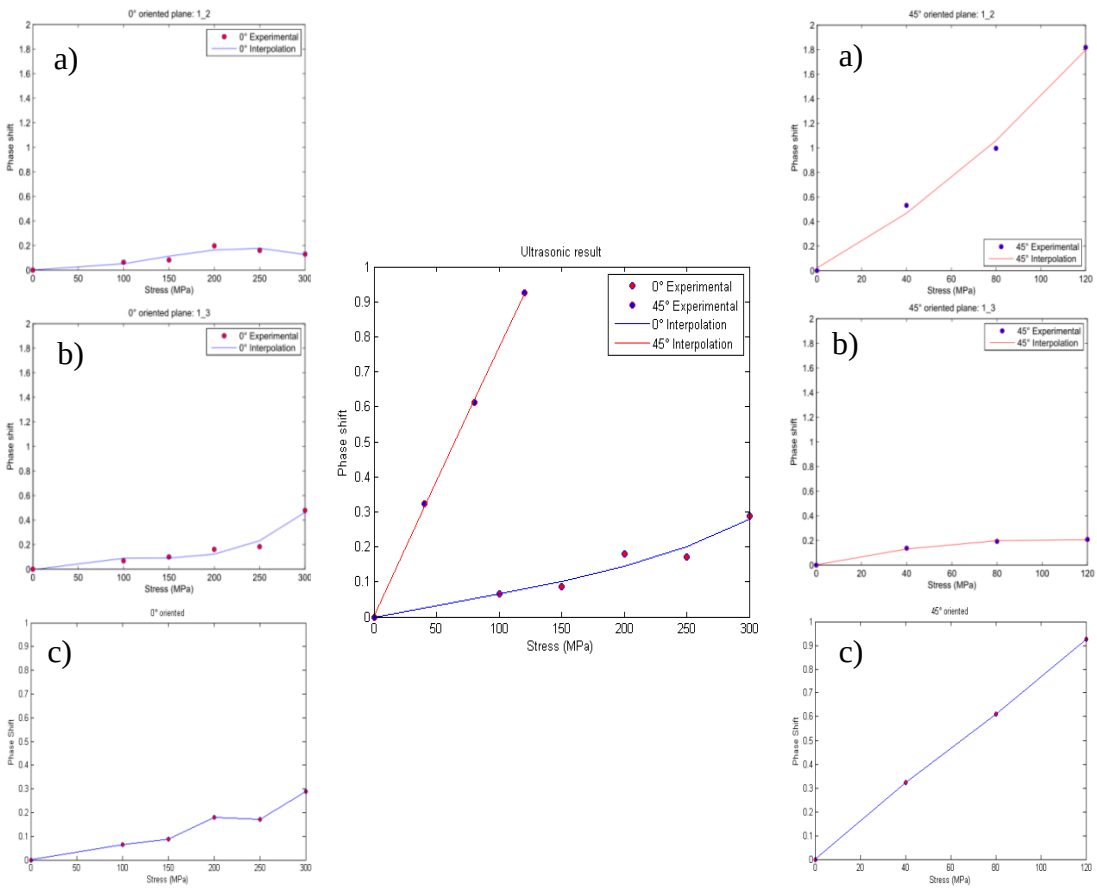

Figure 135 : Phase shift indicators evolution with increasing tensile stress for samples oriented at 0° and 45° (Resp; Left and Right) and for the two tested principal plane 1-2, 1-3 and the average on the two plane (Resp: a, b and c)

The evolution of this parameter was plotted for both samples' orientation as well as for the two principal planes considered for the rigidity measurements, i.e. 1-2 and 1-3. The average on the two principal planes is also represented. All the results can be found on the Figure 135.

Contrary to the previously discussed indicators of damage, the phase shift does detect an increase of the damage state as function of the applied tensile stress load. Then, if one look at the central figure that compares the evolution of the indicator for the two samples' orientation, one can see a clear difference of the evaluated damage state. The increase of damage is more important for the samples oriented at 45° from the fiber's axis. This result is in correlation with the elastic modulus losses and void volume fraction evolution. This can be verified on the Figure 136 on which those three indicators of the damage state are presented.

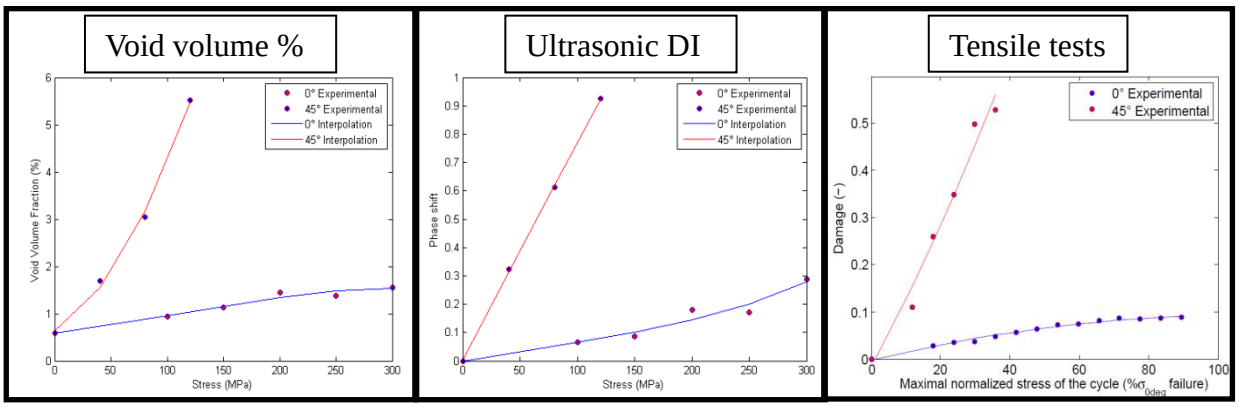

Figure 136 : Evolution of the void volume fraction evolution measured with X-ray tomography; Signal phase shase shift measured with an ultrasonic method and the elastic modulus loss measured during incremental cycling tensile tests

4) Guided Lamb waves

As was discussed in the literature review section, Lamb waves are very effective to study and evaluate the damage state of complex media. Indeed, recall that because of its guided properties, a Lamb wave can investigate efficiently complex structures over long

distances. Because of the necessity to have an ultrasonic damage evaluation method that can be used to inspect various automotive parts, it was quickly chosen to investigate the sensibility of guided waves. A clear difference was indeed observed with the proposed phase shift indicator. Consequently, the current part is dedicated to the study of the sensitivity of guided Lamb waves to different states of damage induced in the polyamide 66/6 reinforced by woven glass fibers composite material. The samples used in the previous section were considered for the investigation of guided waves. However, prior to considering the polyamide 66/6 reinforced by woven glass fibers, preliminary tests are performed on an aluminum plate with defects of various sizes. Both the evolution of the time shift and the signal amplitude will be investigated in order to be linked with the evolution of damage magnitude.

a) Preliminary investigation on an aluminum plate

This is an aluminum plate of 470 x 470 x 5 mm with several defects within. Most of them consist of holes of different diameter but a large notch was also induced. A photo of this tested plate is visible in Figure 137, information on the different investigated defect is also proposed in the Table 27. The guided waves investigations were performed in transmission using two *Panametrics V103* contact sensors of 1 MHz polarized longitudinally. A waveform generator (*Agilent Technilogy model*) was used to create the emitting signals. The signal is amplified after reception by an amplifier (from *Krohn-Hite model 7500) a*nd eventually captured using an oscilloscope. The two transducers were spaced by 4 cm and a coupling gel, *Sofranel coupling Gel-D* is used for both transducers to increase the transmission between the two media. For these tests a burst of 5 cycles were generated, frequencies of 500 Hz and 1 MHz were considered in order to investigate the difference in sensibility in terms of damage detection. For each frequency, a transmitted signal was acquired and used as a reference.

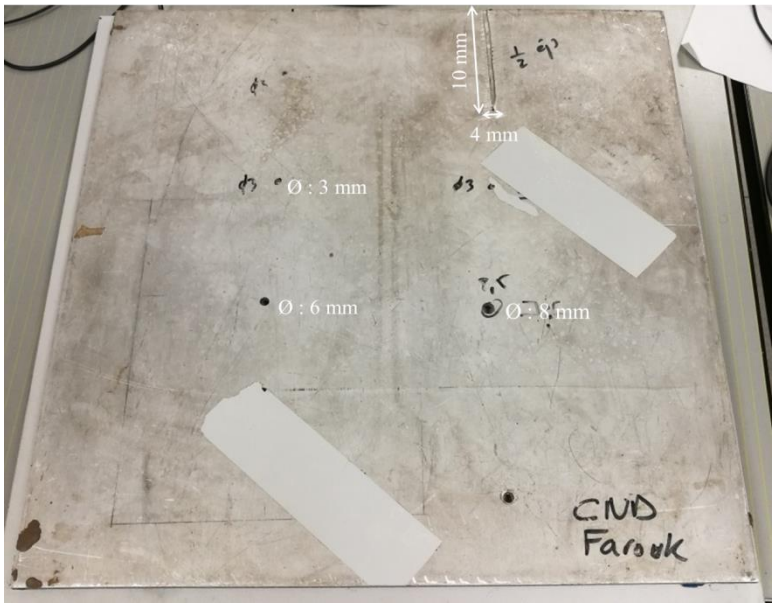

Figure 137 : Investigated aluminum plate. Several defects are appearing in the plate, mostly holes of different diameter. A large notch is also visible

As can be seen on Figure 138, there is a clear decrease of the signal amplitude when a defect is located on the path between the transducers. On this figure, the recorded signal is plotted, for an input frequency of 500 KHz and 1 MHz (Figure 138 a and b respectively), for the through holes of 3, 6 and 8 mm as well as for the large notch. The reference signal is plotted in red for comparison purpose. The decrease of the amplitude seems to be function of the diameter of the holes, and is even more important for the case of the large notch. This can be explained by the fact that the 4mm large notch stretches over a distance of 10 mm. Therefore, contrary to the case when holes are considered, the ultrasonic waveform cannot propagate around the defect. Consequently, the amount of energy lost when passing through the notch will be more important.

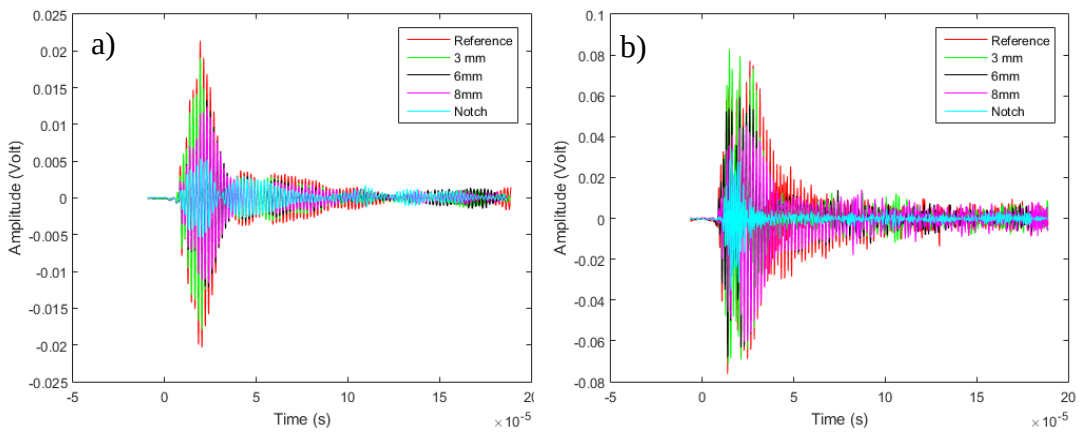

Figure 138 : Transmitted signal for different defects and a reference case when a burst of a) 500KHz and b) 1MHz is emitted

In order to quantify this reduction more precisely, it was chosen to calculate the energy E_S of the transmitted signal x(t). The latter was considered as a damage indicator because it takes into account the full response of the guided waves signal. The integral is indeed calculated on the entire response signal between the first positive peak and the time when the signal became only noise. The energy was calculated for all the acquired signals using this definition:

$$E_s = \int abs(x(t))^2 \, dt$$

The signal energy function of the size of the defects is indicated in Table 27 for both considered frequencies. The signal energy with and without normalization by the energy of the reference signal are determined. Indeed, a significant difference in the magnitude of the energy is noted between 500 KHz and 1 MHz because the two transducers are centered at 1 MHz. However, after a normalization of the calculated energy by their respective reference signal, both evolutions of the absolute energy are close and indicate a correlation with the size of the considered defect. This damage indicator is effective to distinguish large defect on samples. It will be now applied on the woven fiber reinforced polyamide 66/6.

Type of defect	Circular through hole	Circular non-through hole	Circular through hole	Circular through hole	Notch
Dimensions	Diameter : 3 mm	Diameter : 3 mm	Diameter : 6 mm	Diameter : 8.5 mm	4*100*2.5 mm
Normalized Signal energy - 500 KHz	0.358	0.659	0.413	0.390	0.106
Normalized Signal energy – 1 MHz	0.422	0.841	0.686	0.561	0.084
Signal energy 500 KHz	0.0022	0.0041	0.0026	0.0024	0.0007
Signal energy – 1 MHz	0.044	0.087	0.071	0.058	0.008

Table 27 : List of defects on the investigated plate and their respective dimensions the reference signal energy measured using a 500 KHz signal and a 1MHz signal is respectively of 0.006 $V^2.s^{-1}$ and 0.104 $V^2.s^{-1}$.

The energy of the signal was shown to be a good indicator of the defect appearing in the steel plate. If no mode conversion is induced by the defect this indicator remains an efficient way to quantify damage. The appearance/disappearance of mode can induce false positive detection of damage or unexpected jump in the signal energy value. The transmitted mode will then be analyzed, before considering the use of signal energy as damage indicator, for the composite material investigation presented further on.

b) Investigations of the woven glass fiber reinforced polyamide 66/6 samples damaged by tension

As aforementioned, the polyamide 66/6 woven glass fiber reinforced is considered in this section. More precisely, the samples that were damaged in tension and described in the Table 12 of section IV)-4) is used for this investigation. The same equipment described in

previous section will be considered here. In addition, the robot arm from the polar-scan will be used to move precisely the receiver from one position to another on the tested samples.

As in the previous subsection, frequencies of 500 KHz and 1 MHz are planned for use. However, a main frequency of 500 KHz was observed during preliminary analysis of the transmitted guided waves in the frequency domain for both emitted frequencies. Therefore, it was chosen to consider only the 500 KHz here in order to have a transmitted signal with the main frequency at really center. Consequently, the waveform generator is used to emit a 500 KHz burst of 5 cycles. The emitting transducer is fixed on the sample and the receiving transducer is moving so that the distance between the two transducers, noted d_i, goes from 4.25 cm to 7.25 cm a signal is recorded every 0.5 cm. The receiving transducer is attached to a robot arm in order to control precisely the displacement between each increment measurement. The experimental set-up is summarized in Figure 139. The two transducers are on the same surface of the sample, which allows controlling the sample more easily than with the method presented in section V)-3) that require an access to both surface of the sample.

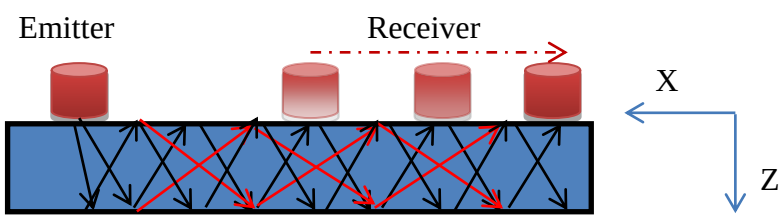

Figure 139 : Experimental set-up of the guided waves experiment

Analysis of dispersion curves/Lamb waves modes

In order to check that guided waves are indeed generate with this experimental set-up, the dispersion curves will be calculated based on the signals recorded at different positions. Indeed, as mentioned in the review section (V)-1)-c)), a representation of the dispersion curves can be obtained by applying a 2D Fast Fourier Transform (2D FFT) on the obtained wave signals. The mode(s) that propagate in the tested composite specimen can be determined consequently. In addition, mode conversion can be induced by defect in a

structure; this can be helpful to detect a major change in a material. The result from the 2D FFT is plotted for the undamaged sample in the 0° configuration in Figure 140 in the wavenumber/frequency domain. The dispersion curves, for the mode S_0, A_0, S_1 and A_1, obtained from the *Disperse* software is plotted as well in order to determine the propagating mode. The stiffness tensor obtained from periodic homogenization (Table 23) was used for the computation of the dispersion curves in continuous lines. It is noticed that the propagating mode is really close to the curves of the S_0, S_1 and A_1 modes. This can make the determination of the specific propagating mode troublesome. The stiffness tensor obtained from the ultrasonic measurement was then considered in order to reduce this ambiguity. It is plotted in dashed lines for the three modes S_0, A_0, S_1 and A_1 as well. The transmitted mode now seems so be closer to the curves of the S_1 mode. However, it remains difficult to determine with full certainty the propagating mode because of the modes' proximity.

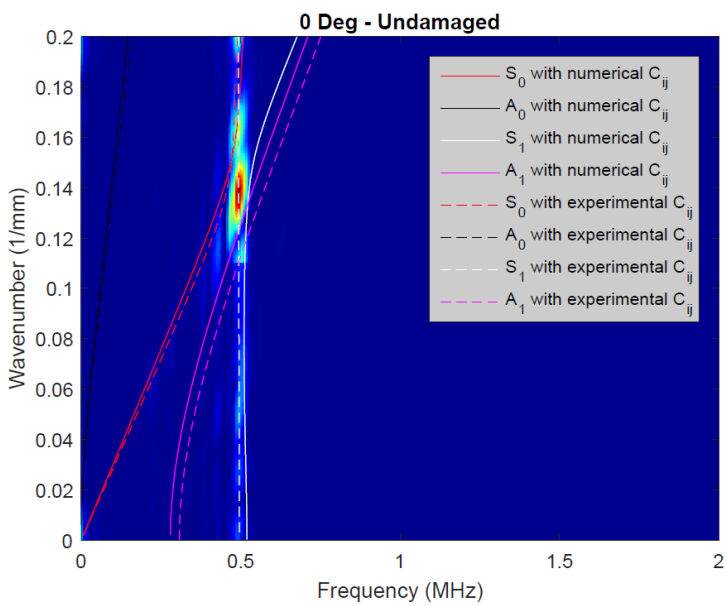

Figure 140 : 2D Fast Fourier Transform for the undamaged specimen in the 0° configuration for mode S_0, A_0, S_1 and A_1. The stiffness matrix obtained by periodic homogenization was used for the modes represented by mean of continuous lines. Whereas the matrix obtained by ultrasonic acquisitions was used for the ones plotted in dashed lines.

The phase velocity was measured in order to identify the transmiting mode otherwise. As mentioned above, when guided waves were considered, the phase and group velocities of the transmitted waves are different, so they need to be carefuly measured to avoid misconceptions. Two signals measured in the sample for different emitter-receiver distance d_i are plotted in Figure 141 to explain the difference phase and group velocity measurement methods. Indeed, to measure the group velocity the wave packet is analyzed as a whole by considering the envelope of both signals as visible in Figure 141-a. The time delay t_{GR1} and t_{GR2} that correspond to the center of the envelope of the wave packet is then used to compute the group velocity. However, to calculate the phase velocity, the displacement of a specific features in the signal is given for different emiter-receiver distances. However, due to the change of the waveform induced by the dispersion effect the measurement can become difficult.The zero-crossing method [106], [107] was then used to obtain the phase velocity. The idea of this method is to measure the time at which the signal crosses 0 amplitude for signals measured at different emitter-receiver distance d_i. The advantage of this method is that it does not take into account the amplitude of the signal, which changes because of the dispersive effect on the signal mention earlier. An example of the zero-crossings method is illustrated in Figure 141-b. The corresponding times (t_{PH1} and t_{PH2} here) are then used to obtain the phase velocity using the slope of the $d_i(t_{PHi})$.

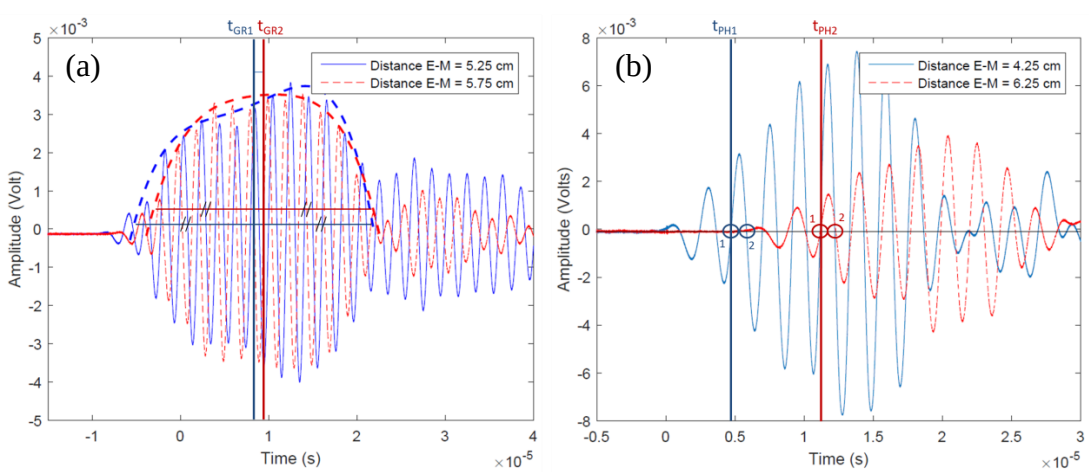

Figure 141 : Two transmitted signals with an example of (a) group and (b) phase velocity measurement

Here to know the phase velocity of the transmitted mode, a distance from emmiter to receiver from 4.25 to 7.75 cm was considered and a time t_{PHi} was measured for each d_i. The identified times were plotted as function of the distance on Figure 142, the slope of this curve can then give the phase velocity. As indicated, this velocity is of 3629 m/s, the latter is compared with the phase velocities numerically obtain using the *Disperse* software. In a similar way than in Figure 140, the phase velocity dispersion curves obtained using the two introduced stiffness tensor are indicated for comparison purposes in Figure 143. As a results, the transmitted mode in the sample is a S_1 mode and the phase velocity obtained from Figure 142 is closer to the numerical phase velocity calculated using the stiffness tensor from ultrasonic measurement of section V)-3), which is in agreement with the Figure 140. As a result, it is assumed that a S_1 mode is transmitted in the sample for the considered frequency range.

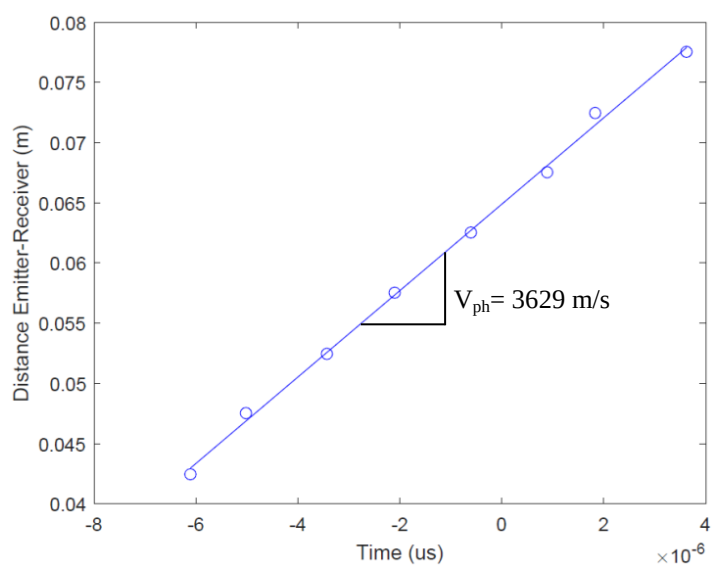

Figure 142 : Distance/time evolution obtained for the undamaged samples oriented at 0° used in order to calculate the phase velocity

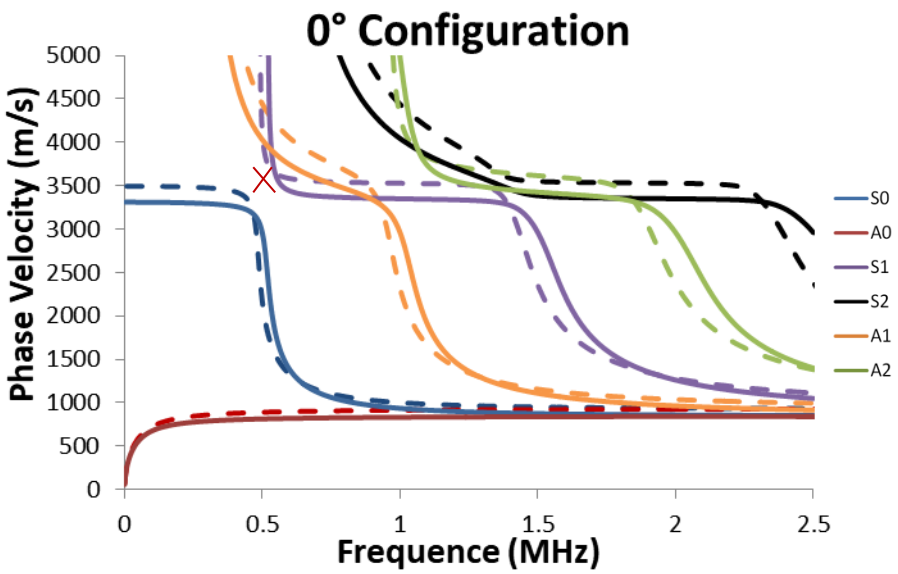

Figure 143 : Phase velocity/Frequency dispersion curves for sample in the 0° configuration. The stiffness matrix obtained by periodic homogenization was used for the modes represented by mean of continuous lines. Whereas the matrix obtained by ultrasonic acquisitions was used for the ones plotted in dashed lines.

Then, the samples in the 45° configurations were analyzed as well in order to determine the transmitted mode. The appearing mode is between the S1 and A1 modes as visible in Figure 144. The phase velocity was then computed but when compared with numerical results (Figure 145), the transmitted mode still cannot be clearly identified to be S1 or A1. This difficulty to determine the transmitted wave mode could also be explained by a remaining discrepancy between the real material's elastic behavior and the one measured with ultrasound. Therefore, the dispersion curves obtained with the *Disperse* software must be considered with caution.

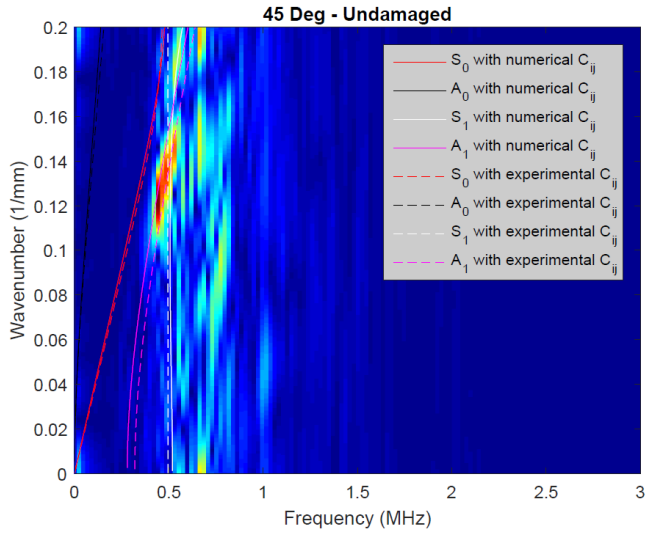

Figure 144 : 2D Fast Fourier Transform for the undamaged specimen in the 45° configuration for mode S_0, A_0, S_1 and A_1. The stiffness matrix obtained by periodic homogenization was used for the modes represented by mean of continuous lines. Whereas the matrix obtained by ultrasonic acquisitions was used for the ones plotted in dashed lines.

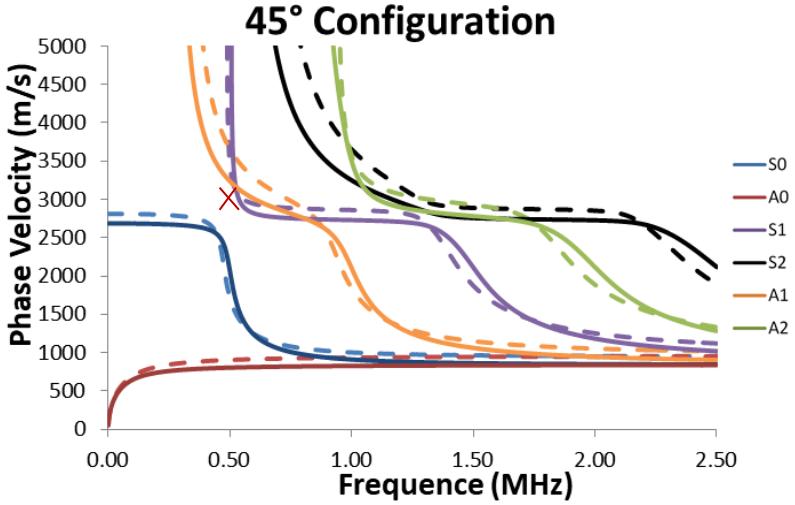

Figure 145 : Phase velocity/Frequency dispersion curves for sample in the 45° configuration. The stiffness matrix obtained by periodic homogenization was used for the modes represented by mean of continuous lines. Whereas the matrix obtained by ultrasonic acquisitions was used for the ones plotted in dashed lines.

Analysis of signals measured on top/bottom surface of the specimen

An experimental methodology was then proposed to determine whether the mode propagating in the specimen in the 45° orientation is symmetric or antisymmetric. Indeed, as aforementioned the two possible modes are either a S_1 or a A_1 mode. Two transducers in receiving mode are placed on each side of the plates and are linked together. Another transducer is then set as an emitter and placed on the upper side of the plate. The three transducers are *Panametrics V103* transducers with a central frequency of 1 MHz. A waveform generator is used to generate a burst of 5 cycles at a frequency of 500 kHz. Finally, a gain is applied on both receiving signals that are then recorded on an oscilloscope. All this experimental set-up is visible in Figure 146. Both 0° and 45° configuration of sample were analyzed.

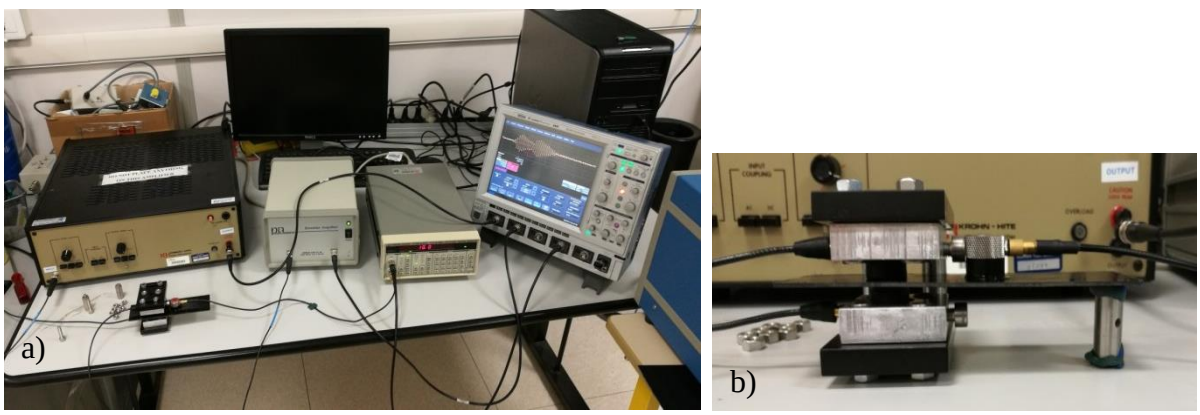

Figure 146 : a) Complete experimental set-up used to measure the top and bottom signals from a transmitted Lamb waves. b) Zoom in on the transducers holder system

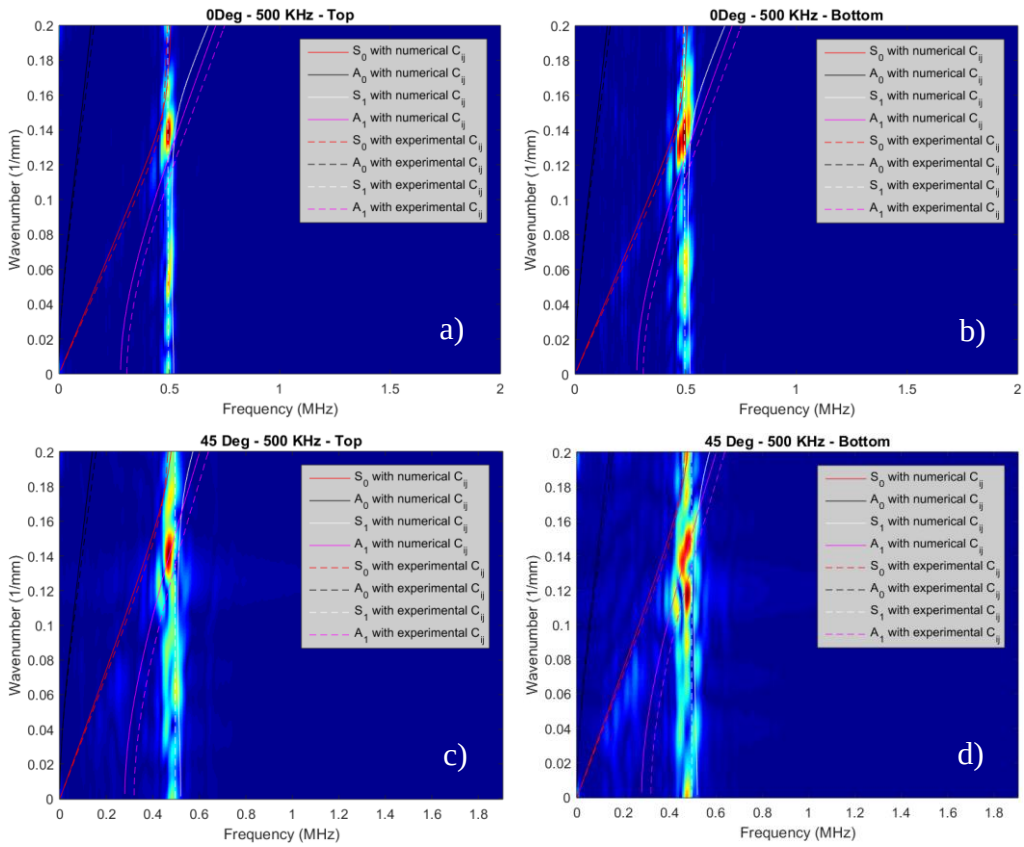

Figure 147 : 2D Fast Fourier Transform for (a) the signal recorded on the top surface in the 0° configuration and (b) the signal recorded on the bottom surface in the 0° configuration. 2D Fourier transform for (c) the signal recorded on the top surface in the 45° configuration and (d) the signal recorded on the bottom surface in the 45° configuration.

The distance between the emitter and the receiver is set from 4.25 to 8.75 cm. A signal is recorded every 0.5 cm. The resulting 2D FFT is plotted for the sample in the 0° configuration on Figure 147-a and Figure 147-b as well to verify the quality of the measurements on each side of the plate (i.e. top and bottom). As for the Figure 140, clear modes are appearing and are still close to the curve of S_1 mode; consequently the S_1 is still assumed to be the transmitted mode in the 0° configuration. The resulting 2D FFT is then plotted in Figure 147-c and Figure 147-d for the specimen in the 45° configuration. As observed before, the transmitted mode appears between the curves of the S_1 and A_1 modes.

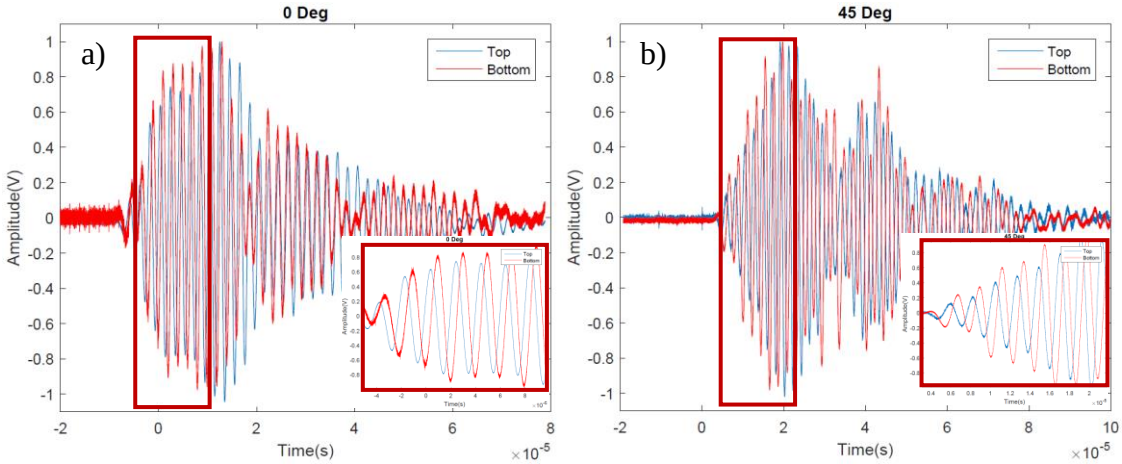

Figure 148 : Typical signals measured on top and bottom surface of sample in the (a) 0° configuration and (b) 45° configuration

The spectrogram for both configurations is then investigated in an attempt to detect a hidden mode. As visible in Figure 149, an additional mode is actually clearly visible for the 45° configuration case, at 26 µs and at a frequency of 0.24 us. It moves in time when the distance between the emitter and receiver increases. The group velocity could be roughly estimating from the spectrograms. It was found to be of 1136 m/s by linear regression in a similar manner than Figure 142. It must be emphasized that only the order of magnitude could be obtained. But as in this frequency range the two modes have distinctive velocity, this estimation is sufficient to determine which this mode is. As a consequence, this mode was assumed to be an A_0 one after comparison with the phase velocities dispersion curves from Figure 145. However, this mode cannot be imaged on the experimental 2DFFT because of the insufficient spatial resolution. Indeed, the numerical wavenumber was found to be 0.36 mm^{-1}, which means that the spatial resolution must be at a minimum of 2.7 mm. As a consequence, this A_0 mode will not be considered in further analysis. To conclude, as the first wave packet from top and bottom in the 0° and 45° configuration exhibit the same time of arrival, the main transmitted mode is assumed to be a S_1 mode whereas the mode appearing at 26 µs is assumed to be an A_0 mode.

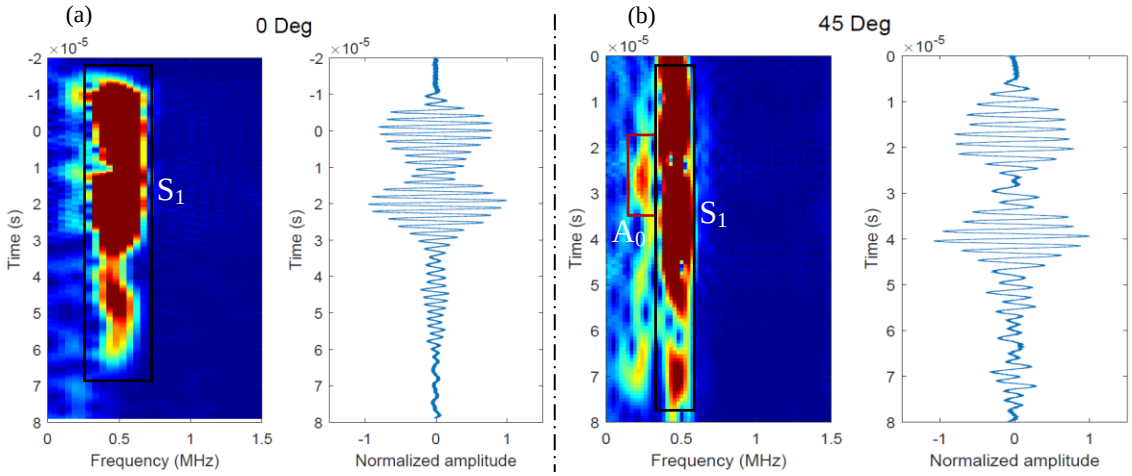

Figure 149 : Spectrogramme d'un signal transmis dans un échantillon dans (a) la configuration 0° et (b) la configuration 45 ° avec le signal temporel correspondant

Investigation of damaged samples

The 2D Fast Fourier Transform of the others specimens in the 0° configuration were then calculated in a similar way than for the undamaged specimen. The result for the different specimens is summarized in Figure 150. As for the undamaged sample, it is difficult to determine which mode propagates in the tested composite specimens without further analysis. However, based on the additional analysis of phase velocity described earlier, a S_1 mode is assumed to propagate in the other specimens in the 0° configuration. No noticeable mode conversion or difference could be found between the 2D FFT of the undamaged specimen and any of the other damaged samples. Consequently, other signal processing methods must be considered to evaluate the damage state induced by tensile tests for sample in the 0° configuration.

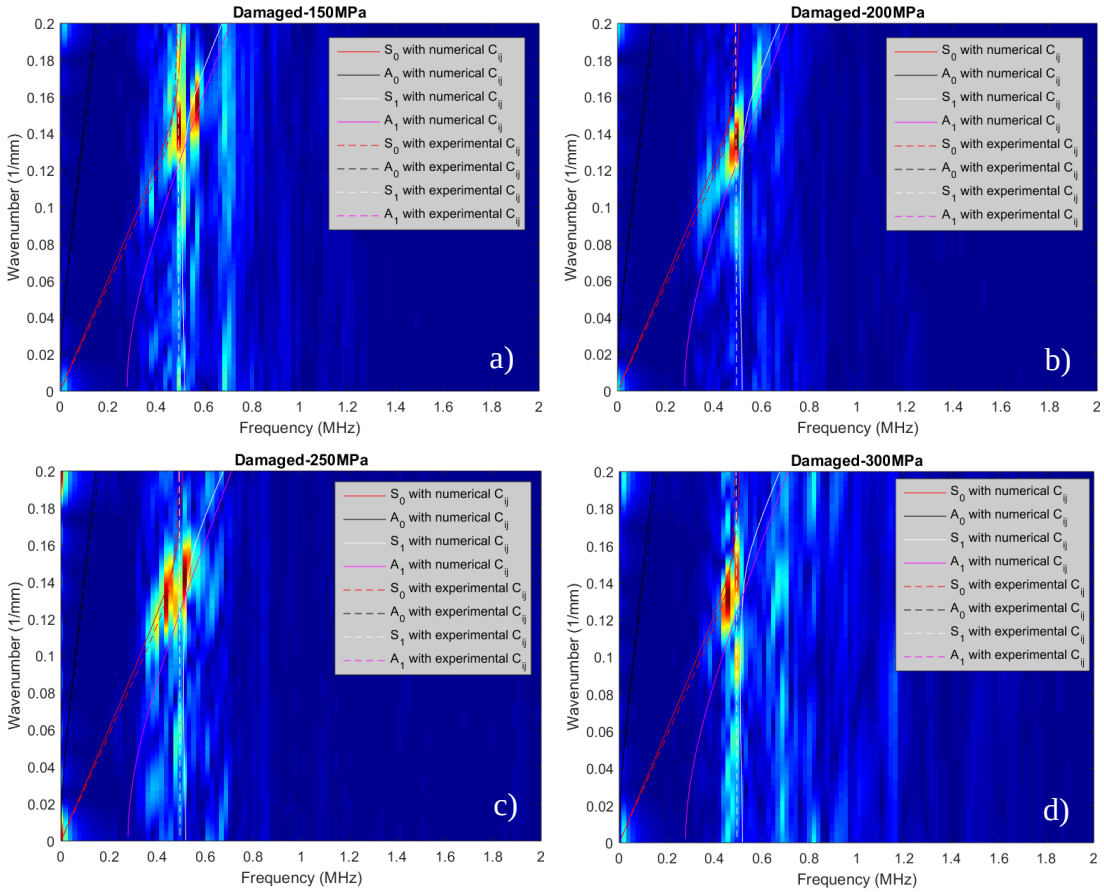

Figure 150 : 2D Fast Fourier Transform for the samples, in the 0° configuration, loaded in tension at a) 150, b) 200, c) 250 and d) 300MPa.

The stiffness matrix obtained by periodic homogenization was used for the modes represented by mean of continuous lines. Whereas the matrix obtained by ultrasonic acquisitions was used for the ones plotted in dashed lines.

In a similar manner, the samples in the 45° configuration submitted to tensile tests were analyzed in order to identify a potential mode conversion effect. However, when the loading level reaches 80 MPa and 120 MPa the 2DFFT (Figure 151), gives inconclusive results. For those samples, no transmitted mode can be really distinguished. This is mostly due to signal attenuation when the tensile loading exceeds 80 MPa as will be discussed in the next subsection.

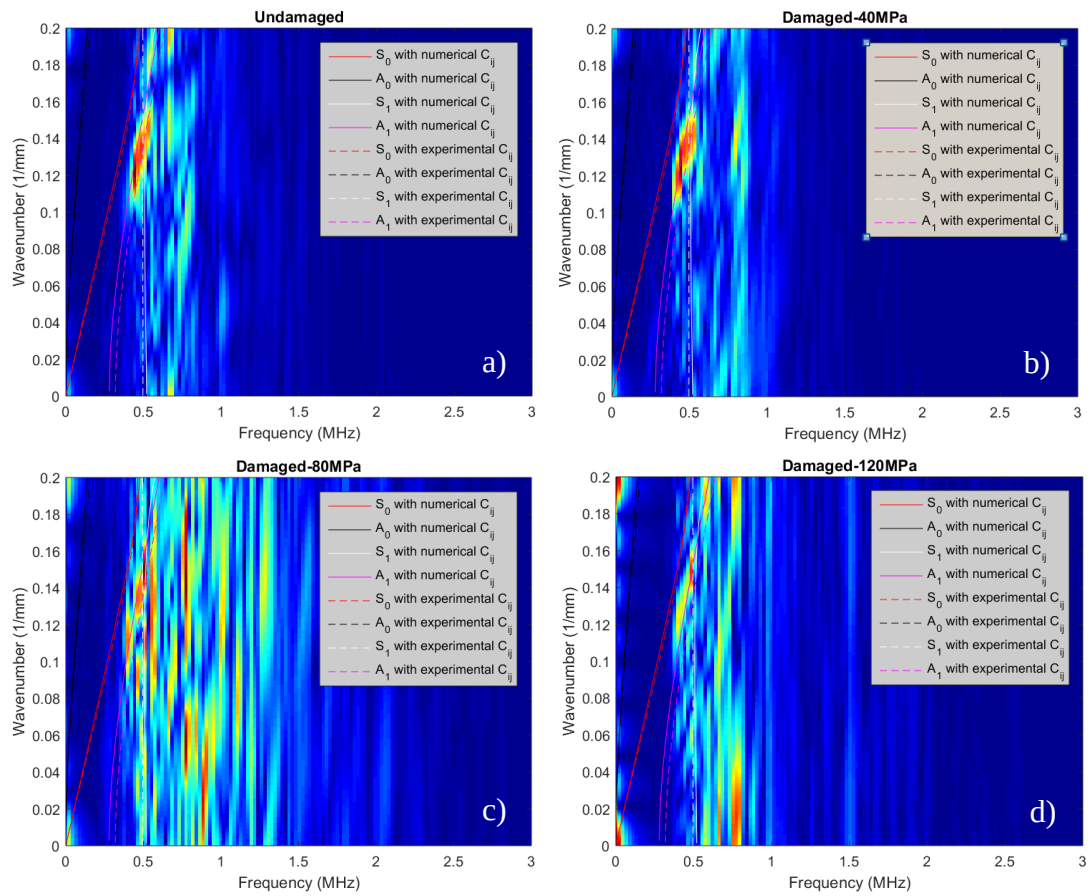

Figure 151 : 2D Fast Fourier Transform for the samples, in the 45° configuration, a) undamaged and loaded in tension at b) 40, c) 80 and d) 120MPa.

The stiffness matrix obtained by periodic homogenization was used for the modes represented by mean of continuous lines. Whereas the matrix obtained by ultrasonic acquisitions was used for the ones plotted in dashed lines.

Investigation of proposed damage indicators

In a next attempt, the evolution of the signal's amplitude was then investigated as in the previous section. It was observed in section V)-4)-a) that the evolution of the signal energy could be a good indicator to quantify the criticality of the damage state in a sample. The undamaged sample and the sample loaded at the highest level, for both sample

configurations, were considered for a first approach. That is to say a sample loaded in tension until 300 MPa along the warp's axis and a sample in the 45° configuration loaded in tension until 120 MPa. The time signal is plotted in Figure 152 for all those considered samples for a distance of 7.5 cm between the two transducers.

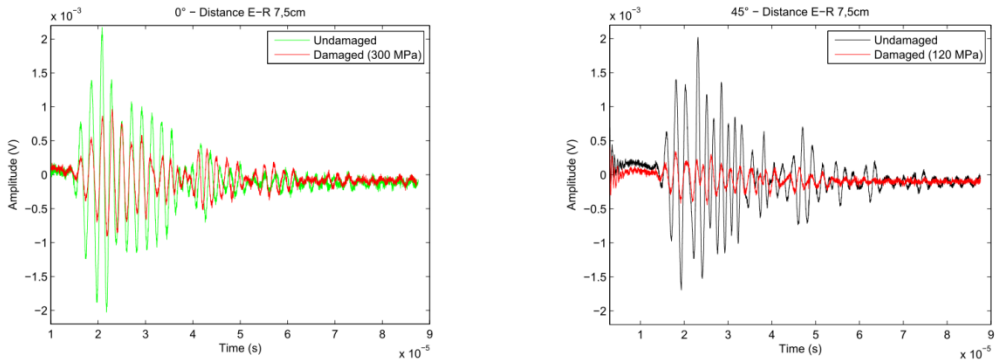

Figure 152 : Time signal of guided waves propagation inside an undamaged and a highly damage sample for a): Sample oriented at 0° from the yarns direction; b): Sample oriented at 45° from the yarns direction

First of all, an attenuation of the signal, between the undamaged and damaged sample, is noted for both fiber orientations. So a variation of the damage state can be detected with this ultrasonic technique. During a first analysis, the attenuation is noticed to be higher for the samples oriented at 45° from the yarns direction; as expected based on the results presented in the previous sections of this manuscript. Those observations are also noted for other distance between emitter and receiver.

In order to quantify this evolution in the damage state, the two damage indicators used to investigate the defects on the aluminum plate were then used. Each indicator is calculated for each experimentally considered transducer's positions. As a reminder, the first indicator is just the highest amplitude of the signal response. The second proposed damage indicator is the energy of the signal which is calculated as the area of the absolute response signal.

$$DI_3\ (i) = \frac{1}{n_{max}} * \sum_{i=0}^{n_{max}} Max(x(t)) \tag{V.65}$$

$$DI_4\ (i) = \frac{1}{n_{max}} * \sum_{i=0}^{n_{max}} \int abs(x(t))^2\ dt \tag{V.66}$$

The calculated damage indicators are indicated in Table 28 for the samples damaged at the highest level as well as for the reference samples. As a first observation, both indicators show a clear evolution between the undamaged and heavily damaged case. Both indicators also exhibit a higher decrease for the samples oriented at 45° from the fiber's axis than the samples oriented at 0° from the fiber's axis. This is clearly in agreement with the observation made in the previous part. Those two indicators seem to be relevant to evaluate damage in the considered composite material.

	Undamaged	**Damaged**	**Difference**
$\boldsymbol{DI_3}$ **| 0° (V)**	0.0214	0.0199	0.0015
$\boldsymbol{DI_4}$ **| 0° (V^2/s)**	$1.480\ 10^{-7}$	$1.441\ 10^{-7}$	$3.925\ 10^{-9}$
$\boldsymbol{DI_3}$ **| 45° (V)**	0.0243	0.0210	0.0032
$\boldsymbol{DI_4}$ **| 45° (V^2/s)**	$1.467\ 10^{-7}$	$1.302\ 10^{-7}$	$1.645\ 10^{-8}$

Table 28 : Values of the two proposed damage indicators for the two considered sample' orientations

The next step is to study the capability of our two indicators to quantify increasing state of damage for the other tested composite samples. Those results will be compared to the other damage indicators proposed in the present manuscript. As a reminder, the considered stress levels are indicated in the Table 29.

Applied stress 0° (MPa)	0	100	150	200	250	300
Applied stress 45° (MPa)	0	40	80	120	--	--

Table 29 : Stress level of each sample considered for the experimental set-up using guided waves

The same experimental procedure is considered for those samples. The calculated values of the two damage indicators are plotted in Figure 153 for both considered samples' orientation.

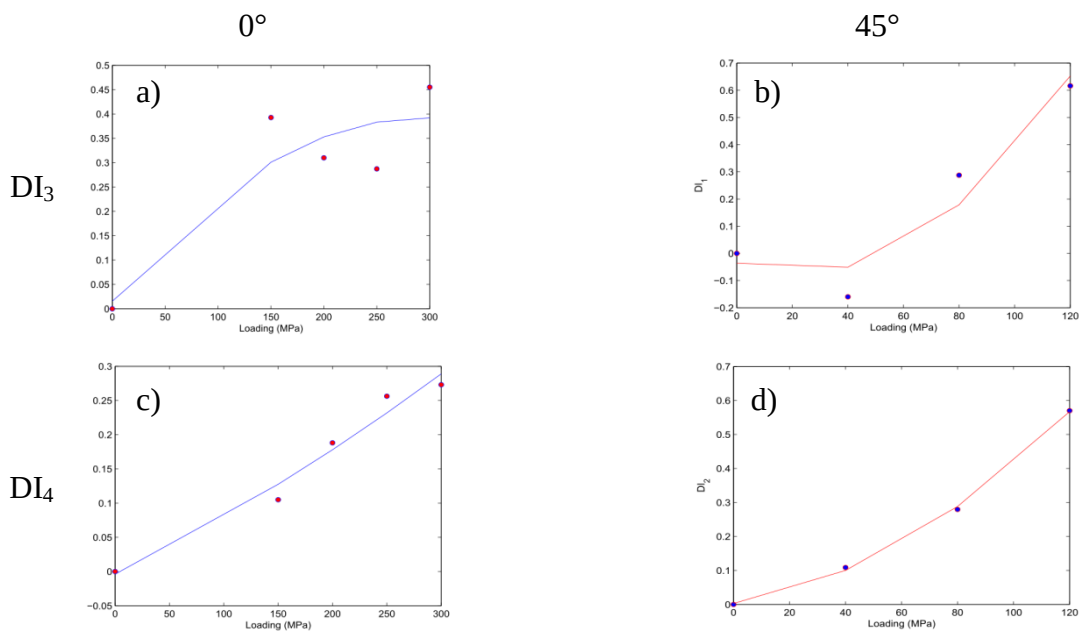

Figure 153 : Evolution the damage indicators DI_3 for the samples oriented at 0° and 45° in respectively a) and b).

Evolution the damage indicators DI_4 for the samples oriented at 0° and 45° in respectively c) and d)

Contrary to the preliminary results, the DI_3 indicator does not seems to be reliable to distinguish the different damage states. Indeed, its evolution is not a clear function of the

tensile loading. This is especially relevant for the samples oriented along the fiber's axis, for which the indicator value starts to decrease after 150 MPa until 250 MPa. For the samples oriented at 45° from the fiber's axis, the DI_3 indicator announces a lower damage state for the samples preliminary loaded at 40 MPa than for the undamaged sample. These two results are in contradiction with the observations made in the previous sections of this manuscript. This first indicator seems not to be reliable to quantify low amount of damage. It could be used as an alert to prevent failure in a structural part but not accurately evaluate the actual damage state.

However, the DI_4 indicator (which is the signal energy) appears to be better in agreement with the trend observed with the damage estimations from tensile tests, X-ray tomography etc…. i.e. an evolution of the damage state as function of the loading level for the two considered sample orientations. In addition, a more important increase of the global damage state before breakage is also noted for the samples oriented at 45° from the fiber's axis. This is particularly relevant in Figure 154 which proposes a comparison of the two samples orientation for the two proposed damage indicators.

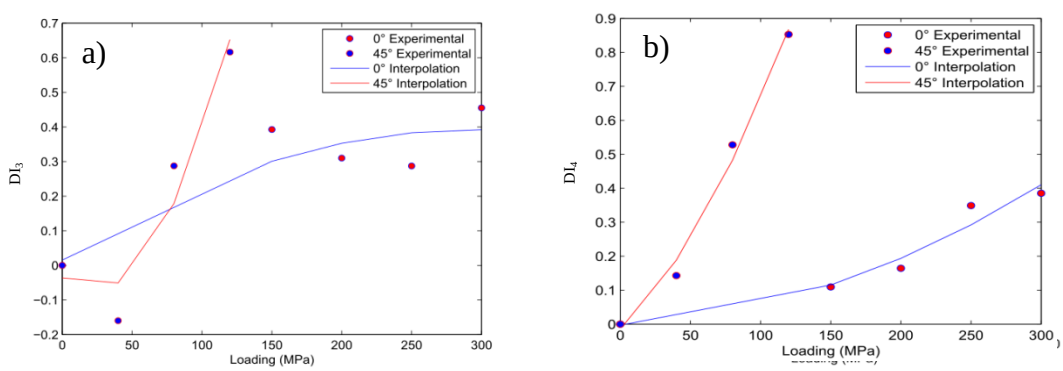

Figure 154 : Comparison of the evolution of the two considered damage indicator, DI_3 in (a) and DI_4 in (b), for the two considered samples' orientation

5) Conclusion

This chapter described an investigation of the different ultrasonic based Non Destructive Evaluation (NDE) methods that were considered for this study. A

bibliographical review of many techniques based on ultrasound was firstly held. It was meant to be focused on techniques that are currently under investigations by research teams for an application on composites materials.

The samples damaged during tension tests were first investigated by mean of ultrasonic C-scan in transmission. However, only macroscopic damage appearing on most damaged samples in the 45° configuration could be imaged.

Then, because it was investigated in previous works, the stiffness components measurement technique was chosen. In addition, it could provide a lot of information on the residual stiffness properties of the tested material. A different evolution of the stiffness properties between the sample tested in tension along the warp axis and the sample tested in tension at 45° from the warp axis was indeed observed. This means a decrease mostly of the stiffness components as function of the loading direction (namely C_{11}, C_{12}, C_{13} …) for samples in the 0° configuration. On the other hand, for samples in the 45° configuration, almost all the stiffness components in the main plane of the sample (namely the plane of the woven reinforcement) were impacted. A damage indicator based on the ultrasonic measurement made for the stiffness components was then proposed. It consists of a measurement of the phase shift between a pristine sample, used as a reference, and the tested one for different incidence angles. It was shown to indicate a higher value for the samples in the 45° configuration than for the ones in 0° configurations. This result is in agreement with the observations made during the tensile tests or during the X-ray tomography investigation, in respectively chapters III) and IV). Using this method of stiffness constants measurements, an evolution of the residual mechanical properties of the tested samples can be consequently obtained. This evolution can be used to later confirm numerical results from finite elements for example. In addition, this method could give a realistic estimation of the damage state of the tested specimens by considering investigations in multiple directions. However, this method remains complicated for use on-site in its current form. Another method that could more easily be used must then be considered.

It was then chosen to use guided waves to investigate the damage growth in samples. First, preliminary investigations on a steel plate with different induced defects showed that the energy of the transmitted signal could be used to classify those defects by size. The same method was consequently performed on the polyamide 66/6 reinforced with woven glass fibers samples. It was shown to be able to quantify the damage state when used on samples damaged by tension at a stepwise loading increment. Its evolution was shown to be in accordance with the observation made in the previous sections; that is to say a higher increase of the damage state for the sample in the 45° configuration than for the ones in the 0° configuration.

An investigation of the propagated guided waves mode was proposed beforehand but does not give conclusive results to quantify the induced damage. When compared with the results from the *Disperse* software, the mode S_1 was found to propagate in the samples oriented along the yarn's axis. For the undamaged sample in the 45° configuration, both S_1 and A_1 modes were found to propagate. However, neither mode conversion nor apparitions of additional modes were observed in the damaged state of the samples in both configurations. In this frequency range, the analysis of the propagated wave mode does not seem to be able to characterize the damage state. It was just observed that when an applied loading of 80 MPa is reached, the attenuation in the transmitted signal is too high to properly use a 2D Fast Fourier Transform to distinguish any transmitted mode.

VI) Validation on samples impacted by drop weight

Contents

1) Drop weight impact tests 221

2) X-Ray tomography investigations of the impacted plates 225

3) Ultrasonic C-scan results 226

4) Validation of the ultrasonic based damage indicators 232

a) Ultrasonic measurement of stiffness components on the impacted plates ... 232

b) Guided waves based approach 235

5) Conclusion 239

In the chapter V), the damage state, induced by tensile tests, of samples were investigated by mean of ultrasonic based methods. However, in the automotive industry the investigation of damage after impact, as well as, the study of fatigue post-impact is of highest importance. Hence, the present chapter is dedicated to the validation of the experimental approaches developed in chapter V). It focuses on the results for woven glass fibers reinforced polyamide 66/6 plates damaged at different impact energies. More specifically, drop weight test on geometrically adapted plates is considered. The damage introduced through the impact is visually inspected and then is investigated via ultrasonic C-scan imaging, in transmission and reflection. The related experimental results are deeply discussed. The last subsection deals with the validation of the different proposed damage indicators based on ultrasound. The evolution of stiffness components, with the impact energy, is firstly obtained via ultrasonic measurements based on the method used in section V)-3)-a). The two first damage indicators are consequently evaluated. Guided waves are then used to investigate the samples. An attempt is made to validate the remaining two

damage indicators. However, it must be pointed out that another signal processing was required to detect the damage induced in those samples.

1) Drop weight impact tests

Four woven glass fibers reinforced polyamide 66/6 plates of 100 mm x150 mm x1.53 mm (fibers oriented) were impacted at different drop weight energies, which are respectively: 10, 15, 17.5 and 20 Joule. The specimens were all cut along the fibers axis (in 0° configuration). Information about the tested plates are sum-up in the Table 30. The impact tests were performed in the LAMPA at ENSAM Angers campus with the help of Pr. Laurent Guillaumat. A 16 mm diameter impactor of 1.02 kg was used. The plates were clamped during the tests, a force sensor is mounted on the impactor and a displacement sensor is installed below the plates (Figure 155). Both force vs time and displacement vs time curves could therefore be extracted from the experiments, and they are plotted on the Figure 156-a and Figure 156-b. The evolution of the energy E(t) is then computed as $E(t) = \int_0^{z(t)} F(t)dz$, with F the contact force and z the deflection, and plotted in Figure 156-c. Using the evolution of the energy, the real impact energy E_i and the absorbed energy E_a are finally estimated as indicated in Figure 156-c. The real impact energy corresponds to the maximal energy whereas the absorbed energy corresponds to the energy that remains when the applied load returns to zero. This information is summed-up in Table 30. The absorbed energy E_a can also be estimated as the difference between the impact energy E_i and the rebound energy E_r or: $E_a = E_i - E_r$. They are calculated from the kinematic energy relation: $E_i = \frac{1}{2}m{v_i}^2$ and $E_r = \frac{1}{2}m{v_r}^2$. The two velocities are measured from the displacement vs time curve respectively before and after the time when the impactor rebound on the plate. It was found the evaluation of the absorbed energies using the integral calculus and using the kinematic energies gives similar results. The absorbed energies given in Table 30 were estimated using the first method.

On the force vs time curve, the plate impacted at 10 J exhibit measured force amplitude clearly lower than the measured value for the other impacted samples. The same observation can be done on the displacement time curve. In addition, the curves for the 20 J shows important oscillation of the displacement; it must be mentioned that this effect is only due to the saturation of the displacement transducer (sensor). This saturation may

induce errors in the calculation of the energy; consequently the measured impact energy and the absorbed energy for the samples impacted at 20 J could be incorrect.

Plate number	**8**	**9**	**7**	**10**
Drop height (m)	1.00	1.50	1.75	2.00
Expected impact energy (J)	10.00	15.00	17.50	20.00
Measured impact energy (J)	8.92	14.45	16.36	17.59(*)
Absorbed energy (J)	3.24	6.65	7.73	4.48(*)

Table 30 : Drop height and impact energies of the four impacted composite plates. The displacement sensor saturates during the test. The values with (*) must be considered with caution because of the displacement sensor saturation noticed during some impact tests

Figure 155 : Drop weigh test machine installation of LAMPA at ENSAM Angers

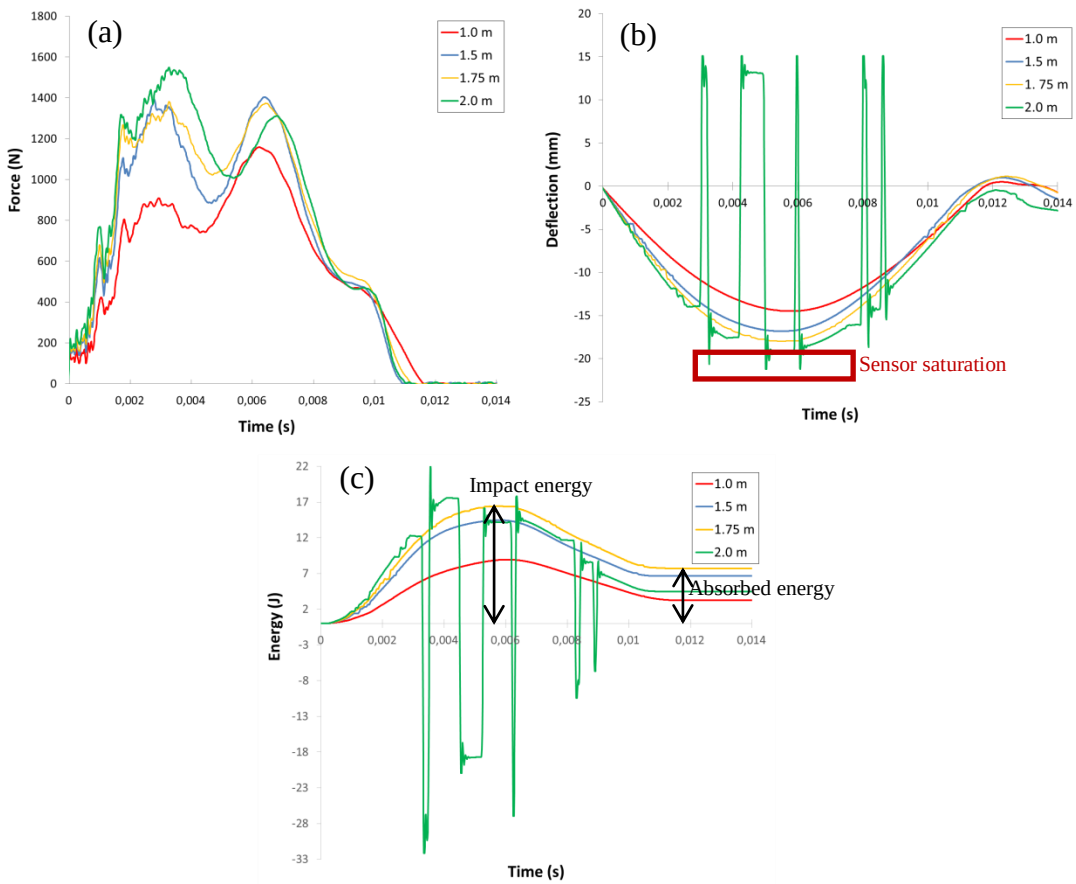

Figure 156 : (a) Force time curves, (b) displacement time curves and (c) Energy time curves for the four considered drop weight energies. The displacement sensor saturates during the 20 J impact test.

Visual observations have been performed on both sides on the four impacted plates; they are shown in Figure 157 and Figure 158. It can be observed that the 10 J impacted plate does not exhibit any visible damage on any side of the sample. However, all the other plates contain visible damage on the opposed side to the impacted surface, this is especially significant on the 17.5 and 20 J plates. When observed with more attention, one can note that only confined damage area, with a dimension of 696.21 µm, was induced by the 15 J impact. More important crack network is visible on sample surface oppose to the impact. The crack network appears to be more expanded for sample impacted with an energy of 17.5 J than for the one impacted at 20 J.

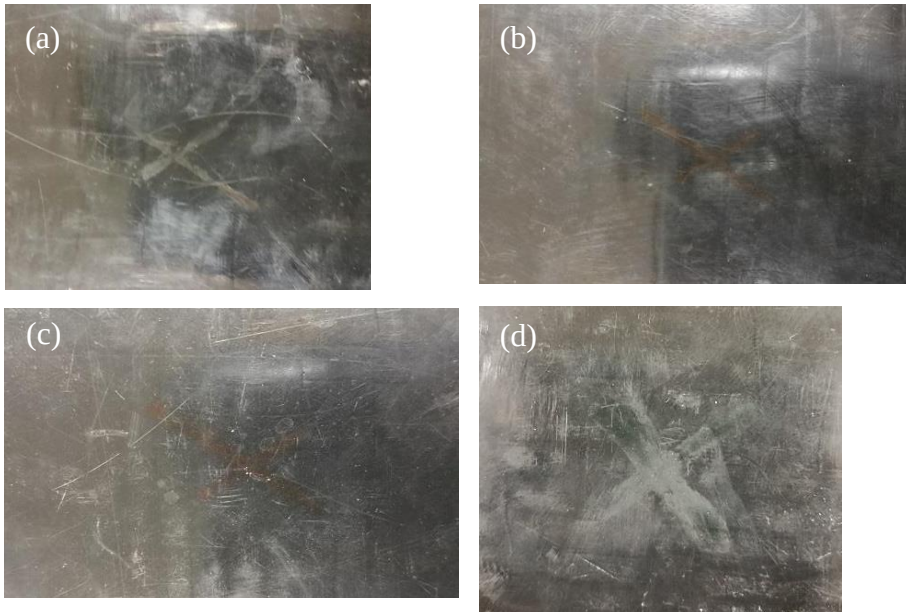

Figure 157 : Visual observation of the plates on the impacted side for an impact energy of (a) 10, (b) 15, (c) 17.5 and (d) 20 J

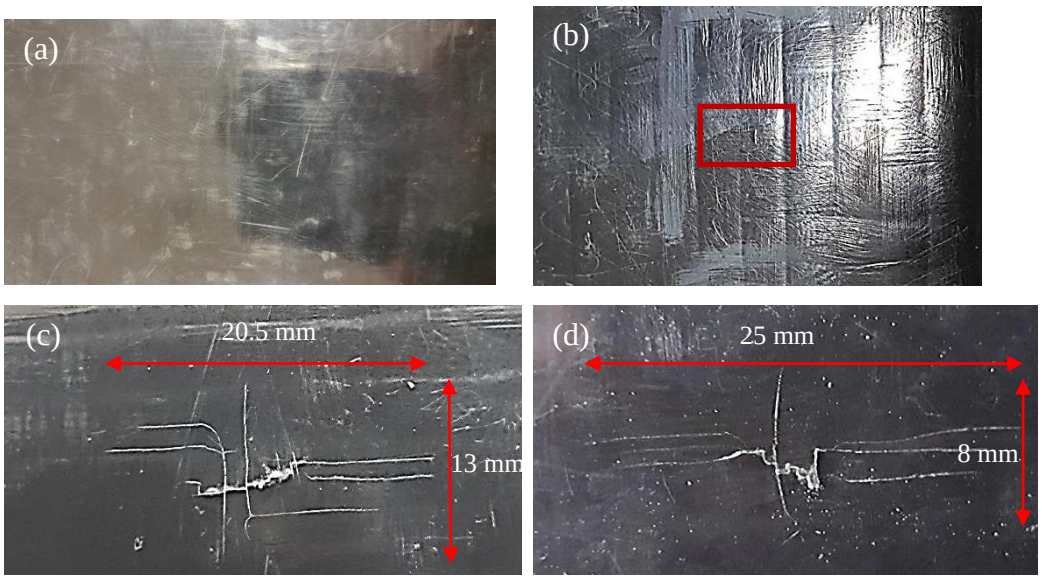

Figure 158 : Visual observation of the damage in the plates on the opposite of the impacted side for an impact of (a) 10, (b) 15, (c) 17.5 and

2) X-Ray tomography investigations of the impacted plates

The four plates were investigated using the X-ray tomography method presented and used earlier in this manuscript. The same acquisition parameters as the ones in section IV)-4) were considered for this investigation. It is worth reminding that volumes of 16.5 x 16.5 x 1.5 mm were obtained from those acquisitions. All the acquisitions were centered where the plates were impacted. First of all, no particular damage was noticed on the plate impacted at 10 J. The observed defects, such as micro-porosity and void near the yarn's extremities does not look larger in size or present a larger extent than what has been observed on undamaged samples investigated on chapter IV) For the sample impacted at 15 J, the crack visible on the surface was imaged. It was found to be a superficial crack with a dimension of 0.7 mm compatible with the results found in the upper section. The other two samples impacted at 17.5 J and 20 J, exhibit larger crack network with associated fibers breakage. Images from those samples are respectively represented in Figure 159 and Figure 160. For both samples, the damaged area remains located in the first layer of the composite.

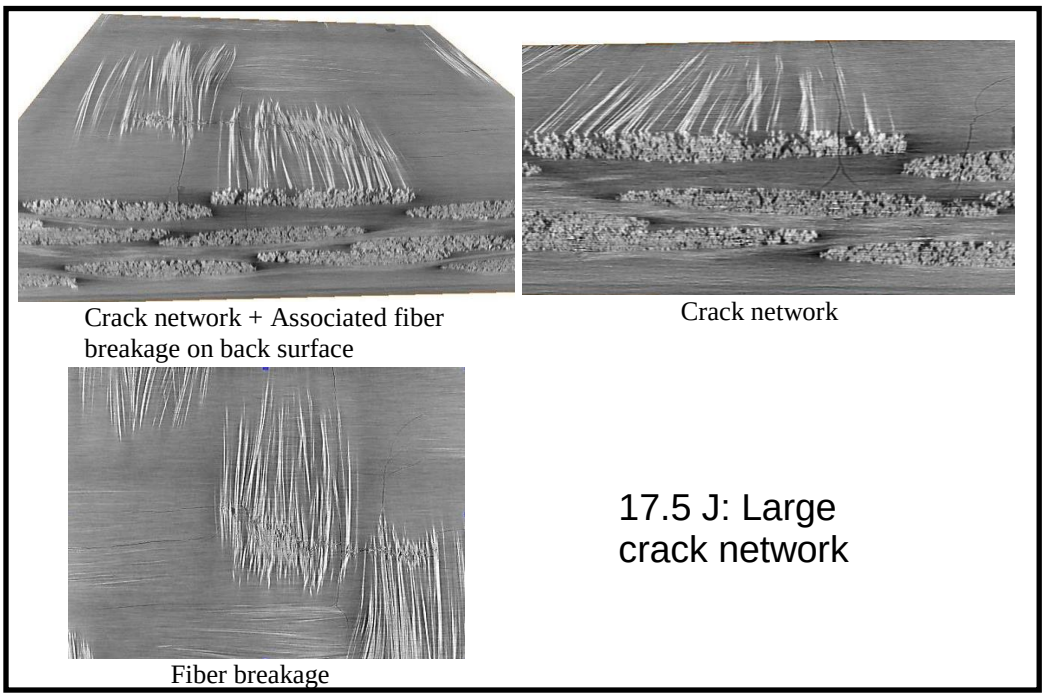

Figure 159 : X-ray tomography observations performed on the impacted at an energy level of 17.5 J

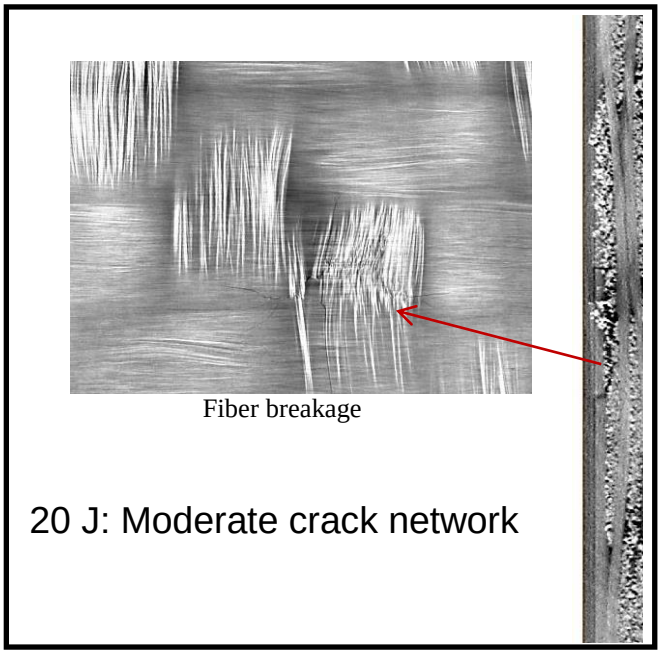

Figure 160 : X-ray tomography observations performed on the sample impacted at an energy level of 20 J

3) Ultrasonic C-scan results

On all the investigated plates, ultrasonic C-scan tests were performed both in transmission and in reflection. The ultrasonic polar C-scan of Georgia Tech Lorraine, with a spatial resolution of 0.3 mm, was used to localize the defects in the plates. Figure 161 depicts some of the C-scan imagings in transmission, obtained by using 10 MHz immersion transducers, performed on undamaged samples. A relatively low amount of damage can be noticed on those plates. It can be assumed that those damages were introduced during the cutting process. Indeed, the specimens have been machined using a water cooled tile cutter. It is assumed that those defects are not excessively important.

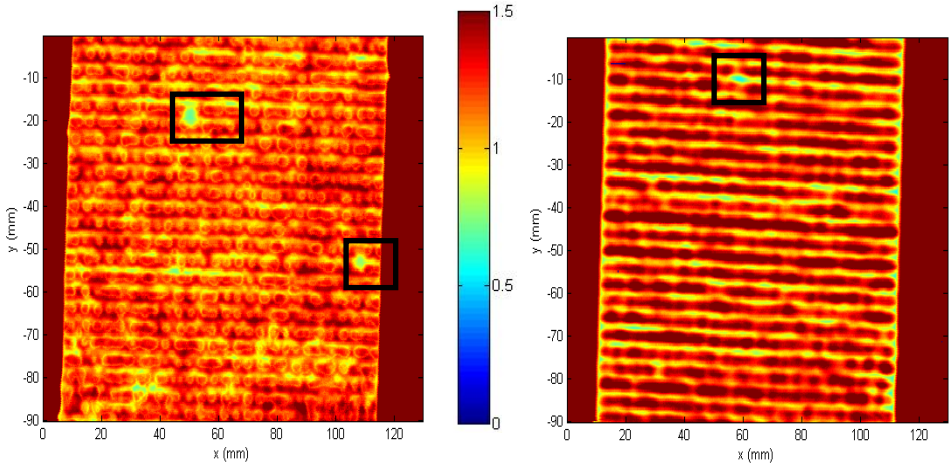

Figure 161 : Ultrasonic C-scan in transmission on specimens prior impact tests with some visible defects

After the impact tests, the four tested plates were inspected with a C-scan in transmission using 5 and 10 MHz immersion transducers. The resulting imagings for each frequency are respectively given in Figure 163 and Figure 162. It can be noted that for both tested frequencies, no defects can be noted on the plates submitted to a 10 J impact. However, for all the other impacted plates a defect can be observed in the center of the plate near the impact region. This is in agreement with the visual inspection discussed earlier in this section; therefore it can be assumed that not important damage was induced for the 10 J impact. It remains difficult however to make a clear distinction between each of the other three tested plates.

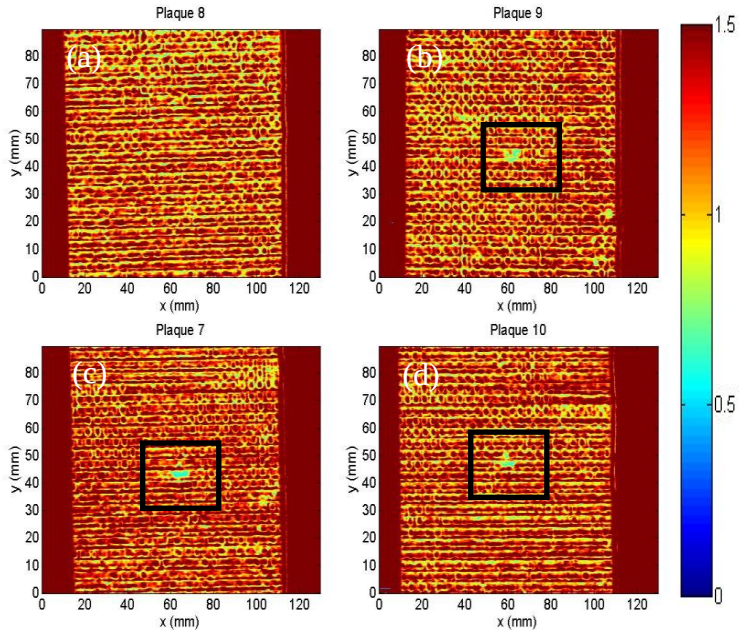

Figure 162 : Ultrasonic C-scan imaging in transmission with 10 MHz transducers for the plates impacted at an energy level of (a) 10, (b) 15, (c) 17.5 and (d) 20 J

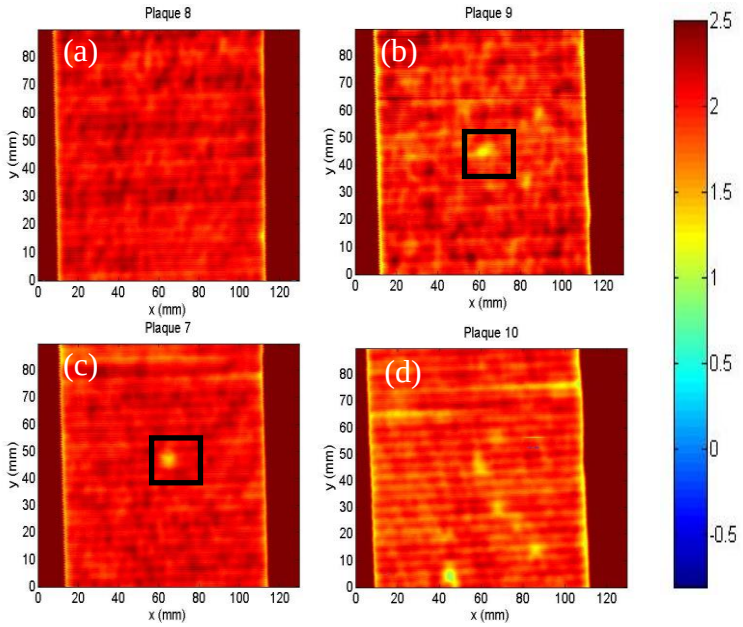

Figure 163 : Ultrasonic C-scan imaging in transmission with 5 MHz transducers for the plates impacted for an impact of (a) 10, (b) 15, (c) 17.5 and (d) 20 J

VI) Validation on samples impacted by drop weight

Finally, ultrasonic C-scans in reflection were carried out on the four samples. A 10 MHz immersion focused transducer was used for the investigations. This study is considered in order to localize the defects along the thickness of the samples. To do so, two scans were performed on each sample, one on the impacted side and other on the opposite side. The obtained imagings for the plate impacted at 20 J are all shown in Figure 164. On both investigated surfaces the location of damage induced by the impact could be identified. It can be found at the area where the black lines intersect. B-scan observations along the thickness are proposed along those black lines. For the B-scan imaging performed on the surface with the damage visible, discontinuity appear near the impact location. However, it is not possible to locate the position along the thickness of the defect because of reverberation effect that seems to be induced. On the imaging from the impacted surface, one can see that no damage is noted on the first reflection line; an unaltered line is actually clearly visible. However, a permanent indentation, that could not be detected prior this investigation, is also identified at the location of the impact. This defect is caused by the impact and is usually referred to as a Barely Visible Indentation Damage (BVID). This visible indentation is used during visual inspection to indicate the presence of internal impact induced damage as explained in the Figure 165. For the plate impacted at 20 J, this permanent indentation was actually not noticeable by naked eye earlier on. The permanent indentation was consequently in the Barely Visible Indentation Damage (BVID) domain.

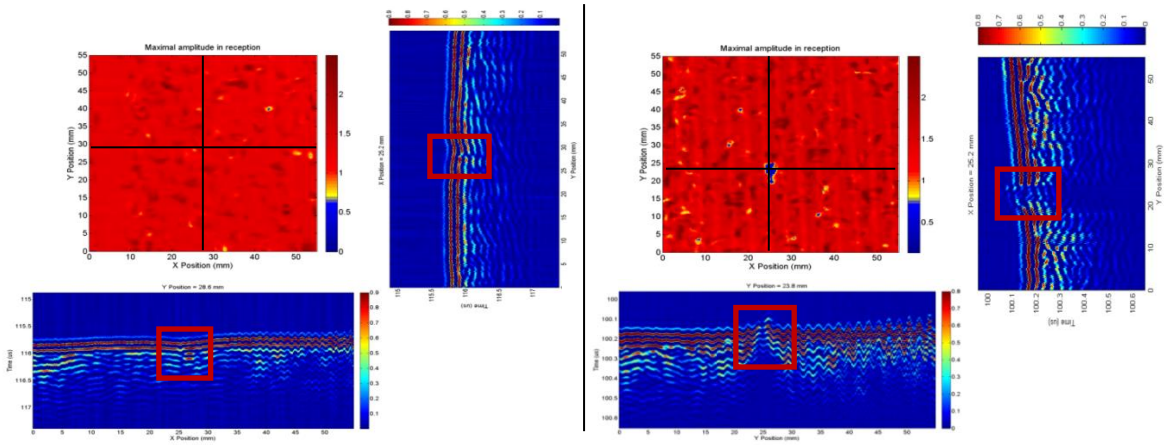

Figure 164 : Ultrasonic imaging in reflection of the plate impacted at 20 J. Impacted side (Left) and the opposite one (Right). B-scan in the X and Y directions for both side.

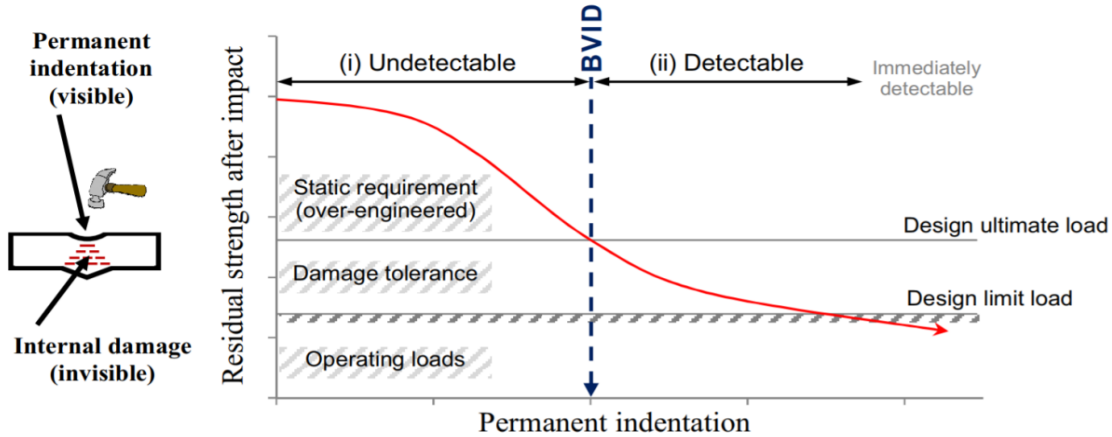

Figure 165 : Impact damage tolerance and permanent indentation concept [123]

In order to display the size, in plane, of this permanent indentation more clearly, the time of arrival of the first positive peak is extracted and plotted as a map in Figure 166-a. Then the depth of the indent is estimated using the B-scans. To do so, the difference, of time of arrival of the first peak, near the impact location and far from it is measured, and visualized in Figure 166-b. By considering a sound propagating velocity in water of 1478.8 m/s, as measured in section V)-3), the depth of the permanent indentation is estimated as 0.074 µm ± 0.014 µm. The same analysis was performed for the three other impacted plates. The size of the permanent indentation is reported in Table 31.

A permanent indentation of 4.2 x 3.6 x 0.074 mm was seen on the plate impacted at 20 J; for the impacted at 17.5 J it reaches 3.8 x 2.8 x 0.088 mm. The size of the indentation continues to decrease with the impact energy, and reaches 3.2 x 3.0 x 0.045 mm. For the plate impacted at 10 J, no noticeable indentation was observed using both B-scan and C-scan observation. It remains difficult to claim that no indentation was induced by the10 J impact because of the measuring conditions and the time sampling. Indeed, the latter is just sufficient to observe the indentation on the plate impacted at 15 J. However, it can be mentioned that we are no longer in the BVID domain. The evolution of the permanent indentation size is in agreement with the observation made using X-ray tomography. In

addition, based on those results, a relation between the size of the permanent indentation and the apparition of internal defect can be proposed. Here, for an indent size below 3.2 x 3.0 x 0.045 mm, only superficial subsurface damage could be observed. The analysis of the observed permanent indentation can provide an estimation of the potential internal induced damage. Of course in order to be reliable, more impact energy levels need to be considered and repeated. The present analysis provides a preliminary investigation of this method's potential.

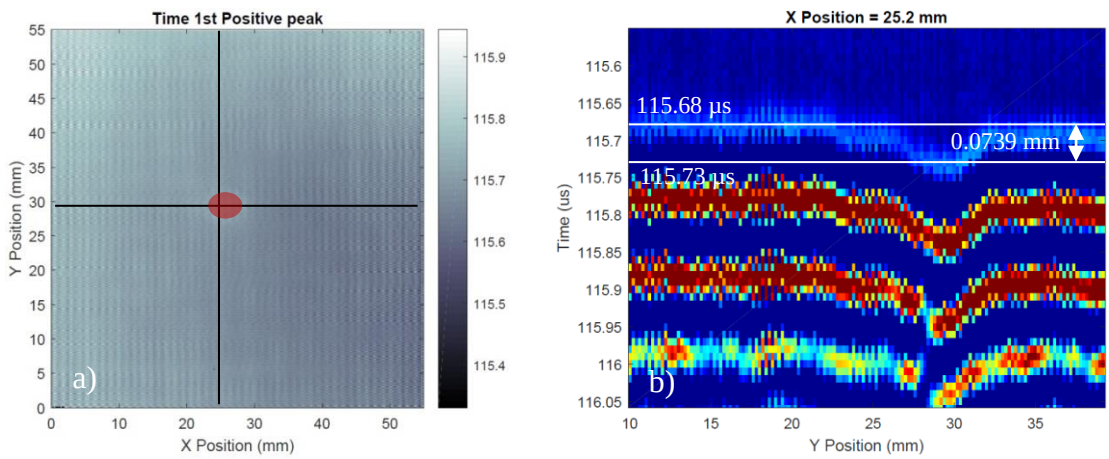

Figure 166 : (a) Times of arrival map for the first peak in the plate impacted at 20 J. The permanent indentation is highlighted in red (b) Zoom in on one of the b-scan from Figure 164.

Impact energy	**10 J**	**15 J**	**17.5 J**	**20 J**
Size in plane (mm) ± 0.2 mm	--	3.2 x 3	3.8 x 2.8	4.2 x 3.6
Depth (mm) ± 0.014 mm	--	0,045	0,088	0,074

Table 31 : Permanent indentation size measured using ultrasonic C-scan method in reflection

4) Validation of the ultrasonic based damage indicators

a) Ultrasonic measurement of stiffness components on the impacted plates

The four impacted plates are investigated with the ultrasonic method of stiffness components measurement described in the previous chapter. Since those plates are bigger than the tensile samples presented in the two previous sections, the three main planes of the samples are investigated whereas only two could be used for the tensile samples. Therefore, the nine stiffness components may be identified as for the first undamaged sample presented in the section V)-3)-a). The nine obtained stiffness components for the four plates are represented on the Figure 167. The components obtained on the undamaged sample in section VI)-2)-a) are also added on those graphs. It must be pointed out that those results come from another experiment campaign; therefore the measurement uncertainties could not be comparable to those determined for the present section. However, the stiffness components identified on the sample impacted at 10 J are close to the ones acquired on tensile tests samples.

When compared to the stiffness components evolution performed in chapter V), the observed scheme is different from the ones observed for samples damaged by tension. This indicates that this method can still evaluate damage state that results for different kind of mechanical solicitations. A global decrease of the components is noticed starting from 17.5 J at the exception of C_{12}, C_{44} and at a lower level the C_{55}. However, it must be noted that the uncertainty on the C_{12} and C_{44} is very important; it remains difficult to be sure of the evolution depicted. This is in accordance with the estimation of damage from other techniques. That said the damage state of the sample impacted at 17.5 J clearly differs from the two samples impacted at lower energy. It is difficult however to conclude on the sensitivity of the method to detecting the damage on the sample impacted at 15 J. A decrease of the components C_{11} and C_{13} from 10 J compared to 15 J is noted but remains low in amplitude compared to the decrease from 15 J to 17.5 J. The following important

point is to know if the difference, in terms of damage level, between the sample impacted at 17.5 J and the sample impacted at 20 J could be determined. However, as for the investigation by mean of X-ray tomography, it is difficult to draw a definitive conclusion. Indeed, only minor evolution of the components is noted between 17.5 J and 20 J. Therefore, others impact energies should be considered to determine the correct evolution of stiffness components when increasing the impact energy.

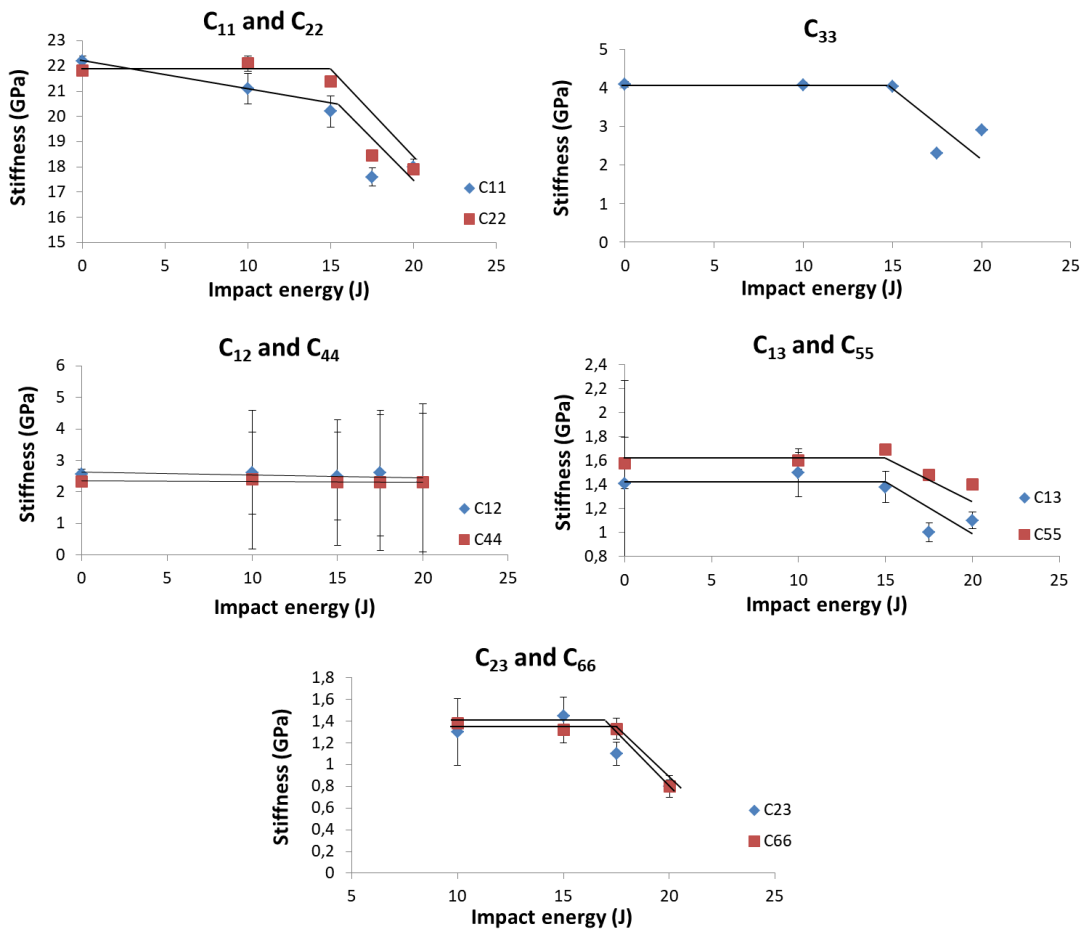

Figure 167 : Evolution of the nine stiffness components of the tested composite material when increasing drop weight energy

In a similar manner, as for the samples damaged by quasi-static tension loading, the proposed ultrasound based damage indicators are calculated in this subsection. It is worth recalling, that the first damage indicator is calculated as the Frobenius norm of the

computed stiffness tensor. The second indicator is calculated as the average, over the three investigated main planes of the composite, of the phase shift between signals propagating in the damaged sample and signals propagating in a reference undamaged sample. They are referred to as DI_1 and DI_2 later in this section as in section V)-3)-d). The evolution of the two indicators is plotted in Figure 168 as function of the chosen impact energy.

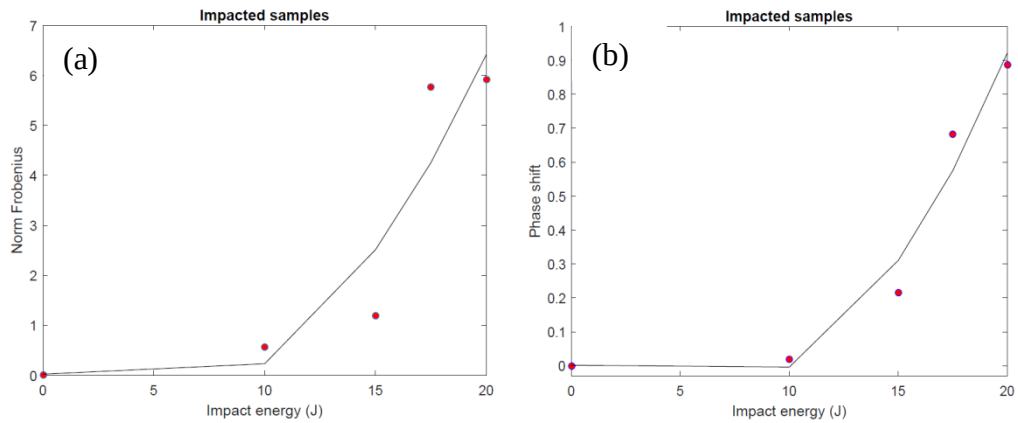

Figure 168 : (a) Evolution of the Frobenius norm of the stiffness tensor obtained by ultrasound method and (b) evolution of the phase shift indicator with the impact energy

The two indicators exhibit a similar evolution when increasing the impact energy. For both curves, the indicator starts to increase noticeably after an impact of 15 J. A step between 15 J and 17.5 J is visible for both cases. It is more pronounced however for the Frobenius norm. Finally, the value of the indicator continues to increase until 20 J. This observed evolution of the two proposed indicators is in agreement with the samples analysis performed using X-Ray tomography. Indeed, no noticeable damage was detected on the samples impacted at 10 J, whereas a minor damage was seen on the 15 J impacted samples and, finally, the two other samples exhibit large cracks network.

b) Guided waves based approach

The same experimental procedure using guided waves, introduced in V)-4), in used on the four impacted composite plates. Two 1 MHz *Panametrics V103* contact transducers are used in transmission. They are put on the surface of the plate on each side of the location were the plate was impacted. Each of the transducers is spaced of 3 cm from the impact location. A burst of 5 cycles of a 500 KHz cycles is emitted using a waveform generator (*Agilent Technilogy model*). The transmitted signal is amplified after reception by an amplifier (from *Krohn-Hite model 7500)* and recorded with an oscilloscope. The transmitted signals recorded for each of the four plates are plotted in Figure 169-a. However, the transmitted amplitude of the signal clearly not decreases with the level of impact energy. This is not in agreement with the evolution of the damage indicator DI_4 proposed in V)-4). Therefore, the quantification of damage using the signal energy is not reliable. Another approach is considered to evaluate the damage; it is based on the time of arrival change. The time shift is calculated by cross correlation whereas; the correlation coefficient R_{xy} is expressed as:

$$R_{xy}(\tau) = \frac{\sum_{i=1}^{N}(x_{i+\tau})(y_i{}^*)}{\sqrt{\sum_{i=1}^{N}(x_{i+\tau})^2}\sqrt{\sum_{i=1}^{N}(y_i)^2}} \qquad \text{(VI.1)}$$

With: x the investigated signal and y the signal from the reference plate and * is the complex conjugate.

Recall that when using this method, the investigated signal (x) is shifted in time by different given τ, the correlation coefficient R_{xy} is calculated for each τ. When a maximal value of R_{xy} is found, the associated τ is the time shift between the signals x and y. This is of course true if the value of the correlation coefficient is sufficiently high (typically higher that 0.9). Otherwise, the two compared signals are too different from each other and the value of time shift found may not be induced by difference in time of arrival.

The correlation coefficient is plotted function of the time lag in Figure 169-b. The signal recorded on the plate impacted at an energy level of 10 J was used as a reference. Here, the time lag that correspond to the highest correlation coefficient increase with the drop height impact. Indeed, as observed in the previous subsection no damage could be detected on this sample. The values of time lag are indicated in Table 32. The estimation of the time lag does seem to be relevant to detect damage.

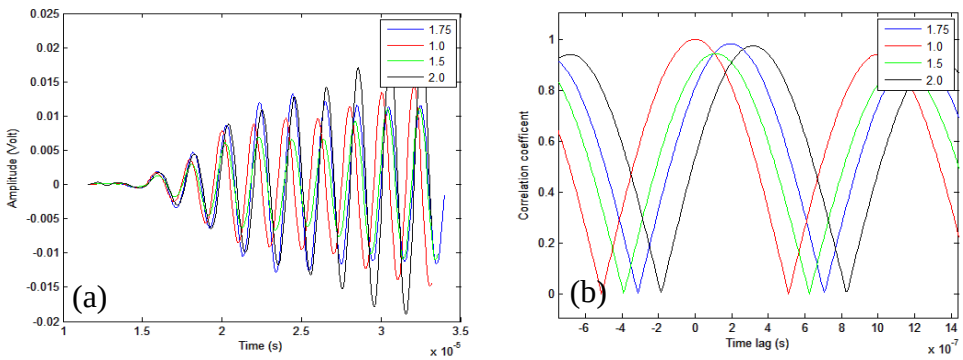

Figure 169 : (a) Transmitted guided wave signals measured on the plates impacted at different energy levels. (b) Cross-correlation results obtained on the plates impacted at different energy levels with considering the plate impacted at 10 J as a reference

10 J	**15 J**	**17.5 J**	**20 J**
0	1.12e-7	1.92e-7	3.20e-7

Table 32: Time lag obtained with cross correlation with the 10 J impacted plate considered as a reference

Now, the experimental procedure is extended in order to consider measurement over all the size of the plate. The two transducers are now attached to the robot arm already used in the previous section. The robot then scans a 70 mm long line on the plate impacted at 20 J. A schematic representation of this experimental set-up can be found in Figure 170.

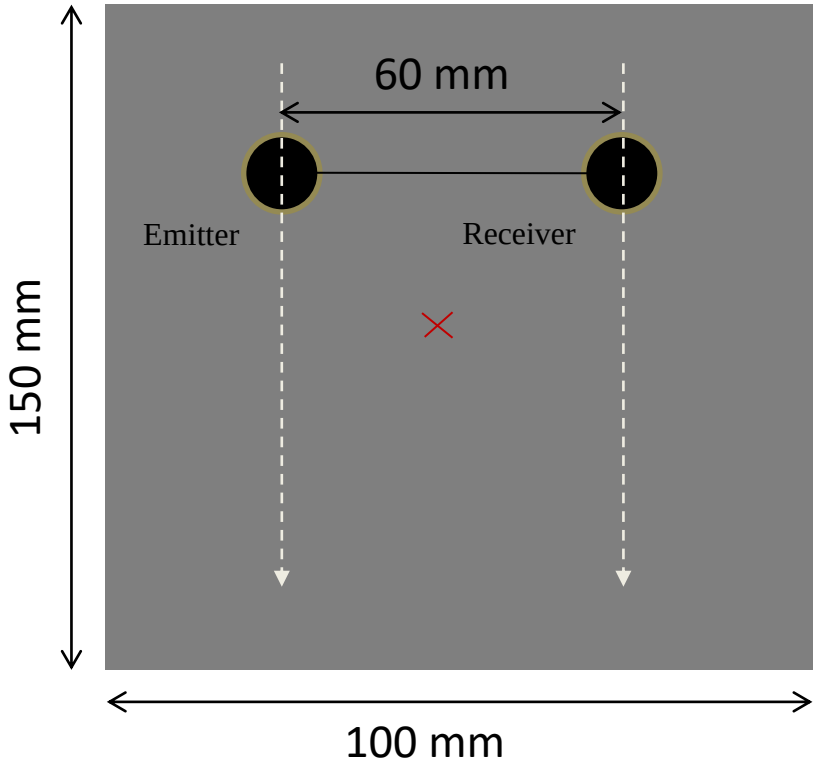

Figure 170 : Schematic representation of the experimental set-up for the guided waves investigations of the plate

A 125 µs signal is recorded every 0.3 mm. In order to evaluate the repeatability of the method, 6 measurements are performed. The highest value of cross correlation coefficient and the associated time lag are evaluated. The signal recorded on the first position (far from the impact location) is considered as a reference signal. It is worth noting that on every position a value of correlation coefficient sufficiently high, i.e. higher than 0.9, was obtained; at the exception of the measurement depict in yellow (Figure 171-a). Consequently, this result must be examined with caution and could even be considered as not relevant. When the time lag function of the position is analyzed, it is increasing around 25 cm when the impact was performed on the plate (Figure 171-b). However, important variation is noted between the 6 measurements. Even if the yellow curve is not considered, important difference between the remaining measurements is still noted. This can be attributed to the coupling between the plate and the transducers that do not remains constant for every measurement. This can be verified on the representation in amplitude of the

measured signal (Figure 172). Indeed, with this experimental set-up, the amplitude is varying a lot from a measurement to another. So the attenuation in amplitude cannot be induced only by the impact from damage. Nevertheless, the difference in time near the impact location is high enough to be used to detect damage (Figure 171-b). It is yet difficult to discuss the sensibility of this set-up; the latter requires to be upgraded to avoid a loss of coupling between sample and transducers. One proposed solution is to change the system that holds the transducers in order to add springs inside.

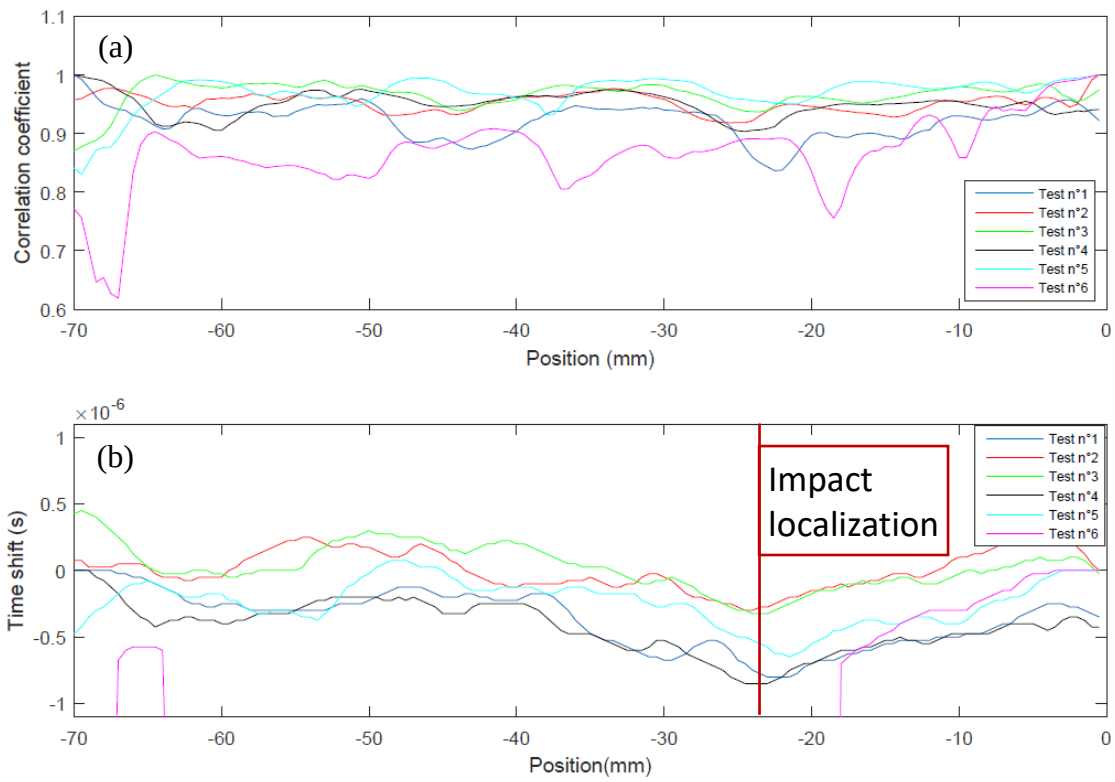

Figure 171 : (a) Evolution of the maximum correlation coefficient with the transducers position. (b) Evolution of the time lag with the transducers position

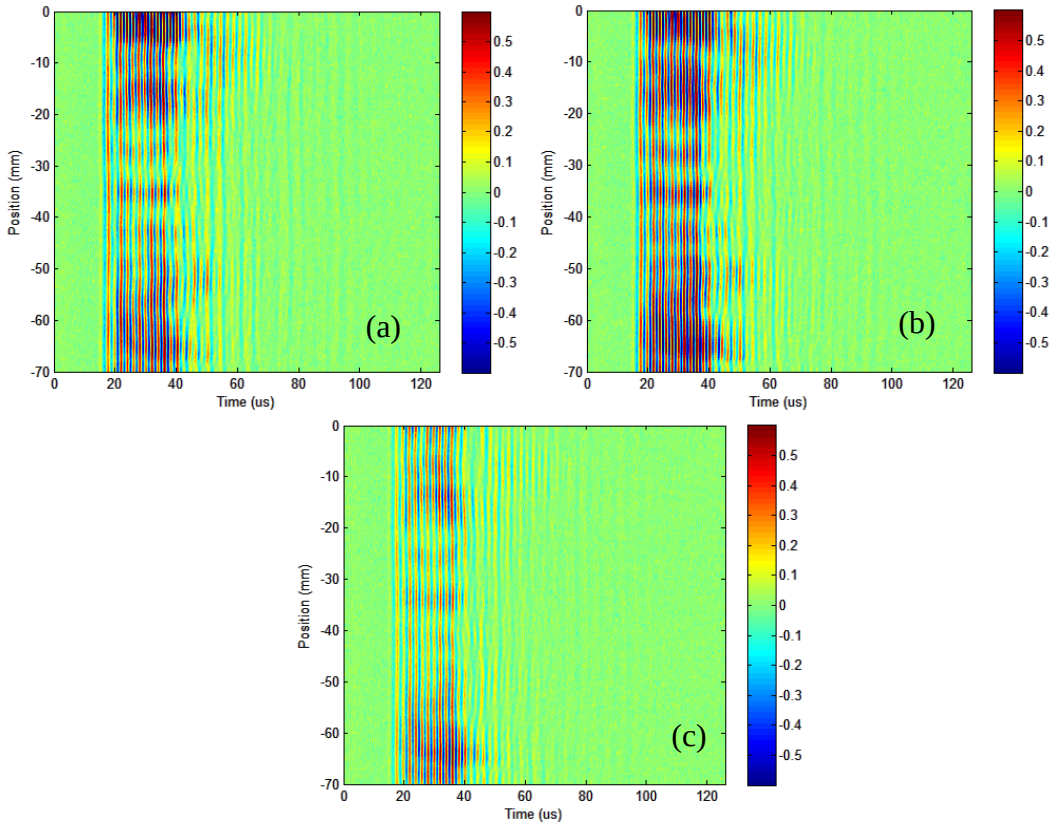

Figure 172 : Example of three typical L-scans obtained from the plate impacted at 20 J

5) Conclusion

This chapter was dedicated to the validation of the obtained ultrasonic results on impacted samples. Drop weight impact solicitation was chosen because it is more close to events that composite parts may undergo both during their manufacturing or life in service. The chosen energy levels of impact were selected in order to remain in the Barely Visible Impact Damage (BVID) range. By doing so, the capability of ultrasound to detect those small damages can be experienced. The drop weight impact tests were performed. At impact energies of 10 J, 15 J, 17.5 J and 20 J were chosen.

The samples were investigated using X-ray tomography after the impact tests. Cracks were observed most in the 17.5 J and 20 J impacted plates. The main damaged area is located for both cases in the first ply on the non-impacted surface. Some meta-delamination was even imaged for the samples impacted at 20 J. However, for the sample impacted at 15 J, only a small subsurface crack was noticed on the non-impacted surface whereas no particular damage could be distinguished on the sample impacted at 10 J.

Then, ultrasonic C-scan in transmission and reflection were used to display the damaged area. Using C-scan in transmission, a damaged area can be noticed for samples impacted at 15 J, 17.5 J and 20 J. Nothing was observed for the sample impacted at 10 J. Ultrasound in reflection was used afterward to measure the size of the Barely Visible Indentation Damage (BVID). This permanent indentation is used in the industry during visual inspection to estimate the induced internal damage. Here, the permanent indentation were barely visible by naked eye but could be precisely measured using ultrasound. This permanent indentation was found to increase in size and depth with the energy level of impact. The size of the permanent indentation of the sample impacted at 15 J could be used at a damage threshold. Indeed, below this energy level, no damage was detected using X-ray tomography.

The decrease of stiffness components with the energy level of impact, calculated using the method from section V)-3), was found to exhibit a specific scheme. This latter is different from the ones observed for samples in 0° and 45° configuration damaged by tension. Here, a global decrease of the components could be observed starting from 15 J. The in-plane components C_{12} and C_{44} remain unaltered by the impact tests. It is logical to observe an important decrease of the out plane components when submitted to impact. Those results are of primary importance for the estimation of the residual mechanical behavior of the impacted plate. The two proposed indicators, the Frobenius norm of the stiffness tensor and the multi angle phase shift, were then calculated in a same manner as in chapter V). Their evolution was shown to be in adequacy with the X-ray tomography analysis. With this result, the first two indicators were found to be suitable to quantify the damage induced by impact which validates as well the results from chapter V). However,

the proposed damage indicator based on guided waves could not be validated in this chapter using the experimental results presented in this chapter. Indeed, it was observed that the energy of the signal could not be used to quantify nor detect the damage induced by impact. But, the time shift, compared with a reference state, estimated by cross-correlation was found to be a better damage indicator, when the area near the impact location is investigated. An experimental set-up was made up in order to investigate the whole sample. Even though the location of the impact was accurately detected, this set-up still requires to be updated. In fact, the variation in the quality of the coupling between the transducers and the plates can lead to major deviation.

VII) Concluding remarks and further works

1) Concluding remarks

The current work has two main objectives, first it was aimed at investigating the growth of damage in a polyamide 66/6 reinforced with woven glass fiber. This composite material developed by DuPont is used by the cars manufactures PSA to replace some of the metallic parts. This material can help reduce the weight of cars without decreasing their mechanical resistance and lifetime. Then, this work was also focused on the study of Non Destructive Evaluation (NDE) methods, based on ultrasound, and more specifically on their capability to quantify different induced damage states on composite materials. Several NDE methods were considered to evaluate damage induced using several mechanical loading.

In order to propose a suitable experimental approach founded on NDE methods, the investigation of the mechanical and damage behavior of the composite material was performed by mean of static tensile tests. Two samples orientation were chosen: oriented along the warp axis (later referred as 0° configuration) and oriented at 45° from the warp axis (later referred as 45° configuration). From a macroscopic point of view, the two configurations exhibit different mechanical responses. For the 0° configuration, a linear brittle stress/strain behavior with limited induced damage was witnessed. Whereas for the 45° configuration, a non-linear ductile stress/strain behavior with higher appearance of damage was observed. Evolution of damage was calculated as the elastic modulus on stress/strain curve decreases. Using Digital Image Correlation (DIC), the two dimensional strain fields showed in addition that, in 0° configuration, the tensile test induced only strain along the loading direction. For the other configuration, the mechanical response also first exhibits an increase of the strain along the loading direction. However, after some time, the response exhibits a coupling between in-plane shear and tension. This response was found to be induced by reorientation of fibers along the loading direction. This difference in terms of mechanical response also induces different rupture mechanisms after tensile tests between each sample configuration. Smooth cracks in the 0° configuration and cracks in

stair shape with delamination visible on sample edges for the 45° configuration, were observed.

The damage mechanisms at the microscopic scale were then investigated. The initiation of damage by fibers/matrix debonding was first observed by means of Scanning Electronic Microscopy (SEM). Because of some issues during the SEM tests, the following of the study was done using X-ray tomography. Samples in 0° and 45° configuration damaged by tensile tests was found to exhibit different damage schemes in links with the stress/strain response. In the first case, low scale damage was found to grow, whereas for 45° configuration large scale damage can appear for high levels of loading, mostly fibers buckling and delamination. This difference in terms of growing state was also observed when analyzing the void volume fraction evolution with increasing the loading level on the 3D volumes reconstructed from X-ray tomography. The evolution of the void volume fraction as a function of the applied stress level, exhibited a similar increase as the evolution of the macroscopic damage estimated from the Young's modulus reduction.

Different Non Destructive Evaluation (NDE) methods based on ultrasound were then investigated. First, the ultrasonic C-scan does not give interesting results on the samples in 0° configuration. Only macroscopic damage on the samples in 45° configuration could be imaged. Other methods were consequently considered, first the computation of stiffness components based on phase velocities measurements. The evolution of the anisotropic damage was obtained on samples in 0° and 45° configuration damaged by tensile tests. This evolution was in agreement with the evolution of the 2D strain field computed from DIC. That is the components function of the loading direction that decrease for 0° configuration and every in-plane components, including in-plane shearing, decreasing for the other configuration. Then two damage indicators were proposed and were found to give a correct quantification of the induced damage. The first damage indicator is the Frobenius norm of the stiffness tensor, the second damage indicator is the phase shift for all the incident angles and all the investigation planes considered for the measurement of phase velocities.

Then guided waves are used to inspect the same samples. Indeed, because of the more complex apparatus required for the previous method, the latter can be apply less easily on site than guided waves based methods. First the wave modes were investigated but no mode conversion could be observed with increasing the applied loading levels. Therefore, other damage indicators were proposed in order to quantify the damage state. The evolution of the signal energy with the induced damage was found to be the more effective. Its efficiency was first validated using a steel plate with different kind of defect induced on it. This indicator was then applied on the composite samples preliminary damaged by means of tensile tests. The evolution of the signal energy was found to be in agreement with the phase shift damage indicator as well as with the other damage estimation methods.

Finally, a validation of the proposed methods using samples preliminary damaged by drop weight impacts was proposed. Several impact energies were considered, they were chosen in order to remain in the BVID domain. The damage induced on the plate was found to increase with the impact energy when observed by means of X-ray tomography. The permanent indentation was evaluated as well using pulse-echo measurements. Its size was found to increase with the impact energy which makes the estimation of the indentation a good indicator of the internal damage. The stiffness measurement method introduced in chapter V), was able to detect a clear increase of the damage state starting from 17.5 J as impact energy. Indeed, starting from this level of energy, all the stiffness components, at the exception of the C_{12} and C_{44} components, decrease with increasing the impact energy. The phase shift damage indicator was found to be able to detect a real change in the damage state starting from an impact energy value of 15 J. Finally, as the damage indicators from guided waves, based on the signal amplitude, could not detect the damage from impact, damage evaluation using time shift was considered. The latter was estimated by cross correlation and found to be able to quantify increasing damage state. The damage location can be detected when investigation on the whole sample is considered. However, the proposed experimental set-up requires some adjustment in order to avoid fluctuation in coupling between the transducers and the sample.

2) Further works

As aforementioned, enhancement in the signal processing when considering guided waves based methods should be investigated in future work. As an example, two methods dealing with the propagation of guided waves are investigated in the appendix section. Those two methods are respectively based on the analysis of the non-linear response of propagated elastic waves and on the analysis of the late arrival signals (or coda part of the signal). They could be interesting alternatives even though some limitations are highlight in the investigation.

Then, in order to consider more diffuse damage that could appear before a catastrophic failure, the fatigue behavior of the material need to be investigated. Indeed, fatigue damage is known to be one of the most difficult to detect in composite material. Often when they are detected by NDE method the material has seen its stiffness and strength decrease to a large extent. The case of fatigue post-impact should also be considered.

Numerical modeling of the wave propagation in the investigated composites is also a challenging topic that deserves to be studied. Indeed, the layering aspect of the composite material and the waviness of the fabric made the real propagation of wave more difficult to predict. As an example, the dispersion curves of the material could be influenced by these effects, even not if the high frequency regime is not considered. Consequently, the homogenous anisotropic hypothesis considered in this work for computing the dispersion curves may be too inadequate.

VIII) References

[1] C. Atas and O. Sayman, "An overall view on impact response of woven fabric composite plates," *Compos. Struct.*, vol. 82, pp. 336–345, 2008.

[2] M. Karayaka and P. Kurath, "Deformation and Failure Behavior of Woven Composite Laminates," *J. Eng. Mater. Techology*, vol. 116, no. April 1994, pp. 222–232, 1994.

[3] L. Marcin, "Modelisation du comportement, de l'endommagement et de la rupture de materiaux compositea renforts tisses pour le dimensionnement robuste de structures," Université Bordeaux 1, 2010.

[4] P. Boisse, N. Hamila, A. Madeo, G. Hivet, D. Isola, P. Boisse, N. Hamila, A. Madeo, and G. Hivet, "The bias-extension test for the analysis of in-plane shear properties of textile composite reinforcements and prepregs : a review," *Int. J. Mater. Form.*, vol. 10, no. 4, 2017.

[5] P. Ladeveze and E. Le Dantec, "Damage modelling of the elementary ply for laminated composites," *Compos. Sci. Technol.*, vol. 43, pp. 257–267, 1992.

[6] P. Cazuc, "Advancing lightweighting solutions to the industry," *DuPont - Autofocus #23*, 2013. [Online]. Available: http://www.arpae-summit.com/paperclip/exhibitor_docs/14AE/DuPont_138.pdf.

[7] S. Latieule, "Dossier automobile - Les matériaux biosourcés s'imposent en douceur," *Formule Verte #18*, 2014. [Online]. Available: http://averousl.free.fr/fichiers/Formule Verte Juin 2014.pdf.

[8] N. Piccirelli and A. Giocosa, "Les composites dans l'industrie automobile," *Techniques de l'ingénieur*, 2011. [Online]. Available: http://www.techniques-ingenieur.fr/base-documentaire/ingenierie-des-transports-th14/carburants-batteries-et-materiaux-alleges-pour-vehicule-propre-42629210/les-composites-dans-l-industrie-automobile-am5600/.

[9] P. Passebon, "Les composites ont rendez-vous avec les hautes cadences," *Industrie & technologies*, 2015. [Online]. Available: http://www.industrie-techno.com/2-automobile-les-composites-ont-rendez-vous-avec-les-hautes-cadences.36589.

[10] L. Fery, "Quels composites pour l'automobile de demain?," *Industrie & technologies*, 2013. [Online]. Available: http://www.industrie-techno.com/quels-composites-pour-l-automobile-de-demain.23015.

[11] R. N. Yancey, *Challenges, Opportunities, and Perspectives on Lightweight Composite Structures: Aerospace Versus Automotive*. Elsevier Ltd, 2016.

[12] A. M. Abdelhay and M. I. Mubark, "ULTRASONIC EVALUATION OF SURFACE ROUGHNESS USING NORMAL INCIDENCE PULSE - ECHO TECHNIQUE," *e-Journal Nondestruct. Test.*, vol. 9, no. 4, 2004.

[13] S. Gholizadeh, "A review of non-destructive testing methods of composite materials," in *Procedia Structural Integrity*, 2016, vol. 1, pp. 50–57.

[14] E. G. Henneke, W. W. Stinchcomb, and K. L. Reifsnider, "Some ultrasonic methods for characterizing response of composite materials," in *International Sympozium on Ultrasonic materials Characterization*, 1980.

[15] F. Dal Maso and J. Mézière, "Calcul des propriétés élastiques des tissus utilisés dans les matériaux composites," *Rev. l'institut Français du Pétrole*, vol. 53, no. 1, pp. 857–870, 1998.

[16] J. Cunningham, "Woven or unwoven fibres?," *Materials for Engineering*, 2013. [Online]. Available: http://www.materialsforengineering.co.uk/engineering-materials-features/woven-or-unwoven-fibres/48611/.

[17] W. Albouy, "De la contribution de la visco-élasto-plasticité au comportement en fatigue de composite a matrice thermoplastique et thermodurcissable," INSA Rouen, 2013.

[18] G. Couégnat, "Approche multiéchelle du comportement mécanique de matériaux composites à renfort tissé," École des Mines d'Alby-Carmaux, 2008.

[19] B. Vieille and L. Taleb, "About the influence of temperature and matrix ductility on the behavior of carbon woven-ply PPS or epoxy laminates: Notched and unnotched laminates," *Compos. Sci. Technol.*, vol. 71, no. 7, pp. 998–1007, 2011.

[20] W. Albouy, B. Vieille, and L. Taleb, "Influence of matrix ductility on the high-temperature fatigue behavior of off-axis woven-ply thermoplastic and thermoset laminates," *Int. J. Fatigue*, vol. 63, pp. 85–96, 2014.

[21] S. D. Pandita, G. Huysmans, M. Wevers, and I. Verpoest, "Tensile fatigue behaviour of glass plain-weave fabric composites in on- and off-axis directions," *Compos. Part A Appl. Sci. Manuf.*, vol. 32, no. 10, pp. 1533–1539, 2001.

[22] BASF_Corporation, "Conditioning of Ultramid modlings," 2016.

[23] M. Chanda and S. K. Roy, *Plastics Technology Handbook*. CRC Press, 2007.

[24] A. Launay, Y. Marco, M. H. Maitournam, and I. Raoult, "Modelling the influence of temperature and relative humidity on the time-dependent mechanical behaviour of a short glass fibre reinforced polyamide," *Mech. Mater.*, vol. 56, pp. 1–10, 2013.

[25] BASF_Corporation, "MECHANICAL PERFORMANCE OF POLYAMIDES

WITH INFLUENCE OF MOISTURE AND TEMPERATURE – ACCURATE EVALUATION AND BETTER UNDERSTANDING," 2003.

[26] M. F. Arif, F. Meraghni, Y. Chemisky, N. Despringre, and G. Robert, "In situ damage mechanisms investigation of PA66/GF30 composite: Effect of relative humidity," *Compos. Part B Eng.*, vol. 58, pp. 487–495, 2013.

[27] G. W. Ehrenstein and R. P. Theriault, *Polymeric materials: structure, properties, applications*. 2001.

[28] M. F. Ashby and D. R. H. Jones, *Matériaux 2. microstructure et mise en œuvre*. Paris, 1991.

[29] M. F. Herman, *Encyclopedia of Polymer Science and Technology, Concise*. 2013.

[30] V. Miri, O. Persyn, J. Lefebvre, and R. Seguela, "Effect of water absorption on the plastic deformation behavior of nylon 6," *Eur. Polym. J.*, vol. 45, no. 3, pp. 757–762, 2009.

[31] A. Malpot, F. Touchard, and S. Bergamo, "Etude du comportement en fatigue d ' un composite à matrice thermoplastique tissé de fibres de verre pour application automobile Study of the behaviour of a woven glass-fibre-reinforced composite with a thermoplastic matrix for automotive application," in *Journées Nationales des Compositees 19*, 2015, pp. 1–9.

[32] T. Osada, A. Nakai, and H. Hamada, "Initial fracture behavior of satin woven fabric composites," *Compos. Struct.*, vol. 61, pp. 333–339, 2003.

[33] P. Boisse, N. Hamila, E. Vidal-sallé, and F. Dumont, "Simulation of wrinkling during textile composite reinforcement forming . Influence of tensile , in-plane shear and bending stiffnesses," *Compos. Sci. Technol.*, vol. 71, no. 5, pp. 683–692, 2011.

[34] A. Gay, J. Roche, P. Lapeyronnie, and P. Bertrand, "Non-destructive inspection of initial defects of PA6 . 6-GF50 / aluminum self-piercing riveted joints and damage monitoring under mechanical static loading," *Int. J. Damage Mech.*, vol. 26, no. 8, pp. 1127–1146, 2017.

[35] J. L. Rose, K. M. Rajana, and M. K. T. Hansch, "Ultrasonic Guided Waves for NDE of Adhesively Bonded Structures," *J. Adhes.*, vol. 50, no. 1, pp. 71–82, 1995.

[36] P. Cawley and D. Alleyne, "The use of Lamb waves for the long range inspection of large structures," *Ultrasonics*, vol. 34, no. 2, pp. 287–290, 1996.

[37] Z. Su, L. Ye, and Y. Lu, "Guided Lamb waves for identification of damage in composite structures : A review," *J. Sound Vib.*, vol. 295, pp. 753–780, 2006.

[38] M.-L. Pastor, C. Garnier, and C. Pescay, "Comparison of two Non-destructive Tests in Carbon/Epoxy Composites," *J. Mater. Sci. Eng.*, vol. 4, no. 10, 2010.

[39] L. Satyanarayan, J. M. Vander Weide, and N. F. Declercq, "Ultrasonic polar scan imaging of damaged fiber reinforced composites," *Mater. Eval.*, pp. 733–739, 2010.

[40] J. Liu and N. F. Declercq, "Ultrasonic geometrical characterization of periodically corrugated surfaces," *Ultrasonics*, vol. 53, pp. 853–861, 2013.

[41] Q. Shen, M. Omar, and S. Dongri, "Ultrasonic NDE Techniques for Impact Damage Inspection on CFRP Laminates," *J. Mater. Sci. Res.*, vol. 1, no. 1, pp. 2–16, 2011.

[42] A. Osman, U. Hassler, V. Kaftandjian, and J. Hornegger, "An automated data processing method dedicated to 3D ultrasonic non destructive testing of composite pieces," in *IOP Conference Series Materials Science and Engineering International - Symposium on Ultrasound in the Control of Industrial Processes (UCIP 2012)*, 2012, no. 42(1):2005.

[43] C. Garnier, M.-L. Pastor, F. Eyma, and B. Lorrain, "The detection of aeronautical defects in situ on composite structures using Non Destructive Testing," *Compos. Struct.*, vol. 93, no. 5, pp. 1328–1336, Apr. 2011.

[44] J. Dong, B. Kim, A. Locquet, P. McKeon, N. F. Declercq, and D. S. Citrin, "Nondestructive evaluation of forced delamination in glass fiber-reinforced composites by terahertz and ultrasonic waves," *Compos. Part B Eng.*, vol. 79, pp. 667–675, 2015.

[45] Cenaero, Sirris, and Multitel, "Comparison and complementary of non-destructive evaluation technologies on composite materials," Yutz, France, 2013.

[46] F. Destic and C. Bouvet, "Impact damages detection on composites materials by THz imaging," *Case Stud. Nondestruct. Test. Eval.*, vol. 6, no. Part A, pp. 53–62, 2016.

[47] D. K. Hsu and D. J. Barnard, "An exploration of the utilities of terahertz waves for the NDE of composites," 2010.

[48] M. F. Markham, "Measurement of the elastic constants of fibre composites by ultrasonics," *Composites*, vol. 1, no. 2, pp. 145–149, 1969.

[49] P. Marguères, F. Meraghni, and M. L. Benzeggagh, "Comparison of stiffness measurements and damage investigation techniques for a fatigued and post-impact fatigued GFRP composite obtained by RTM process," *Compos. Part A Appl. Sci. Manuf.*, vol. 31, pp. 151–163, 2000.

[50] P. Marguères and F. Meraghni, "Damage induced anisotropy and stiffness reduction evaluation in composite materials using ultrasonic wave transmission," *Compos. Part A Appl. Sci. Manuf.*, vol. 45, pp. 134–144, 2013.

[51] W. Hufenbach, T. Ritschel, R. Böhm, and A. Langkamp, "Ultrasonic determination

of anisotropic damage in fibre and textile reinforced composite materials," in *Conference on Damage in Composite Materials*, 2006.

[52] S. Baste and C. Aristégui, "Induced anisotropy and crack systems orientations of a ceramic matrix composite under off-principal axis loading," *Mech. Mater.*, vol. 29, no. 1, pp. 19–41, 1998.

[53] A. Dalmaz, D. Ducret, R. El Guerjouma, P. Reynaud, P. Franciosi, D. Rouby, G. Fantozzi, and J. C. Baboux, "Elastic moduli of a 2.5D C f / SiC composite : experimental and theoretical estimates," *Compos. Sci. Technol.*, vol. 60, 2000.

[54] J. L. Rose, J. J. Ditri, Y. Huang, D. P. Dandekar, and S.-C. Chou, "One-sided ultrasonic inspection technique for the elastic constant determination of advanced anisotropic materials," *J. Nondestruct. Eval.*, vol. 10, no. 4, pp. 159–166, 1991.

[55] S. I. Rokhlin and W. Wang, "Ultrasonic evaluation of in plane and out of plane elastic properties of composite materials," *Rev. Prog. Quant. Nondestruct. Eval.*, vol. 8, no. B, pp. 1489–1496, 1989.

[56] S. I. Rokhlin and W. Wang, "Double through transmission bulk wave method for ultrasonic phase velocity measurement and determination of elastic constants of composite materials," *J. Acoust. Soc. Am.*, vol. 91, no. 6, pp. 3303–3312, 1992.

[57] M. Mah and D. R. Schmitt, "Determination of the complete elastic stiffnesses from ultrasonic phase velocity measurements," *J. Geophys. reasearch*, vol. 108, no. October 2003, pp. 1–11, 2016.

[58] E. Grippon, S. Baste, E. Martin, C. Aristegui, and G. Couégnat, "Caractérisation ultrasonore et modélisation multi-échelle de l'endommagement sous charge d'un composite 3D SiC/SiC," in *Congrés Français de Mécanique*, 2013, pp. 3–8.

[59] B. Audoin, S. Baste, and B. Castagnede, "Estimation de l'intervalle de confiance des constantes d'élasicité identidiées à partir des vitesses de propagation ultrasonore," *Compte rendus Acad. des Sci.*, vol. 312, no. 2, pp. 676–686, 1991.

[60] M. Kersemans, I. De Baere, J. Degrieck, K. Van Den Abeele, L. Pyl, F. Zastavnik, H. Sol, and W. Van Paepegem, "Nondestructive damage assessment in fiber reinforced composites with the pulsed ultrasonic polar scan," *Polym. Test.*, vol. 34, pp. 85–96, Apr. 2014.

[61] N. F. Declercq, J. Degrieck, and O. Leroy, "On the influence of fatigue on ultrasonic polar scans of fiber reinforced composites," *Ultrasonics*, vol. 42, no. 1–9, pp. 173–177, 2004.

[62] N. F. Declercq, J. Decrieck, and O. Leroy, "Ultrasonic polar scans Numerical simulation on generally," *Ultrasonics*, vol. 45, pp. 32–39, 2006.

[63] N. F. Declercq, J. Degrieck, and O. Leroy, "Simulations of harmonic and pulsed

ultrasonic polar scans," *NDT E Int.*, vol. 39, no. 3, pp. 205–216, 2006.

[64] S. W. Herbison and N. F. Declercq, "Theoretical and experimental ultrasonic investigation of a thin plate with regions of different periodic double-corrugations," *J. Acoust. Soc. Am.*, vol. 123, no. 5, 2008.

[65] S. W. Herbison and N. F. Declercq, "Diffraction phenomena associated with a composite plate containing an interior periodically corrugated interface," *J. Acoust. Soc. Am.*, vol. 123, no. 5, 2008.

[66] S. W. Herbison, "Ultrasonic Diffraction Effects On Periodic Surfaces," Georgia Institute of Technology, 2011.

[67] M. Kersemans, W. Van Paepegem, D. Van Nuffel, G. Luyckx, I. De Baere, J. Gu, H. Sol, K. Van Den Abeele, and J. Degrieck, "Polar Scan Technique for Material Characterization and Identification of New Operating Regimes," in *International Conference on Experimental Mechanics*, 2010, vol. 1, pp. 1–12.

[68] J. L. Rose, *Ultrasonic waves in solid media*. 1999.

[69] N. Adnan H., *Wave propagation in layered anisotropic media*, North Holl. North Holland: Elsevier, 1995.

[70] W. H. Ong, N. Rajic, W. K. Chiu, and C. Rosalie, "Determination of the elastic properties of woven composite panels for Lamb wave studies," *Compos. Struct.*, vol. 141, pp. 24–31, 2016.

[71] E. Moreno, N. Galarza, B. Rubio, and J. A. Otero, "Phase Velocity Method for Guided Wave Measurements in Composite Plates," *Phys. Procedia*, vol. 63, pp. 54–60, 2015.

[72] W. Gao, C. Glorieux, and J. Thoen, "Laser ultrasonic study of Lamb waves : determination of the thickness and velocities of a thin plate," *Int. J. Eng. Sci.*, vol. 41, pp. 219–228, 2003.

[73] H. J. Shin and S.-J. Song, "Observation of Lamb Wave Mode Conversion on an Aluminum Plate," in *15th World Conference on Non-Destructive Testing*, 2000.

[74] P. Mckeon, S. Yaacoubi, N. F. Declercq, S. Ramadan, and W. K. Yaacoubi, "Baseline subtraction technique in the frequency – wavenumber domain for high sensitivity damage detection," *Ultrasonics*, vol. 54, no. 2, pp. 592–603, 2014.

[75] D. N. Alleyne and P. Cawley, "A 2-dimensional Fourier transform method for the quantitative measurement of Lamb modes," *Proc. IEEE Ultrason. Symp.*, vol. 2, pp. 1143–1146, 1990.

[76] M. R. Karim and A. K. Mal, "Determination of the elastic constants of composites

through the inversion of Leaky Lamb Waves data," *Rev. Prog. Quant. Nondestruct. Eval.*, vol. 9, 1990.

[77] K. Imano and T. Endo, "Experimental Study on the Mode Conversion of Lamb Waves in a Metal Plate of Stepped Thickness Using Optical Detection," *Int. J. Soc. Mater. Eng. Resour.*, vol. 17, no. 2, pp. 201–204, 2010.

[78] W. Li, Y. Cho, J. Lee, and J. D. Achenbach, "Assessment of Heat Treated Inconel X-750 Alloy by Nonlinear Ultrasonics," *Exp. Mech.*, vol. 53, no. 5, pp. 775–781, 2013.

[79] J. Jingpin, M. Xiangji, H. Cunfu, and W. Bin, "Nonlinear Lamb wave-mixing technique for micro-crack detection in plates," *NDT E Int.*, vol. 85, pp. 63–71, 2017.

[80] U. Rabe, T. Helfen, M. Weikert, S. Hirsekorn, H.-G. Herrmann, C. Boller, D. Backe, F. Balle, and D. Eifler, "Nonlinear ultrasonic testing of carbon fibre reinforced plastics in the very high cycle fatigue regime," *Proc. Meet. Acoust.*, vol. 16, no. 2012, pp. 1–6, 2012.

[81] G. Ren, J. Kim, and K.-Y. Jhang, "Relationship between second- and third-order acoustic nonlinear parameters in relative measurement," *Ultrasonics*, vol. 56, pp. 539–544, 2015.

[82] U. Dahlen, N. Ryden, and A. Jakobsson, "Damage identification in concrete using impact non-linear reverberation spectroscopy," *NDT E Int.*, vol. 75, pp. 15–25, 2015.

[83] M. Meo, U. Polimeno, and G. Zumpano, "Detecting damage in composite material using nonlinear elastic wave spectroscopy methods," *Appl. Compos. Mater.*, vol. 15, pp. 115–126, 2008.

[84] K. E. Van Den Abeele, A. Sutin, J. Carmeliet, and P. a. Johnson, "Micro-damage diagnostics using nonlinear elastic wave spectroscopy (NEWS)," *NDT E Int.*, vol. 34, pp. 239–248, 2001.

[85] L. . Ostrovsky and P. A. Johnson, "Dynamic nonlinear elasticity in geo materials," *Riv. del Nuovo Cim. della Soc. Ital. di Fis.*, vol. 24, no. 7, pp. 1–46, 2001.

[86] L. . Ostrovsky, S. N. Gurbatov, and J. N. Didenkulov, "Nonlinear Acoustics in Nizhni Novgorod (A Review)," *Acoust. Phys.*, vol. 51, no. 2, pp. 114–127, 2005.

[87] K. Van Den Abeele and J. De Visscher, "Damage assessment in reinforced concrete using spectral and temporal nonlinear vibration techniques," *Cem. Concr. Res.*, vol. 30, no. 9, pp. 1453–1464, 2000.

[88] V. Genovés, L. Soriano, M. V Borrachero, J. Eiras, and J. Payá, "Preliminary study on short-term sulphate attack evaluation by non-linear impact resonance acoustic spectroscopy technique," *Constr. Build. Mater.*, vol. 78, pp. 295–302, 2015.

[89] K. E. -a. Van Den Abeele, P. a. Johnson, and A. Sutin, "Nonlinear Elastic Wave

Spectroscopy (NEWS) Techniques to Discern Material Damage, Part II: Single-Mode Nonlinear Resonance Spectroscopy (NWMS)," *Res. Nondestruct. Eval.*, vol. 12, no. 1, pp. 17–30, 2000.

[90] A. Quiviger, J.-P. Zardan, J.-F. Chaix, C. Payan, V. Garnier, J. Moysan, and J. Salin, "Caracterisation Ultrasonore de Fissures dans les Bétons Méthodes Linéaires et Non Linéaires," *10éme Congrés Français d'Acoustique*, p. , 2010.

[91] K. E. -a. Van Den Abeele, P. a. Johnson, and a. Sutin, "Nonlinear Elastic Wave Spectroscopy (NEWS) Techniques to Discern Material Damage, Part I: Nonlinear Wave Modulation Spectroscopy (NWMS)," *Res. Nondestruct. Eval.*, vol. 12, no. 1, pp. 17–30, 2000.

[92] F. Aymerich and W. J. Staszewski, "Experimental Study of Impact-Damage Detection in Composite Laminates using a Cross-Modulation Vibro-Acoustic Technique," *Struct. Heal. Monit.*, vol. 9, no. 0, pp. 541–553, 2010.

[93] T. B. Helfen, "Nichtlinearer Ultraschall zur Charakterisierung von Ermüdungsschäden während der Hochfrequenz - Beanspruchung von C - Faser - Kunststoffverbunden," Universitat des Saarlandes, 2014.

[94] M. Herraiz and A. F. Espinosa, "Coda Waves-A Review," *Pageoph*, vol. 125, no. 4, pp. 499–577, 1987.

[95] P. Fröjd and P. Ulriksen, "Amplitude and phase measurements of continuous diffuse fields for structural health monitoring of concrete structures," *NDT E Int.*, vol. 77, pp. 35–41, 2016.

[96] R. Livings, V. Dayal, and D. Barnard, "Coda wave interferometry for the measurement of thermally induced ultrasonic velocity variations in CFRP laminates," *AIP Conf. Proc.*, vol. 1706, 2016.

[97] R. Livings, V. Dayal, and D. Barnard, "Feasibility of detecting fatigue damage in composites with coda waves," *AIP Conf. Proc.*, vol. 1650, pp. 1130–1139, 2015.

[98] G. Briotti and C. Scarponi, "Ultrasonic NDI Detection of Delaminations on," *J. Reinf. Plast. Compos.*, vol. 20, no. 1, pp. 76–87, 2001.

[99] Z. Liu, J. Huang, and J. Li, "Comparison of four techniques for estimating temporal change of seismic velocity with passive image interferometry," *Earthq. Sci.*, vol. 23, no. 5, pp. 511–518, 2010.

[100] J. E. Michaels and T. E. Michaels, "Detection of structural damage from the local temporal coherence of diffuse ultrasonic signals," *IEEE Trans. Ultrason. Ferroelectr. Freq. Control*, vol. 52, no. 10, pp. 1769–1782, 2005.

[101] Y. Zhang, O. Abraham, V. Tournat, A. Le Duff, B. Lascoup, A. Loukili, F. Grondin,

and O. Durand, “Validation of a thermal bias control technique for Coda Wave Interferometry (CWI),” *Ultrasonics*, vol. 53, no. 3, pp. 658–664, 2013.

[102] Y. H. Kim, S. Song, and S. Kwon, “Measurement of phase velocity dispersion curves and group velocities in a plate using leaky Lamb waves,” in *Conference and exhibition on Non Destructive Evaluation 2002 - ISNT*, 2002.

[103] S. V Lomov, D. S. Ivanov, I. Verpoest, A. E. Bogdanovich, D. Mungalov, M. Zako, T. Kurashiki, and H. Nakai, “Predictive analyses and experimental validations of effective elastic properties of 2D and 3D woven composites,” in *13th European Conference on Composite Materials (ECCM-13)*, 2008.

[104] R. El Guerjouma and S. Baste, “Evaluation of anisotropic damage in ceramic-ceramic (SiC-SiC) composite by ultrasonic method,” in *Ultrasonic international*, 1989, pp. 895–900.

[105] S. Baste and B. Audoin, “On internal variable in anisotropic damage,” *Eur. J. Mech.*, vol. 10, no. 6, pp. 587–606, 1991.

[106] E. Ž. L. Mažeika, L. Draudvilienė, “Influence of the dispersion on measurement of phase and group velocities of Lamb waves,” *Ultrasound*, vol. 64, no. 4, pp. 18–21, 2009.

[107] L. Draudviliene, H. Ait Aider, O. Tumsys, and L. Mazeika, “The Lamb waves phase velocity dispersion evaluation using an hybrid measurement technique,” *Compos. Struct.*, vol. 184, no. October 2017, pp. 1156–1164, 2018.

[108] S. Eckel, F. Meraghni, P. Pomarède, and N. F. Declercq, “Investigation of Damage in Composites Using Nondestructive Nonlinear Acoustic Spectroscopy,” *Exp. Mech.*, 2016.

[109] “DIN IEC 268-2:1994-08,” *Elektroakustische Geräte – Tl. 2 Allg. Begr. und Berechnungsverfahren (lEC 268-2 1987 + A1 1991) Dtsch. Fassung HD 483.2 S2 1993*.

[110] “DIN EN 60268-3:2014-03,” *Elektroakustische Geräte – Tl. 3 Verstärker (IEC 60268-32013), Dtsch. Fassung EN 60268-32013*.

[111] N. Yoder, “PeakFinder (Version 13 Aug 2014). File Exchange. MATLAB Central,” 2014. [Online]. Available: http://www.mathworks.com/matlabcentral/fileexchange/25500-peakfinder.m. [Accessed: 01-Jun-2015].

[112] S. C. Stähler, C. Sens-Schönfelder, and E. Niederleithinger, “Monitoring stress changes in a concrete bridge with coda wave interferometry.,” *J. Acoust. Soc. Am.*, vol. 129, no. 4, pp. 1945–1952, 2011.

[113] Y. ZHANG, “Contrôle de santé des matériaux et structures par analyse de la coda

ultrasonore," Université Nantes Angers Le Mans, 2013.

[114] B. N. Cox and G. Flanagan, "Handbook Composites of Analytical Methods for Textile," 1997.

[115] F. Praud, G. Chatzigeorgiou, Y. Chemisky, and F. Meraghni, "Modélisation multi-échelle des composites tissés à matrice thermoplastique sous chargements cycliques non proportionnels," in *JNC 20 : Journées Nationales sur les Composites 2017*, 2017.

[116] B. Vieille and W. Albouy, "About the applicability of a simple model to predict the fatigue life and behavior of woven-ply thermoplastic laminates at T > T g," *Compos. Part B Eng.*, vol. 61, pp. 181–190, 2014.

[117] F. A. Myers, "Stress-state effects on the viscoelastic response of PPS based thermoplastic composites," in *Advances in Thermoplastic Matrix Composite Materials*, ASTM STP 1., G. M. Newaz, Ed. ASTM International, 1989, pp. 154–162.

[118] C. Potel, "Propagation et Contrôle Non Destructif dans les solides - AC03," in *Master's degree course From Master Sciences et Technologie Mention "Acoustique et Mécanique."*

[119] M. Kersemans, N. Lammens, J. Degrieck, K. Van Den Abeele, L. Pyl, F. Zastavnik, H. Sol, and W. Van Paepegem, "Extraction of bulk wave characteristics from a pulsed ultrasonic polar scan," *Wave Motion*, vol. 51, no. 7, pp. 1071–1081, 2014.

[120] G. Huang, F. Song, and X. Wang, "Quantitative modeling of coupled piezo-elastodynamic behavior of piezoelectric actuators bonded to an elastic medium for structural health monitoring: A review," *Sensors*, vol. 10, no. 4, pp. 3681–3702, 2010.

[121] C. M. Yeum, "Lamb Wave Mode Decomposition," 2016. [Online]. Available: https://datacenterhub.org/resources/150.

[122] T. Planès and E. Larose, "A review of ultrasonic Coda Wave Interferometry in concrete," *Cem. Concr. Res.*, vol. 53, pp. 248–255, 2013.

[123] N. Hongkarnjanakul, "Modélisation numérique pour la tolérance aux dommages d'impact sur stratifié composite : de l'impact à la résistance résiduelle en compression," 2013.

IX) Appendix

1) Appendix 1: Damage investigation using nonlinear acoustic methods on different woven fiber reinforced composite materials

The next presented study was done in close collaboration with Sebastian Eckel during his internship at both LEM3 lab and LUNE lab from Georgia Tech Lorraine. Some of the work described here was summarized and published in a paper [108]. The goal was to verify the ability of the nonlinear acoustic method to accurately quantify the damage level on composite material. Three experimental damage evaluation acoustic methods will be presented and discussed in this first appendix. First, the NEWS (Nonlinear Waves Modulation Spectroscopy) method is considered and then the NRUS method (Nonlinear Resonant Ultrasound Spectroscopy). These two very well know nonlinear acoustic methods are among the methods that were introduced in subsection V)-1)-d) from the literature review on ultrasonic based NDE methods. Between these two investigated methods, a complementary study of the resonance frequency shift function of the induced damage is presented.

Several fiber reinforced composite materials available at the LEM3 lab were tested. All these samples are woven glass fabric reinforced composites and were submitted to tension along the axis of the fiber. The three composites selected are: a vinylester, an epoxy and a polyamide 66/6 matrix based composites. Different stress level values were used in order to induce different damage state in the investigated samples. These data are sum-up in the following table:

Material	Sample 1	Sample 2	Sample 3	Sample 4	Sample 5	Sample 6	Sample 7	Sample 8
Vinylester/glass fiber	100	200	300	400	----------	----------	----------	----------
Epoxy/glass fiber	50	100	150	200	250	300	350	400
Polyamide 66/6 glass fiber	45	90	135	180	225	270	315	----------

Table 33 : Materials tested and loading value used on the different sample

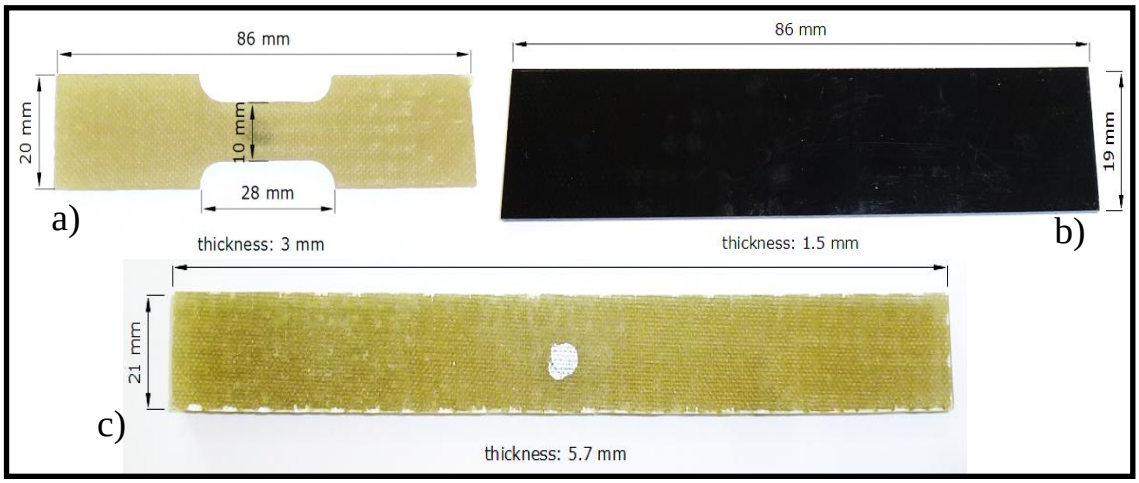

Figure 173 : Photo of the sample of each selected woven composite materials.
a) : Woven glass vinylester composite, b) Woven glass polyamide 6.6/6 composite, c) : Woven glass epoxy composite

The procedure to induced damage is the same as in the chapter III) at the exception that only the extensometer was used to measure the displacement. The dimensions of the three considered material are indicated in Figure 173.

a) Nonlinear Wave Modulation Spectroscopy (NWMS) method

As it was explained in the ultrasonic damage evaluation method review V)-1)-d), for this method two continuous sinusoidal signals (each one with a different frequency) are emitted in the tested sample. The spectral response is then investigated, more particularly the harmonics and sidebands appearance as well as their amplitude.

Experimental set-up

The two continuous sinusoidal signals are generated by the soundcard of a common PC. The parameters of those signals are set using the signal generator *Daqarta* (Ver. 7.60.01), developed by Interstellar Research. The two frequencies are chosen in order to have the difference between the frequencies smaller than the lower of the two frequencies as required by the DIN standard [109]. A speaker system Home Arena 5.1 from TerraTec Electronic GmbH is used to amplify the emitted signal. Two common piezoelectric sensors from a loudspeaker (model XTCPT1) are used in contact with the sample. Coupling gel is used to improve the quality of the contact. The sample response is measured with the help of a laser vibrometer sensor, labelled *Fiber Vibrometer OFV-551*, the latter is control by the *Vibrometer Controller OFV-5000*. Both items are manufactured by Polytech GmbH. In order to improve the reflection of the signal, a dot of silver color paint is put on the investigated samples (Figure 173-c). The laser head is put orthogonally with the sample's surface at a distance of 12cm and manually focused in order to have the maximum reflection from the sample. A second amplifier, named *2.45.70 A model* manufactured by *Nucletudes*, is then used to increase the signal's gain. Finally the resulting signal is recording using an oscilloscope after an averaging of 100 sweeps. The signal is then transform using the FFT, the frequency spectrum is indeed the focus of the investigation. The complete experimental set-up is shown in Figure 174.

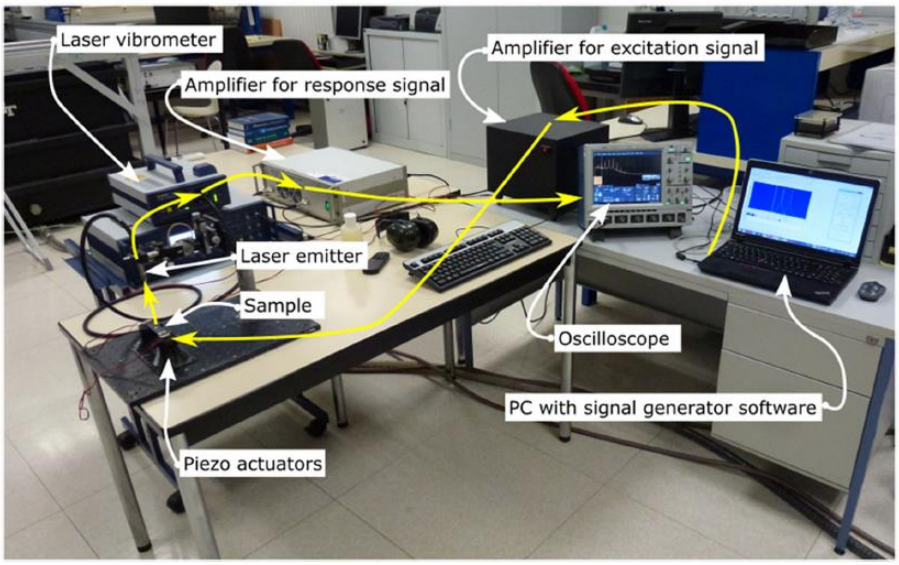

Figure 174 : Experimental set-up. The differents components are labeled and the path's signal is shown by yellow arrows

Signal Post-processing

A Matlab routine has been written to evaluate the frequency spectrum response from the investigated samples. The aim of this routine is to compute the TDFD (Total Difference Frequency Distorsion) according to the standard described in [110]. This TDFD provides a quantification of the signal intermodulation level, it is calculated as follow:

$$TDFD = \frac{\sqrt{\sum_i A_{i,intermodulation}^2}}{A_{excitation\,1} + A_{excitation\,2}} \tag{IX.1}$$

with: $A_{i,intermodulation}$ are the amplitudes of the intermodulation products and $A_{excitation\,1}$ and $A_{excitation\,2}$ respectively are the amplitudes of the two excitation frequencies in the response's spectrum.

It is worth mentioning that the measure of the distortion is widely used in the field of sound system equipment to evaluate the undesired distortion of an amplifier. The introduction of the TDFD in the field of material NDT was consequently considered to be suitable.

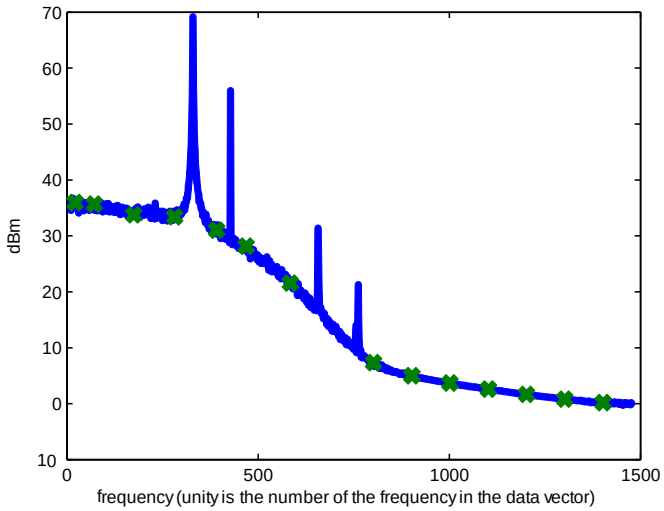

Figure 175 : Spectrum response of an undamaged woven glass fiber reinforced vinylester composite sample excited by 10 kHz and 13 kHz. Markers use to define the “background function” are plotted in green

Before the TDFD calculation, some post-processings on the spectrum are necessary. A damping effect is apparent (Figure 175) and may cause issue with an automotive procedure of TDFD calculation. This effect can be explained by damping: waves at higher frequencies are more damped than waves at lower frequencies. As a consequence, waves of higher frequencies are positioned in a lower power range in terms of amplitude. In order to fix this issue the following procedure is adopted and applied to all the samples’ spectrum:

- Manually identified points on the spectrum that define a “background function” and are clearly not peaks of the spectrum, plotted in green in Figure 175.
- Calculate a spline from those defined points
- Subtract the identified spline from the spectrum
- Use of the “PeakFinder” Matlab function [111] to obtain the spectrum’s peaks and store their respective location and amplitude, as indicated in Figure 176

- The TDFD is then calculated from each spectrum

It is worth mentioning that measurements were done 3 times on each sample, and the same *TDFD*'s values were obtained for the three measurements.

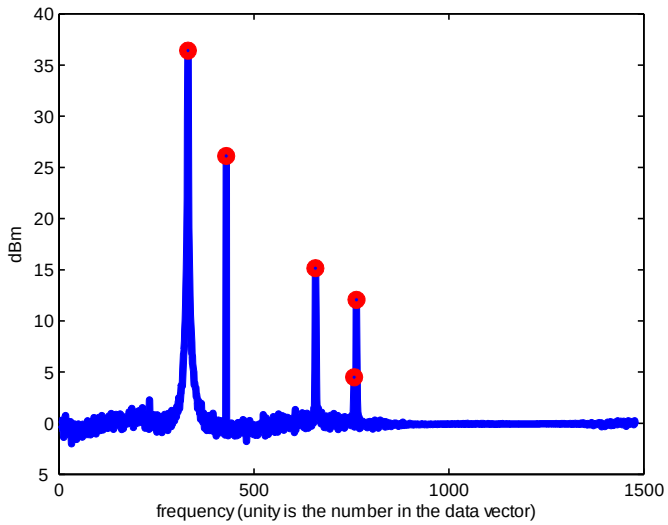

Figure 176 : Spectrum response of an undamaged woven glass fiber reinforced vinylester composite sample excited by 10 kHz and 13 kHz. The background function has been subtract and the identified peak are marked in red

Results and discussion

The different frequency response from the vinylester/glass composite, obtained for samples loaded at different stress levels, are all plotted in Figure 177. As a first observation, it can be noted that the number and amplitude of peak increased with increasing the tensile loading value. The same observation was made for epoxy/glass composite; it was however not the case for the polyamide/glass sample.

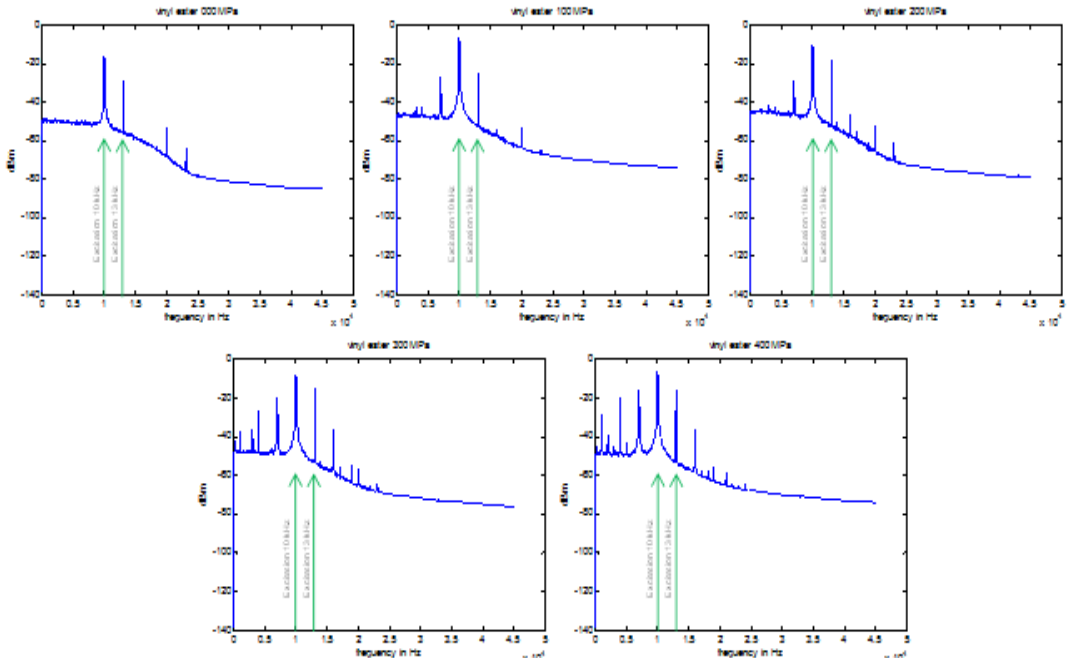

Figure 177 : Frequency response of the vinylester/glass composite submitted to different loading value. The input frequencies are indicate by the green arrow

The evolution TDFD parameter was then calculated for the three considered material. As expected, considering the preliminary observation on the spectral response of the polyamide based composite samples, the TDFD parameter does not seems to exhibit an evolution function of the tensile stress level (Figure 180-c). Indeed, after 180MPa of tension, the parameter value falls to almost the same value of the undamaged sample. One of the explanations could be that the thermoplastic matrix of the composite induces a higher closing effect to the cracks when the tension is released than the two previous thermoset matrixes. More surprising, even if for the first damage state the TDFD parameter increase for the epoxy based samples, a stabilization and even a small decrease is observed on the

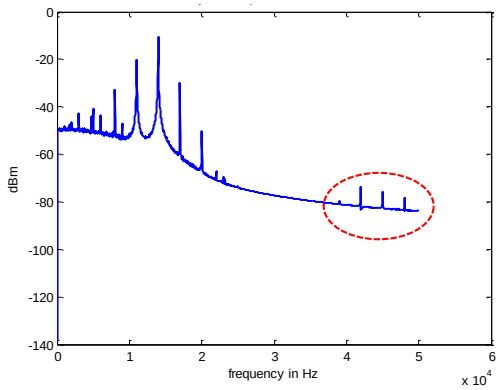

Figure 178 : Frequency response of the epoxy matrix sample submitted to a tensile loading value of 250 MPa

Figure 179 after 200MPa. An increasing evolution of the TDFD parameter function of the stress level is noted for the vinylester base composite level (Figure 180-a).

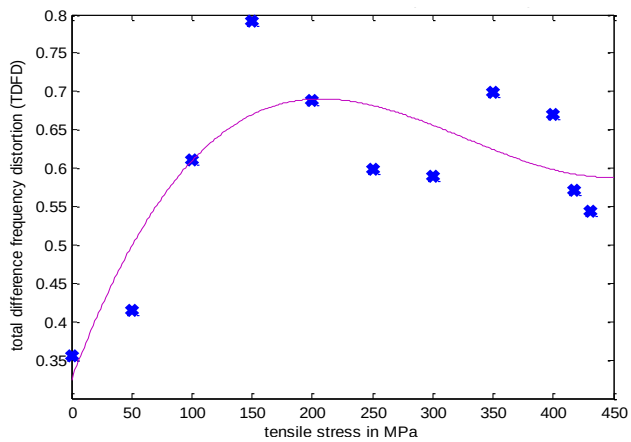

Figure 179 : Standard measure of the nonlinear transmission behavior of the epoxy matrix samples under excitation of 11 kHz and 14 kHz including the plot of a cubic regression

However, it was noticed that for the epoxy matrix based composites the appearance of high frequencies (Higher that 40 KHz as visible in Figure 178) for every tested samples when the tensile loading value exceed 250MPa. Those higher frequencies seem to be sensitive to the damage state. It was consequently propose to modify the TDFD parameter to add a higher weight on those high frequencies. In order to do so, the amplitude of those high frequencies was cubed:

$$TDFD_{alt} = \frac{\sqrt{\sum_i A^2_{i,intermodulation<4kHz} + \sum_k A^3_{k,intermodulation>4kHz}}}{A_{excitation\ 1} + A_{excitation\ 2}}$$

This parameter was used for the three different studied materials and for all the different loading value considered. Input frequencies of 10 kHz and 13 kHz were used for all the tested samples. Evolution of the $TDFD_{alt}$ function of the tensile loading value is plotted on the Figure 180 for all those woven composite materials. Of course, since those higher

frequencies appearance is only noted for the epoxy based composite samples, the new parameter formula gives the same values of TDFD for the other two composite materials.

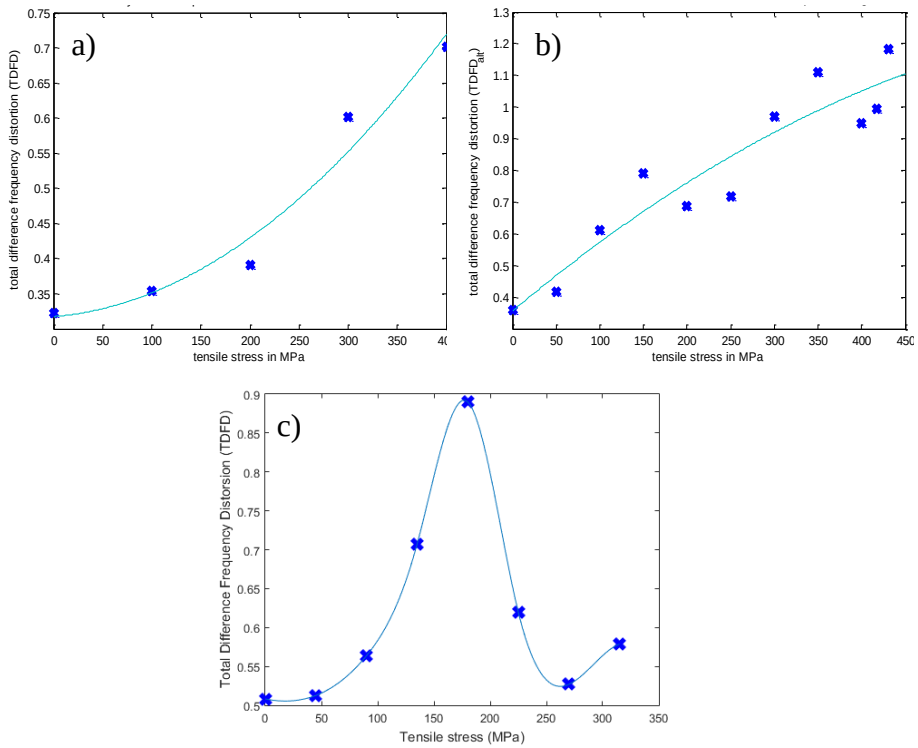

Figure 180 : TDFD parameter function of the loading value for a) Vinylester, b) epoxy and c) polyamide 6.6/6 matrix based woven glass fiber reinforced composites

b) Resonance frequency shift study

A second study was done on the same composite samples that were previously introduced. It was an investigation of a linear effect that is used to detect damage. The experimental set-up is the same as in the previous study; however the input acoustic signal is different. A single white noise is used as an input signal. If one make an average over a significantly high number of acquisitions the frequency resonance mode are clearly observable on the frequency response (Figure 181).

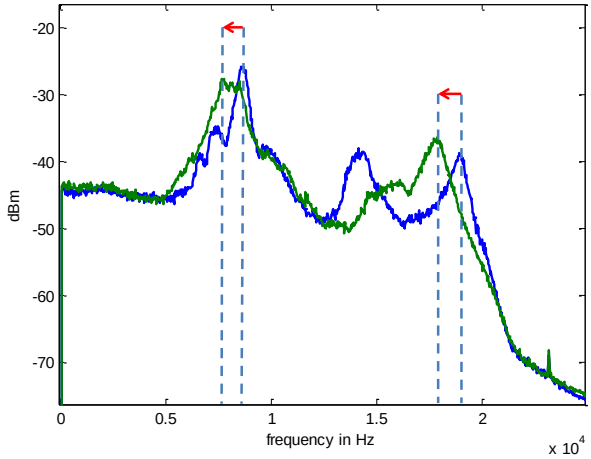

Figure 181 : Frequency response of the undamaged vinylester matrix based sample (In blue) and the 400MPa previously loaded in tension vinylester matrix based sample (in green) for a white noise as input signal

The shift, with an undamaged sample, of the frequency with the maximum amplitude is measured for each damaged samples and for the three considered material. The evolution of this frequency shift is plotted for each material in Figure 182. As for the previous study on NWMS method, a clear damage growth was detected by the method for the epoxy (Figure 182-a) and vinylester matrix based samples (Figure 182-b). However, the frequency shift evolution for the polyamide 66/6 samples, plotted in Figure 182-c, exhibits a great oscillation when the tensile loading value increases. The indicator does not seem to be effective to accurately evaluate the damage state inside the polyamide based samples.

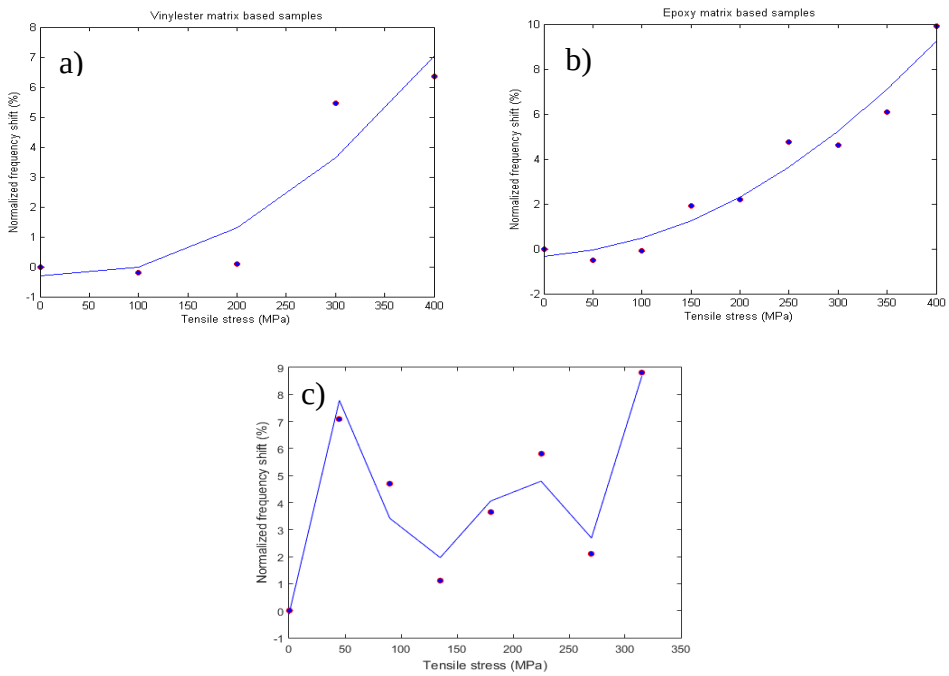

Figure 182 : Normalized frequency shift evolution function of the tensile loading level for the woven glass fiber reinforced and a) Vinylester based samples, b) Epoxy based samples, c) Polyamide 6.6/6 based samples

c) Nonlinear Resonant Ultrasound Spectroscopy (NRUS)

The last considered nonlinear acoustic method is the NRUS. For this method, a single white noise signal is still used as an input signal. However, various input amplitude are considered to investigate a possible nonlinear relation of the frequency with input amplitude when the damage state of the signal increase. For this study, the root mean square of the input signal varies from 0.0092 and 0.2917 Volts. The spectral responses are then plotted for the different amplitudes, to look for this nonlinear relation. In this part the result for only one sample per material are discussed, more specifically the highest damaged sample of each type of composite material. Indeed, they all showed the same tendencies. The considered samples were, a vinylester matrix based sample loaded at 400

MPa, an epoxy matrix based sample loaded at 400 MPa, and a Polyamide 66/6 based sample loaded at 315 MPa.

As it can be observed on the Figure 183, at least three different Eigen frequencies are detected on each composite material, a fourth one is observable on the vinylester based composite samples tested. However, there is no nonlinear relation between the input amplitude and the highest amplitude frequencies; i.e. Eigen frequencies of the sample, for the three tested composite materials. Contrary to what is predicted in the literature, there is no frequency shift when the input amplitude is increasing. Unlike the two other acoustic methods, this last investigated damage evaluation method is not sensitive to the increasing damage state of the samples.

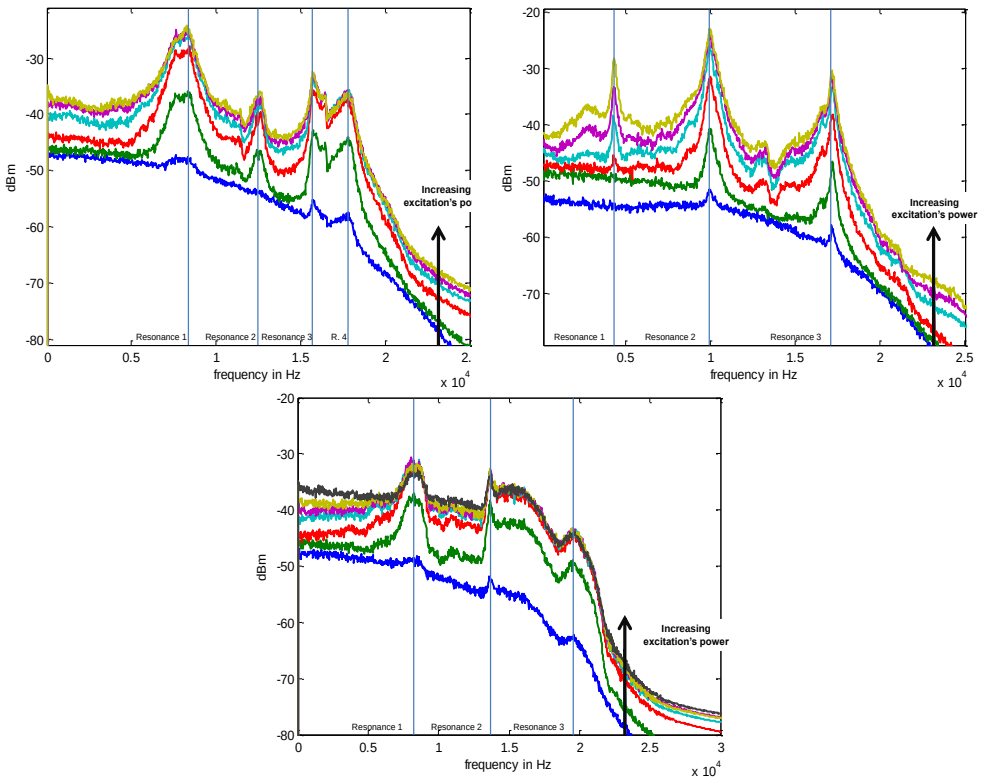

Figure 183 : Spectrum of the epoxy matrix sample damaged by a tensile stress of 400 MPa and excited by white noise under a stepwise increase of the excitation's power for the a) Vinylester samples, b) Epoxy samples, c) Polyamide 66 samples

d) Conclusion

The NWMS as well as the resonance frequency shift study was found successful to evaluate increasing state of damage in the epoxy and vinylester based samples. Yet, as it is known that for loading tests along the fiber's axis only small micros-cracks appear inside the sample, it can be state that both methods are sensitive enough to detect very low level of damage inside composite material. In addition it was observed that the sensitivity to damage of the TDFD parameter, used for the NWMS method, is higher than the normalized resonance frequency shift considered for the other method. Indeed, for the vinylester based composite materials the indicators show an evolution, between the undamaged and the 400 MPa loaded sample, of 100% and 6.2% for respectively the NWMS and the resonance frequency shift method. Similarly, for the epoxy based composite the indicators exhibit an evolution of respectively 200% and 10% between the undamaged and the 400MPa loaded sample. It can be remind that those two methods are respectively nonlinear and linear ultrasound spectroscopy based methods. Hence, the noted difference in sensitivity between those methods are in accordance to the literature review from V)-1)-d) ([83], [84] as an example).

However, those two methods were not able to quantify accurately the damage state for the tested polyamide based composite samples. It may be relative to the different nature of the material matrix. Indeed, both epoxy and vinylester are thermoset matrixes whereas polyamide 66/6 is a thermoplastic matrix. However, further experiments are necessary to assess this hypothesis. Both samples shapes and thickness are in fact different from one sample to another. This make difficult to draw yet a definite conclusion about the origin of the damage indicator evolution's contrast between the polyamide 66/6 based composite and the other investigated materials.

The last considered evaluation method, the NRUS method, was not effective to evaluate damage in any of the tested composite materials. Indeed, unlike what is predicted by the literature, no shift in frequency was noted, for the same sample, when increasing the amplitude of the input signal.

2) Appendix 2: Damage investigation using Coda Waves Interferometry (CWI) technique on a woven carbon fibers reinforced composite material

This study was done in close collaboration with Lynda Chehami during her post-doc position at the LUNE lab from Georgia Tech Lorraine. In this part, the capability of the coda wave interferometry (CWI) technique to evaluate small amount of damage in carbon fibers reinforced polymer based composite samples was investigated. As a recall, a literature review of the CWI technique was proposed in the section V)-1)-e) of this manuscript, and give complementary information about the recent application of this technique. Here the sample was subjected to four points bending at different levels of applied displacement until failure of the sample is reached. Time shift of the later part of the signal (i.e. Coda wave) is investigated by mean of windowed cross-correlation. A description of this chosen post-processing method is also included in the literature review from section V)-1)-e).

a) Presentation of the investigated composite material

It must be emphasized that, contrary to the rest of the thesis manuscript, the investigation of coda waves was performed only on polypropylene sulfide based composite reinforced with eight layers of woven carbon fibers with the following stacking sequence: $[0°/90°, -45°/45°, 0°/90°, -45°/45°]_s$ Indeed, it is known that glass fiber reinforced composite induces a higher attenuation coefficient than for carbon fiber reinforced composite. As explained in the literatures review (Section V)-1)-e)), the Coda Wave Interferometry (CWI) method consists in the study of the later part of the receiving signal. Therefore, to be able to process with more efficiency this coda part with a correct signal to noise ratio it was chosen to consider this carbon fiber reinforced material for the first investigations on this method. Two samples of 160 x 25 x 2.4 mm were produced by water jet cutting. One of those samples is submitted to increasing levels of 4 points bending loading. The method is known to be sensitive to the influence of temperature during the

investigation. Consequently, the other sample is kept undamaged during the experimental procedure and is used as a reference. Acquisitions on this reference sample were performed at the same time than for the damaged sample, i.e. after each four points bending test.

b) Experimental set-up

Monotonic four points bending tests set-up

As mentioned, various displacement levels were consider and applied to one of the carbon fiber composite sample by using four point bending set-up (Figure 184). This is performed in order to investigate the sensitivity to the coda wave interferometry method to quantify this amount of damage accurately. Eleven bending displacement levels were considered, starting from 2 mm to 12 mm with an increment of 1 mm. This 12 mm actually corresponds to the apparition of a visible crack on the surface of the sample and the latter was considered to have consequently reach failure. The resulting force is indicated, for every applied displacement value, in the Table 34. Force/displacement response under bending is plotted in Figure 185 for an applied displacement of 9 and 12mm. The bending test is performed on a tensile test machine (*Zwick Roell Z050*) in compliance with the *ISO 5893* standard. The sample is loaded at a constant displacement of 24mm.min^{-1}. An ultrasonic acquisition is done prior to any bending loading and will be used as a reference. After each bending tests an ultrasonic acquisition is also performed on the reference sample.

Displacement (mm)	**2**	**3**	**4**	**5**	**6**	**7**	**8**	**9**	**10**	**11**	**12**
Force (N)	187	292	399	519	638	761	876	978	1100	1200	1240

Table 34 : Displacement and loading values for monotonic four points bending loading

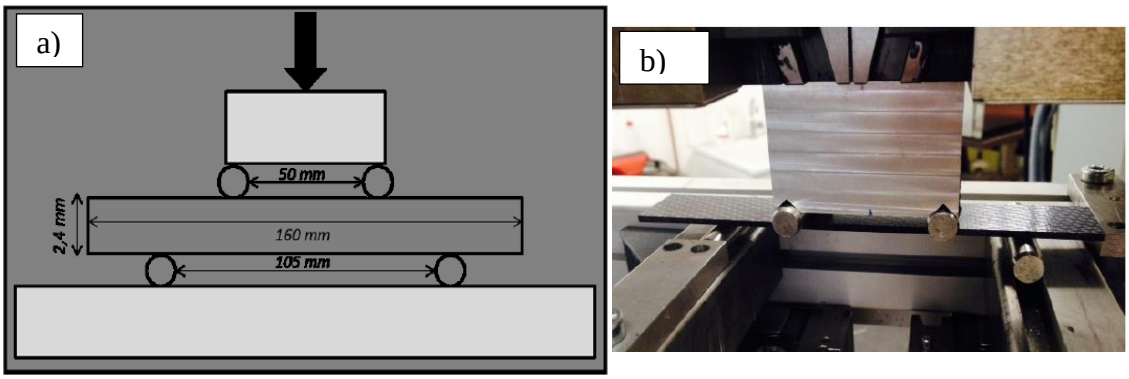

Figure 184 : a) Schematic representation and b) photography of the four points bending setup

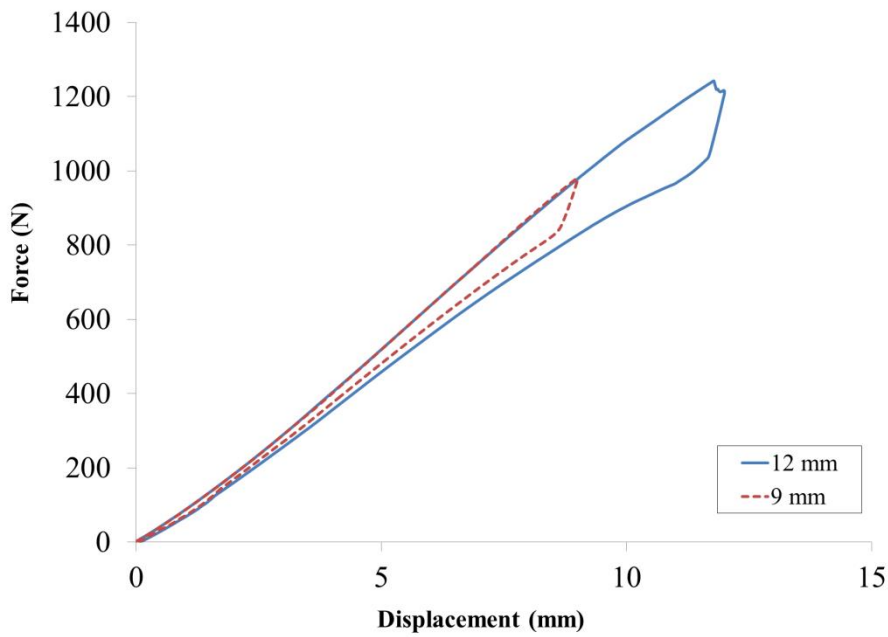

Figure 185 : Force displacement curve for the 12mm and 9mm four points bending tests

A first estimation of the damage was made based on the bending modulus reduction measured after each loading is a similar way than in part III)-4). This estimation of damage was calculated as: $D = 1 - \frac{E_n}{E_0}$; with E_n the unloaded bending modulus for each considered

applied displacement and E_0 the bending loading modulus measured for the first bending test. The evolution of the calculated damage (Figure 186) can be divided into three main steps. From 0 to 3 mm of applied displacement, no evolution is noted yet, micro-cracks are assumed to initiate in the specimen during this step. But after a displacement of 4 mm, a close to linear evolution of the damage could be observed up to 0.13 for a displacement of 8 mm. An abrupt change in the damage sate evolution is noted after this point. The calculated damage then remains around 0.13 from 9 to 11 mm of applied displacement and may indicate a saturation of damage. The displacement of 12 mm actually corresponds to the failure of the sample as mention earlier and consequently this last value of measured damage must be considered with caution.

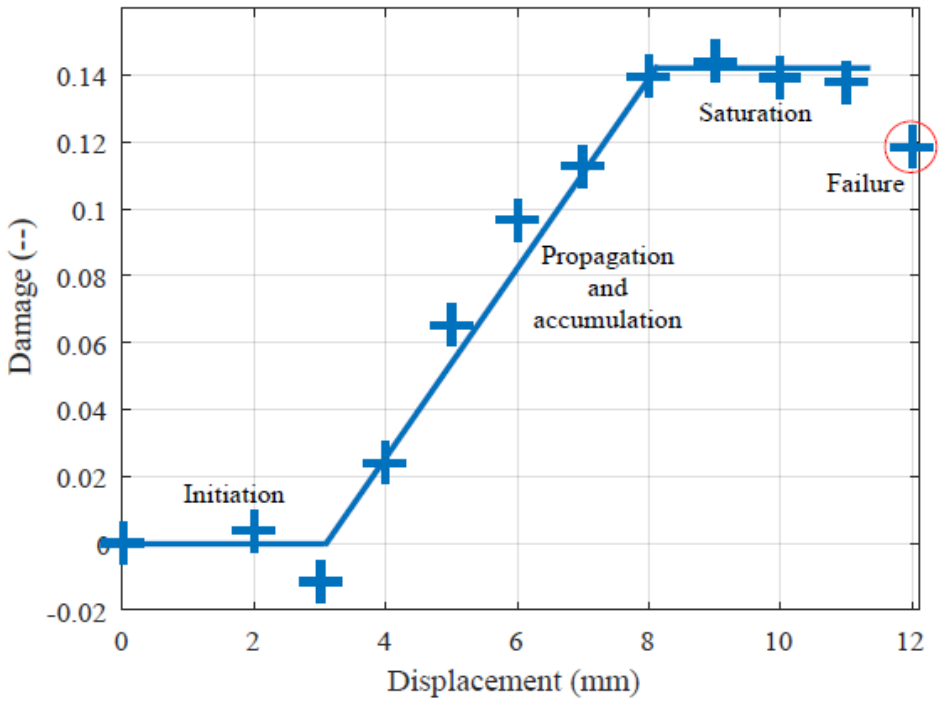

Figure 186 : Evolution of damage, calculated as the reduction of the bending modulus, with increasing the magnitude of the 4 points bending applied displacement

Ultrasonic measurements set-up and processing

All the ultrasonic acquisitions were performed using the following procedure. After each bending tests, two *Panametrics V103* sensors 1MHz PZT disks, polarized longitudinally, are used in transmission. The emitting signal is produce by a waveform generator, *Agilent Technology model*, connected to the first transducer. The emitting signal consists in a sinus burst of 1cycles at a 1MHz frequency with an amplitude of 10 Volt peak-to-peak. The second transducer, in reception, is put at a distance of 83 mm from the first one. The receiving signal is then amplify by 100dB by an amplifier from *Krohn-Hite (model 7500)*, and recorded using an oscilloscope. A coupling gel, *Sofranel coupling Gel-D* is used for both transducers. All the experimental set-up is depict in Figure 187.

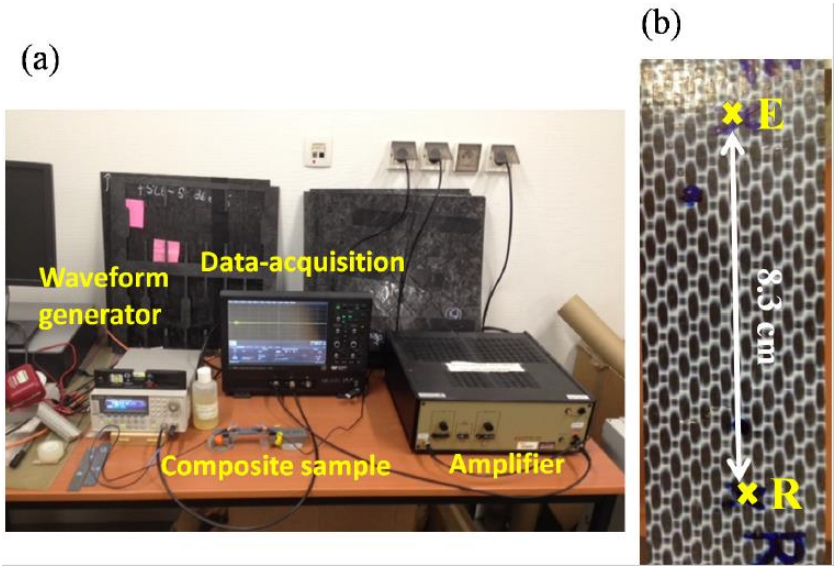

Figure 187 : a) Complete experimental set-up for the ultrasonic signal recording. b) Zoom in on one of the tested sample with indication of transducers position

The length of the recorded signal is set at 1000 µs, after this given time the signal is almost null, as it can be seen in Figure 188, with a low signal to noise ratio which could induce wrong results from the cross-correlation processing later on. Before recording each signal the latter is averaged over 250 measurements, which confers an increasing of the

signal-to-noise ratio. Two signals, respectively recorded before any bending loading and after a bending displacement of 3 mm are plotted in Figure 188. One could see that the first arrivals waveforms [0:150 µs] are relatively similar for the two signals. Some difference in amplitude can be note however; it is probably induce by some slight difference in the transducers coupling with the sample. When look at later arrival part of the signal, difference in time is noted, the 3mm signal appears to be a time shifted version of the other one. This will be more visible after the signal cross-correlation processing discussed later in this section.

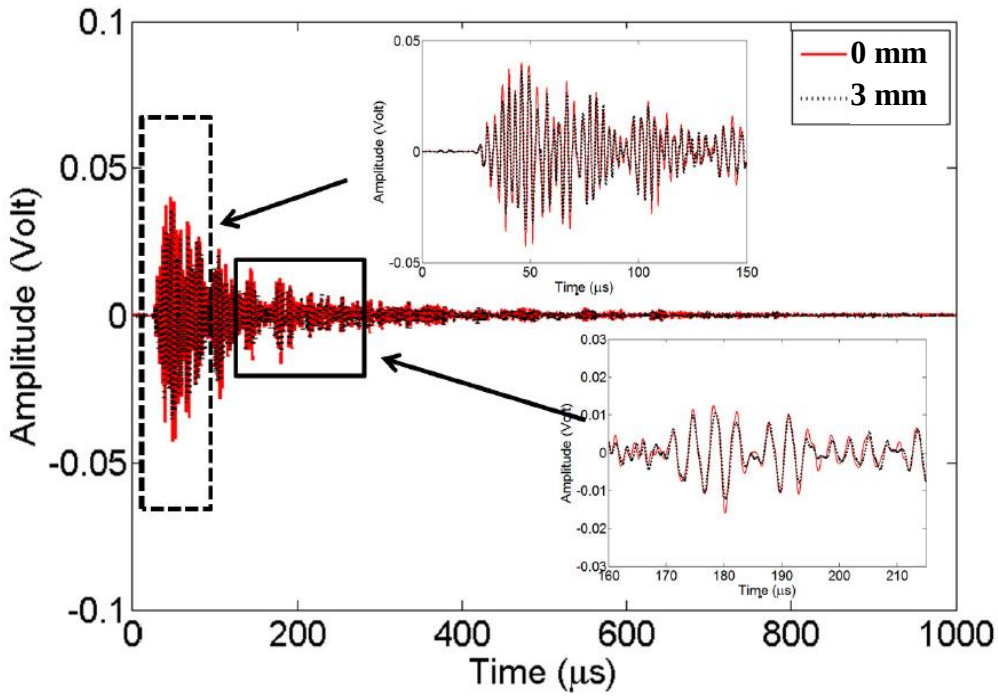

Figure 188 : Signal waveform recorded (in red continuous line) before any loading and (in dashed black line) after 3mm of four points bending applied

In this section, the coda part is considered in the range [200,600] µs where the signal to noise ratio is still relatively high and the multi-scattering regime has started. Indeed, at the considered frequency, the wave was experimentally found to propagate at 3074 m/s in the composite. If a length of 200 µs is considered, the wave has a sufficient amount of time to travel several times in the sample. All the coda parts will consequently have a length of

Tt=400 µs and a sampling time of Δt=0.002 µs. As it was mentioned in [96], [112] for example, when the sample's perturbation is small, the induced relative velocity change of the signal's coda part can be considered as constant. In such a case, the time lag increase with the arrival time. The damage state induced by four point bending will be considered to match this hypothesis. This will be verified with the experimental results that will be presented further on. In order to have a good estimation of δt, the cross correlation must be performed on small part of the signal (i.e. window) where the variation of δt over the time arrival is sufficiently low to be considered as constant. The length T of the windows must satisfy the interferometry hypothesis which is : $T*\Delta F<<1$, with ΔF is the frequency band of the coda signal [113]. In this study, the frequency band of the coda part is of 400 KHz, the time window T must be at minimum 2.5 µs. Here T was set to 50 µs for each window. The cross-correlation coefficient R(ts) is then calculated for each windows by shifting this window over each ts increment with ts between [-T:T]. The time lag that corresponds to the maximum of correlation is measured as well for each window. Each window is spaced by T/2 in order to consider overlapped windows. This allowed smoothing the evolution of the δt with the time arrival. Before choosing the coda part the whole recorded signals, of 1000 µs long, were all adjusted in time in order to have the first wave packet arrival at the same time than for the reference signal. Indeed, the two transducers were positioned by hand after each 4 points bending tests on the sample on marks draw in the samples. This adjustment in the first wave packet arrival was done to reduce influence of bad transducers positioning that could interfere with a correct estimation of relative velocity change. In addition, the applied loading may induce small change in size of the sample which may introduce additional time shift in the calculation of the velocity change. It can be mentioned that on the raw data however, there is no major shift of the first pulse from all the signals recorded after bending tests when compare with signal recorded before any applied loading at the exception of the signals recorded after 6mm of applied displacement.

For the sample 1, submitted to 4 points bending test, all signals are compared with the first signal recorded for this sample prior to any loading. For the sample 2, that is kept undamaged, all signals are compared with the 1st signal recorded from this sample 2. It was

recorded at the same time than the first signal from the sample 1. The evolution of the cross-correlation coefficient and the time lag with the arrival is plotted in Figure 189 for both the damaged and reference sample. The signals for the all the applied loading considered are plotted on each graph accordingly.

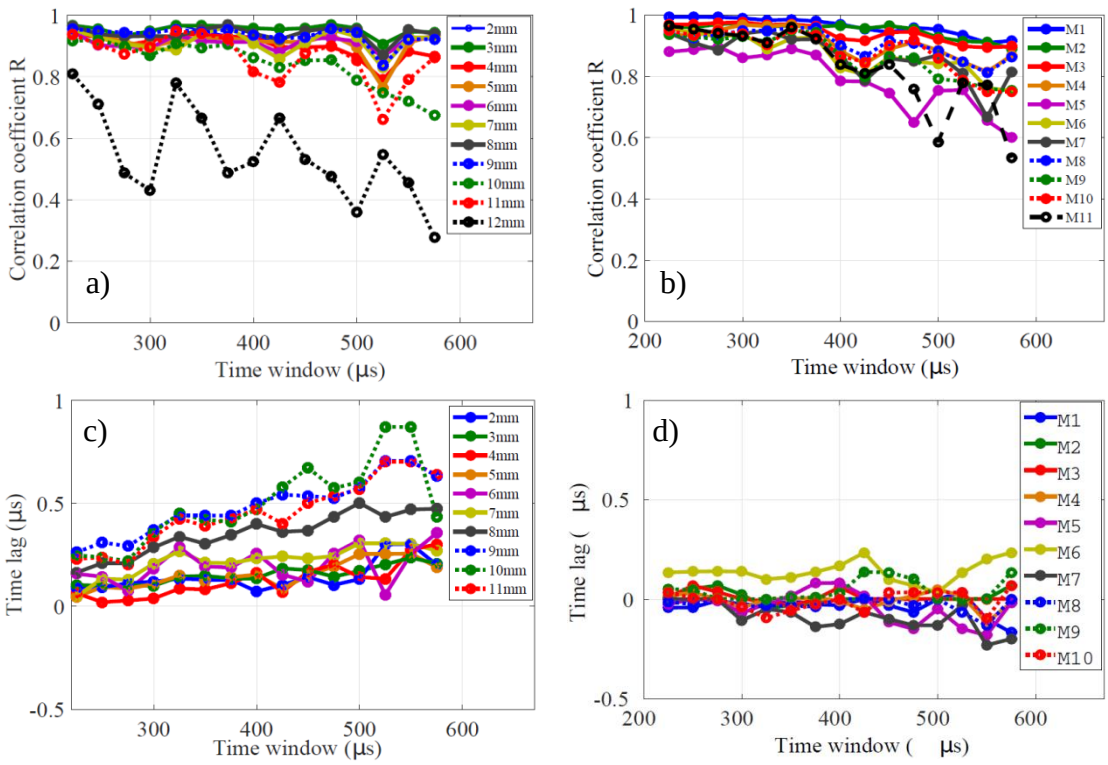

Figure 189 : a) Normalized cross-correlation coefficient between the sample loaded (200-1200N) and the sample before loading. b) Normalized cross-correlation coefficient for the reference sample between different moment and the first signal record for this sample. c) Time shift between the sample loaded (200-1200N) and the sample before loading. d) Time shift coefficient for the reference sample between different moment and the first signal record for this sample

As observed in Figure 189-a, no major evolution of the cross-correlation is observed for the sample damaged from 2mm to 11mm. Its value remains close to 0.8 which indicate

important similarity with the signal before any loading. However, an important decrease of the coefficient is noted after 12mm of loading apply; its value oscillates around 0.5. Here the similarity with the signal before any loading is too low and it was consequently choose to not calculate time shift for this sample. Indeed, since the signals are not similar, the results from the cross-correlation could not be function of simple time-shift only. For the reference sample, the cross-correlation coefficient (in Figure 189-b) remains sufficiently high and does not evolve significantly as the experiment going on.

As mentioned, the time lag that corresponds to the maximum of correlation is extracted for each window on each signal. The results is plotted in Figure 189-c for the sample submitted to four points bending. As explained earlier, the results for the 12mm loading were not considered because of the lower correlation coefficient obtained from Figure 189-a for this loading. A clear evolution of the time lag is observed when increased the displacement loading; it is even more pronounced after 8mm. The time lag increases with the time arrival which confirmed the hypothesis made before. For the reference sample however, the evolution of time lag with the time arrival is limited for every measurement performed; at the exception of the signal recorded after a 6mm loading was applied to the other sample. The time lag is distant from the other measurements but remains mostly constant with the time arrival.

Finally, the relative velocity change $\delta V/V$ is calculated from each signals by estimated the slope of $\delta t/t$ from the Figure 189-c and Figure 189-d. This relative velocity change is then calculated as $\delta V/V = -\delta t/t$ if the effective velocity change is considered as homogenous over the whole sample. The evolution of the relative velocity change $\delta V/V$ for sample 1 with applied displacement is plotted in Figure 190. The same graph is plotted for sample 2 for all the recorded signals on the same figure. For the reference sample (n° 2), the relative velocity change does not appear to be significant at the exception of the measurements number 6 and 10 (Whose correspond to the applied displacement of 7 and 11mm respectively). However, for the sample 1 an evolution of the relative velocity change is noted which seems to involve 3 main steps. This evolution is actually really similar to the

decrease of the bending modulus observed in Figure 186. In order to confirm it, both the normalized decrease of the bending modulus (E_n/E_0) and the relative velocity change are plotted on the same graph in Figure 191. Indeed, from 2mm to 5mm no major change of δV/V can be noted. Then, from 5mm to 9mm an almost linear decrease of the relative velocity variation is observed. Finally, from 9m to 11mm a saturation of the evolution of the damage indicator occurs around 12%. The sample eventually reaches failure for an applied displacement of 12mm, with a large crack that appears between the two transducers.

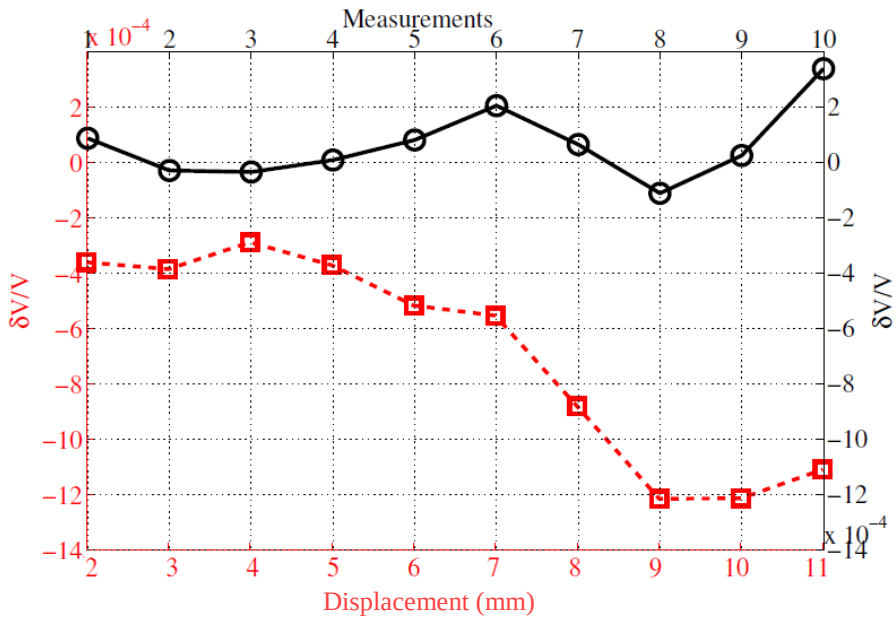

Figure 190 : Variation of δV/V over the whole recorded signals for the sample 1 (in dashed red line) and the sample 2 (in continuous black line)

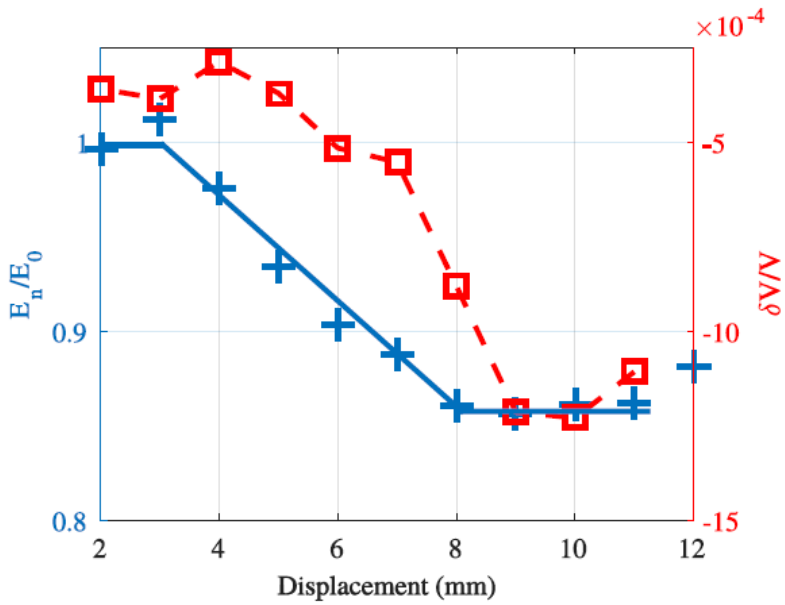

Figure 191 : Relative velocity changes (dashed line) and the normalized bending modulus evolution (continuous line) obtained for different loading values

c) Conclusion

In this section coda wave interferometry technique was found sensitive enough to detect early appearance of damage in a woven carbon fiber composite sample. The damage was induced by mean of four points bending with increasing applied displacement. A reference sample, that remains undamaged, was used in addition in order to estimate the influence of temperature change during the experiment on a sample. For both samples, relative velocity change (δV/V) was calculated by means of cross-correlation comparison with signals recorded before any applied displacement. The relative velocity change was found to starts increasing after 4mm of applied displacement, following with a near linear evolution up to 9 mm and finally saturation of progressive damage until 11mm. The stabilization of δV/V after 9mm was attributed to damage saturation and was confirmed by comparison with the evolution of the bending modulus of the sample when increasing the applied four point bending displacement. Further investigations could be considered to confirm this result.

Some noticeable evolution of δV/V was observed on the reference sample and could induce wrong interpretation on measured signal. Its evolution remains nevertheless lower when compared to the other sample. The observed decreasing of δV/V on the sample subjected to four points bending couldn't then be ascribed to temperature evolution.

This method could therefore worth further investigation in order to confirm the relation between the evolution of damage state and cracks propagation and the relative velocity variation obtain from the coda part investigation. Those additional investigation could help to determine what are the case when the method could be consider under simple hypothesis and when some caution must be taken when interpreting the results. Consequently, at the moment this method should still be used with caution because of the known sensitivity of the method to the transducer's positions on the tested sample and to the ambient temperature change. Nevertheless, the overall methodology is very promising for structural health monitoring because of its sensitivity to small defects, nondestructive aspects and the continuous time monitoring of the health condition of composites. It could be used as a complementary signal processing technique in order to increase the amount of information to analyze to make a proper decision about the damage state of a part. Future investigations should also consider samples submitted to fatigue damage; such tests are indeed closer to the solicitation that a structure may undergo in the industrial field.

DETECTION DE L'ENDOMMAGEMENT DANS UN COMPOSITE TISSE PA66/6|FIBRES DE VERRE A L'AIDE DE TECHNIQUES ULTRASONORES EN VUE D'UNE PREDICTION DE LA DURABILITE DE PIECES AUTOMOBILES

RESUME : Ces travaux de thèse portent sur l'étude expérimentale approfondie d'un composite à base polyamide 66/6 renforcé par des fibres de verres tissées suivant un motif sergé 2/2. L'objectif est de proposer des solutions de Contrôle Non Destructif (CND) basées sur les ultrasons afin de détecter différents niveaux d'endommagement induit. Pour cela, une étude approfondie des mécanismes d'endommagement apparaissant lors de sollicitations en traction suivant l'axe des fibres et hors axes est réalisé. Le cas d'impact induit par poids tombant est également étudié. En effet, ces différents cas de sollicitions entraînent l'apparition de différents mécanismes d'endommagement. Ces derniers, ainsi que leur ordre d'apparition, sont caractérisés par Microscopie Electronique à Balayage (MEB) et tomographie à rayons X principalement. L'évaluation de la réduction du module élastique pré et post chargement ainsi que la fraction volumique de vides montrent une évolution de l'endommagement plus importante lors de chargement en traction hors axes des fibres que lors de chargement suivant l'axe. Lors des essais d'impact par poids tombant, différents niveaux d'énergie sont considérés en restant proche du domaine des BVID en vue d'éprouver la sensibilité des méthodes de CND. Deux méthodes de CND par ultrasons étudiées durant ce projet peuvent être mises en avant. Premièrement, par mesure de la vitesse de propagation des ondes dans plusieurs directions du composite, le tenseur de rigidité est estimé dans tous ces cas de sollicitation mécanique pour différents niveaux d'endommagement. Des indicateurs d'endommagement basés sur ces mesures montrent une évolution de l'état d'endommagement similaire à celle discutée précédemment. Deuxièmement, une étude de la détection de l'endommagement par ondes guidées est menée. Aucun changement des modes transmis n'est visible lors de l'augmentation de l'état d'endommagement. L'évolution de l'énergie du signal transmis est alors proposée et validée comme indicateur d'endommagement efficace pour des chargements en traction mais pas pour l'impact. La mesure du décalage temporel a en revanche permis une localisation et une quantification de l'endommagement induit par impact.

Mots clés : Matériau composite, Contrôle Non Destructif (CND), Ultrasons, Endommagement

DAMAGE DETECTION IN PA 66/6|GLASS WOVEN FABRIC USING ULTRASONIC TECHNIQUES TOWARDS DURABILITY PREDICTION OF AUTOMOTIVE PARTS

ABSTRACT: The present study is focused on the experimental study of a polyamide 66/6 based composite reinforced by a 2/2 twill weave glass fabric. The aim is to propose Non Destructive Evaluation (NDE) methods based on ultrasound that can efficiently distinguish different damage states. In order to do so, an investigation of the damage mechanisms induced by different types of mechanical solicitations. Tension along and off the axis of the fibers was considered as well as the case of drop weight impact. Those solicitations were shown to induce different damage mechanisms. The latter were characterized by means of Scanning Electronic Microscopy (SEM) and X-Ray tomography mostly. The decreasing of the elastic modulus and the void volume fraction evolution were shown to be more significant for the samples loaded in tension off-axis. During the drop weight impact tests, the energies were considered in order to remain close to the Barely Visible Impact Damage (BVID) regime and to experience the capability of the ultrasound based NDE methods. Two NDE methods investigated during this study deserve to be highlighted. Firstly, the stiffness tensor was estimated by means of phase velocities measurements in different propagation direction. Damage indicators based on results from this method were proposed. They were found to give results similar with those from the evaluation of damage discussed earlier on. Secondly, a study of the damage detection using guided waves was performed. No mode conversion effect was observed from this investigation. Consequently, the signal energy was proposed as damage indicator and was found to be suitable to detect damage induced by tension but not by impact. The measure of time shift allowed obtaining a localization and evaluation of the damage induced by impact.

Keywords: Composite material, Non Destructive Testing (NDT), Ultrasonic wave, Damage

ARTS ET MÉTIERS ParisTech

ParisTech INSTITUT DES SCIENCES ET TECHNOLOGIES PARIS INSTITUTE OF TECHNOLOGY